Università degli Studi di Udine

DPIA
Ph.D. degree in Industrial and Information Engineering
Cycle XXXIII

Flexural Vibration Measurement and Sound Radiation Estimate of Thin Structures with Multiple Cameras

Ph.D. student:
Roberto Del Sal

Tutor:
Roberto Rinaldo

Cotutor:
Paolo Gardonio

Year 2021

Acknowledgements

My heartfelt thanks to my thesis supervisors Prof. Roberto Rinaldo and Prof. Paolo Gardonio who provided me with wise guidance whenever I needed it. In addition, I would like to thank Prof. Alessandro Zanarini who helped me through the experimental part of the thesis providing his technical equipment and expertise. My gratitude goes to Prof. Andrea Fusiello whose contribution was essential for the successful outcome of this work. I would also like to thank Dr. Loris Dal Bo and Dr. Emanuele Turco for their support throughout the Ph.D. program.

Final and most important thanks to my mother and my father. For everything.

Contents

Abstract

This thesis presents a simulation and experimental study focussed on the measurement of flexural vibration and on the estimate of the sound radiation of distributed structures by optical means and in particular by using multiple, i.e. more than two, synchronous cameras. The study considers two model problems composed by a cantilever beam and a plate excited by a tonal force at the first three fundamental resonance frequencies of flexural vibrations. The study has therefore considered the measurement of the deflection shapes at these frequencies, which accurately approximates the first three flexural mode shapes. The study is organized in four parts. The first part introduces the state of the art about the topic and revises the theoretical principles concerning optical measurements. The second part presents a simplified optical model employed to simulate how the accuracy of the measurements of the first three flexural deflection shapes of the structures here considered varies with respect to: a) the distance of the cameras from the structure; b) the angle of aperture between pairs of cameras; c) the elevation angle formed by the optical axis of the camera and the plane of the structure; d) the resolution of the cameras and e) the number of cameras. The principal objective of the study was indeed to show how the accuracy of the measurements can be significantly increased by using multiple cameras. The third part of the study provided experimental results taken on a beam rig and camera setup assembled using off-the-shelf devices. The experimental study focussed on the first flexural deflection shape of a cantilever beam and confirmed the findings of the simulation studies. The simulations and experiments presented in this work, quantify and confirm that the use of multiple cameras allows good vibration measurement accuracy, even at low spatial camera resolutions. Since the frame-rate and cost of cameras is limited by the amount of data they can process in each time unit, these results suggest that multiple, relatively cheap, high-speed, low-spatial resolution cameras can be used to perform vibration measurements in practical applications. The fourth part of the study examines the sound radiation generated by vibrating structures. In particular, it is evaluated how the accuracy of the estimate of the sound radiation emitted by the reconstructed first three flexural deflection shapes of a plate varies with respect to: a) the distance of the cameras from the structure; b) the azimuthal angle between the cameras; c) the elevation angle of the cameras; d) the resolution of cameras and e) the number of cameras. The principal objective of this fourth part was to understand if the results obtained on the influence on the flexural vibration measurements of the parameters listed above, could be applied to the case study of the estimate of the sound radiation.

Chapter 1

Introduction

This first chapter aims to introduce the two main topics that will be studied in this thesis: first, the measurement of flexural vibration of thin structures with multiple optical cameras and second the estimate of sound radiation of thin structures from the measured flexural vibrations with multiple optical cameras. To start with, the principal features of flexural vibrations of thin structures are recalled here. Then, the typical sensors for vibration measurements are revised. In parallel, the principles of sound radiation by thin structures and the sensors used to measure acoustic field are revised. Finally, vibration measurement with optical cameras are thoroughly introduced.

1.1 Vibration of distributed mechanical systems

This section presents an overview of the vibration theory of distributed structures.

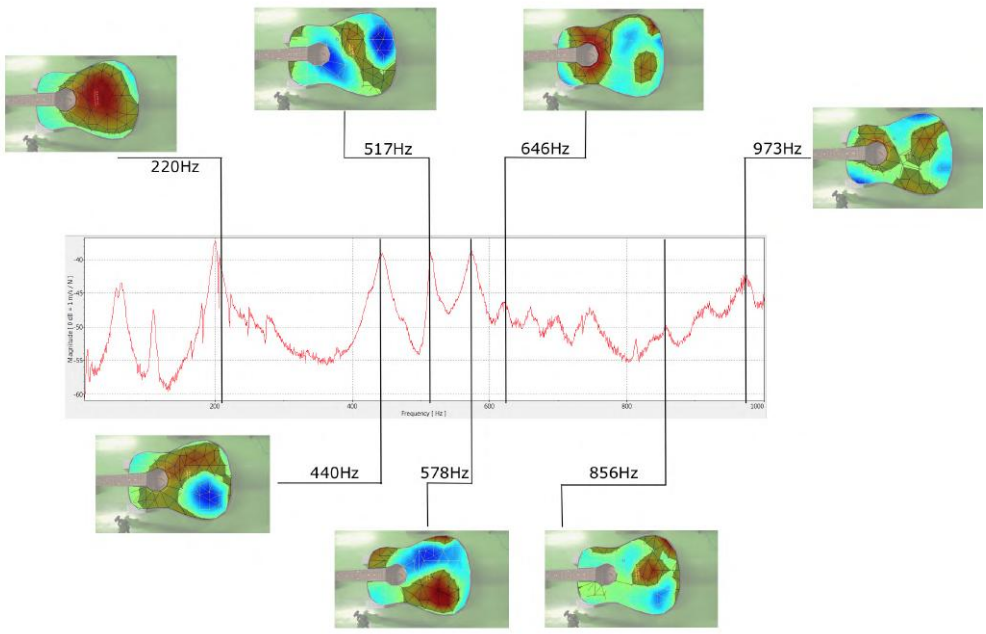

Figure 1.1: First seven natural mode shapes for the flexural vibration of a guitar body.

The vibrational characteristics of a distributed structure are mainly dependent from the distributed mass and the distributed stiffness properties of the structure itself. These mechanical effects determine a number of frequencies, the so-called natural frequencies, at which the structure vibrates showing specific displacement patterns also called natural modes. In general, when a structure is excited harmonically at a generic frequency ω, these vibration patterns coexist. More specifically, the flexural response is given by the superposition of second order modal resonant responses, each characterized by a specific resonance frequency, which is close to the natural frequency, and by the respective spatial distribution given by the natural mode shape. Normally, when the structure is excited harmonically at its resonance frequency, the flexural response is controlled by the resonant mode shape [2], [3]. For example, Fig. 1.1 shows the first seven natural mode shapes for the flexural vibration of a guitar body.

Many examples of the application of modal analysis can be found in the design of surfaces (cars, trains, ships, etc) and air vehicles (helicopters, aircrafts, rockets). Experimental modal analysis can be conducted by using both contact and contactless sensors: the former include accelerometers and strain gauges while the latter consider optical sensors. The following Section 1.2 briefly summarizes the principal aspects of these techniques.

1.2 Sensors for vibration measurements

Experimental modal analysis consists on the measurement and study of the spatial response, i.e. the deflection shape, of a structure. Three types of excitations can be used: a single frequency excitation, a random excitation or an impact excitation. The first two are usually obtained through a mechanical shaker which infers a sine or a random signal through the structure. The latter can be obtained with a modal impact hammer. The applied force is measured using contact sensors, such as accelerometers or strain gauges, or using contactless sensors, such as optical sensors. In this section, a brief review of the sensors previously mentioned is presented and the advantages and disadvantages of each device are discussed.

1.2.1 Seismic sensors

Seismic sensors are contact sensors used to measure the acceleration of a structure. They are made of a small elastic piezoelectric element with on top a seismic block mass. The piezoelectric element measures the inertial force exerted by the mass, which is actually proportional to the base acceleration of the sensor. Accelerometers are widely used for dynamic measurements of mechanical structures thanks to their low cost and ease of implementation. On the other hand, accelerometers can only provide measurements at discrete locations. This represents one of the main disadvantages of these sensors. Indeed, in order to fully characterize the dynamics of a distributed structure, a large number of accelerometers is required, which results in a consistent increment of the costs for the measurement

setup and in a significant increment of mass on the test structure, so that the measured mode shape may be affected by consistent errors [4].

Figure 1.2: Example of an accelerometer.

1.2.2 Strain sensors

Strain sensors are contact sensors which measure strain based on the variation of a specific quantity of the sensor. The most common strain sensor are strain gauges, which measure induced strain on a specimen (normally a thin wire) from the variation of its electric resistance or piezoelectric properties. Other types of strain sensors can be found on the market such as capacitive strain gauges or inductive strain gauges. All these devices measure induced strain but in slightly different ways: for example in capacitive strain gauges, the strain is measured from the relative distance between the plates of a capacitor; in inductive strain gages, strain is measured from the variation of inductance of a LVDT (i.e. Linear Variable Displacement Transducer) sensor. Similarly to accelorometers, strain sensors are easy to implement and low cost. However, they can present wiring issues and induce mass loading or stiffening effects on the test structure. Furthermore, as accelerometers, strain gauges only provide measurements at discrete points of the structure, therefore a high number of devices is required to describe completely the dynamics of the structure. This issue causes a raise in the cost of the measurement system [4].

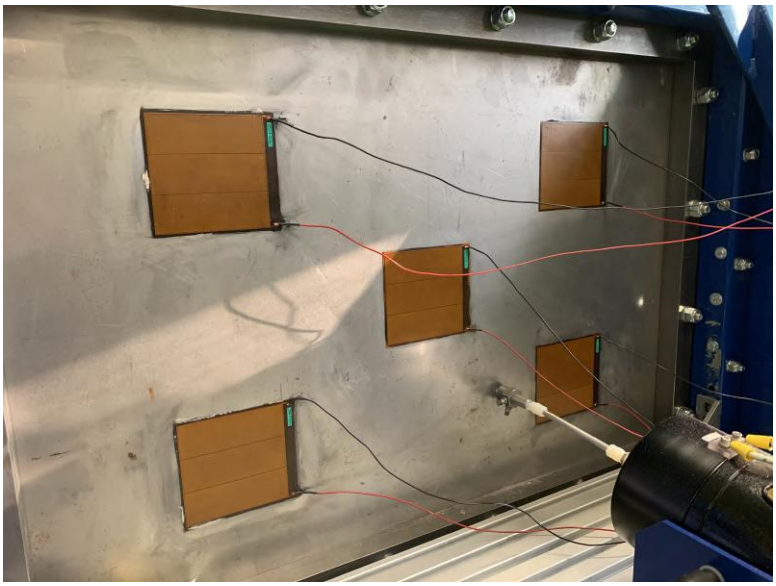

Figure 1.3: Piezoelectric patches implied for flexural vibration measurements of a thin plate.

1.2.3 Optical sensors

As mentioned before, the most relevant limits of the contact techniques concern the addition of mass, stiffening effects and the possibility to measure only in discrete positions of the test structure. In order to avoid this kind of issues, contactless techniques, such as optical measurement systems, have been developed: the most reliable optical methods are pattern interferometry, laser Doppler interferometry, and photogrammetry [4]. The interferometry technique is based on the superposition of two coherent light patterns which create an interference fringe pattern: by measuring the displacement between these patterns it is possible to measure the vibration of the studied structure [5]. This technique considers a light beam which is split into two waves: one is sent towards the studied structure while the other one is considered as the reference wave. The former wave impinges the structure and is reflected. As a result, this wave suffers from a shift of phase with respect to the reference wave. This discrepancy in phase allows to estimate the displacement of the vibrating structure. The first technologies developed were photograph-based speckle interferometry, holographic interferometry (HI), electronic speckle pattern interferometry (ESPI) and digital speckle shearography (DSS) [4]: in all of these, the phase shift between the reflected wave and reference wave is the discriminant for the evaluation of the displacement. Another interferometry technique is the Laser Doppler Vibrometer (LDV) whose working principle is similar to the techniques discussed above, although in this case the discriminant is the shift in frequency between the reflected and the reference wave. In order to perform a 3D measurement, three laser vibrometer devices are required. An LDV measurement system presents several advantages in comparison with the interferometry techniques previously seen. For example an LDV has a wide frequency working range and can be applied to very small objects. On the other hand, LDV provides single points measurement only at a time, thus the measurements are usually very time-consuming.

Moreover, three laser vibrometer devices are required in order to perform a 3D measurement, thus LDV is also a very expensive technique. The last technique reviewed in this section is the photogrammetry technique: this is a non-contacting, image based, full-field measurement system in which the vibrations of the tested structure are measured with reference to specific points of the structure. Photogrammetry is generally employed for measurements in which vibrations are characterized by low frequencies and high-displacements [6], [7]. This technique can also be used in harsh environments [5] and, in contrast to LDV, it is not very sensitive to ambient vibration [8]. Photogrammetry is also widely implemented to detect transient phenomena (i.e. the test object is time-variant or sensitive to temperature [9]). The principal disadvantages of this technique concern the limited frequency range in which photogrammetry can be applied and the time-consuming post processing of the acquired data.

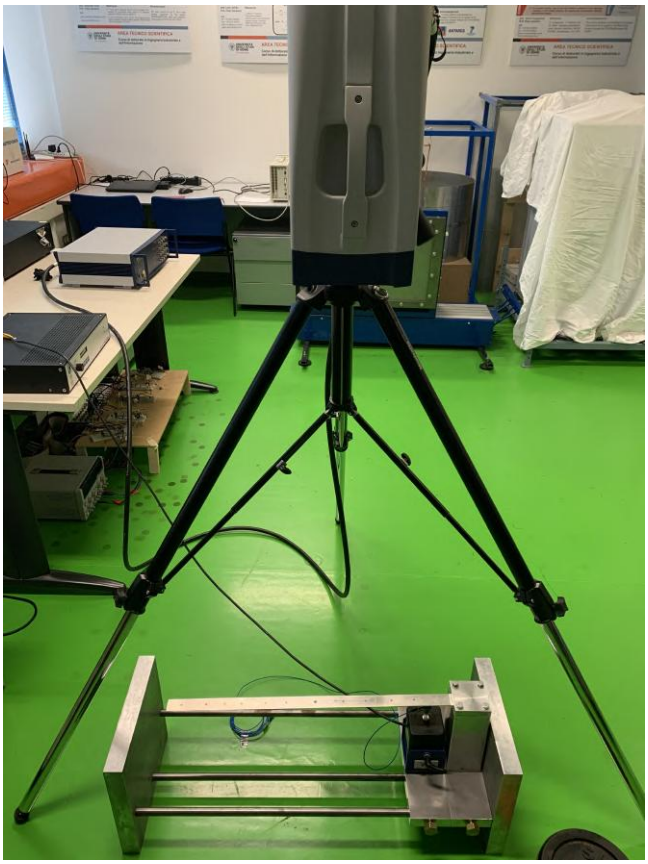

Figure 1.4: Setup for vibrations measurements comprehensive of a vibrometer.

A comprehensive comparison between sensors for vibration measurements is shown in Table 1.1.

Table 1.1: Comparison between vibration measurements sensors [4].

Point-wise sensors (Accelerometers, strain gages)	**Interferometry (ESPI, DSS)**	**Laser Doppler Vibrometer**	**Photogrammetry**
Contact	Non-contact	Non-contact	Non-contact
Easy to obtain transfer functions	Needs post processing to obtain transfer functions	Easy to obtain transfer functions	Needs post processing to obtain transfer functions
Data only at the location of transducers	Data on entire visible surface of the object	Data at pre-defined points on visible surface of the object	Data on entire visible surface of the object
Sensitivity for each point depends on the transducer	Sensitivity goes down as the field of view gets larger	Sensitivity is related to laser light wavelength	Sensitivity goes down as the field of view gets larger
Wide frequency range	Better for low frequency measurements	Widest frequency range	Better for low frequency measurements
Not sensitive to rigid body motions motions	Calibration is highly sensitive to changes in setup conditions	Calibration is highly sensitive to changes in setup conditions	Calibration is less sensitive to changes in setup condition
Inexpensive	Expensive	Very expensive	Expensive
Low spatial resolution	Very high resolution	High spatial resolution	Very high spatial resolution (DIC)
Hard to extract rigid and flexible modes with one type of transducer	Applicable for simpler spatial deformation	Applicable for simpler spatial deformation	Very accurate for spatially complex deformations
Fast measurement	Very fast measurement	Very time consuming measurement	Very fast measurement
Very fast data processing	Fast data processing	Fast data processing	Can be time consuming (DIC) or fast (PT) data processing
Can be real-time	Can be real-time	Can be real-time	Usually works off-line
Only measures displacement, strain or acceleration	Measures both displacement and strain	Measures velocity; can measure strain (with extra equipment)	Measures both displacement and and strain (DIC)
Difficult to be used for rotating structures due to wiring	Applicable for rotating structures	Difficult to be used for rotating structures	Appropriate to be used for rotating structures

1.3 Sound radiation by distributed mechanical systems

This section briefly introduces the concept of sound radiation and the devices that are most frequently used to measure sound radiation for scientific purposes. Acoustics is defined as the dynamics of small perturbations of a compressible fluid whereas sound is the resulting of a wave phenomenon in which the energy emitted by a source is transported through a medium (for example the air) via pressure waves. Therefore, the energy is propagated in the surrounding space through vibrations and fluctuations of the medium. The sound wave can be detected by a receiver, such as for example the human ear, or an instrument, such as for example a microphone. A sound wave is normally composed by harmonic components. In summary, sound pressure or acoustic pressure is the local pressure deviation from the ambient (average or equilibrium) atmospheric pressure, caused by a sound wave [2].

Sound waves can produce undesired effects. In this case they are normally referred to as noise. Detection of noise is crucial in many engineering fields particularly where it is desirable to minimize unwanted sound radiation due to the vibrations of a structure or machine. Thus, in the last years, the study of sound radiation by distributed mechanical systems has became more and more relevant particularly for surface (e.g. cars, trains, ships) and air transportation vehicles (e.g. helicopters, aircrafts etc.) for industrial machinery and for public and private buildings [10].

1.4 Sensors for sound radiation measurements

A mechanical vibrating system is considered as a source of sound. One way to derive the sound radiation by a flexible body is to discretize the surface of the body into small elements, whose size could be eventually brought down to be infinitesimal, and then calculate individually the sound radiation of each element, which is then combined with radiation of all other elements to get the resulting sound field. For example Fig. 1.5 shows the sound radiation of a guitar estimated from the measured vibration of the body.

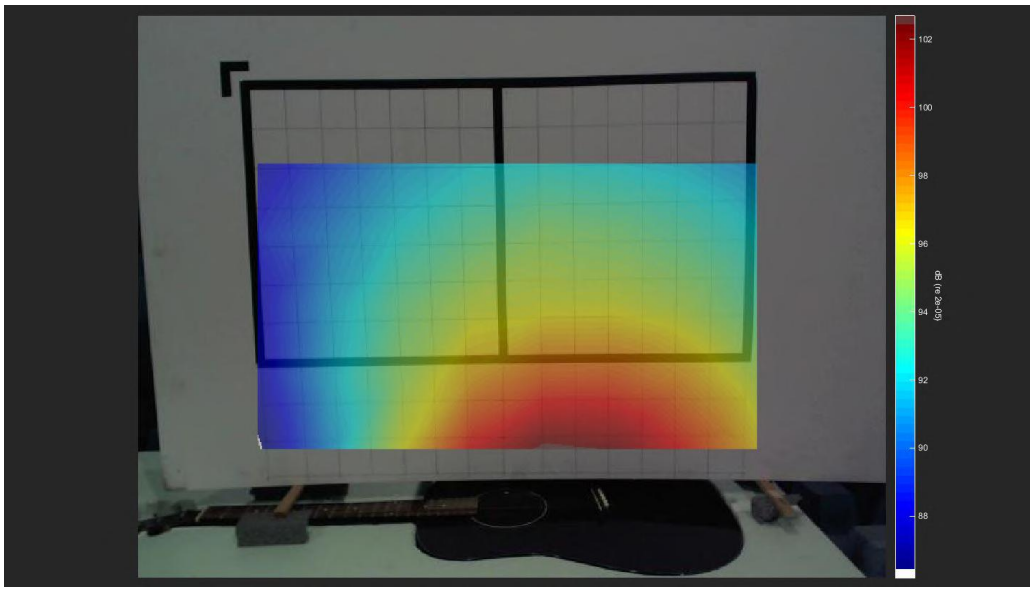

Figure 1.5: Estimate of the sound radiation emitted by a guitar.

In a certain point of the surrounding space, the detected sound pressure is the sum of the contribution of the radiated sound of each of the elementary components of the source [2]. In air, sound pressure can be measured using a microphone. Sound radiation probes are also often used in engineering studies. These devices measure the sound pressure and the particle velocity at a given point of the sound field. Multiplying the measure of acoustic pressure and particle velocity, it is possible to calculate the acoustic intensity. In the following subsections these devices will be briefly reviewed as they are the most commonly used sensors for sound radiation measurements.

1.4.1 Microphones

A microphone is an electro-acoustic transducer that converts sound pressure into electric signals. In engineering applications there are different types of microphones, however the most commonly used are condenser microphones and piezoelectric microphones. A condenser microphone works on a capacitive principle which recalls the capacitive strain gauges working principle. It is composed by a metal diaphragm that forms one plate of a capacitor. A metal disk is placed close to the diaphragm. When a sound field impinges the transducer, the capacitance between the diaphragm and the metal disk varies with respect to the variation of the sound pressure. In this way, an electric signal proportional to the sound pressure can be produced based on the variation. Piezoelectric microphones use piezoelectric crystals which produce an electric signal when they undergo the acoustic pressure load by means of the inverse piezoelectric effect. These microphones have low sensitivity levels, however they are durable and able to measure high amplitude pressure ranges. However, the floor noise level on this type of microphone is generally high. Thus, these microphones are mainly used for shock pressure measurement applications or for underwater measurements of sound.

Figure 1.6: Example of a capacitive microphone.

1.4.2 Sound radiation probe

A sound radiation probe is a hot-wire anemometric device, i.e. a thermal transducer, equipped with a microphone. Hot-wire anemometers allow to calculate the particle velocity from electric voltage measurements. This technique is characterized by very high spatial resolution and frequency response characteristics. The working principle is based on the fact that the acoustic flow of the fluid has a cooling effect on the wire, which reduces its resistance. Measuring the change of the resistance gives a signal proportional to the volume flow rate of the fluid. Thus, multiplying the sound pressure measured by the microphone and the velocity of the fluid detected by the hot-wire it is possible to calculate the acoustic intensity emitted by the source.

Figure 1.7: Example of a sound probe.

1.5 Vibration measurements with cameras

The interest in optical techniques has received increasing attention in the literature, since, thanks to the recent advances in optical hardware and computational power, they allow accurate contactless measurement of vibrations. A comprehensive review of the optical techniques used in the context of vibration measurements can be found in [4]. Among these techniques, this study is focused on image-based systems, which rely on photogrammetry and scene reconstruction by means of digital images. Generally, optical measurement techniques can be categorized in two groups: those based on laser beams, such as LDV, ESPI and DSS, and those based on white light, i.e. the so called image-based systems, such as photogrammetry.

The first studies on perspective and photogrammetry belong to Leonardo Da Vinci [11]. In its early stages, this technique was predominantly employed for aerial and terrestrial applications related to military activities. The advances in digital camera technologies and the consequent fall in the costs of application of these appliances opened the doors of the scientific field to photogrammetry. Indeed the possibility to buy relatively low cost high resolution cameras brought to a vast range of applications in mechanical and civil engineering that have developed into several branches of photogrammetry such as the close range photogrammetry, videogrammetry, dynamic photogrammetry, computer vision etc. [12].

The early applications of photogrammetry concerned 2D problems that required the use of only one fixed camera (i.e. detection of in-plane displacements of a structure). The introduction of the stereovision concept (Pulfrich and Fourcade [11]) led to the 3D photogrammetry which expanded the field of interest to out of plane deformations. In the early stages, 3D photogrammetry only concerned rigid body displacements, until Peters and Ranson introduced in 1980 the possibility to employ 3D photogrammetry to measure the mechanical stress/strain that occured during deformation in structures [13]. Moreover, Peter and Ranson introduced the concept of subset which was expanded by Sutton, Chu and colleagues [14], [15] to introduce 2D Digital Image Correlation (2D DIC) on a specimen. There, the idea is to monitor in time, through a series of consecutive images, the displacement of a predefined pattern on the test object in order to reconstruct the displacement of the object itself.

The most recent improvements in photogrammetry concern the use of multiple cameras [16]: the application of the stereovision principles extended to multiple cameras, which have brought to the possibility of measuring objects from multiple views improving the reliability and the accuracy of the measurement [1]. Some specific techniques proposed in the literature are based on single camera setups. In [17], the authors propose a single camera stereo acquisition procedure using a four-mirror adapter that creates artificial images with multiple views in the image sensor. These images are further processed to retrieve the vibration information. A similar idea is considered in [18], where information about the vibration periodicity is exploited to limit the camera frame-rate. Similar setups are considered in [19], [20]. In the last years photogrammetry and DIC have been applied to the field of experimental

solid mechanics [21], aerospace industry [22], 3D shape measurement [23], civil engineering and bridge inspection [24].

In conclusion, the recent improvements in camera technologies has significantly raised the interest on photogrammetry for measuring the vibrations of flexible distributed structures. Stereophotogrammetry, point tracking and target-less vision are the new frontier of innovation in measuring vibrations [4].

Figure 1.8: Multi-camera optical setup for flexural vibration measurements of a thin beam.

1.5.1 Principles of digital photogrammetry

As mentioned in the previous section, digital photogrammetry is a non-contacting measurement technique which involves the use of imaging sensors: these sensors can be CCD, i.e. charge-coupled devices, CMOS, i.e. complementary metal-oxide semiconductors, or infrared cameras.

In-plane displacements can be detected using a single camera while out-of-plane displacements (i.e. 3D measurements) are performed using stereo cameras which simultaneously record a series of images from fixed positions. Optical targets or patterns are identified in the recorded images and tracked to reconstruct deformations. In order to successfully detect these optical targets, a calibration process is needed: this technique allows to define both intrinsic and extrinsic parameters of the cameras [25]. Usually, calibration is performed by recording several images of a predefined pattern, generally a checkerboard pattern, from cameras deployed in fixed position (i.e. the position that will be subsequently used for the vibration measurement).

In broad terms, point-tracking (PT), digital image correlation (DIC) or target-less approaches are the three categories in which photogrammetry can be divided based on the type of targets used [4].

- *Point tracking*

  The point tracking technique is based on the identification of the coordinates of discrete points, the so-called markers, printed to the structure. To simplify their identification, the markers are usually high contrast circular points or retroreflective targets. During the post processing step of the measurement, an algorithm is used to identify the markers in each image while the triangulation technique is implemented to find the coordinates of each identified marker. To derive the displacement of the studied structure, the coordinates of the markers in each different image, which represents a different time stage, are compared to the coordinates at a reference image, which represents a reference time stage (usually the first one).

- *Digital image correlation*

  Digital image correlation considers a high contrast random pattern attached on the structure composed by elements, which are usually smaller that the ones used in 3D point tracking (3DPT). In DIC, the algorithm for the identification of the markers is based on grey-scale variations. Thus, this technique creates overlapping subsets which, because of the random disposition of the markers on the pattern, are composed by unique light intensity values. The algorithm will reconstruct the displacement of the structure by recognizing each unique subset through different images, i.e. through different time steps. The sequence of images is thus correlated with respect to the reference image to find the position of the measured structure [26]. In conclusion, DIC is a full-field measurement technique that allows to measure displacements and strain of flexible distributed structures.

- *Target-less approaches*

  Normally, target-less approaches are not as accurate as 3DPT or DIC [27] but they present the big advantage that they do not need any marker attached on the structure. Thus, they can be implemented where there is no possibility of patterning the surface of the object. In fact, in target-less approaches internal features or edges of the structure are assumed as the discriminant for the displacement detection of the structure. The most common algorithms used to detect the structure are thus edge detection, pattern matching and blob detection [28], [29]. The edge detection algorithm can be based on wavelet and sub-pixel methods [30], [31]. In this case it is possible to identify the edge of a structure by examining the variation of grey level intensity value during the vibration. The pattern matching method [29] and cross correlation method [32], [33] are based on the identification of the maximum similarity between portions of two or more images. In this case, it is possible to reconstruct the displacement of the structure by evaluating

the position of similar fragments of images through different time steps.

1.6 Preliminary considerations and motivation for this study

This thesis investigates the measurement of flexural vibrations and sound radiation estimate of distributed structures with multiple, i.e. more than 2, cameras operating synchronously [1], [4], [11], [12]. Apart from specific techniques based on single camera setups, such as those presented in Refs. [17], [34], in general, two high frame-rate and high-resolution cameras are necessary to reconstruct the 3D transverse displacements produced by flexural vibrations of thin structures by means of triangulation using 3D point tracking (3DPT) [7], [25], [35], [36], [37], [38], [39] or 3D digital image correlation (3D DIC) [15], [40], [41], [42], [43], [44], [45], [46]. Normally, the amplitude of flexural vibrations of distributed structures tends to decrease asymptotically with frequency [15]. Therefore, even if the measurement were limited in the low audio frequency range, say below 1 kHz, high frame-rate and high spatial-resolution cameras would be necessary to generate a good quality measurement [47], [48], [49], [50], [51], [52]. However, the frame-rate of cameras is limited by the amount of data ought to be processed and stored for each recorded frame, that is by their spatial-resolution [36]. Therefore, in practice, a compromise has to be found between the resolution of the cameras, that is the accuracy of the measurement, and the speed of the cameras, that is the maximum frequency of the measurement. As a matter of fact, the performance of the device is limited by the maximum data flow, in bits per second, that can be stored or transmitted. This is quite a critical point, particularly in view of the idea of using the measured flexural vibration field of flexible thin structures to estimate their sound radiation, which necessarily involves audio frequencies. More specifically, in first instance, frequencies comprised between 10 Hz and 1 kHz, for the so-called low audio frequency range. In this respect, Shechtman, Casp and Irani [53] showed that, multiple cameras can be employed to increase the accuracy of triangulation.

1.7 Scopes and objectives

Based on the considerations made in the previous section, the aim of this thesis is to investigate how the number of cameras (2, 4, 6, 8, 12 cameras) and their setting (distance and orientation with respect to the beam, i.e. elevation angle and aperture angle between pairs of cameras) affect the accuracy of flexural vibration measurements and sound radiation estimate of distributed structures. The idea is to explore if multi-cameras setups with rather low spatial-resolution cameras, which can be run at high frame-rates, could be effectively employed to measure flexural vibrations and sound radiation estimate of distributed structures [1].

1.8 Contribution of the thesis

The principal contributions of the thesis can be listed in the following points:

1. Derivation of a mathematical model for multiple cameras photogrammetry based on:
    - pinhole camera model;
    - linear triangulation with multiple cameras;
    - reduction of the triangulation error with non linear methods.
2. Experimental validation of the mathematical model based on a test rig composed by a cantilever beam and four synchronized cameras;
3. Parametrical study on the accuracy of flexural vibration measurements of a cantilever beam and a plate with respect to:
    - distance of the cameras from the test structure;
    - angle of aperture between the cameras;
    - resolution of the cameras;
    - disposition and number of cameras.
4. Parametrical study on the accuracy of the estimate of the sound radiation produced by the flexural vibrations of a plate with respect to:
    - distance of the cameras from the test structure;
    - angle of aperture between the cameras;
    - resolution of the cameras;
    - disposition and number of cameras.

1.9 Structure of the thesis

The thesis is divided in seven main chapters.

- This first chapter has introduced the concepts of vibration and sound radiation of a distributed mechanical structures and the most common devices used to measure these quantities;
- The second chapter presents an overview of the principal aspects of positions measurements of bodies with stereo-cameras and computer vision techniques;
- The third chapter is focused on the measurement of flexural vibrations of a cantilever beam with arrays of cameras. The model problem is introduced and studied through simulations. In

particular the following parametric studies are presented to show how the cameras setup influences the measurements:

1. distance of the cameras from the test structure;
2. angle of aperture between the cameras;
3. resolution of the cameras;
4. disposition and number of cameras.

- The fourth chapter expands the results presented in the previous one by focusing on vibration measurements of a plate with arrays of cameras. The model problem is introduced and studied through simulations. Also in this case the following parametric studies are presented to show how the cameras setup influences the measurement:

  1. distance of the cameras from the test structure;
  2. angle of aperture between the cameras;
  3. resolution of the cameras;
  4. disposition and number of cameras.

- In the fifth chapter, the results obtained from the simulation studies on the accuracy of the flexural vibration measurements of a cantilever beam studied in the third chapter, are experimentally validated. More specifically, the results concerning the following parameters are presented:

  1. resolution of the cameras;
  2. disposition and number of cameras.

- The sixth chapter is focused on the estimate of the sound radiation of the plate structure considered in the fourth chapter starting from the vibration field measured with arrays of cameras. The chapter first introduces the principles of sound radiation and then presents the approach used to estimate the sound radiation. Finally, it presents a thorough parametric study to assess how the following parameters influence the estimate of the sound radiation:

  1. distance of the cameras from the test structure;
  2. angle of aperture between the cameras;
  3. resolution of the cameras;
  4. disposition and number of cameras.

- The seventh and last chapter recalls the work done and summarizes the principal conclusions of the study.

Chapter 2

Vibration measurements with cameras

This chapter introduces the functioning of cameras and the techniques normally employed to reconstruct the vibrations of rigid and flexible objects. First, the optics of the first *pinhole camera*, i.e. the so called *camera obscura*, which is composed by a dark box with a small aperture and a back image plane, is revised. In particular, the so called *pinhole camera model* [54] is introduced, which describes the imaging process. The imaging process of film cameras is then introduced with respect to the pinhole model. The optics of cameras is quite similar to that of camera obscuras. In fact they are composed by an eye which works as the center of projection and a dark box with a sensitive film in the back image plane. Digital cameras use a photoelectric sensor which is characterized by an array of photoelectric tiles, which detect and discretize the image into an array of points called pixels. The pinhole model is employed to describe the imaging process of film and digital cameras, too. The model is slightly revised since the image plane is moved in front of the centre of projection. Finally, the reconstruction of displacements of objects using a pair of cameras is discussed. The classical triangulation method is introduced and the fundamental constraints for the displacement sensitivity, with respect to geometrical constraints, are revised (e.g. sensitivity of displacement measurements with respect to geometrical constraints of the camera vision system).

2.1 Camera obscura

The simplest model for the acquisition of images (*imaging*) is the *pinhole camera model*. This model replicates the imaging occurring in a *camera obscura*. As shown in Fig. 2.1, this camera is characterized by a dark box, which has a small aperture in C, called *center of projection* (or *point of view*), and a back plane, called *image plane*.

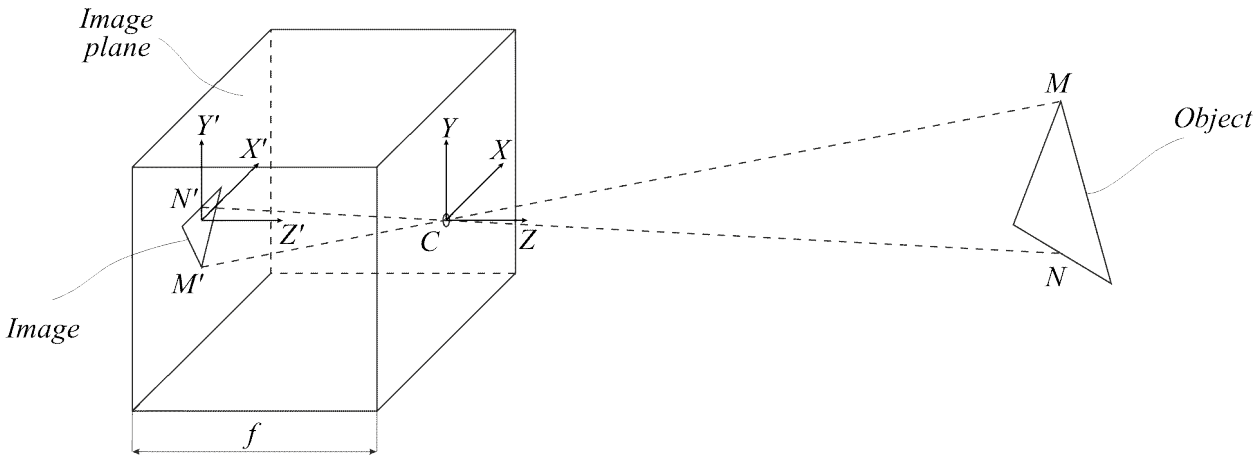

Figure 2.1: Camera obscura or first pinhole camera model.

To describe the imaging process of the camera obscura, a point M on the scene with coordinates (X, Y, Z) and its projection trough C on the image plane with coordinates (X', Y', Z') are considered. Assuming the so called *focal length* f is the distance between the *centre of projection* C and the image plane, and considering the similarity between the triangles MCN and $M'CN'$, the following two equations can be derived:

$$\frac{-X'}{f} = \frac{X}{Z}, \tag{2.1}$$

$$\frac{-Y'}{f} = \frac{Y}{Z}. \tag{2.2}$$

Therefore, the following transformation relates the object coordinates to the image coordinates:

$$X' = -f\frac{X}{Z}, \tag{2.3}$$

$$Y' = -f\frac{Y}{Z}, \tag{2.4}$$

$$Z' = f. \tag{2.5}$$

As highlighted in Fig. 2.1, the projected image is turned upside down and left-right and this is the reason of the minus sign in Eqs. 2.3 and 2.4. These equations define the image created by the so-called *perspective projection* process. The division by Z is responsible of the *perspective effect*: that is, the change of dimension of the image of an object depending on its distance from the camera obscura.

If the observed object is thin compared with the average distance from the camera, it is possible to approximate the perspective projection with the *orthographic projection* (or *weak perspective*). Thus, if the depth Z of the points of the object vary in a range $Z_0 \pm \Delta Z$, with $\frac{\Delta Z}{Z_0} << 1$, then it is possible to

approximate the scale factor f/Z with the constant f/Z_0. In this case, Eqs. 2.3 and 2.4 become:

$$X' = -f\frac{X}{Z_0}, \tag{2.6}$$

$$Y' = -f\frac{Y}{Z_0}. \tag{2.7}$$

Eqs. 2.6 and 2.7 give the so-called *orthographic projection* with a scale factor f/Z_0.

2.2 Classical film and digital cameras

As mentioned in the introduction of this chapter, over the years the evolution of optical instruments has moved from camera obscuras (Fig. 2.2 (a)) to film cameras (Fig. 2.2 (b)) and, later, to digital cameras (Fig. 2.2 (c)). As shown schematically in Fig. 2.2 (b), classical film cameras are composed by three principal elements: the camera obscura, the optical eye, which is equipped with optical lenses and a shutter, and the photosensitive film, which is scrolled along the back wall of the dark camera. According to the sketch depicted in Fig. 2.2 (c), in digital cameras, instead of a film, a photodetector is used inside the dark box.

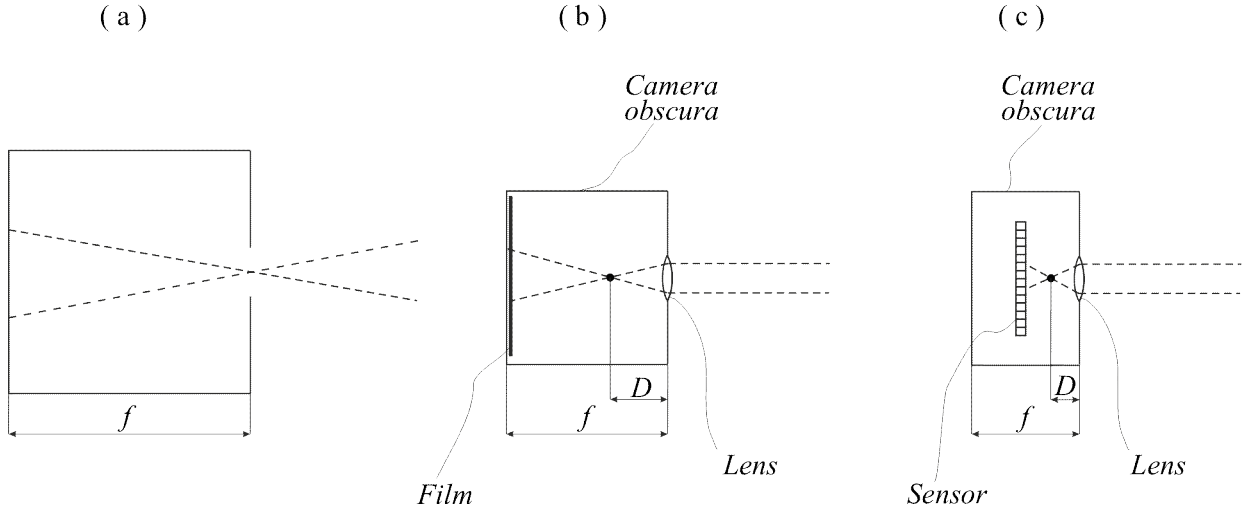

Figure 2.2: Comparison between (a) camera obscura, (b) classical film camera and (c) digital camera.

The introduction of lenses changed the optics inside a camera. As explained in Appendix A, an important aspect to notice is the change of the meaning of focal length. In fact, in both camera obscuras and cameras there is a quantity called focal length but it indicates different quantities. As discussed in the previous section, in camera obscuras the focal length indicates the distance between the center of projection and the image plane, and, as shown in Fig. 2.1 and 2.2 (a), it is denoted as f. Instead, in cameras, the concept of focal length is used in two different contexts (see Appendix A). First, the focal length f is used in the pinhole model of the optics of the camera and it represents the distance between the image plane and the centre of the lens. Second, the focal length D is used to describe the optics of the lenses of the camera and, in this case, it represents the distance between the

focal point and the center of the lens. As shown in Appendix A, in this case, the focal length is defined as the distance between the point where all the parallel light rays of the scene converge and the centre of the lens.

The following two subsections present the principal features of classical film cameras and more recent digital cameras technologies.

2.2.1 Classical film cameras

The principal components of a classical film camera are:

1. the *camera obscura*, which is a small enclosure with a front opening where the diaphragm and eye are fixed, and a back mechanism that holds and slides forward the film after each shoot;

2. the *film*, which is a long spool of flexible plastic coated with special chemicals, based on compounds of silver, which are sensitive to light. The film is normally stored into a plastic cylinder to avoid that light could spoil the film;

3. the *eye*, which is fixed on the front aperture of the camera obscura and is formed by one or more (magnifying) lenses that can be translated axially to move the focus with respect to the back plane of the camera obscura;

4. the *diaphragm* mechanism, that generates a circular aperture behind the lenses to let the light enter into the camera obscura for a specific period of time, called *exposure time*, which is normally of the order of fractions of a second unless the picture is taken in poor light conditions (e.g. during night);

5. the *shutter* mechanism, that commands the diaphragm mechanically via a button placed on the case of the camera.

By pressing a button on the camera, the shutter is activated to briefly open the lens diaphragm so that light enters to the camera obscura through the lens and then impinges the photosensitive film. The impinging light causes reactions to take place in the chemicals of the film, which fixate the picture. The film needs to be developed. The developing process involves several chemical reactions on the film, which turns it into an array of "negative" pictures. The negatives are then printed into paper to get the photo.

2.2.2 Digital cameras

Digital cameras are built like ordinary film cameras except that, instead of the photosensitive plastic film, they have a photodetector sensor which captures the incoming light and turns it into electrical signals. This light detector can be of two types, either a *Charge-Coupled Device (CCD)* or a *Complementary*

Metal-Oxide Semiconductor (CMOS) image sensor. To describe the functioning of digital cameras it is crucial to introduce the concept of *pixel*. In digital imaging, a pixel is a physical point in a raster image, i.e. a grid discretization of the image. Each pixel is a sample of the image. The more samples has the image the more accurate is the representation of the object. In color imaging, a color is typically represented by three or four components such as red-green-blue, i.e. RGB, or cyan-magenta-yellow-black, i.e CMYB.

In a digital camera, the light from the scene meant to be photographed zooms into the dark camera via the eye. The incoming "picture" hits the image sensor chip, which breaks it up into thousands or millions of pixels. The sensor measures the color of each pixel and converts it into a signal which is then processed and transformed into a digital signal. The digital photograph is thus an array of numbers which give the RGB colors of each pixel.

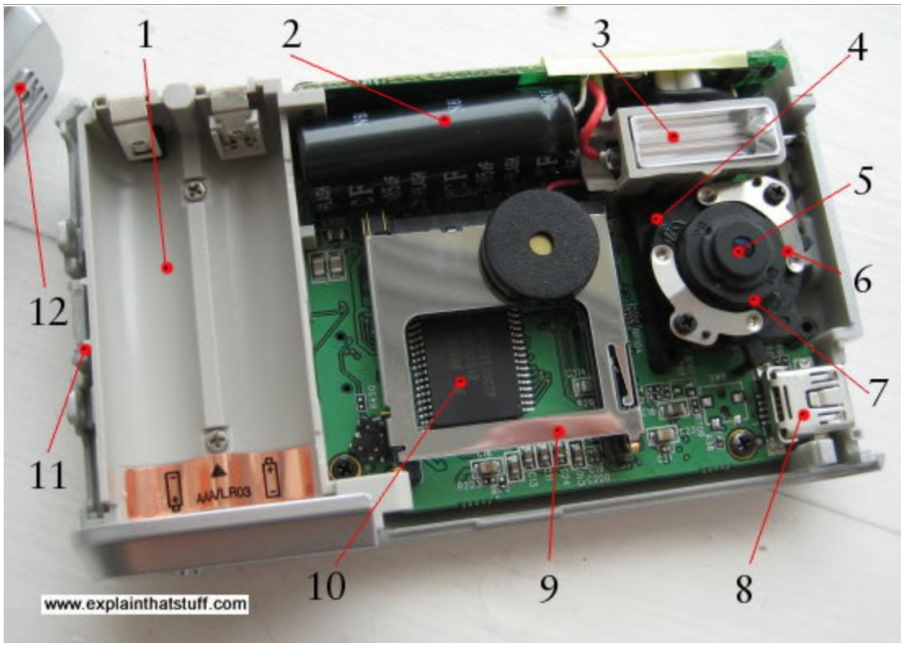

Figure 2.3: Main components of a digital camera (www.explainthatstuff.com).

Since the thesis is focused on a measurement system based on cameras, their principal components are listed below with reference to Fig. 2.3.

1. *Battery compartment*: in this example, the camera takes two 1.5-volt batteries, so it works on a total voltage of 3 volts (3 V);

2. *Flash capacitor*: the flash has to be fired when it is needed, thus a capacitor is used to store the necessary energy;

3. *Flash lamp*: it can be operated by the capacitor or directly by the batteries, depending on which kind of flash is used;

4. *LED*: it is a small red light that indicates when certain camera options (e.g. self-timer) are operating;

5. *Lens*: the lens catches the light from the object and focuses it on the image sensor (CCD or CMOS);

6. *Focusing mechanism*: it is a switch-operated focus that moves the lens between two positions for taking either close-ups or distant shots;

7. *Image sensor*: in a digital camera, this is the light-detecting microchip, which uses either CCD or CMOS technology. In Fig. 2.3 the chip is hidden underneath the lens;

8. *USB connector*: used to download the photos on other devices (e.g. laptop);

9. *SD (secure digital) card slot*: space used for allocating an external memory;

10. *Processor chip*: the main digital "brain" of the camera, which controls all its functions. Normally it is made by a miniaturised integrated circuit;

11. *Wrist connector*: the strap that keeps the camera tied;

12. *Top case*: covers the camera;

13. *LCD display*: shows the taken photo. It is normally located on the rear of the camera (not shown in Fig. 2.3)

2.2.3 Optics of digital cameras

In a digital camera the image plane is made of a *CCD (Charge-Coupled Device)* or a *CMOS (Complementary Metal-Oxide Semiconductor)* matrix of photodetectors. Normally, a CCD is a 50 mm^2 matrix with $n \times m$ photosensitive cells (e.g. $n \times m = 4000 \times 4000 = 16 \times 10^6$), which convert the incident light into electrical potentials. Typically, the cells are organized according to the *Bayer mask pattern*, which, as shown in Fig. 2.4, is characterized by a regular pattern of cells sensitive to the RGB colors. For example, the Bayer mask shown in Fig. 2.4 is characterized by alternating strings of cells so arranged $RGRGRG\ldots$ and $GBGBGB\ldots$. The array of potentials is then converted into three $N \times M$ digital matrices: one for the red, one for the green and one for the blue colors. The three matrices have standard dimensions, which are summarized in Tab. 2.1. These matrices are normally stored into image files that can have different formats. For example, TIFF files store the raw data of the three matrices. Alternatively, JPEG files compress the data of the three matrices according to the specific JPEG standard. Images are normally displayed on computer screens using an inverse Bayer

mask technique. Alternatively, they are printed on paper by depositing the colors of the three matrices pixel by pixel.

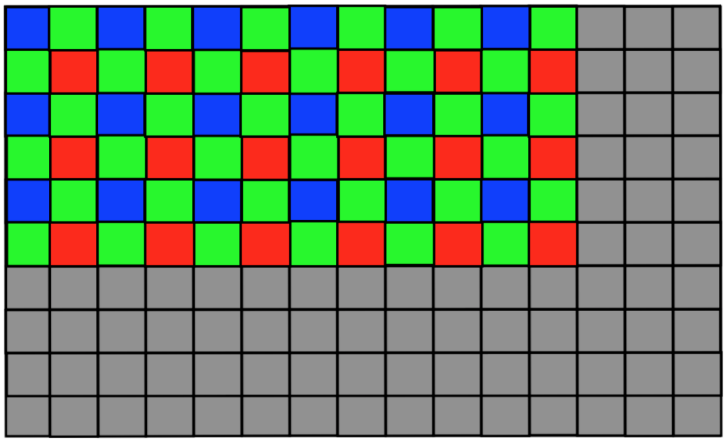

Figure 2.4: Bayer mask.

Table 2.1: Matrix standard dimensions.

Format	**4:3**	**24:36**
	800×600	800×533
	1024×768	1024×682
	1280×1024	1280×853
	1600×1200	1600×1066

2.3 Pinhole model

As discussed above, a camera is composed by several components, although its working principle can be schematically represented by three main elements: the lens, the focal point and the back plane where the film or the photosensitive sensor are placed. As shown in Fig. 2.5 (a) the back plane is normally indicated as the so-called *image plane*. The dashed lines shows the light paths from points M and N of the object, which via the lens are projected on the image plane at positions M' and N' respectively. The solid lines show a simple geometric reconstruction of this imaging process, via straight lines that start from points M and N, pass through the centre of projection C and arrive to the points M' and N' in the image plane. This optics is normally studied with the so-called *pinhole camera model* which, as shown in Fig. 2.5 (b), is characterized by a virtual image plane placed in front of the centre of projection C. As discussed in Appendix B, with this model, a positive focal length f can be considered such that the projected image will no more appear turned upside-down nor left-right.

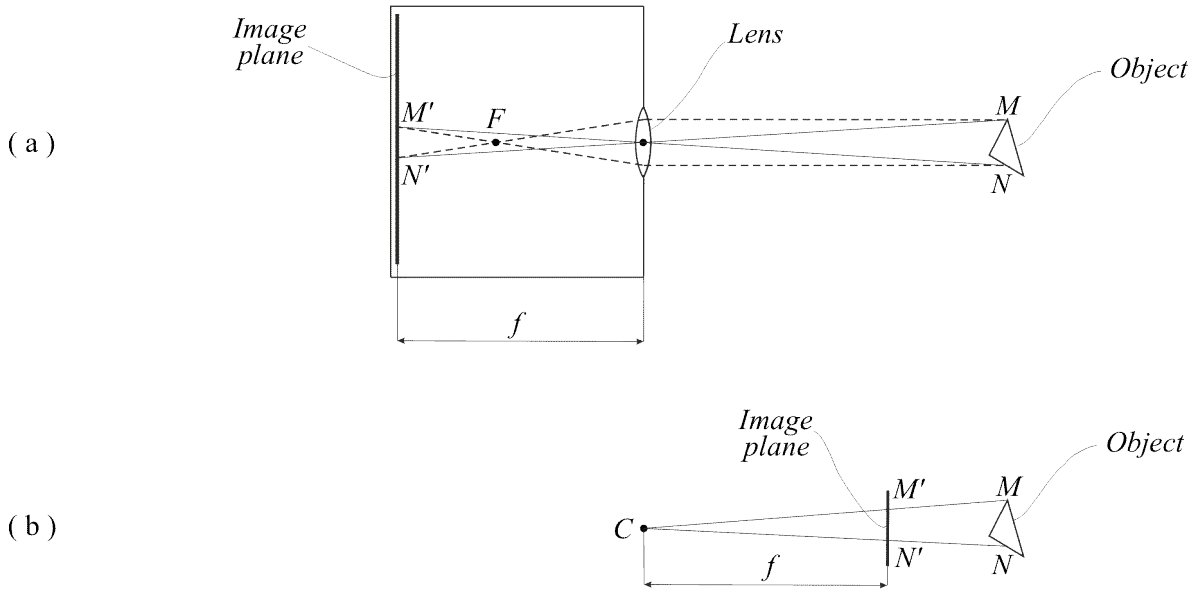

Figure 2.5: Comparison between (a) practical and (b) theoretical pinhole model.

Since in this thesis the *pinhole camera model* is used, it is important to study its geometry in detail. As shown in Fig. 2.6, the pinhole model is characterized by the so called *centre of projection* C, placed at a distance f (*focal length*) from the *image plane*. The line orthogonal to the image plane passing through C is called *principal axis* or *optical axis*. The plane parallel to the image plane, which includes the center of projection, is called *focal plane*. To properly define the perspective projection produced by the camera, two systems of reference are introduced. First, the right-handed global system of reference $CXYZ$, also called *camera standard reference system*, which is centered in the centre of projection and has the Z axis parallel to the optical axis and the X and Y axes parallels to the rectangular image plane. Second, a local right-handed 2D system of reference Ouv, which is located on the image plane and has the centre O on the intersection with the optical axis Z, i.e. on the *principal point*, and the u,v axes parallel to the edges of the rectangular image plane.

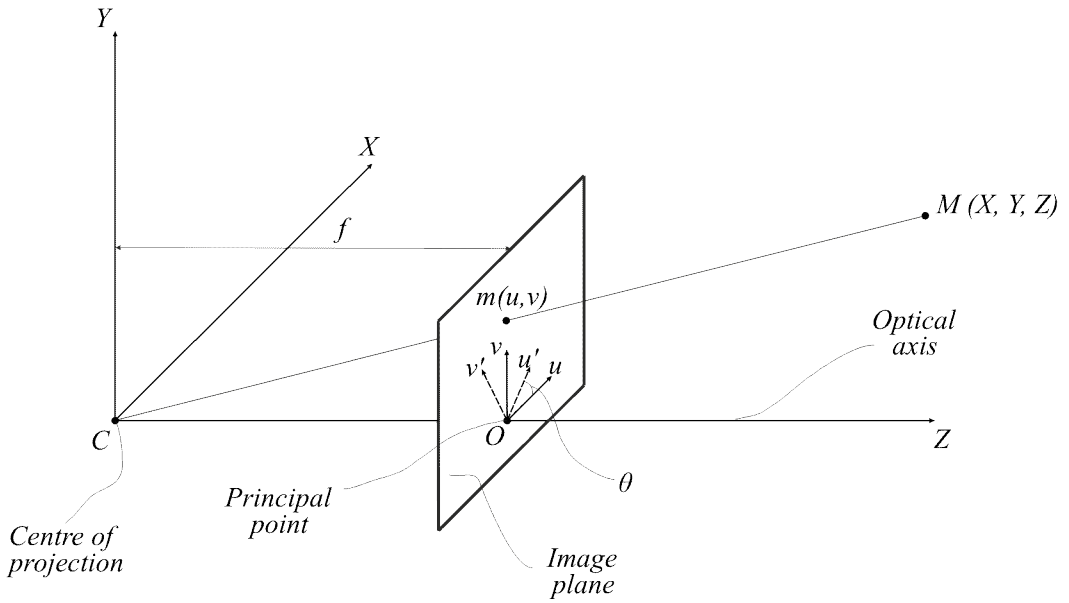

Figure 2.6: Pinhole model.

Having introduced these two reference systems, it is possible to express a generic point M both in the 3D space coordinates as $\mathbf{M} = [X, Y, Z]^T$ and in the 2D camera coordinates as $\mathbf{m} = [u, v]^T$.Therefore, after some geometrical considerations, the following equation can be derived:

$$\frac{f}{Z} = \frac{u}{X} = \frac{v}{Y}. \tag{2.8}$$

This expression can be split into the following two coordinates transformation relations:

$$\begin{cases} u = \dfrac{f}{Z}X \\ v = \dfrac{f}{Z}Y \end{cases}, \tag{2.9}$$

which form the so-called *perspective projection*. Since each equation shows Z in the denominator, the transformation is non-linear. This transformation can be written in matrix notation if the *homogeneous coordinates*, introduced in Appendix C, are employed, such that:

$$\mathbf{m} = \begin{bmatrix} u \\ v \\ 1 \end{bmatrix}, \qquad \mathbf{M} = \begin{bmatrix} X \\ Y \\ Z \\ 1 \end{bmatrix}. \tag{2.10}$$

Since the third coordinate is set as 1, it is possible to rewrite Eq. 2.9 for the perspective projection as

follows:

$$Z\begin{bmatrix} u \\ v \\ 1 \end{bmatrix} = \begin{bmatrix} fX \\ fY \\ Z \end{bmatrix} = \begin{bmatrix} f & 0 & 0 & 0 \\ 0 & f & 0 & 0 \\ 0 & 0 & 1 & 0 \end{bmatrix} \begin{bmatrix} X \\ Y \\ Z \\ 1 \end{bmatrix}, \tag{2.11}$$

which can be written in compact matrix notation as follows:

$$\mathbf{m} = \frac{1}{Z}\mathbf{PM}, \tag{2.12}$$

where:

$$\mathbf{P} = \begin{bmatrix} f & 0 & 0 & 0 \\ 0 & f & 0 & 0 \\ 0 & 0 & 1 & 0 \end{bmatrix}. \tag{2.13}$$

Neglecting the scale factor Eq. 2.12 becomes:

$$\mathbf{m} \simeq \mathbf{PM}. \tag{2.14}$$

The matrix $\mathbf{P}$ represents the geometric model of the camera and it is called *perspective projection matrix* (*PPM*). A realistic model for the camera should take into account two factors:

- the rigid transformation between the local reference system of the camera and the global reference system;
- the pixelation, that is the coordinates discretization from meters in the sensor plane to pixels in the image plane.

Normally, the pixelation assumes that the origin the local reference system Ouv is located at the top left corner of the image plane rather than the principal point $\mathbf{O}$. In order to take in account these considerations, matrix $\mathbf{P}$, defined in Eq. 2.13, has to be pre-multiplied by a matrix $\mathbf{V}$ defined as follows:

$$\mathbf{V} = \begin{bmatrix} k_u & 0 & u_0 \\ 0 & k_v & v_0 \\ 0 & 0 & 1 \end{bmatrix}, \tag{2.15}$$

where (u_0, v_0) are the coordinates of the principal point, k_u and k_v are the *effective pixel dimensions* in u, v measured in pixel/m. The matrix $\mathbf{P}$ becomes:

$$\mathbf{P} = \begin{bmatrix} k_u & 0 & u_0 \\ 0 & k_v & v_0 \\ 0 & 0 & 1 \end{bmatrix} \begin{bmatrix} f & 0 & 0 & 0 \\ 0 & f & 0 & 0 \\ 0 & 0 & 1 & 0 \end{bmatrix} = \begin{bmatrix} fk_u & 0 & u_0 & 0 \\ 0 & fk_v & v_0 & 0 \\ 0 & 0 & 1 & 0 \end{bmatrix} = \mathbf{K}\left[\mathbf{I}|\mathbf{0}\right], \tag{2.16}$$

where:

$$\mathbf{K} = \begin{bmatrix} \alpha_u & 0 & u_0 \\ 0 & \alpha_v & v_0 \\ 0 & 0 & 1 \end{bmatrix}, \qquad \Big[\mathbf{I}|\mathbf{0}\Big] = \begin{bmatrix} 1 & 0 & 0 & 0 \\ 0 & 1 & 0 & 0 \\ 0 & 0 & 1 & 0 \end{bmatrix}. \tag{2.17}$$

Here $\alpha_u = fk_u$ and $\alpha_v = fk_v$ are the focal lengths expressed with reference to vertical and horizontal pixel positions respectively. The quantities $\alpha_u, \alpha_v, u_0, v_0$ are called *intrinsic parameters* and the $\mathbf{K}$ matrix is thus called *intrinsic parameter matrix*. The most general camera model takes into account also a rotation parameter θ of the system of reference Ouv with respect to the global system of reference. More specifically, the angle θ defines the angle between the local axes u, v and the global axes X, Y. In this case, the matrix $\mathbf{P}$ is given by [54]:

$$\mathbf{P} = \begin{bmatrix} fk_u & fk_u \cot\theta & u_0 \\ 0 & fk_v/\sin\theta & v_0 \\ 0 & 0 & 1 \end{bmatrix}. \tag{2.18}$$

Often, the parameter $fk_u \cot\theta$ is defined as skewγ.

2.4 Angle of view

In photography, the *angle of view* (AOV) describes the angular extent of a given scene that can be detected by a camera. Often, the angle of view is called with the more general term of *field of view* and it does not only depend on the lens, but also on the sensor. The angle of view may be measured horizontally (from the left to right edge of the frame), vertically (from the top to bottom of the frame), or diagonally (from one corner of the frame to its opposite corner). For a lens projecting a rectilinear image, the angle of view can be calculated from the geometry shown in Fig. 2.7 as follows:

$$AOV = 2 \arctan \frac{d}{2f}, \tag{2.19}$$

where, according to in Fig. 2.7, d represents the size of the film (or sensor) in the direction measured and f is the effective focal length.

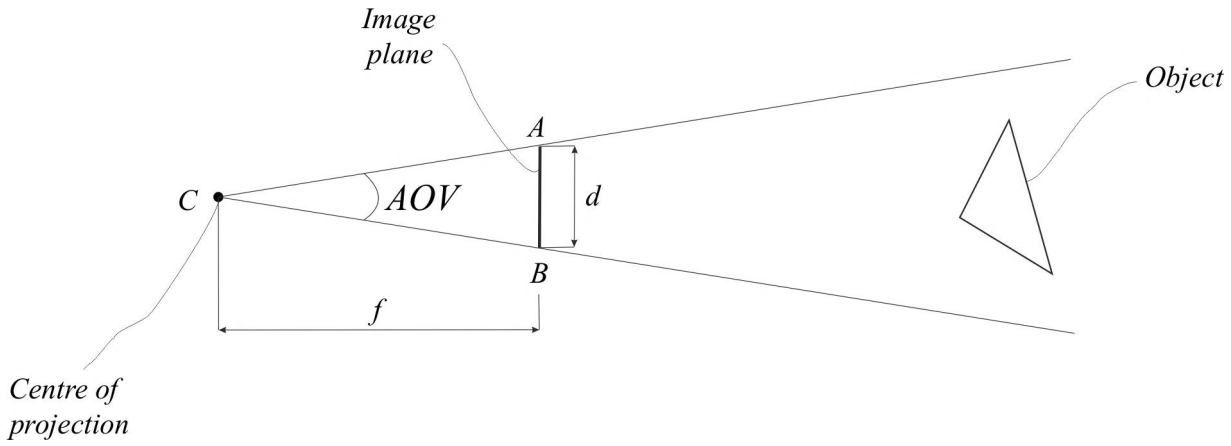

Figure 2.7: Angle of view: general scheme with a detected object.

For example, for a 35 mm film which is 36 mm wide and 24 mm high, $d = 36$ mm would be used to obtain the horizontal angle of view and $d = 24$ mm for the vertical angle. So, from Eq. 2.19, the following horizontal, vertical and diagonal AOVs are straightforwardly derived in Eq. 2.20:

$$\begin{aligned} AOV_h &= 2 \arctan \frac{d}{2f} = 2 \arctan \frac{36}{2 \times 50} \simeq 39.6^\circ, \\ AOV_v &= 2 \arctan \frac{24}{2 \times 50} \simeq 70^\circ, \\ AOV_d &= 2 \arctan \frac{43}{2 \times 50} \simeq 46.8^\circ. \end{aligned} \tag{2.20}$$

The lens of a camera is defined as *normal*, when it has a focal length comparable with the diagonal of the photosensitive element (sensor or film). For example, for cameras with a 35 mm film, which has dimension 24×36, the normal lens should have a focal length of 50 mm. Taking as a reference the 50 mm focal length, it is possible to distinguish *wide-angle* lenses (< 50 mm) and *telephoto* lenses (> 50 mm).

As discussed above, film cameras have a film of standard dimensions 36×24 mm. In digital cameras the same proportions are preserved. Digital sensors are usually smaller than 35 mm films, and this causes the lens to have a narrower angle of view than with the 35 mm film, which is identified by a constant factor for each sensor, also called the *crop factor*. For lenses projecting rectilinear (i.e. non-spatially-distorted) images of distant objects, the effective focal length and the image format dimensions completely define the angle of view.

Chapter 3

Beam flexural vibration measurements with arrays of cameras

This chapter considers the problem of measuring, with multiple cameras, the time-harmonic flexural vibrations of a cantilever beam. More specifically, it is focussed on the measurement of the beam flexural deflection shapes at the first three resonance frequencies, which gives a good estimate of the shape of the first three flexural natural modes. The study is structured in two parts. The first part introduces the model problem studied here and provides a brief revision of the theoretical aspects on vibrations measurements that will be used along this chapter. The second part presents a simulation study on the principal features of flexural vibration measurements with multiple cameras by means of triangulation. The chapter is organized in four sections. Section 3.1 introduces the model problem considered in this study, which is given by the measurement of the time-harmonic flexural vibration of a cantilever beam. Section 3.2 briefly recalls the pinhole model and linear triangulation formulation used to simulate the measurement of the beam flexural vibrations with multiple cameras. Section 3.3 presents a comprehensive parametric study, which shows how the distance, the angle of separation, the resolution and the number of cameras influence the accuracy of the measurements. Finally, Section 3.4 summarizes the principal conclusions of this chapter.

3.1 Model problem

Fig. 3.1 shows a sketch of the model problem considered here, which is composed by a cantilever thin beam made of aluminium whose dimensions and physical properties are summarised in Table 3.1. The transverse vibration of the beam is measured at 25 points aligned along the longitudinal axis of the beam. The points are evenly distributed along the length of the beam with a spacing of 25 mm. The simulation study assumes the points have infinitesimal dimension whereas the beam used for the experiments has been marked with circles having 5 mm diameter, as it will be seen in Chapter 5. The

positions of these points are measured by multiple cameras such that triangulation can then be used to reconstruct the transverse displacements of the beam generated by the flexural vibrations. As discussed in Chapter 2, in general, a camera is composed by several components, although its working principle can be schematically represented by three elements as shown in the sketch (b) of Fig. 3.1: first, the camera obscura; second, the lenses, which are characterized by an optical axis and a focal point at distance f (also called focal length) and third, the photosensitive sensor, which is normally located in the back plane of the camera obscura. Normally, the photosensitive sensor is either a charge-coupled device (CCD) or a complementary metal-oxide semiconductor (CMOS).

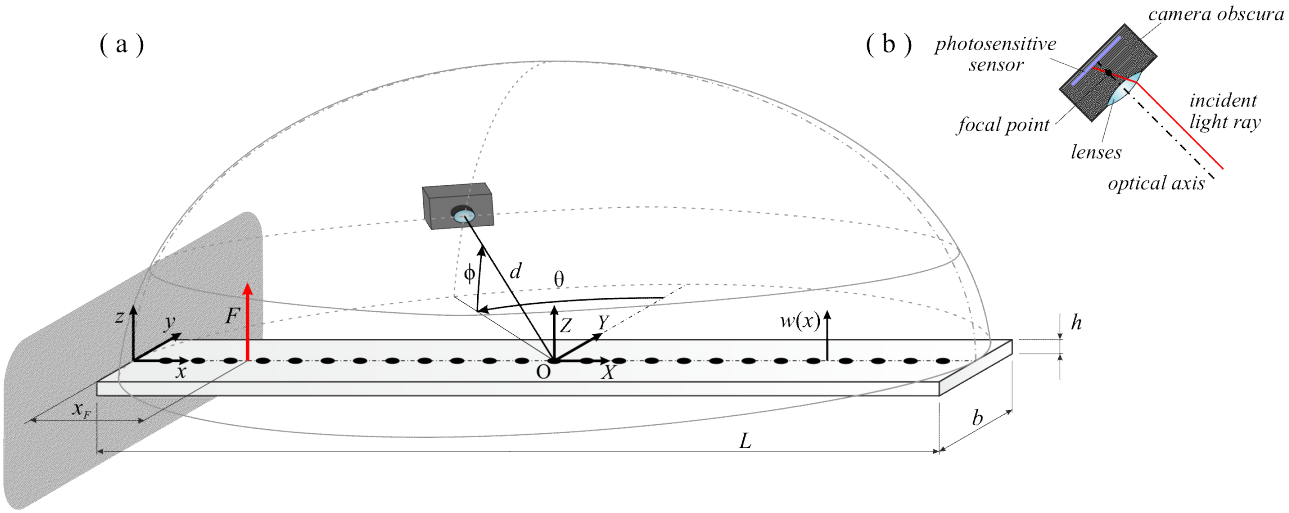

Figure 3.1: Model problem for the measurement of flexural vibration of a cantilever beam.

As specified in Fig. 3.1, two Cartesian systems of reference are employed to define the positions of the beam points and the positions of the cameras, which are respectively:

a) the *beam coordinate frame of reference* x, y, z which is located at the clamped end of the beam;

b) and the so-called *world coordinate frame of reference* X, Y, Z which is located in the middle of the beam.

For simplicity, the two systems of reference will be called respectively "beam system of reference" and "world system of reference". The former reference system is used to define the flexural vibrations of the beam whereas the latter is used for triangulation. The transverse displacement $w(x, t)$ along the beam is due to the flexural vibrations of the beam in the x, z plane, which are generated by a transverse time-harmonic force at position x_F. The cameras are oriented in such a way as their optical axis points to the origin O of the world system of reference X, Y, Z and thus their image plane [54] is tangent to a hemisphere centred in O. Moreover, the base edge of the rectangular photosensitive sensor is oriented parallel to the base plane X, Y of the hemisphere. As shown in Fig. 3.1, the position of the camera is identified by the position of its focal point C, which is defined by spherical coordinates with respect to the world system of reference X, Y, Z i.e.:

a) the radial distance d;

b) the azimuthal angle θ;

c) the elevation angle ϕ.

The flexural vibration of the beam is governed by the following wave equation [2], [3]:

$$EI_z \frac{\partial^4 w(x,t)}{\partial x^4} + \rho A \frac{\partial^2 w(x,t)}{\partial t^2} = F(x,t). \tag{3.1}$$

Here E and ρ are the Young's modulus of elasticity and the density of the material of the beam. Also, $A = bh$ and $I_z = bh^3/12$ are the area and the area moment of inertia of the beam cross respectively, where L, b ,h are the length, width and thickness of the beam. Finally, $F(x,t)$ is the transverse force acting on the beam, which in this case is a time-harmonic point force acting at position x_F, such that

$$F(x,t) = \delta(x - x_F)\mathrm{Re}\Big\{F_0(\omega)e^{j\omega t}\Big\}. \tag{3.2}$$

In this expression, $F_0(\omega)$ is the amplitude of the force, ω is the angular frequency, $j = \sqrt{-1}$ and $\delta(.)$ is the Dirac delta function. As shown in Ref. [2], [3], the flexural response of the beam can be expressed as the linear combination of the natural modes $\phi_n(x)$ and the modal coordinates (or generalized coordinates) $q_n(t)$:

$$w(x,t) = \mathrm{Re}\Big\{\sum_{n=1}^{\infty} \phi_n(x) q_n(t)\Big\}. \tag{3.3}$$

The natural modes of a cantilever beam are given by

$$\phi_n(x) = (\cosh(k_n x) - \cos(k_n x)) - \sigma_n(\sinh(k_n x) + \sin(k_n x)), \tag{3.4}$$

where $\sigma = (\sinh(k_n L) - \sin(k_n L))/(\cosh(k_n L) + \cos(k_n L))$ and k_n is the modal wavenumber, whose values are summarized in Table 3.2. Also, the modal coordinates are given by

$$q_n(t) = \frac{\phi_n(x_F)}{M[\omega_n^2 + j2\xi\omega_n\omega - \omega^2]} F_0(\omega)e^{j\omega t}. \tag{3.5}$$

Here, $M = \rho AL$ is the mass of the beam, ξ is the modal damping ratio, which is assumed equal for all modes, and ω_n is the natural frequency, which is given by

$$\omega_n = \sqrt{\frac{EI_z}{\rho A}} k_n^2. \tag{3.6}$$

In general, the modal overlap [2] of flexural vibrations in a thin beam grows slowly and proportionally to $\sqrt{\omega}$ [58]. Therefore, when the cantilever beam is excited at the resonance frequencies of the low-order

Table 3.1: Physical properties of the beam.

Parameter	Value
Length	$L = 623$ mm
Width	$b = 30$ mm
Thickness	$h = 3$ mm
Density	$\rho = 2700$ kg/m^3
Young's modulus	$E = 6.9 \times 10^{10}$ N/m^2
Poisson ratio	$\nu = 0.31$
Modal damping ratio	$\xi = 0.02$
Position of the force	$x_F = 55$ mm

Table 3.2: Values of $k_n L$ for a clamped-free beam.

n	$k_n L$
1	1.87510
2	4.69409
3	7.85476
4	10.9955
5	14.1372
6,7,...	$(2n-1)\pi/2$

natural modes, the response can be expressed in terms of the modal contribution of the resonant mode only. For instance, the flexural response at the first resonance frequency, i.e. for $\omega = \omega_1\sqrt{(1-2\xi^2)}$, can be satisfactorily expressed as:

$$w(x,t) = \phi_1(x)\mathrm{Re}\{q_1(t)\}. \tag{3.7}$$

This expression shows that, for a given instant of time t, the spatial response $w(x,t)$ coincides with the natural mode $\phi_1(x)$ to within a constant $\mathrm{Re}\{q_1(t)\}$:

$$\mathrm{Re}\{q_1(t)\} = \mathrm{Re}\left\{ \frac{\phi_1(x_F)}{M[\omega_1^2 + j2\xi\omega_1\omega - \omega^2]} F_0(\omega) e^{j\omega t} \right\}. \tag{3.8}$$

In this chapter, the measurement of the three spatial deflection shapes $w(x,t)$ is investigated with respect to the instant t where the time-harmonic function $\mathrm{Re}\{q_1(t)\}$ is maximum, that is for $t = n\pi/\omega$ with $n = 0, 1, 2, \ldots$.

3.2 Pinhole model and linear triangulation with multiple cameras

The simulation study assumes that the line of measurement points, evenly distributed along the length of the beam, have infinitesimal dimension. Therefore, the projection of the points into the plane of the camera is modeled with the classical *pinhole camera model* [54] described in Chapter 2. Also, the reconstruction of the positions of such points is based on a *linear triangulation* formulation for multiple, i.e. more than two, cameras which is also based on the formulation presented in Chapter 2.

As discussed in Chapter 2, the optics of a camera is normally studied with the pinhole camera model which, as shown in Fig. 3.2, is characterized by three elements. First the *optical axis* (also called *principal axis*), second the *center of projection* C (also called *point of view*) and third the rectangular *image plane*. In contrast to the effective optics of cameras, the image plane is located in front of the center of projection C. More specifically, the center of the image plane C_{ip} is located along the segment $\overline{OC}$ at a distance f from the center of projection C. Also, the image plane is oriented orthogonal to the principal axis and its base edge is oriented parallel to the plane formed by the axes X, Y.

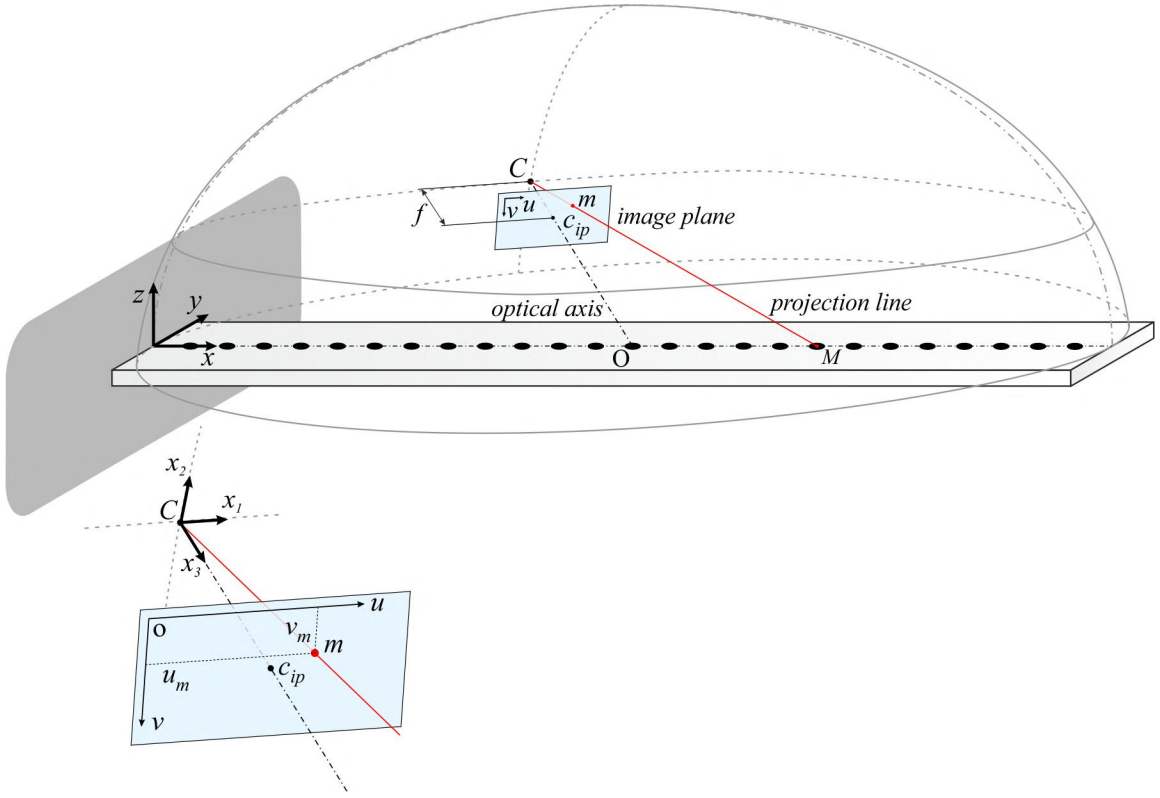

Figure 3.2: Pinhole model: detail on the principal quantities that represent a camera.

The pinhole model considers a cartesian *camera coordinate frame of reference* x_1, x_2, x_3, which is located at the center of projection C with the x_3 axis aligned with the principal axis and the x_1, x_2 axes parallel to the edges of the rectangular image plane. Finally, the image plane is also characterized by a local *image coordinate frame of reference* u, v which, as shown in Fig. 3.2, is located on the top left hand-side corner of the image plane. The image coordinates u, v are expressed in pixels. The pinhole

model assumes that the projection of a point M into the image plane is identified by the intersection between the image plane and the segment $\overline{MC}$ between the point M and the center of projection C.

According to the pinhole model discussed in Chapter 2, the relationship between the 3D coordinates for the point M and the 2D coordinates of its projection onto the image plane can be expressed to within a scale factor with the following matrix relation [54]:

$$\mathbf{m} = \mathbf{PM}, \tag{3.9}$$

where $\mathbf{m} = [u, v, 1]^T$ and $\mathbf{M} = [X, Y, Z, 1]^T$ are the homogeneous vectors with the image plane and world coordinates of point M of the beam. Also, $\mathbf{P}$ is the camera projection matrix [34], which is given by the following expression:

$$\mathbf{P} = \mathbf{K}[\mathbf{I}|\mathbf{0}]\mathbf{G}. \tag{3.10}$$

Here $\mathbf{G}$ is the 4×4 matrix for the transformation from the world homogeneous coordinates $X, Y, Z, 1$ to the camera homogeneous coordinates $x_1, x_2, x_3, 1$ [54]:

$$\mathbf{G} = \begin{bmatrix} \mathbf{R} & \mathbf{t} \\ \mathbf{0} & 1 \end{bmatrix}, \tag{3.11}$$

which is composed by the 3×3 rotation matrix $\mathbf{R}$, the 3×1 translation vector $\mathbf{t}$ and the 1×3 vector of zeros $\mathbf{0}$. In addition, $[\mathbf{I}|\mathbf{0}]$ is the 3×4 camera projection matrix, which encodes the normalized image coordinates on the image plane. Here $\mathbf{I}$ is a 3×3 identity matrix and $\mathbf{0}$ is a 1×3 column vector of zeros. Finally, $\mathbf{K}$ is the camera calibration matrix, used to transform the normalized image coordinates into the image coordinates u, v expressed in pixels [54]:

$$\mathbf{K} = \begin{bmatrix} \alpha_u & \alpha_u\gamma & u_0 \\ 0 & \alpha_v r & v_0 \\ 0 & 0 & 1 \end{bmatrix}. \tag{3.12}$$

In this matrix, $\alpha_u = fk_u$ and $\alpha_v = fk_v$ and $1/k_u$, $1/k_v$ are the width and height of the pixel footprint on the camera photosensor. Also, u_0, v_0 are the coordinates in pixel of the center of the image plane C_{ip}. Finally, γ and r are the skew and aspect ratio parameters, which are normally given by $\gamma = 0$ and $r = 1$ for most cameras [54]. The camera calibration matrix takes into account three effects: first, the conversion from physical dimension to pixels; second, the position of the image coordinates with respect to the center of the image plane C_{ip} and third, the uniform scaling due to the focal length of the camera f.

3.2.1 Linear triangulation

As discussed in Chapter 2, the pinhole model discussed above simply provides a relation between the global coordinates of a point M and the image coordinates of its projection into the image plane of the camera. Therefore, a single camera cannot be used to univocally identify the position of the point M. Indeed, to obtain the true position of the point M, two cameras should be employed such that the position of the point M can be reconstructed from its projections into the image planes of the two cameras by means of linear triangulation. For instance, it is considered the scheme shown in Fig. 3.3, where the beam is equipped with two cameras with the focal points located at positions C_1, C_2 and the image planes oriented orthogonal to the optical axis and the base edge parallel to the plane X, Y. Recalling the pinhole formulation described above, the projections of the point M into the image planes of the two cameras can be expressed in terms of the following two matrix relations

$$\mathbf{m}_1 = \mathbf{P}_1\mathbf{M}, \tag{3.13}$$

$$\mathbf{m}_2 = \mathbf{P}_2\mathbf{M}. \tag{3.14}$$

Here $\mathbf{M} = [X, Y, Z, 1]^T$ is the homogeneous vector with the world coordinates of the point M and $\mathbf{m}_1 = [u_1, v_1, 1]^T$, $\mathbf{m}_2 = [u_2, v_2, 1]^T$ are the homogeneous vectors with the image coordinates of the projections of M into the image planes of the two cameras. Also, $\mathbf{P}_1$, $\mathbf{P}_2$ are the projection matrices of the two cameras. Now, the following cross product vector expressions can be straightforwardly verified:

$$\mathbf{m}_1 \times \mathbf{P}_1\mathbf{M} = 0, \tag{3.15}$$

$$\mathbf{m}_2 \times \mathbf{P}_2\mathbf{M} = 0. \tag{3.16}$$

These two vector expressions eliminate the unknown scaling factor contained in Eqs. 3.13 and 3.14. Each expression provides three linear equations, of which only two are independent, in the unknown homogenous global coordinates of the point M: X, Y, Z, W. Normally the six equations are stacked into the following matrix expression [54]:

$$\mathbf{A}\mathbf{M} = \mathbf{0}, \tag{3.17}$$

where $\mathbf{0}$ is a 6×1 vector of zeroes and $\mathbf{A}$ is the following 6×4 matrix:

$$\mathbf{A} = \begin{bmatrix} [\mathbf{m}_1]_\times & \mathbf{P}_1 \\ [\mathbf{m}_2]_\times & \mathbf{P}_2 \end{bmatrix}. \tag{3.18}$$

In this matrix, $[\ ]_\times$ is the skew-antisymmetric matrix operator, i.e. $[\mathbf{m}_i]_\times = \begin{bmatrix} 0 & -1 & v_i \\ 1 & 0 & -u_i \\ -v_i & u_i & 0 \end{bmatrix}$.

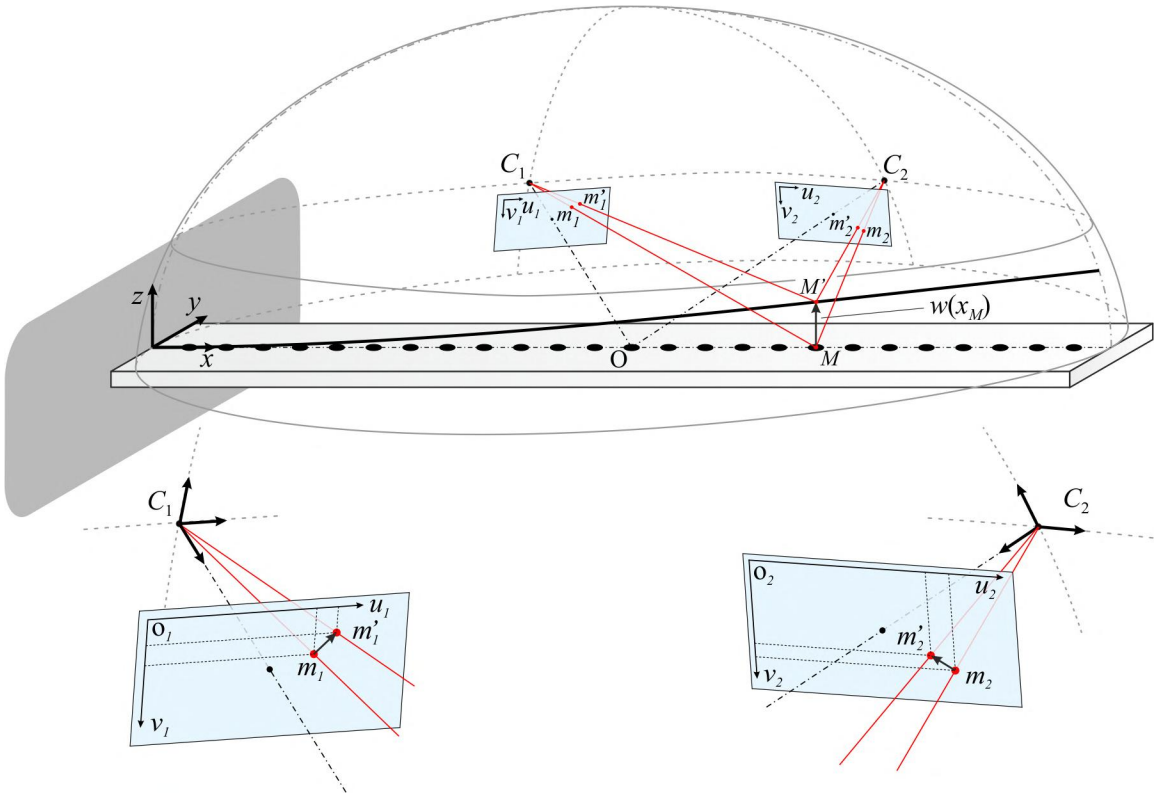

Figure 3.3: Pinhole model: detail on the working principle of the linear triangulation method.

Eq. 3.17 gives a homogeneous linear system of six linearly dependent equations in four unknowns, which can be casted into a set of four linear equations. In practice, the measured coordinates of the projection points $\mathbf{m}_1$, $\mathbf{m}_2$ are affected by errors (e.g., digitalization errors, noise errors, etc.), therefore the resulting four linear equations are linearly independent such that only the trivial solution $\mathbf{M} = \mathbf{0}$ can be obtained explicitly. The non-trivial solution $\mathbf{M} \neq \mathbf{0}$, with $\mathbf{M}(4) = 1$, can be found numerically with the Singular Value Decomposition (SVD) method [54]. These solutions are thus affected by numerical errors. The procedure shown above can be generalized to the case of $N > 2$ cameras. Each one adds 2 independent equations, so that a linear homogenous system of $2N$ equations in four unknowns is obtained. To conclude, it is noted that a single camera setup would provide only two independent equations, which are not enough to determine the 3D coordinates of a point. This reflects the fact that, in practice, at least two intersecting rays are needed to determine a point.

3.2.2 Geometric cost function

As discussed above, the solutions of the system of equations in Eq. 3.17 are derived numerically and are affected by errors. Note that, in the simulations, real or realistic images or videos are not considered, but it is assumed that the projection matrices of the cameras (using the pinhole model) and their relative position were known. The vibration in space of points corresponding to hypothetical markers fixed on the beam was therefore simulated, and the corresponding pixel position in each camera plane was computed with the pinhole model. The errors related to the 3D reconstructed point position are

caused mainly by quantization, due to the pixelization effect of the projection on the image planes of the cameras. To further minimise such errors, the following geometrical projection error $\varepsilon(\mathbf{M})$ is defined:

$$\varepsilon(\mathbf{M}) = \sum_{j=1}^{N} (u_j^r - u_j)^2 + (v_j^r - v_j)^2, \tag{3.19}$$

where u_j,v_j are the coordinates of the image point $\mathbf{m}_j$ of the j-th cameras whereas u_j^r, v_j^r are the coordinates of the estimated point $\mathbf{M}$ mapped into the image plane of the j-th camera by using the projection matrix $\mathbf{P}_j$:

$$u_j^r = \frac{\mathbf{p}_{1,j}^T \mathbf{M}}{\mathbf{p}_{3,j}^T \mathbf{M}}, \tag{3.20a}$$

$$v_j^r = \frac{\mathbf{p}_{2,j}^T \mathbf{M}}{\mathbf{p}_{3,j}^T \mathbf{M}}. \tag{3.20b}$$

Here $\mathbf{p}_{1,j}^T$, $\mathbf{p}_{2,j}^T$, $\mathbf{p}_{3,j}^T$ are the rows vector of the projection matrix $\mathbf{P}_j$

$$\mathbf{P}_j = \begin{bmatrix} \mathbf{p}_{1,j}^T \\ \mathbf{p}_{2,j}^T \\ \mathbf{p}_{3,j}^T \end{bmatrix}. \tag{3.21}$$

Eq. 3.19 gives the sum of the squared geometric distance between each j-th measured image point $\mathbf{m}_j$ and the re-projection point of $\mathbf{M}$, that is $\mathbf{m}_j^r$, which is mapped on the image plane of the j-th camera. The new estimated point $\mathbf{M}$ corresponds to the minimum of the cost function defined in Eq. 3.19 which can be minimized by using numerical methods such as the Gauss - Newton algorithm [54]. The initial point to search the local minima is normally obtained from the solution of Eq. 3.17.

3.3 Parametric studies

As pointed out in the introduction of this chapter, the aim of this study is to investigate if and how multiple cameras can be employed to increase the accuracy of flexural vibration measurements of distributed structures. Therefore, the formulations presented in Sections 3.1 and 3.2 for the flexural response of a beam and for the optical measurement of displacements by means of triangulation have been used to simulate the measurement of the flexural response of the cantilever beam model problem described in Section 3.1. More precisely, the analysis considered the measurement of the first three flexural deflection shapes of the cantilever beam at the first three fundamental resonance frequencies. The reference deflection shapes were derived from Eq. 3.7 with $F_0(\omega) = 1$ N and $t = \pi/\omega$. Also, the measured deflection shapes were simulated using the formulations presented in Section 3.2 with respect to the displacements at the 25 marker points calculated from Eq. 3.7 with $F_0(\omega) = 1$ N and $t = \pi/\omega$.

To provide a background understanding of the problem at hand, a comprehensive analysis is

performed, which shows how the following parameters affect the measurement of the beam flexural response by means of triangulation with a pair or multiple of cameras:

1. the radial distance d of a pair of cameras from the centre of the beam;
2. the aperture angle α between a pair of cameras;
3. the resolution of a pair of cameras;
4. the number of cameras in setups composed by more than 1 pair of cameras.

The pair or multiple cameras setups were arranged in a symmetric position with respect to the vertical planes YZ and XZ that cut the beam in two parts transversely and longitudinally respectively. Therefore, the results presented in the following sections provide background considerations on how the geometry and the characteristics of different setups of cameras affect the measurement of the flexural response of a cantilever beam. The geometries, i.e. their positions and numbers, and the type of cameras, i.e. their resolutions, considered in the parametric studies listed above are summarised in Tables 3.3 and 3.4.

The accuracy of the reconstruction of the deflection shape is analysed with respect to two errors. First, the point errors, which give the reconstruction error at each of the 25 measurement points, normalised with respect to the maximum displacement of the beam:

$$E_i = \frac{|w_i - w_{r,i}|}{w_{max}} 100 \text{ (\% rel. to } w_{max}). \tag{3.22}$$

Here w_i is the transverse displacement of the i-th marker reconstructed by the cameras setup whereas $w_{r,i}$ is the reference transverse displacement of the i-th marker given by Eq. 3.7. Also, w_{max} is the maximum reference displacement i.e. the displacement of the marker at the tip of the beam, given with Eq. 3.7. Second the average error given by the root mean square error over all the 25 measurement points:

$$E_m = \frac{\sqrt{\frac{1}{25}\sum_{i=1}^{25}(w_i - w_{r,i})^2}}{w_{max}} 100 \text{ (\% rel. to } w_{max}). \tag{3.23}$$

The following sections will illustrate how the four parameters listed above influence the measurement of the first three flexural deflection shapes of the cantilever beam shown in Fig. 3.1 using the multiple camera setup depicted in Fig. 3.3. As can be deduced from Figs. 3.4 to 3.28 shown below, the simulation results are reported in a standard framework, which shows:

a) a sketch of the measurement setup with highlighted the varied parameter;

b) the reference deflection shape (grey line) and the measured deflection shapes (colored lines): for clarity, only the best and worst cases are shown;

c) the point errors in % with respect to the maximum displacement of the beam (colored lines): for clarity, only the best and worst cases are shown;

d) the average error in % with respect to the maximum displacement of the beam (colored lines).

Table 3.3: Positions and resolutions of pairs of cameras ($^*k = 0, 1$).

Cases	Radial distance d [mm]	Aperture angle α [°]	Azimuthal angle θ [°]	Elevation angle ϕ [°]	Resolution [pixel]
1 (Figs. 3.4 - 3.6)	500 750 1000 1500	60	±30	25	320×180
2a (Figs. 3.7 - 3.9)	500	16 60 110 160	± 8 ± 30 ± 55 ± 80	10	320×180
2b(Figs. 3.10 - 3.12)	500	170 140 100 60	±90	5 20 40 60	320×180
2c (Figs. 3.13 - 3.15)	500	16 60 110 160	-90 ± 8 -90 ± 30 -90 ± 55 -90 ± 80	10	320×180
2d (Figs. 3.16 - 3.18)	500	170 140 100 60	k180*	5 20 40 60	320×180
3 (Figs. 3.19 - 3.21)	500	60	±30	25	320×180 640×360 1280×720 1920×1080

Table 3.4: Positions and resolutions of multiple cameras setups ($^*k = 0, 1$).

Cases	Radial distance d [mm]	Azimuthal angle θ [°]	Elevation angle ϕ [°]	Resolution [pixel]
4a (Figs. 3.22 - 3.24)	500	± 7 ±7/±14 ±7/±14/±27 ±7/±14/±27/±30 ±7/±14/±27/±30/±47 ±7/±14/±27/±30/±47/±50	15 15/15 15/15/15 15/15/15/5 15/15/15/5/5 15/15/15/5/5/5	320×180
4a′ (Figs. 3.25 - 3.27)	500	±50 ±50/±47 ±50/±47/±30 ±50/±47/±30/±27 ±50/±47/±30/±27/±14 ±50/±47/±30/±27/±14/±7	15 15/15 15/15/15 15/15/15/5 15/15/15/5/5 15/15/15/5/5/5	320×180
4b (Figs. 3.28 - 3.30)	500	±90 ±90/±90 ±90/±90/±90 ±90/±90/±90/±90	8 8/28 8/28/48 8/28/48/58	320×180
4c (Figs. 3.31 - 3.33)	500	-90 (± 7) -90 (±7/±14) -90 (±7/±14/±27) -90 (±7/±14/±27/±30) -90 (±7/±14/±27/±30/±47) -90 (±7/±14/±27/±30/±47/±50)	15 15/15 15/15/15 15/15/15/5 15/15/15/5/5 15/15/15/5/5/5	320×180
4d (Figs. 3.34 - 3.36)	500	k180* k180*/k180* k180*/k180*/k180* k180*/k180*/k180*/k180*	8 8/28 8/28/48 8/28/48/58	320×180
4e (Figs. 3.37 - 3.39)	500	k180*+7 k180*+(7/27) k180*+(7/27/0) k180*+(7/27/0/90) k180*+(7/27/0/90/47) k180*+(7/27/0/90/47/60)	15 15/15 15/15/15 15/15/15/5 15/15/15/5/5 15/15/15/5/5/5	320×180

3.3.1 Distance d of cameras from the beam

The accuracy of the reconstruction of the beam first three flexural deflection shapes with a pair of cameras arranged with fixed azimuthal θ and elevation ϕ angles and increasingly larger distance d from the middle point of the beam is first considered in this subsection with respect to the geometries and resolution of the cameras summarised in Table 3.3 - Case 1.

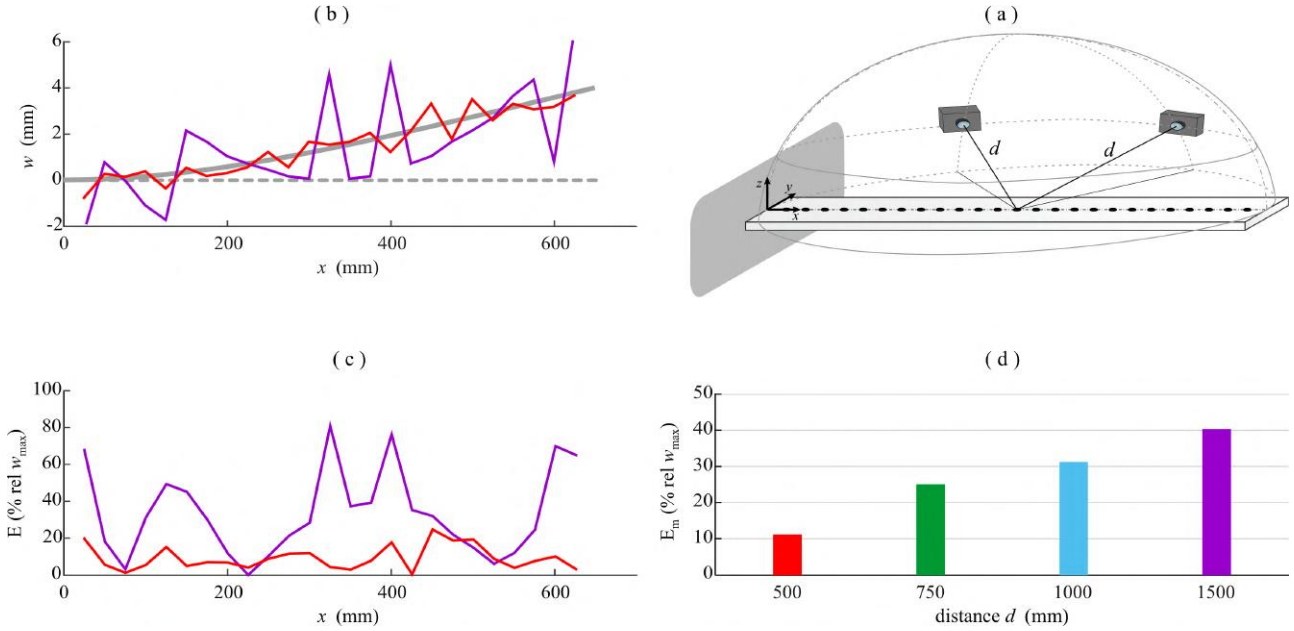

Figure 3.4: First deflection shape: (a) distance case study 1; (b) comparison between reconstructed flexural deflection shapes of the beam (grey line reference shape); (c) percentage error calculated along the beam span; (d) histogram of the mean error. Colored lines reproduce the cases listed in the histogram.

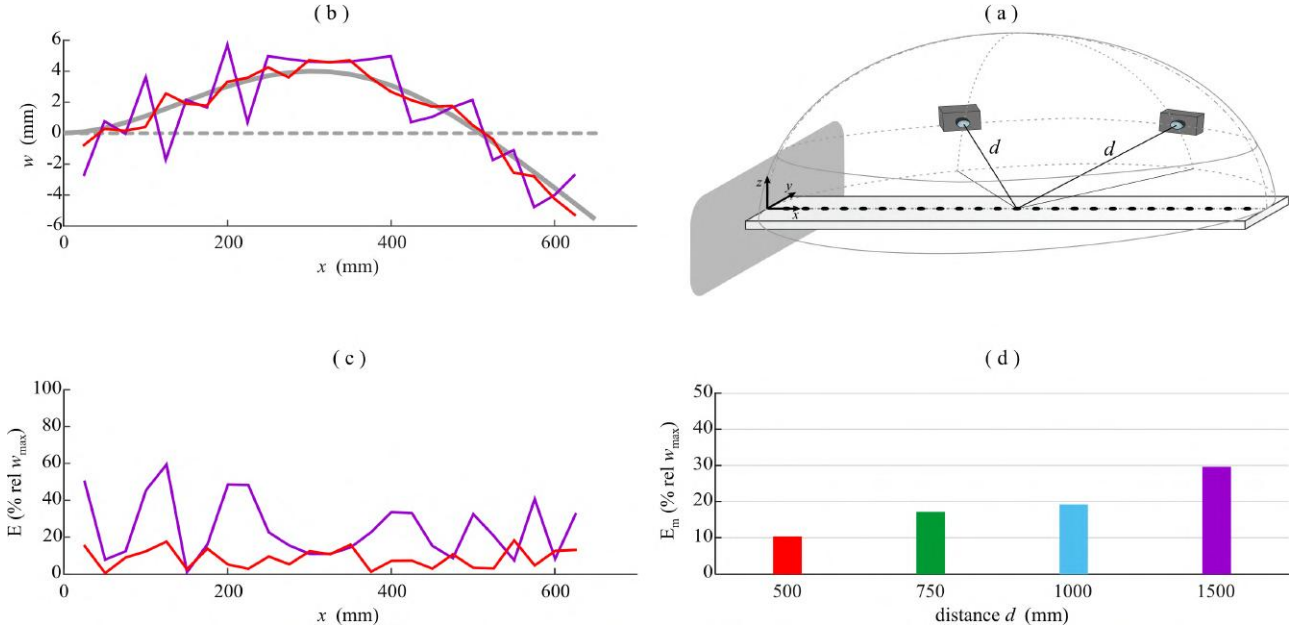

Figure 3.5: Second deflection shape: (a) distance case study 1; (b) comparison between reconstructed flexural deflection shapes of the beam (grey line reference shape); (c) percentage error calculated along the beam span; (d) histogram of the mean error. Colored lines reproduce the cases listed in the histogram.

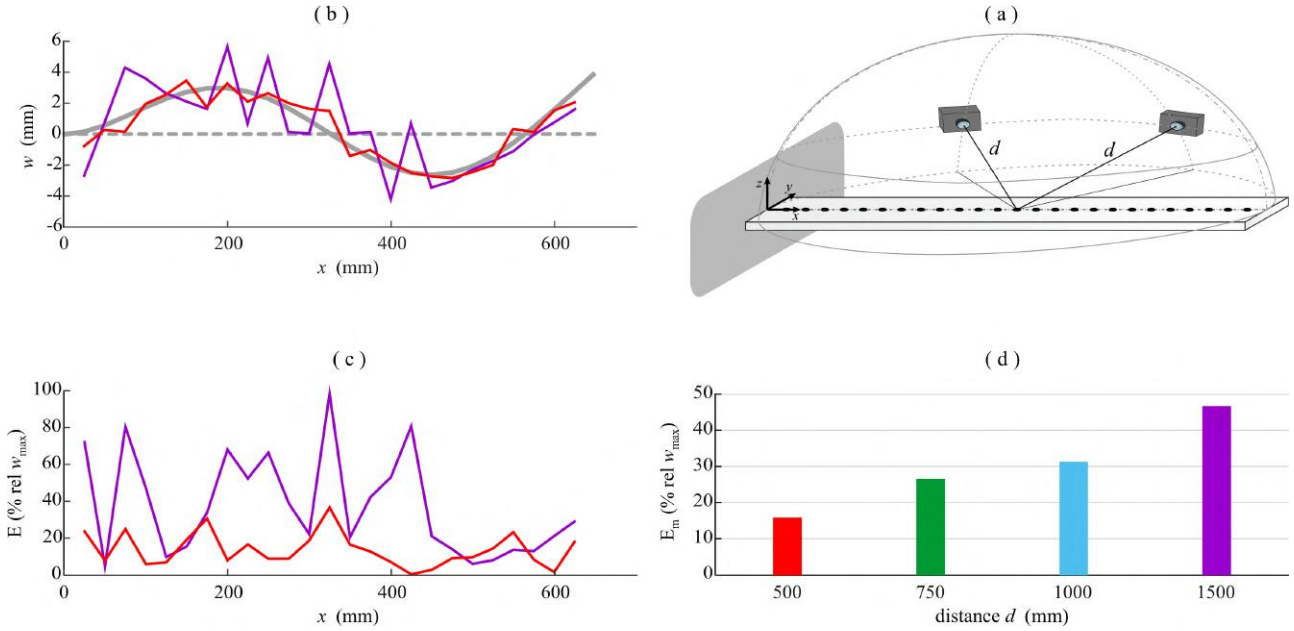

Figure 3.6: Third deflection shape: (a) distance case study 1; (b) comparison between reconstructed flexural deflection shapes of the beam (grey line reference shape); (c) percentage error calculated along the beam span; (d) histogram of the mean error. Colored lines reproduce the cases listed in the histogram.

The results presented in Figs. 3.4 - 3.6 clearly indicate that the accuracy of the measurement decreases as the distance of the cameras from the centre of the beam is increased. For instance, according to the bar Plot (d) in Fig. 3.4, which refers to the first flexural deflection shape the average error grows from about 10% to about 40% when the distance of the cameras is increased from 500 to 1500 mm. Also, Plot (c) in Fig. 3.4 shows that when the cameras are placed at 500 mm distance, the measurement error along the 25 marker points is always smaller than 30% whereas when the cameras are placed at 1500 mm the error can reach a maximum of 80%. Figs. 3.5 - 3.6 show similar behaviors for the errors calculated when the second and the third flexural deflection shapes are considered respectively. More specifically, Fig. 3.5 Plot (d) shows that the average error increases from 10% to 30% while the point error (Plot (c)) grows from a maximum of 20% to a maximum of 60% when the distance is increased from 500 mm to 1500 mm. Similarly, Fig. 3.6 shows that the average error grows from 16% to 47% while the point error goes from a maximum of 40% to a maximum of 100% when the distance is increased from 500 mm to 1500 mm.

3.3.2 Aperture angle α between cameras

The accuracy of the reconstruction of the beam first three flexural deflection shapes is examined in this subsection assuming the pair of cameras is arranged with fixed distance d from the middle point of the beam and with increasingly larger aperture angle α between the two cameras. Note that the accuracy of stereo estimations depends on the ratio between disparity and baseline, i.e. the distance between the centers of projection of the cameras (see Appendix B), for a given focal length: thus, similar results

could be found for different values of the distance d. Four cases are considered. To start with, the first two configurations are considered. In Case 2a, the cameras are arranged over an arc of a circle, which is oriented parallel to the plane of the beam and aligned parallel to the longitudinal axis of the beam, such that the cameras are all characterised by the same elevation angle $\phi = 10°$ and have increasingly larger aperture angles α, therefore, as reported in Table 3.3 - Case 2a, increasingly larger azimuthal angles $\theta = \pm\alpha/2$. In Case 2b, the cameras are arranged over an arc of a circle, which is oriented orthogonal to the plane of the beam and passes through the longitudinal axis of the beam. Therefore, in this case the elevation ϕ angle of the cameras is varied to generate the increasing aperture angle α as summarised in Table 3.3 - Case 2b.

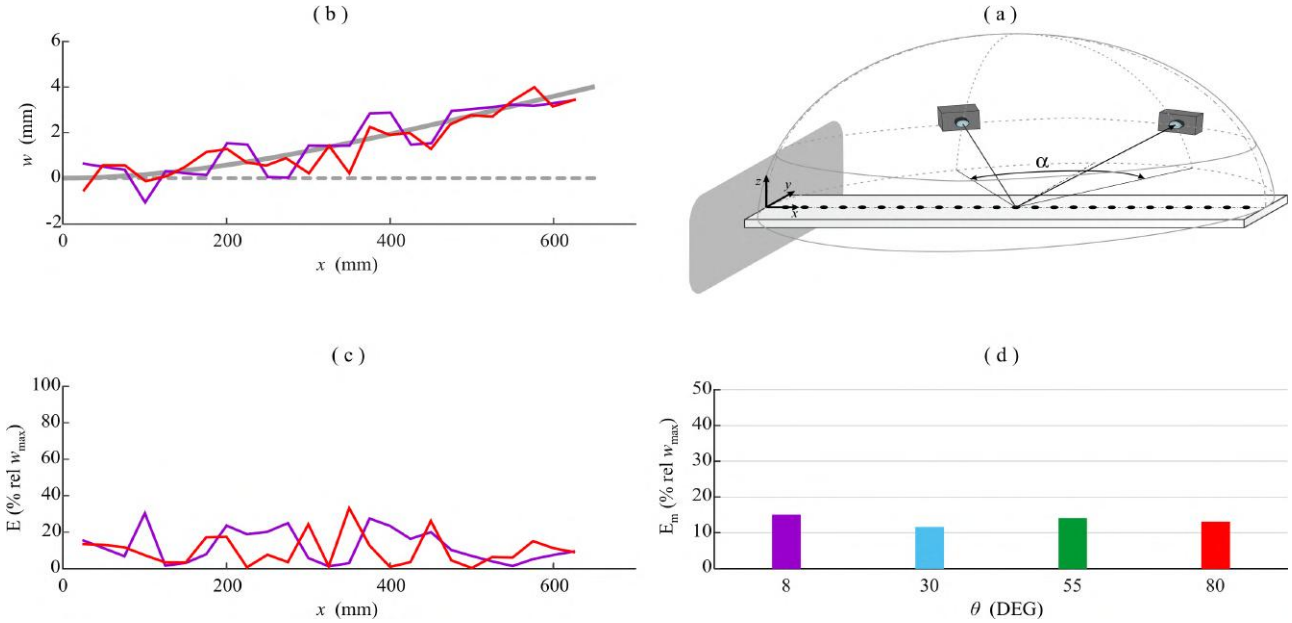

Figure 3.7: First deflection shape: (a) aperture angle case study 2a ($\alpha = 2|\theta|$); (b) comparison between reconstructed flexural deflection shapes of the beam (grey line reference shape); (c) percentage error calculated along the beam span; (d) histogram of the mean error. Colored lines reproduce the cases listed in the histogram.

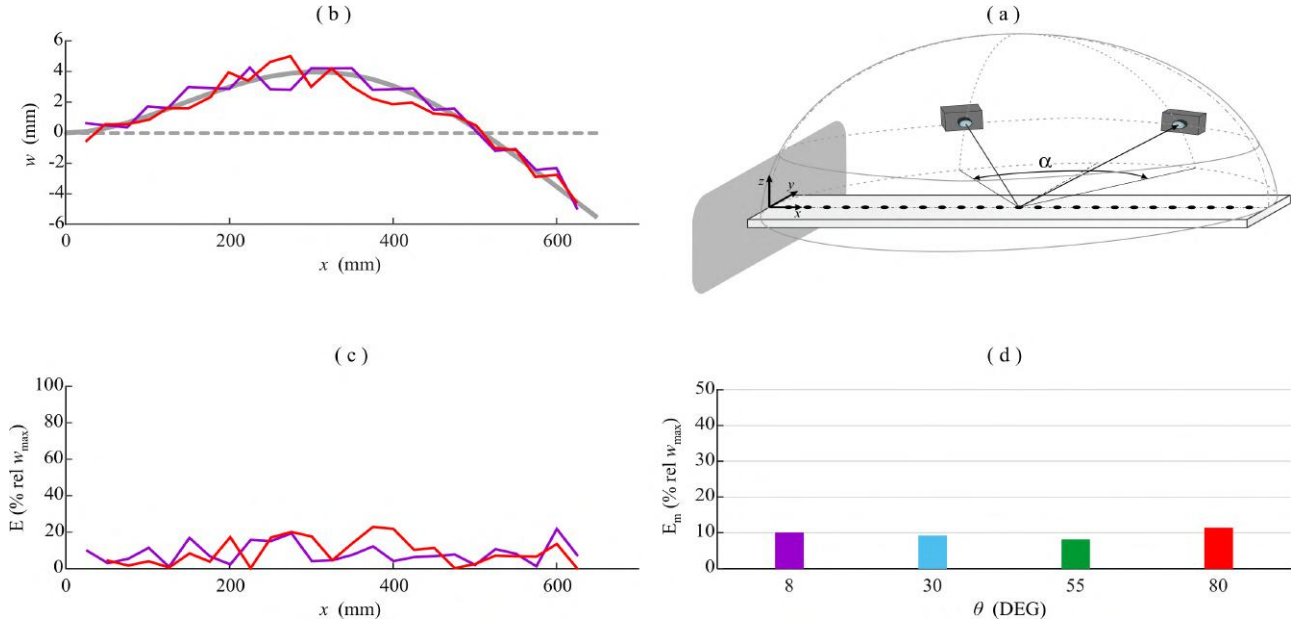

Figure 3.8: Second deflection shape: (a) aperture angle case study 2a ($\alpha = 2|\theta|$); (b) comparison between reconstructed flexural deflection shapes of the beam (grey line reference shape); (c) percentage error calculated along the beam span; (d) histogram of the mean error. Colored lines reproduce the cases listed in the histogram.

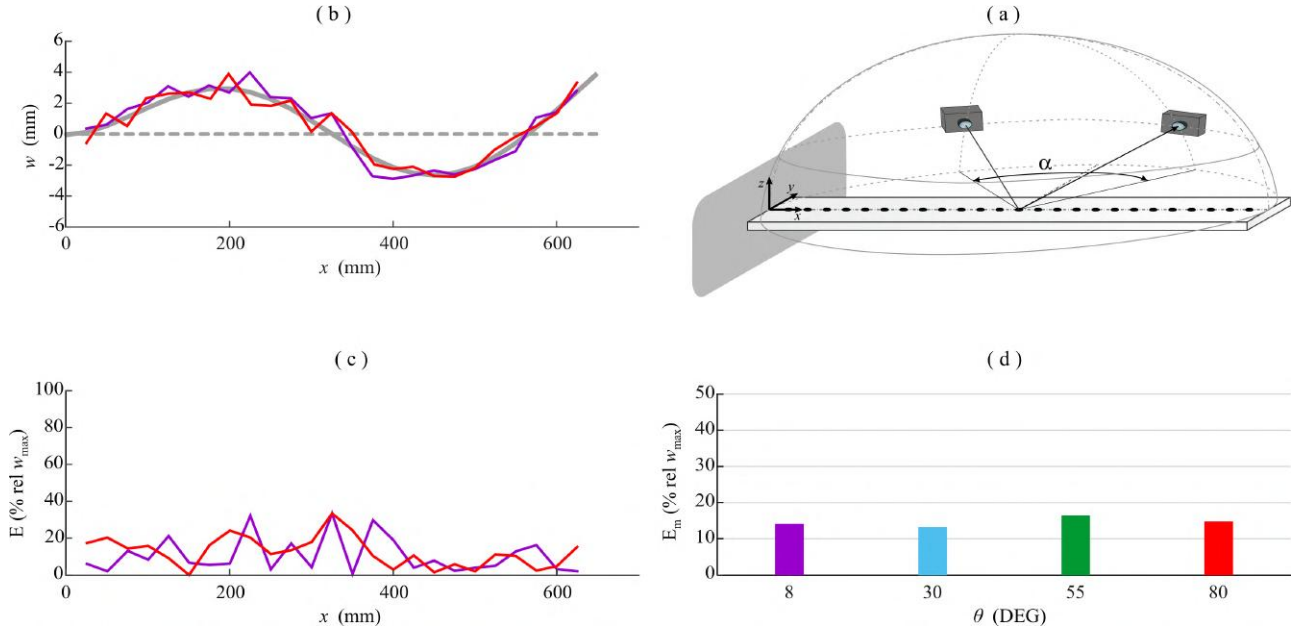

Figure 3.9: Third deflection shape: (a) aperture angle case study 2a ($\alpha = 2|\theta|$); (b) comparison between reconstructed flexural deflection shapes of the beam (grey line reference shape); (c) percentage error calculated along the beam span; (d) histogram of the mean error. Colored lines reproduce the cases listed in the histogram.

The results presented in Figs. 3.7 - 3.9 indicate that, when the cameras are arranged along the arc of a circle oriented parallel to beam plane such that the cameras have a little elevation angle of 10°, the accuracy of the measurement does not vary significantly as the angle of aperture between the cameras is increased. Indeed, the bar Plot (d) of Figs. 3.7 - 3.9 indicates that, for all the three flexural deflection shapes considered, the average error is comprised between 8% and 18%. Also, Plot (c) shows

that the maximum error does never exceed a maximum level of 40%.

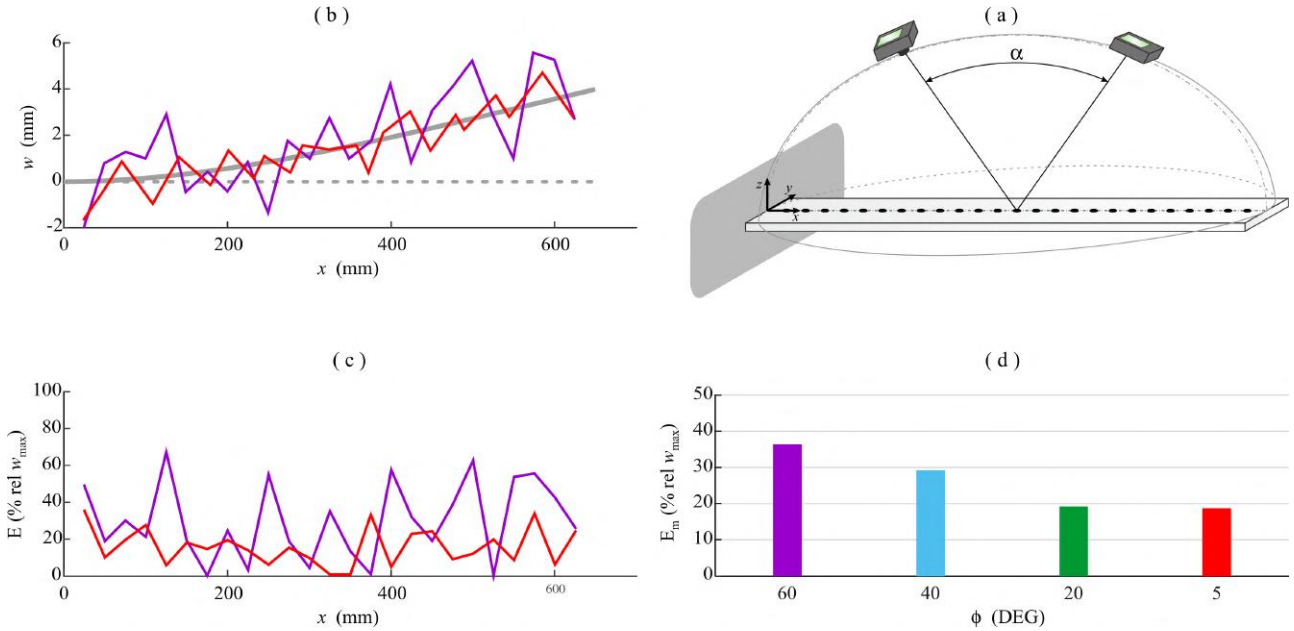

Figure 3.10: First deflection shape: (a) aperture angle case study 2b ($\alpha = 180 - 2\phi$); (b) comparison between reconstructed flexural deflection shapes of the beam (grey line reference shape); (c) percentage error calculated along the beam span; (d) histogram of the mean error. Colored lines reproduce the cases listed in the histogram.

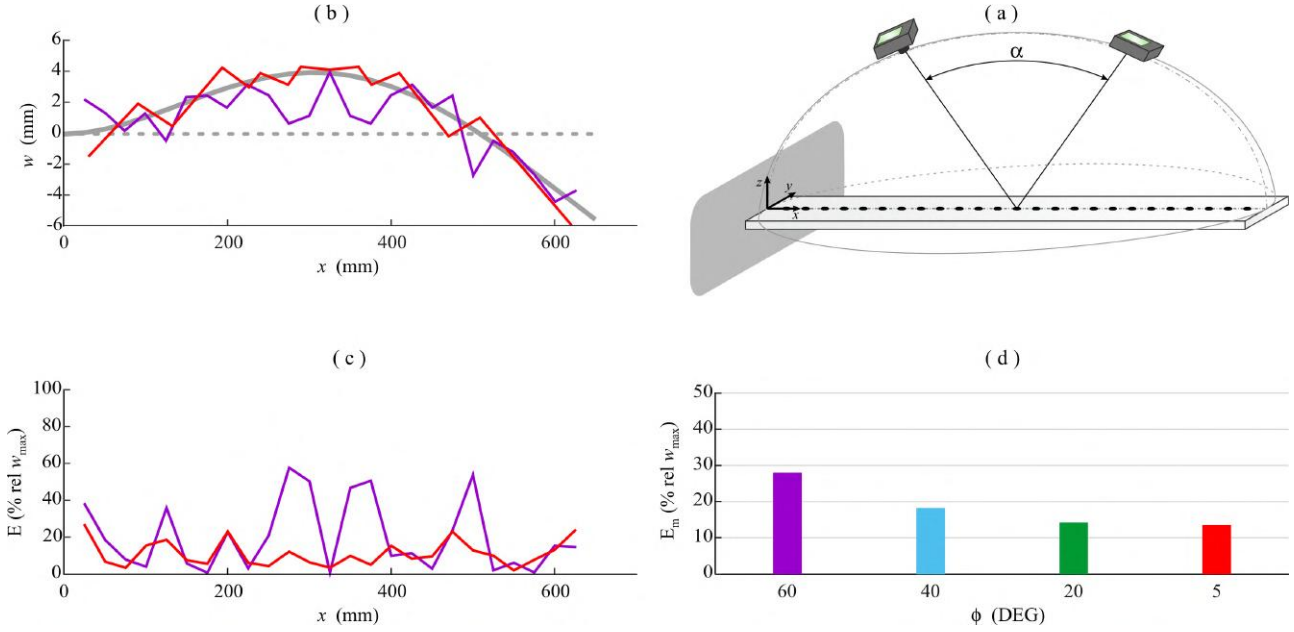

Figure 3.11: Second deflection shape: (a) aperture angle case study 2b ($\alpha = 180 - 2\phi$); (b) comparison between reconstructed flexural deflection shapes of the beam (grey line reference shape); (c) percentage error calculated along the beam span; (d) histogram of the mean error. Colored lines reproduce the cases listed in the histogram.

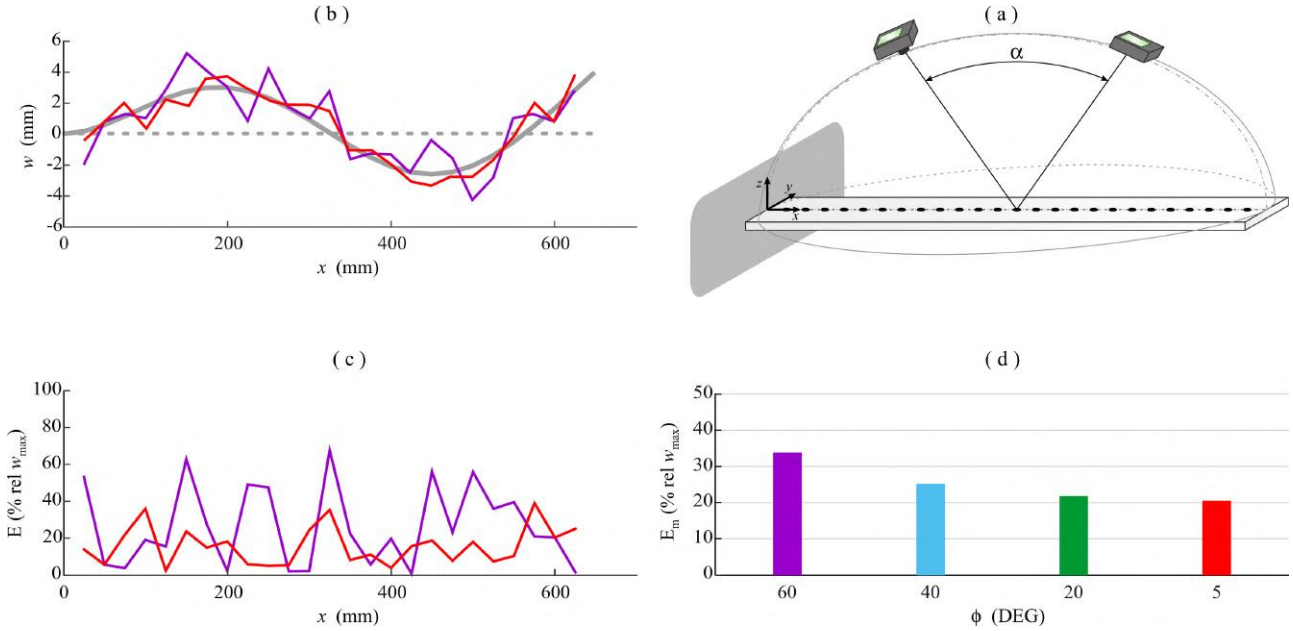

Figure 3.12: Third deflection shape: (a) aperture angle case study 2b ($\alpha = 180 - 2\phi$); (b) comparison between reconstructed flexural deflection shapes of the beam (grey line reference shape); (c) percentage error calculated along the beam span; (d) histogram of the mean error. Colored lines reproduce the cases listed in the histogram.

Instead, the results presented in Figs. 3.10 - 3.12 show that, when the cameras are arranged along the arc of circle, which is oriented orthogonal to the plane of the beam and passes through the longitudinal axis of the beam, the accuracy of the measurement does vary significantly as the angle of aperture between the cameras is increased. Indeed, the bar Plot (d) of Fig. 3.10, which refers to the first flexural deflection shape, indicates that the average error passes from 37% to 18% when the angle of aperture is increased from 60° to 170°. Moreover, when the aperture angle is only 60° rather large errors up to 70% characterise the measurement along the beam, whereas the maximum error for an aperture angle of 170° is of the order of 40% only. Plot (d) in Fig. 3.11, which refers to the second flexural deflection shape, shows that the average error falls from 19% to 12% (Plot (d)) while the point error is characterized by errors up to 60% when the aperture angle is 60° while, when the angle of aperture is 170°, the maximum point error does not exceed 20% (Plot (c)). Plot (d) in Fig. 3.12 Plot (d) shows that, when the third flexural deflection shape is considered, the average error falls from 32% to 20% when the angle of aperture is increased from 60° to 170°. Plot (c) shows that the point error presents a maximum of 70% when the angle of aperture is 60° whereas the maximum error for an aperture angle of 170° is of 40% only. In conclusion, the results presented in Figs. 3.10 -3.12 indicate that the accuracy of the measurement is strongly influenced by the elevation angle of the cameras. The smaller is this angle the greater is the accuracy of the measurement. Therefore, in general, to have accurate measurements, the cameras should be arranged over an arc of a circle, which is oriented parallel to the plane of the beam and placed a small distance from the beam itself, so that the cameras are characterized by small elevation angles.

The third and fourth configurations are now discussed. Cases 2c and 2d consider similar arrangements for the two cameras as those seen in Cases 2a and 2b. However, here, the cameras are rotated by $\pi/2$ around the z axis. Therefore, in Case 2c the cameras are arranged over an arc of a circle, which is oriented parallel to the plane of the beam and aligned orthogonal to the longitudinal axis of the beam, such that the cameras are all characterized by the same elevation angle $\phi = 10°$ and have increasingly larger aperture angles α, therefore, as reported in Table 3.3 - Case 2c, increasingly larger azimuthal angles $\theta = \pm\alpha/2$. In Case 2d, the cameras are arranged over an arc of a circle, which is oriented orthogonal to the plane of the beam and passes across the longitudinal axis of the beam. Therefore, in this case, as reported in Table 3.3 - Case 2d, the elevation ϕ angle varies as the aperture angle is increased.

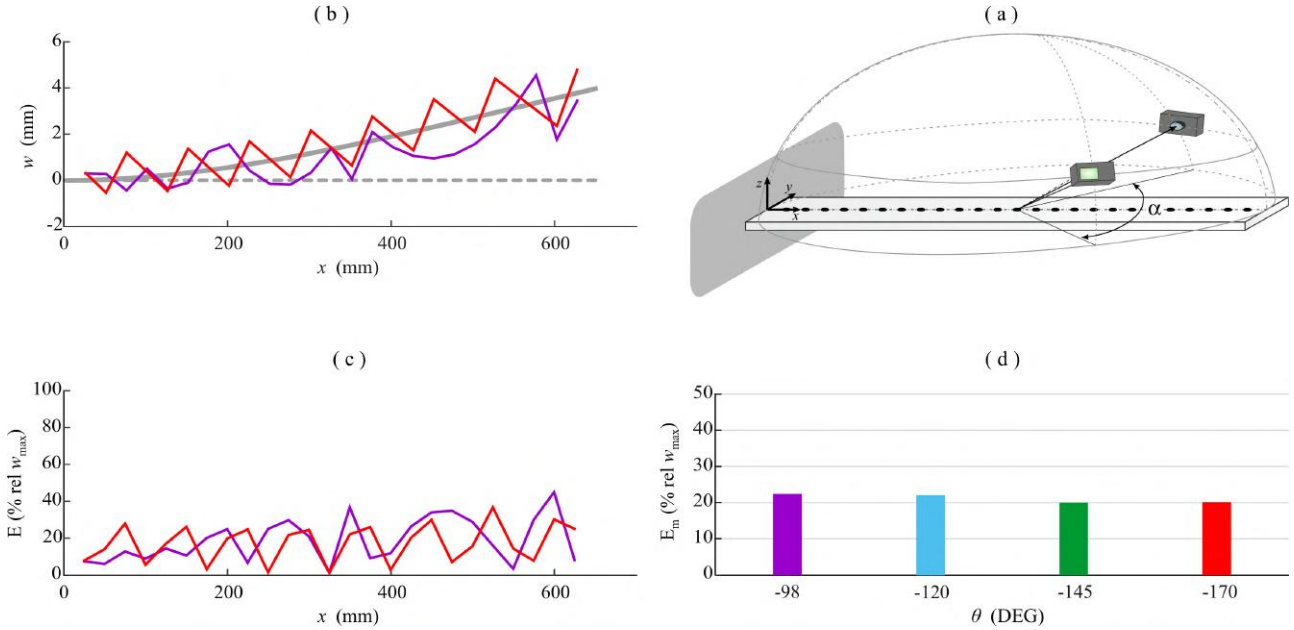

Figure 3.13: First deflection shape: (a) aperture angle case study 2c ($\alpha = 2|\theta|$); (b) comparison between reconstructed flexural deflection shapes of the beam (grey line reference shape); (c) percentage error calculated along the beam span; (d) histogram of the mean error. Colored lines reproduce the cases listed in the histogram.

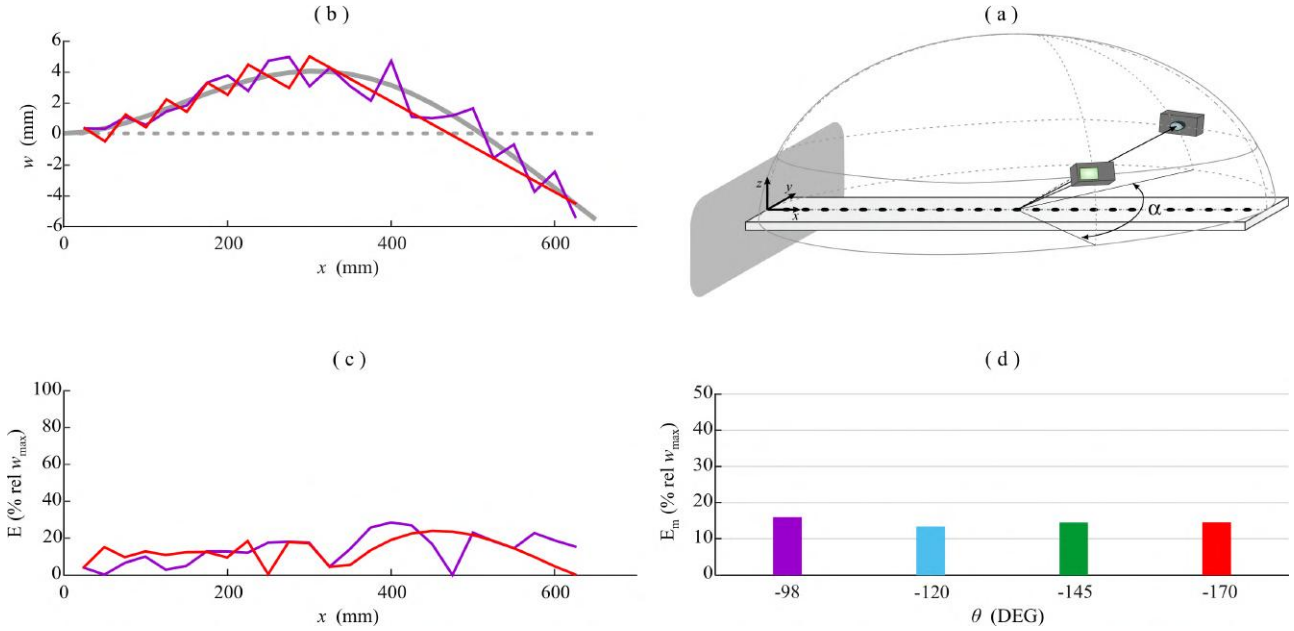

Figure 3.14: Second deflection shape: (a) aperture angle case study 2c ($\alpha = 2|\theta|$); (b) comparison between reconstructed flexural deflection shapes of the beam (grey line reference shape); (c) percentage error calculated along the beam span; (d) histogram of the mean error. Colored lines reproduce the cases listed in the histogram.

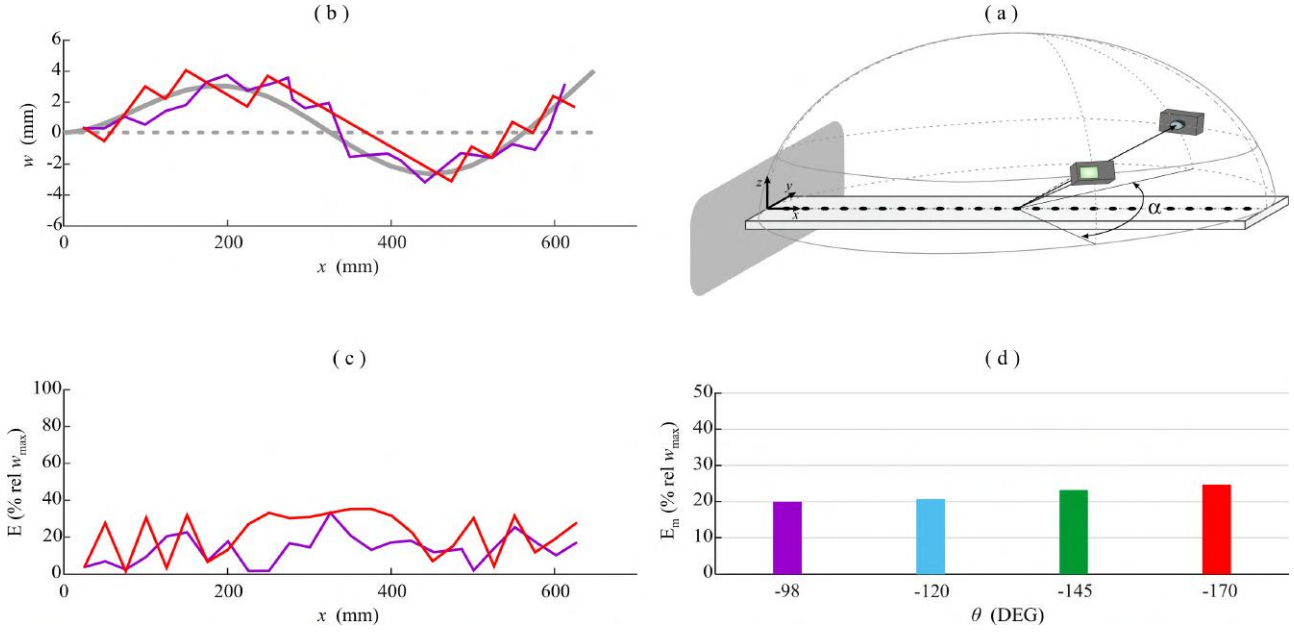

Figure 3.15: Third deflection shape: (a) aperture angle case study 2c ($\alpha = 2|\theta|$); (b) comparison between reconstructed flexural deflection shapes of the beam (grey line reference shape); (c) percentage error calculated along the beam span; (d) histogram of the mean error. Colored lines reproduce the cases listed in the histogram.

The bar Plot (d) of Figs. 3.13 - 3.15 indicates that, for all the three flexural deflection shapes considered, the average error when the two cameras are arranged with small elevation angles across the beam with increasing aperture angles α is always comprised between 12% and 23%. Also, Plot (c) shows that the maximum error does never exceed a maximum level of 40%.

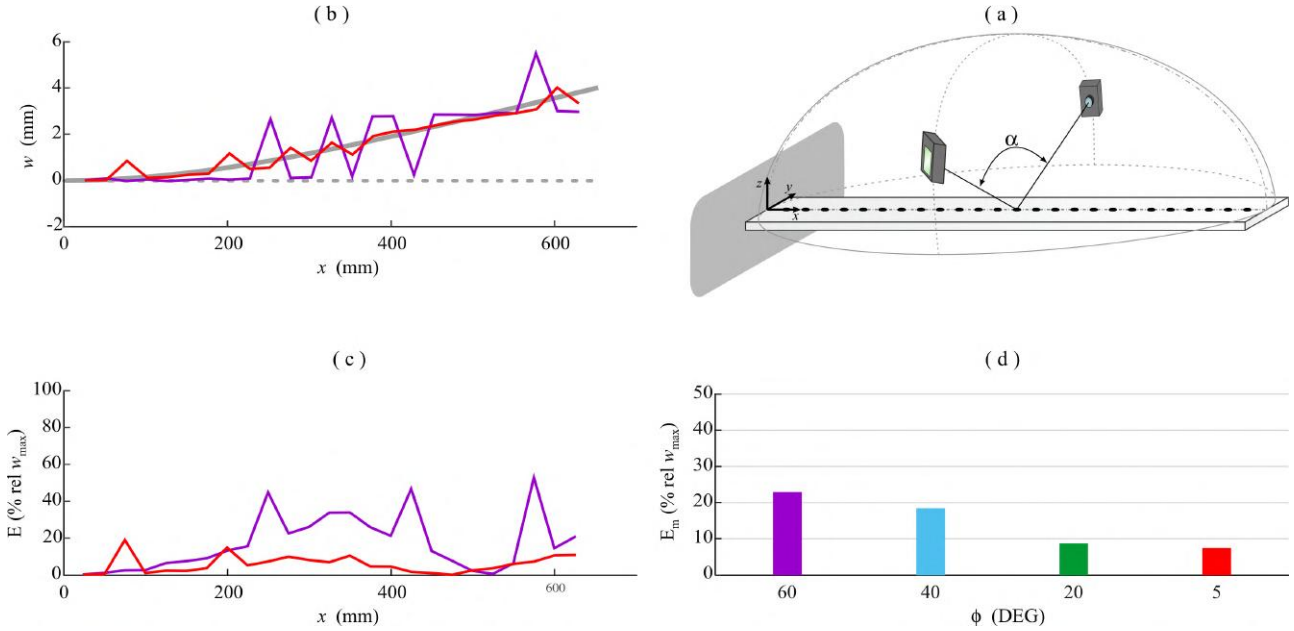

Figure 3.16: First deflection shape: (a) aperture angle case study 2d ($\alpha = 180 - 2\phi$); (b) comparison between reconstructed flexural deflection shapes of the beam (grey line reference shape); (c) percentage error calculated along the beam span; (d) histogram of the mean error. Colored lines reproduce the cases listed in the histogram.

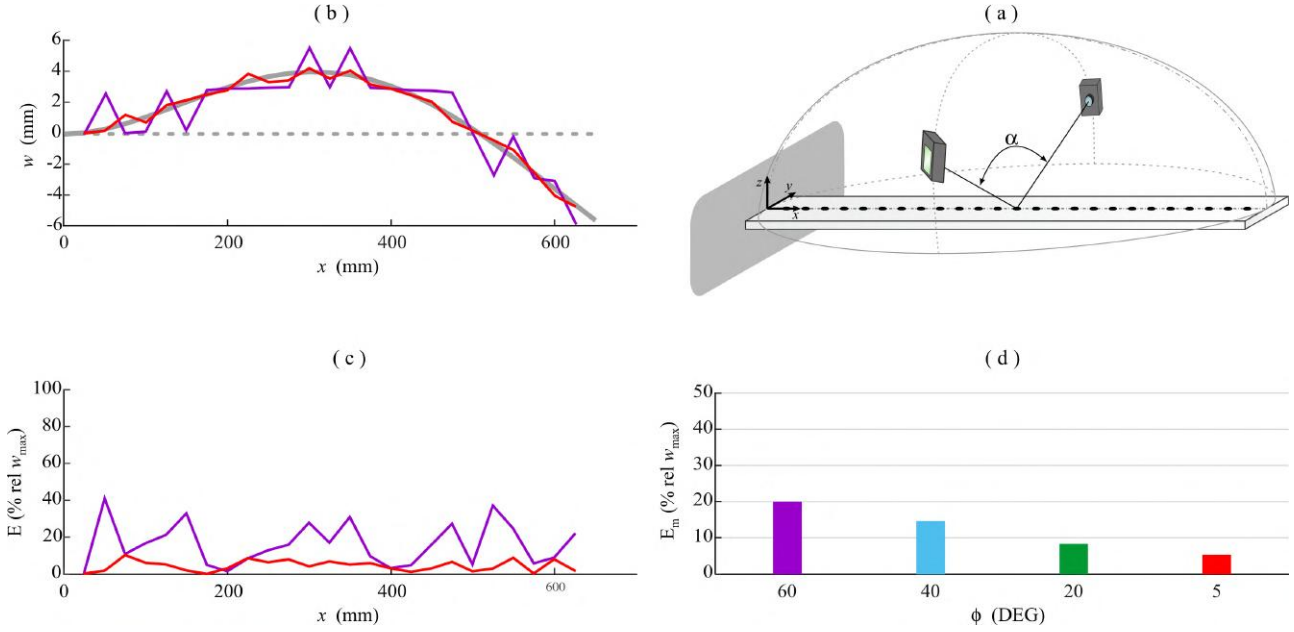

Figure 3.17: Second deflection shape: (a) aperture angle case study 2d ($\alpha = 180 - 2\phi$); (b) comparison between reconstructed flexural deflection shapes of the beam (grey line reference shape); (c) percentage error calculated along the beam span; (d) histogram of the mean error. Colored lines reproduce the cases listed in the histogram.

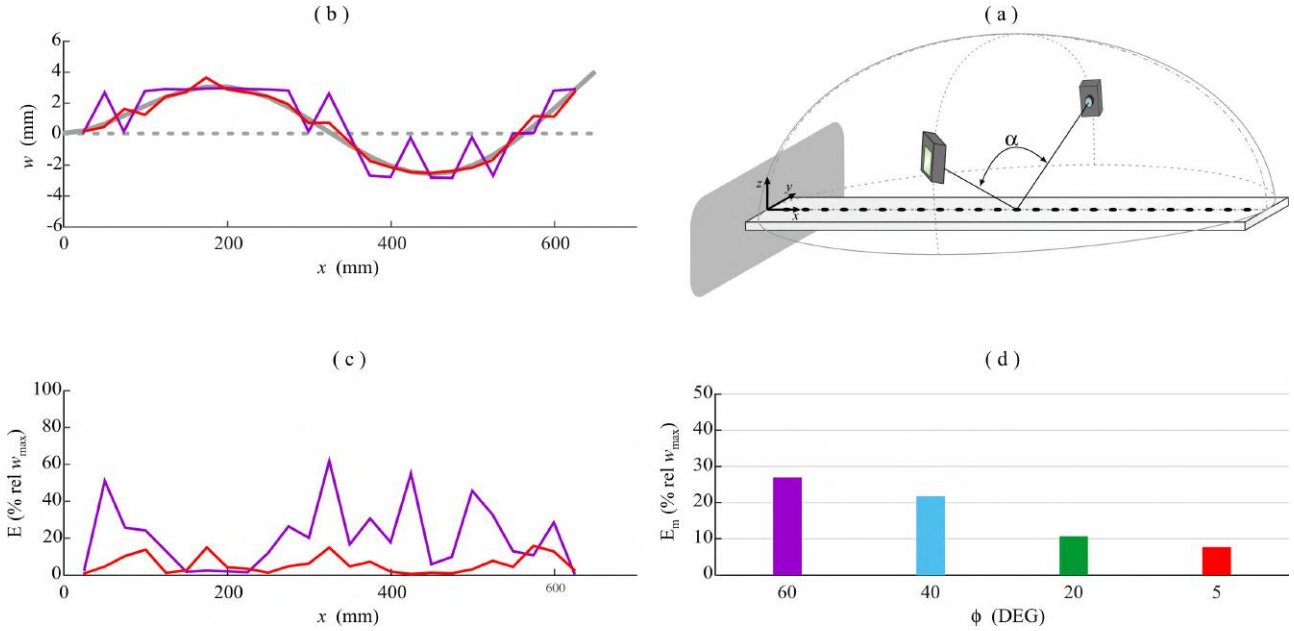

Figure 3.18: Third deflection shape: (a) aperture angle case study 2d ($\alpha = 180 - 2\phi$); (b) comparison between reconstructed flexural deflection shapes of the beam (grey line reference shape); (c) percentage error calculated along the beam span; (d) histogram of the mean error. Colored lines reproduce the cases listed in the histogram.

Moving to Case 2d with the cameras arranged along an arc oriented orthogonal to the beam, the results presented in the bar Plot (d) of Figs. 3.16 - 3.17, for the first and second flexural deflection shapes, indicate that the average error passes from 22-20% to 8-5% when the angle of aperture is increased from 60° to 170°. Moreover, when the aperture angle is only 60° rather large errors up to 40-60% characterise the measurement along the beam, whereas the maximum error for an aperture angle of 170° is of the order of 20% only. Fig. 3.18 shows that the errors that affect the third measurements of the deflection shape are slightly bigger. More specifically, Plot (d) shows that the average error falls from 28% to 9% while the point error, which is shown in Plot (c), falls from a maximum of 70% to a maximum of 20% when the angle of aperture is increased from 60° to 170°.

3.3.3 Resolution of cameras

The accuracy of the reconstruction of the beam first three flexural deflection shape obtained by pairs of cameras characterized by increasingly larger spatial resolution is now investigated. In the simulations, the image plane coordinates associated to the projection of one 3D point are rounded to integer pixel coordinates. Thus, the point coordinates in the image plane are affected by a quantization error, which increases when the camera resolution decreases. The distance d, the azimuthal θ and elevation ϕ angles and the resolutions of the cameras are listed in Table 3.3 - Case 3.

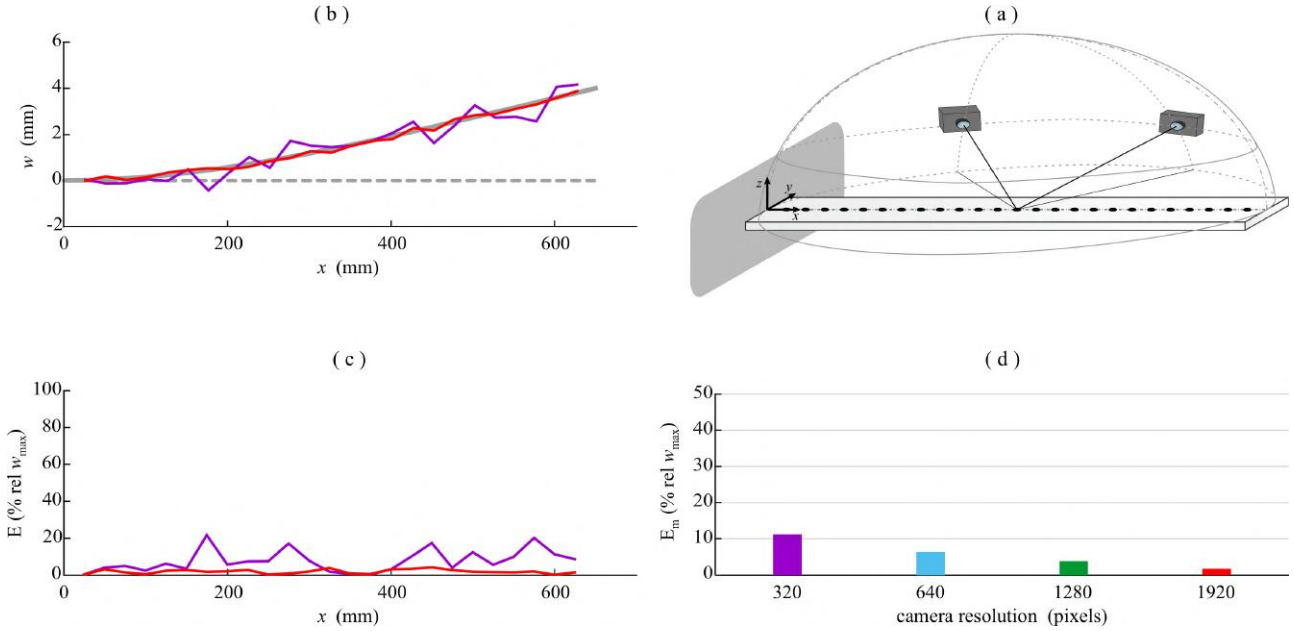

Figure 3.19: First deflection shape: (a) resolution case study 3; (b) comparison between reconstructed flexural deflection shapes of the beam (grey line reference shape); (c) percentage error calculated along the beam span; (d) histogram of the mean error. Colored lines reproduce the cases listed in the histogram.

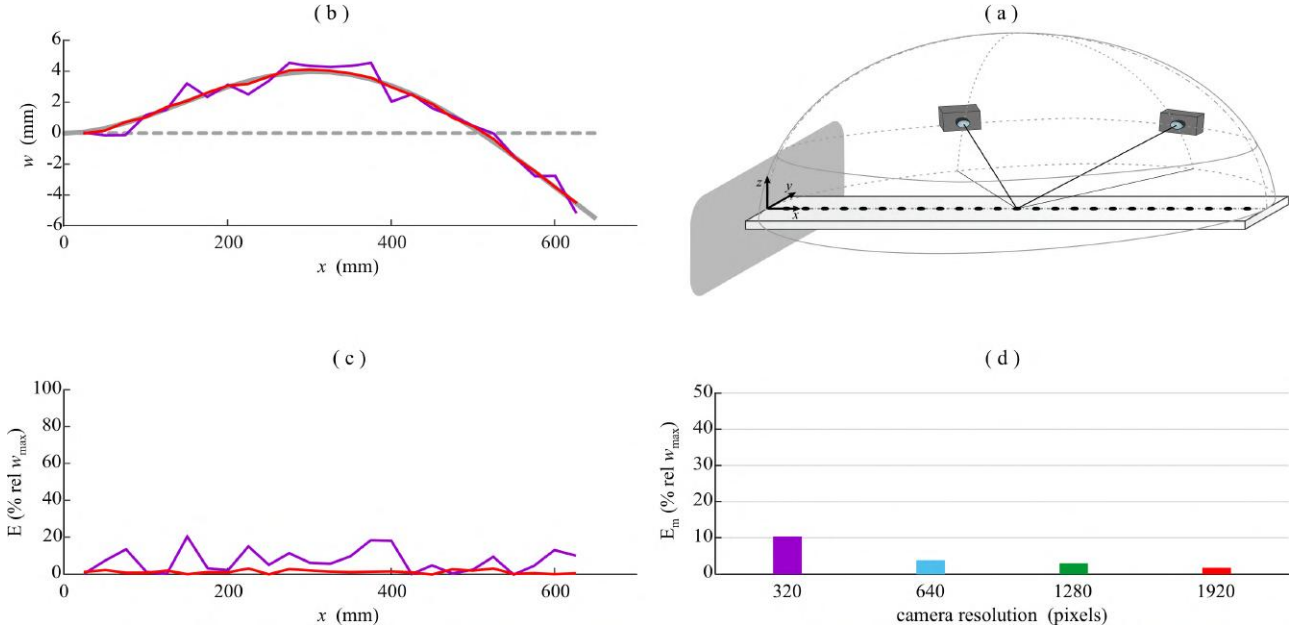

Figure 3.20: Second deflection shape: (a) resolution case study 3; (b) comparison between reconstructed flexural deflection shapes of the beam (grey line reference shape); (c) percentage error calculated along the beam span; (d) histogram of the mean error. Colored lines reproduce the cases listed in the histogram.

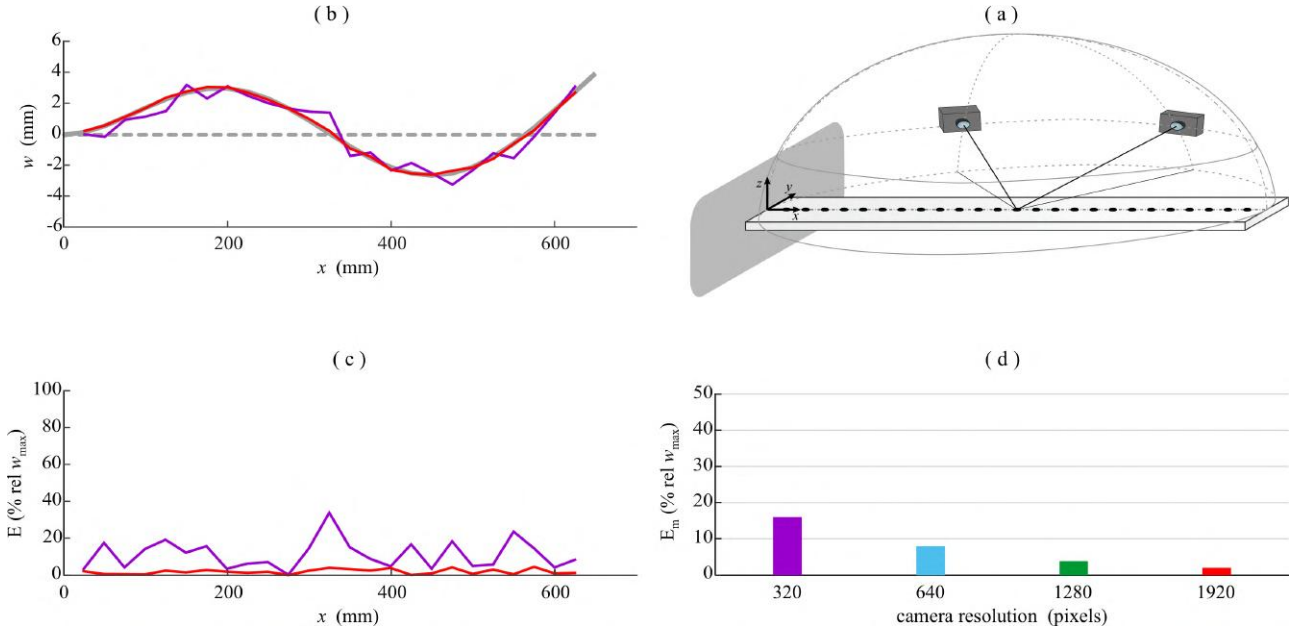

Figure 3.21: Third deflection shape: (a) resolution case study 3; (b) comparison between reconstructed flexural deflection shapes of the beam (grey line reference shape); (c) percentage error calculated along the beam span; (d) histogram of the mean error. Colored lines reproduce the cases listed in the histogram.

As one would expect, the results presented in Figs. 3.19 - 3.21 unequivocally indicate that the accuracy of the measurement increases as the resolution of the cameras is increased. Similar considerations can be done for the three flexural deflection shapes considered. For instance, when the number of pixels is raised from 320×180 to 1920×1080, the bar Plot (d) of Figs. 3.19 - 3.21 suggests that the average error of the measurement falls from about 10-15% to 2%. Moreover, according to Plot (c), the maximum measurement error over the 25 marker points falls from a maximum error of 20%, for the first and second flexural deflection shapes (Figs. 3.19 - 3.20), or 40%, for the third flexural deflection shape (Fig. 3.21), to 3%.

3.3.4 Arrays composed by more than 2 cameras

To conclude, the measurement with a multiple cameras setup composed by more than 2 cameras is examined in this subsection. More precisely, the study considers the sequential addition of pairs of cameras, which are located symmetrically with respect to either the YZ plane centered in the middle of the beam or the XZ plane passing through the longitudinal axis of the beam. This choice was made for convenience and to limit the number of cases considered in the simulations. As a matter of fact, similar arrangements with a different placement of the cameras, or with an odd number of cameras, are certainly possible. With multiple cameras and for a given resolution, the 3D position determined by triangulation is the one that minimizes the mean squared error between the quantized coordinates, derived from pixelization, and the projections of the point in real coordinates. The analysis is organised in two parts. The first part concerns increasingly larger numbers of cameras arranged over an arc of

circumference, which, as for the Cases 2a and 2c discussed in Figs. 3.7 - 3.9 and Figs. 3.13 - 3.15, is oriented parallel to the plane of the beam such that the cameras are all characterised by the same elevation angle ϕ and have either increasingly larger or increasing smaller aperture angles α, that is larger or smaller azimuthal angles θ, in longitudinal and transverse directions with respect to the beam. To avoid redundancy, the exact positions of the cameras are slightly misplaced, both with reference to the azimuthal and the elevation angles. Instead, the second part considers increasingly larger numbers of cameras arranged over arc of circumferences, which, as for the Cases 2b and 2d discussed in Figs. 3.10 - 3.12 and Figs. 3.16 - 3.18, are oriented orthogonal to the plane of the beam and passes either through or across the longitudinal axis of the beam. Here only one configuration is considered where the aperture angle is progressively increased. The exact positions for the various arrangements are summarised in Table 3.4 - Cases 4a, 4b, 4c, 4d. Case 4a is analyzed considering the pairs of cameras are added in reverse order too and is recalled as case 4a$'$. Finally, an additional case 4e is also discussed, where the cameras are arranged in the whole circumference positioned just above the beam.

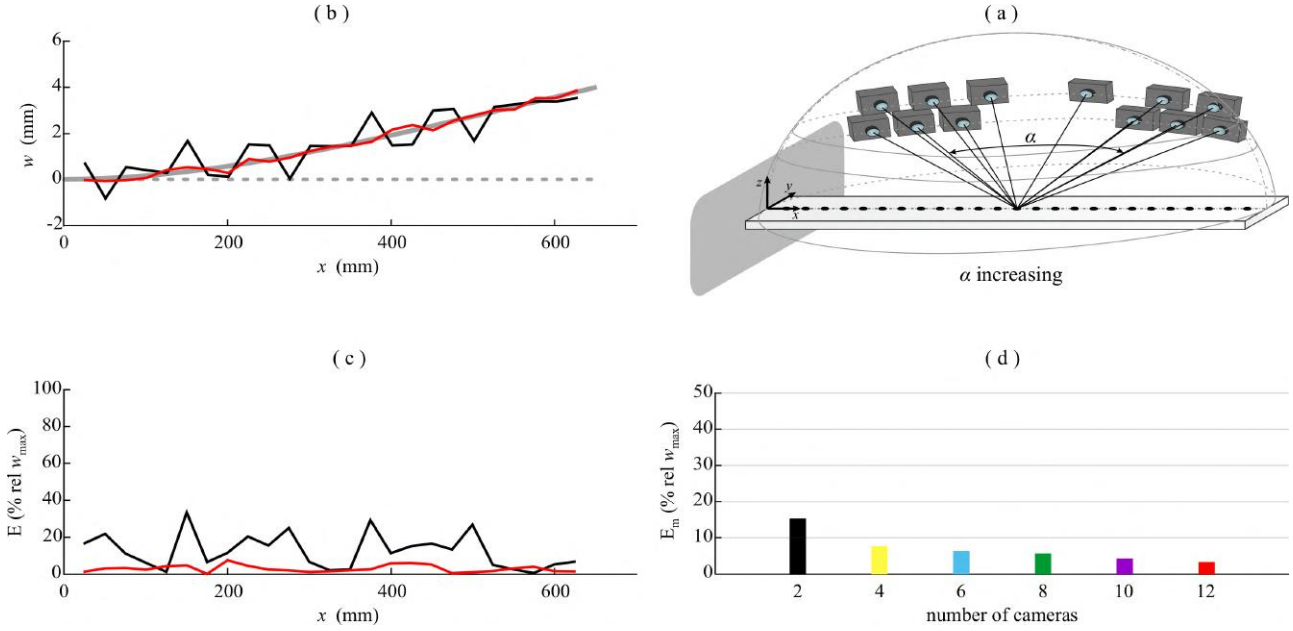

Figure 3.22: First deflection shape: (a) multiple cameras case study 4a; (b) comparison between reconstructed flexural deflection shapes of the beam (grey line reference shape); (c) percentage error calculated along the beam span; (d) histogram of the mean error. Colored lines reproduce the cases listed in the histogram

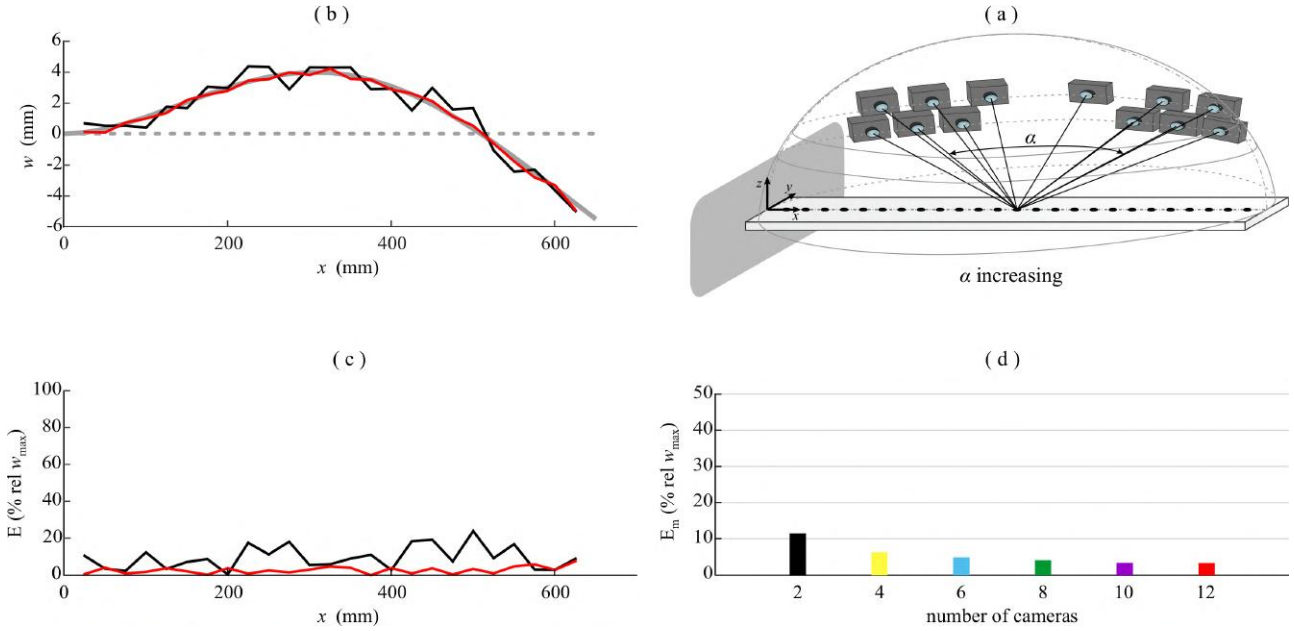

Figure 3.23: Second deflection shape: (a) multiple cameras case study 4a; (b) comparison between reconstructed flexural deflection shapes of the beam (grey line reference shape); (c) percentage error calculated along the beam span; (d) histogram of the mean error. Colored lines reproduce the cases listed in the histogram

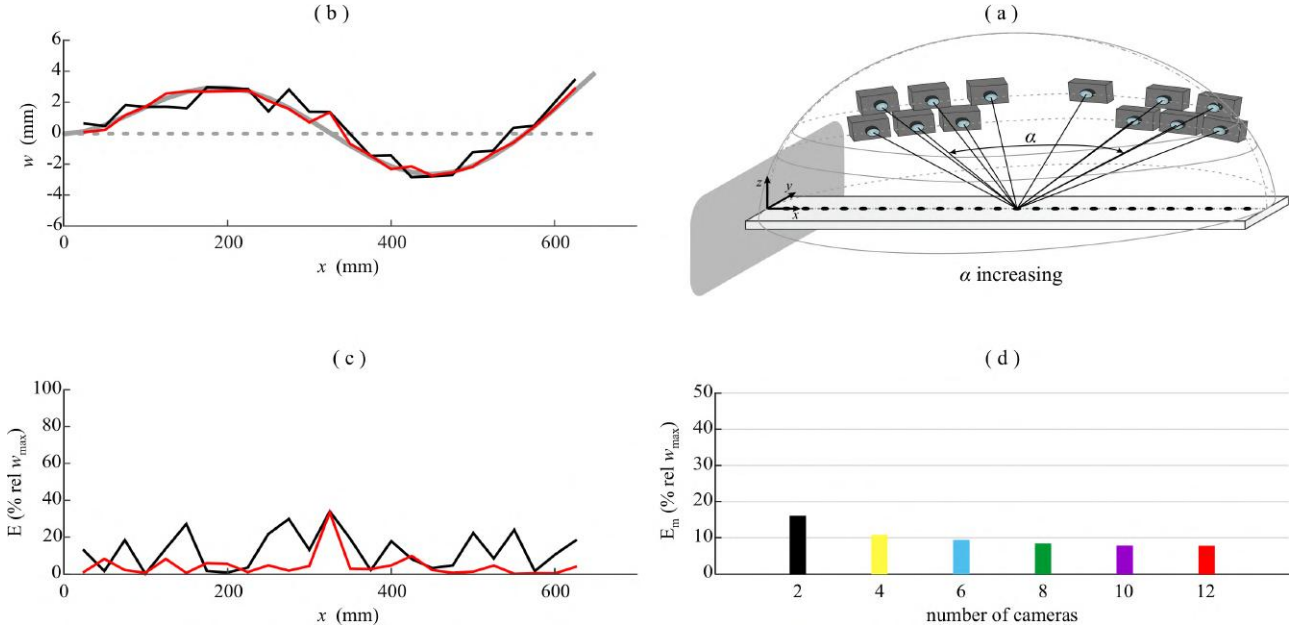

Figure 3.24: Third deflection shape: (a) multiple cameras case study 4a; (b) comparison between reconstructed flexural deflection shapes of the beam (grey line reference shape); (c) percentage error calculated along the beam span; (d) histogram of the mean error. Colored lines reproduce the cases listed in the histogram

To start with, the setup with increasingly larger numbers of cameras arranged over an arc of circumference oriented parallel to the plane of the beam is considered (Case 4a). The results presented in Figs. 3.22 - 3.24 indicate that, as pairs of cameras with increasingly larger aperture angle are added, the accuracy of the measurement significantly increases. Similar considerations can be done from the first and second flexural deflection shapes. For instance, according to Figs. 3.22 - 3.23 Plot (d), when

the measurement setup passes from 2 cameras (1 pair) to 12 cameras (6 pairs) the average error of the measurement falls from 12-15% to 3%. Accordingly, Plot (c) shows that the error over the 25 points of measurement drops from peak values of 30-35% to peak values of 5%. Fig. 3.24 shows that the third flexural deflection shape is affected by slightly bigger errors. In particular, Plot (d) shows that the average error falls from 18% to 8% when the number of cameras is increased from 2 cameras to 12 cameras. The point error, shown in Plot (c) never exceeds 10% when 12 cameras are used, except for one single point in which the error is up to 40%.

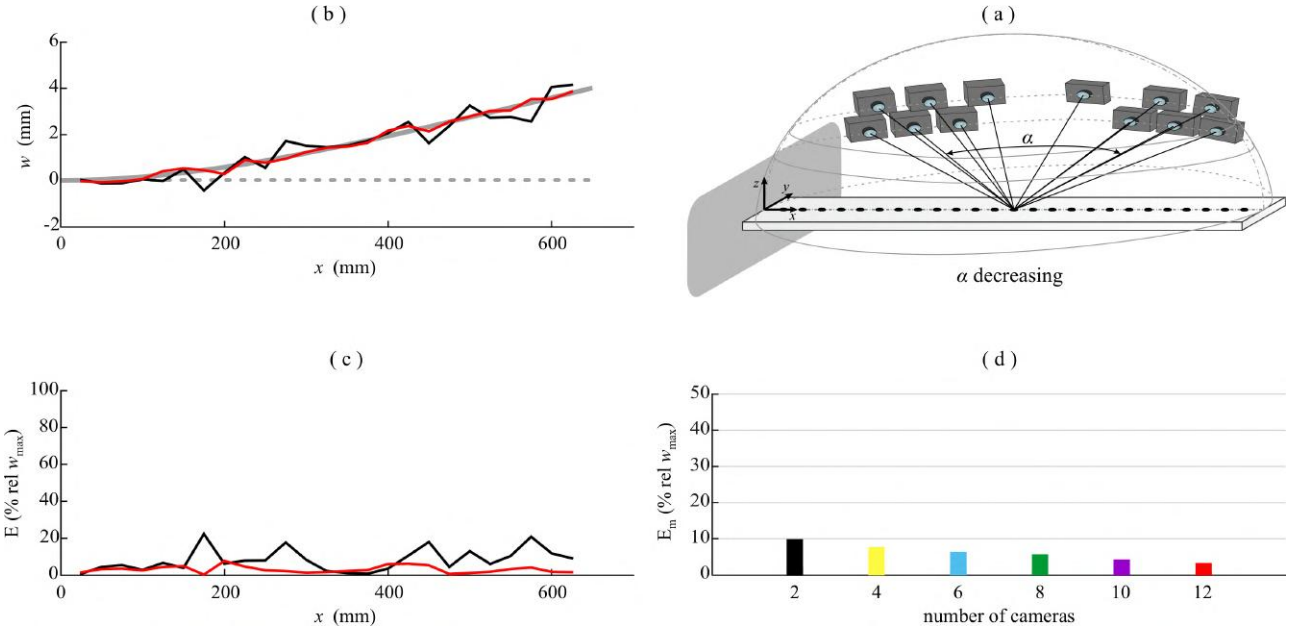

Figure 3.25: First deflection shape: (a) multiple cameras case study 4a′; (b) comparison between reconstructed flexural deflection shapes of the beam (grey line reference shape); (c) percentage error calculated along the beam span; (d) histogram of the mean error. Colored lines reproduce the cases listed in the histogram

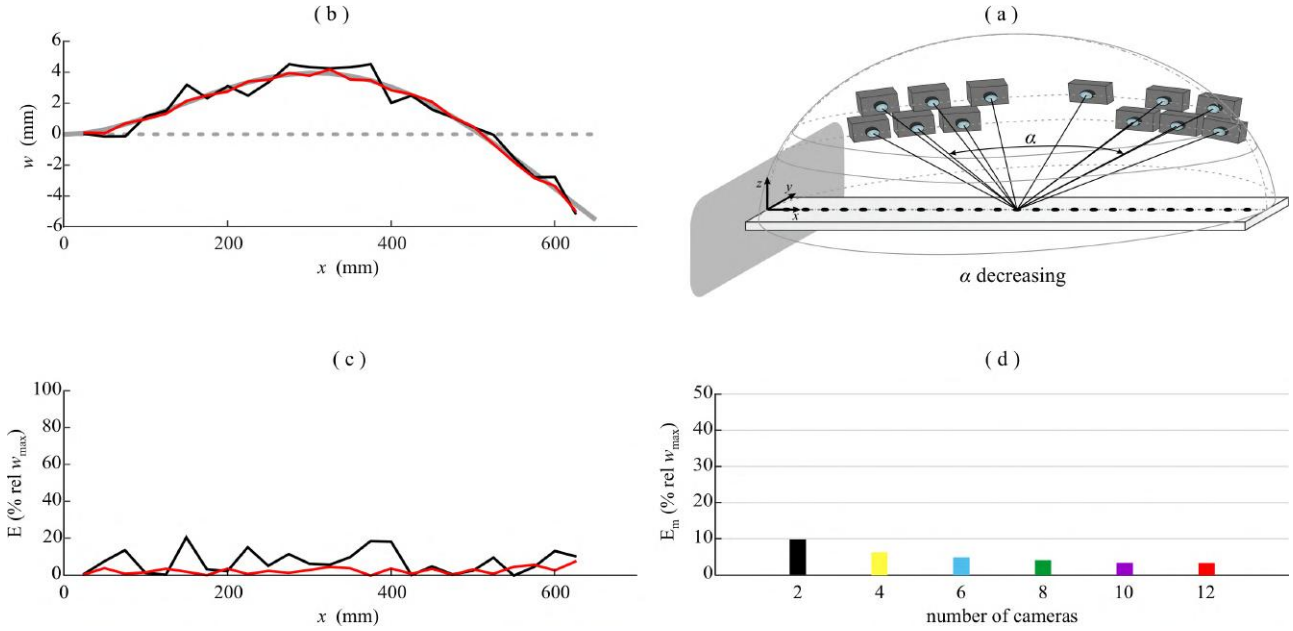

Figure 3.26: Second deflection shape: (a) multiple cameras case study 4a′; (b) comparison between reconstructed flexural deflection shapes of the beam (grey line reference shape); (c) percentage error calculated along the beam span; (d) histogram of the mean error. Colored lines reproduce the cases listed in the histogram

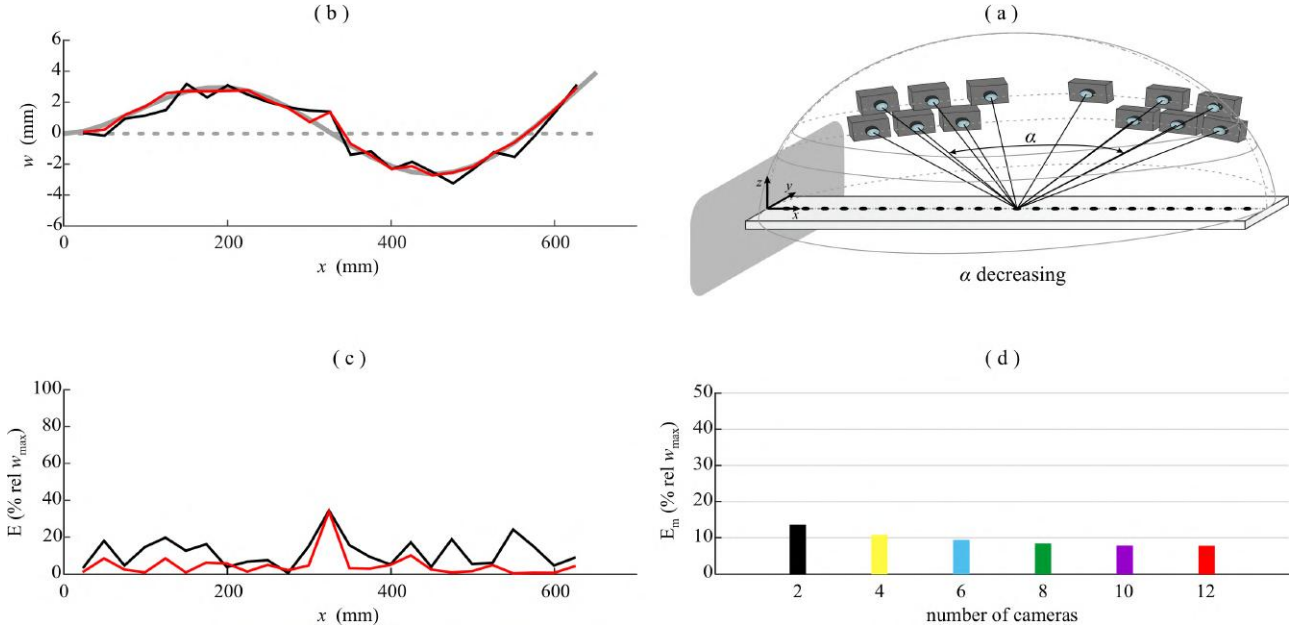

Figure 3.27: Third deflection shape: (a) multiple cameras case study 4a′; (b) comparison between reconstructed flexural deflection shapes of the beam (grey line reference shape); (c) percentage error calculated along the beam span; (d) histogram of the mean error. Colored lines reproduce the cases listed in the histogram

In parallel, the results presented Figs. 3.25 - 3.27 show that, if pairs of cameras with increasingly smaller aperture angle are added (Case 4a′), the average error still tends to drop but at a smaller rate. Indeed, as shown in Figs. 3.25 - 3.27 Plot (d), the average error with the first pair of cameras having a large angle of aperture would be about 10-12% and then fall again to 3% when a total of 12 cameras is used. Similarly, Plot (c) shows that the peak error over the 25 measurement points falls

from 20% to 5% (except for one single point when the third flexural deflection shape is considered, as seen in Fig. 3.27 Plot (d)). As discussed in subsection 3.3.2 (Figs. 3.7 - 3.9, 3.10 - 3.12), the accuracy of the measurement with a pair of cameras increases when the optical axis of the cameras is characterised by a small elevation angle and a large azimuthal angle. Therefore, when the addition of pairs of cameras start from a large aperture angle, that is from larger azimuthal angles, the initial averaged and peak errors are smaller than when the addition of pairs of cameras start from a small aperture angle. Nevertheless, the simulation with 12 cameras allows to obtain an average error of 3% and a peak error over the group of 25 measurement points of 5%.

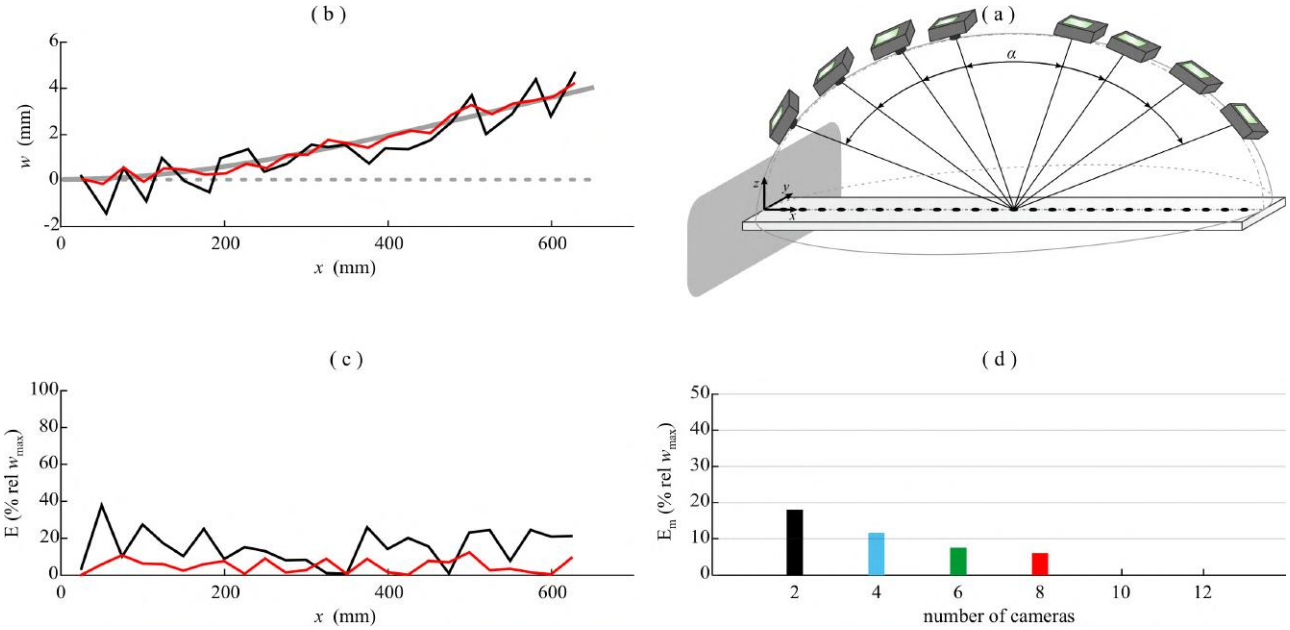

Figure 3.28: First deflection shape: (a) multiple cameras case study 4b; (b) comparison between reconstructed flexural deflection shapes of the beam (grey line reference shape); (c) percentage error calculated along the beam span; (d) histogram of the mean error. Colored lines reproduce the cases listed in the histogram.

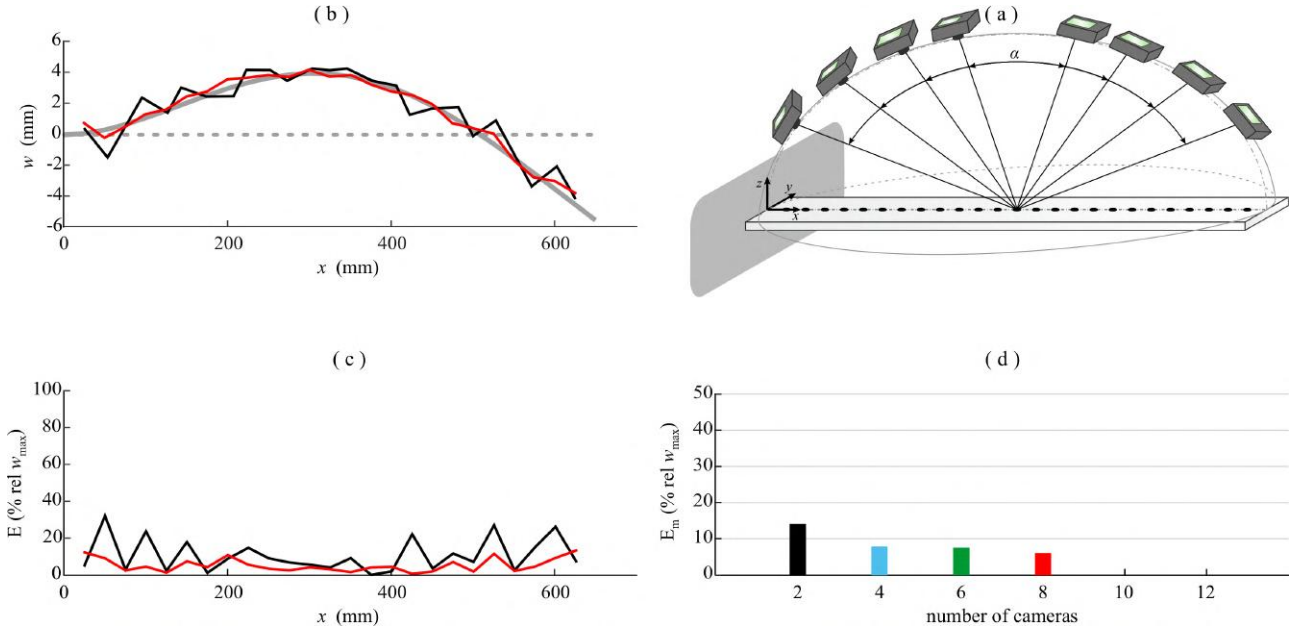

Figure 3.29: Second deflection shape: (a) multiple cameras case study 4b; (b) comparison between reconstructed flexural deflection shapes of the beam (grey line reference shape); (c) percentage error calculated along the beam span; (d) histogram of the mean error. Colored lines reproduce the cases listed in the histogram.

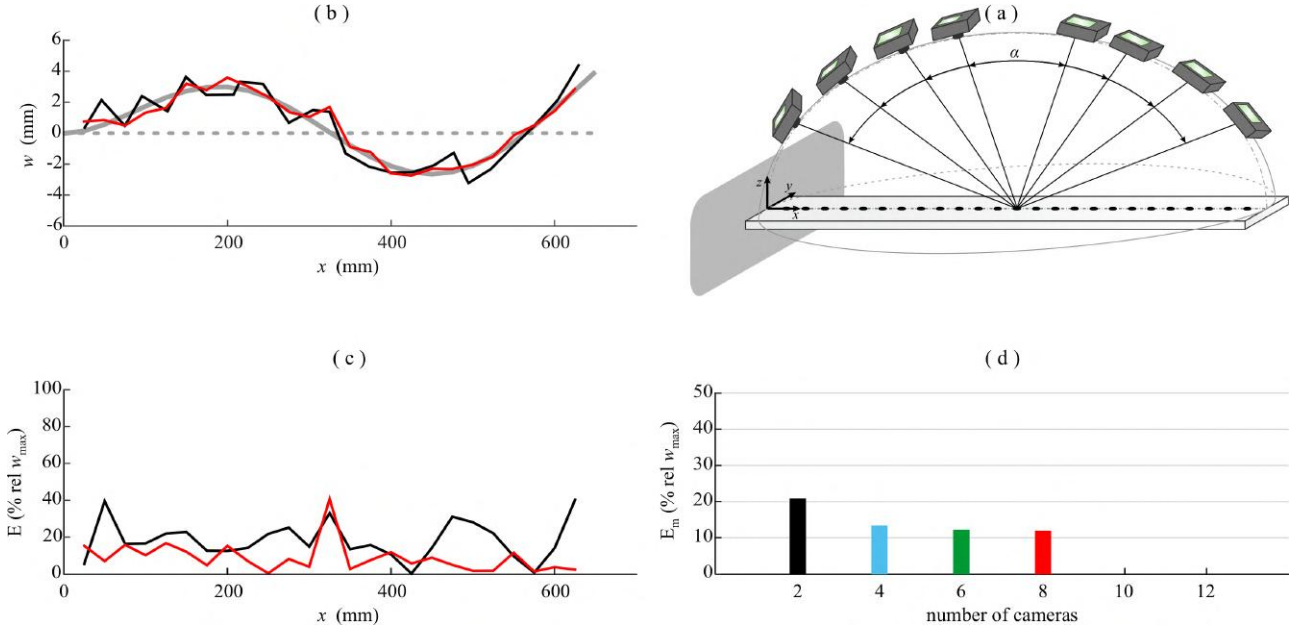

Figure 3.30: Third deflection shape: (a) multiple cameras case study 4b; (b) comparison between reconstructed flexural deflection shapes of the beam (grey line reference shape); (c) percentage error calculated along the beam span; (d) histogram of the mean error. Colored lines reproduce the cases listed in the histogram.

The setup with increasingly larger numbers of cameras arranged over an arc of circumference oriented orthogonal to the plane of the beam and aligned with the beam longitudinal axis is now examined (Case 4b). The results presented in Figs. 3.28 - 3.30 show that, as cameras with increasingly larger aperture angle are added, the accuracy of the measurement significantly increases. Indeed, for the first flexural deflection shape, Plot (d) in Fig. 3.28 indicates that, when the measurement setup

passes from 2 cameras (1 pair) to 8 cameras (4 pairs), the average error of the measurement falls from 18% to 6%. Moreover, Plot (c) shows that the error over the 25 measurement points drops from peak values of 40% to peak values of 10%. Plot (d) in Fig. 3.29, which refers to the second flexural deflection shape, shows that the average error passes from 13% to 6% when 8 cameras are considered in the measurement setup. Plot (c) instead shows that the point error falls from a maximum of 35% to a maximum of 10 %. Again, when the third flexural deflection shape is considered, the error is slightly bigger. More specifically, Plot (d) of Fig. 3.30 indicates that the average error passes from 21% to 11% when the measurement setup passes from 1 pair of cameras to 4 pairs of cameras. Plot (c) shows that the point error is always less than 20% except for one single point in which the error is about 40% both for a setup measurement composed by 2 cameras or 8 cameras. Also in this case, if cameras were sequentially added starting from large aperture angles towards small aperture angles the error for the first pair would have been smaller. As shown above and in subsection 3.3.2, to further reduce these errors it would be sufficient to tilt the arc of cameras laterally so that they are characterized by a smaller elevation angle.

Cases 4c, 4d are now investigated, which consider similar arrangements of the cameras as in Cases 4a, 4b but with the cameras rotated by $\pi/2$ with respect to the z axis.

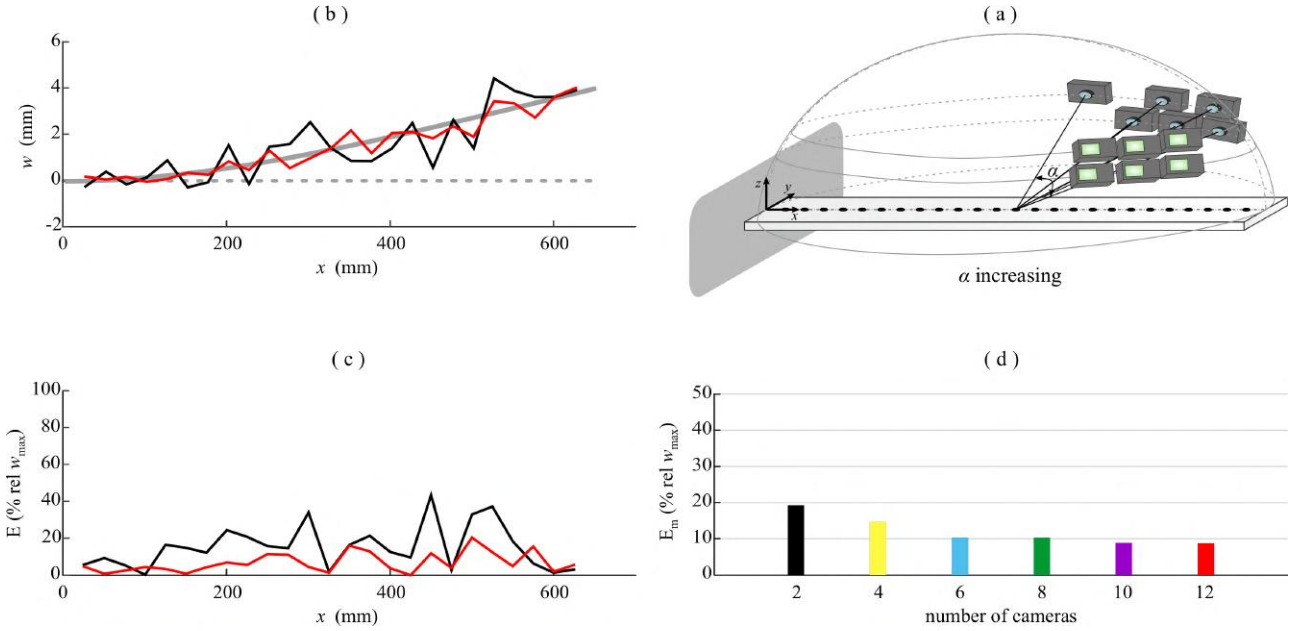

Figure 3.31: First deflection shape: (a) multiple cameras case study 4c; (b) comparison between reconstructed flexural deflection shapes of the beam (grey line reference shape); (c) percentage error calculated along the beam span; (d) histogram of the mean error. Colored lines reproduce the cases listed in the histogram.

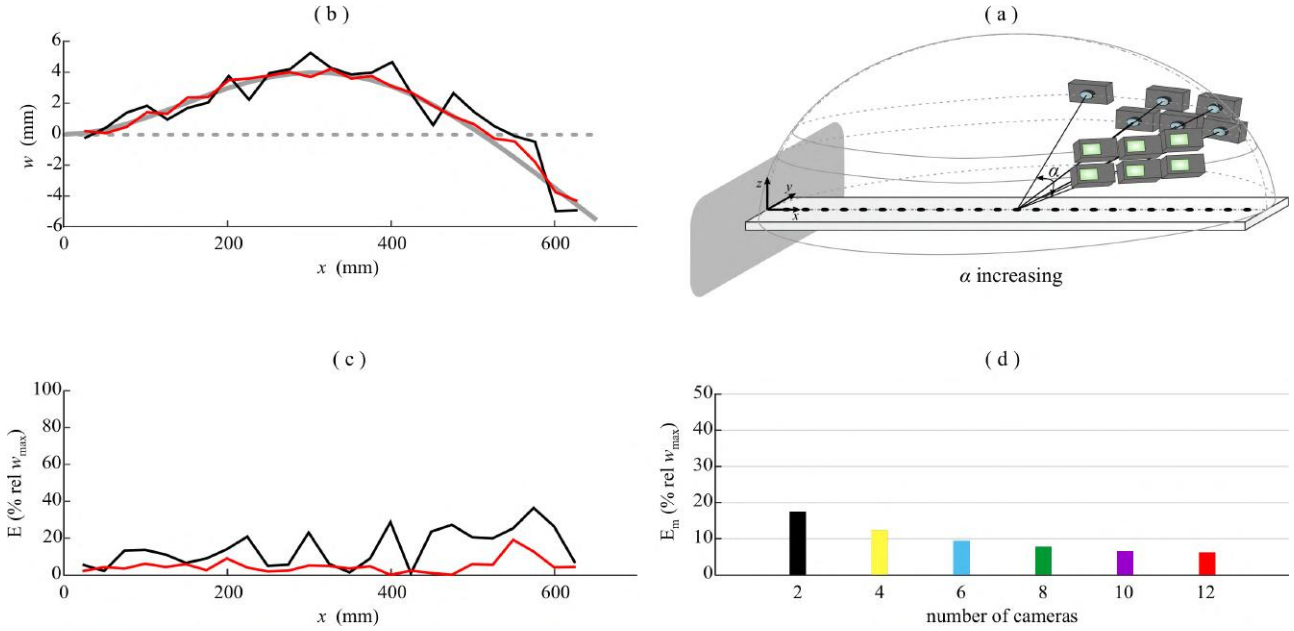

Figure 3.32: Second deflection shape: (a) multiple cameras case study 4c; (b) comparison between reconstructed flexural deflection shapes of the beam (grey line reference shape); (c) percentage error calculated along the beam span; (d) histogram of the mean error. Colored lines reproduce the cases listed in the histogram.

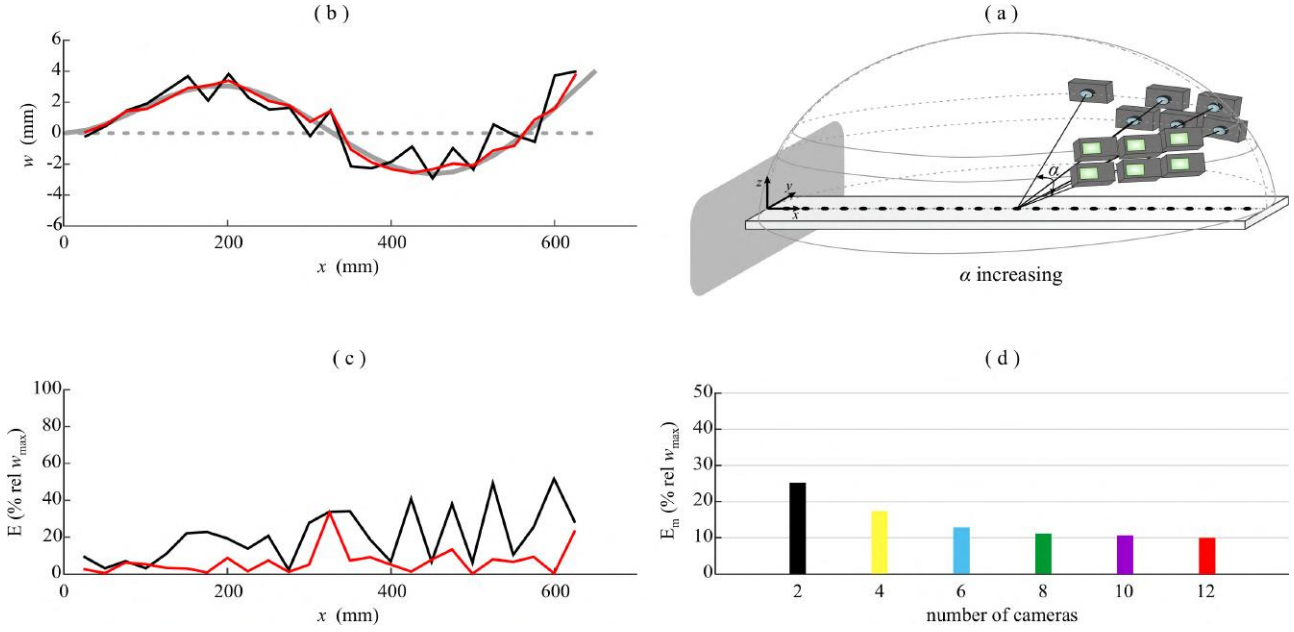

Figure 3.33: Third deflection shape: (a) multiple cameras case study 4c; (b) comparison between reconstructed flexural deflection shapes of the beam (grey line reference shape); (c) percentage error calculated along the beam span; (d) histogram of the mean error. Colored lines reproduce the cases listed in the histogram.

The results presented in Figs. 3.31 - 3.33 indicate that, as pairs of cameras with increasingly larger aperture angle are added, the accuracy of the measurement significantly increases for all the three flexural deflection shapes considered. For instance, according to Plot (d) in Figs. 3.31 - 3.33, when the measurement setup passes from 2 cameras (1 pair) to 12 cameras (6 pairs) the average error of the measurement falls from 20-25% to 7-9%. Accordingly, Plot (c) shows that the error over the 25 points

of measurement drops from peak values of 50% to peak values of 20%.

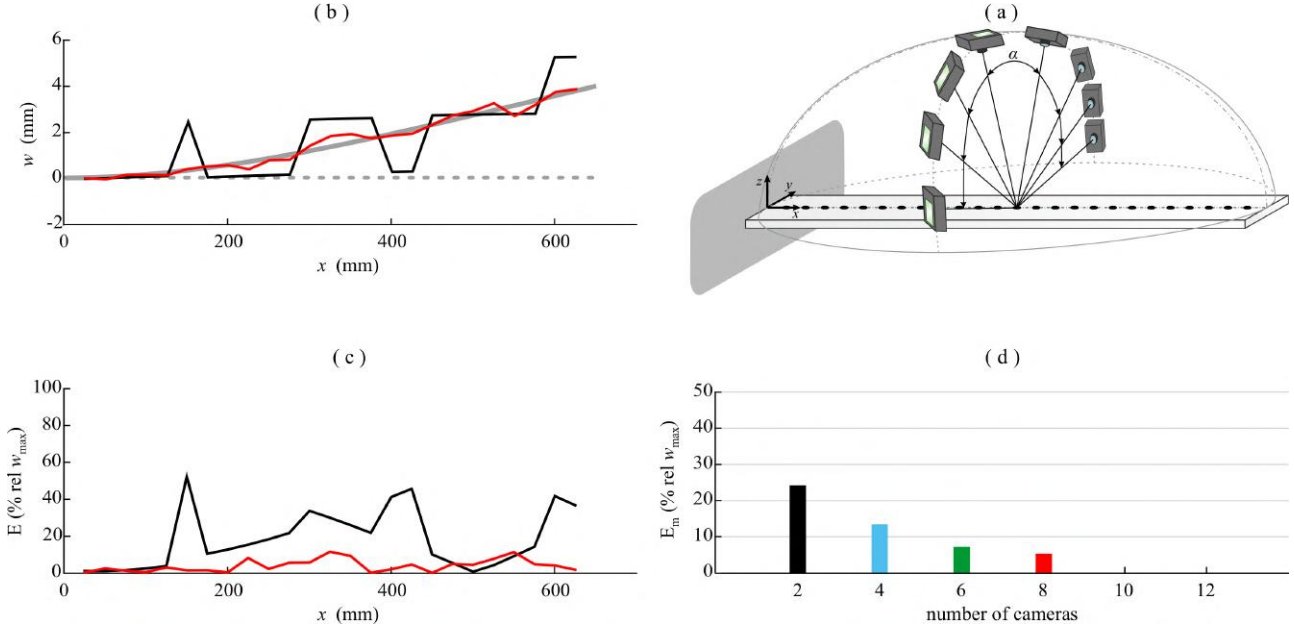

Figure 3.34: First deflection shape: (a) multiple cameras case study 4d; (b) comparison between reconstructed flexural deflection shapes of the beam (grey line reference shape); (c) percentage error calculated along the beam span; (d) histogram of the mean error. Colored lines reproduce the cases listed in the histogram.

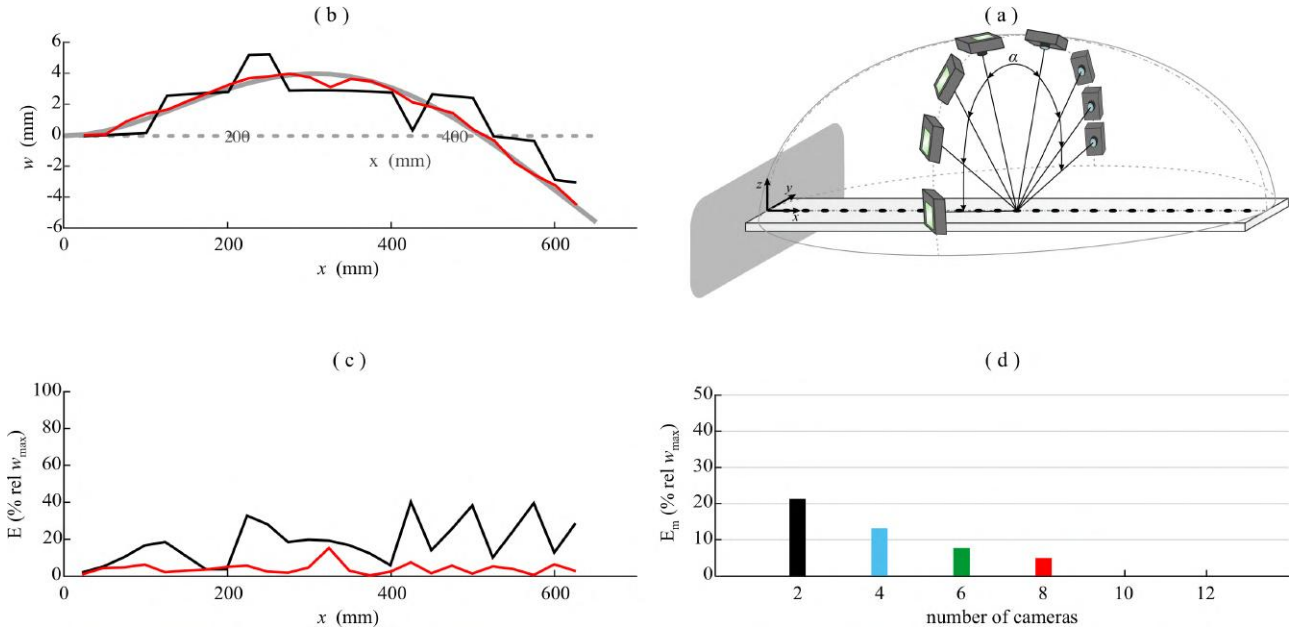

Figure 3.35: Second deflection shape: (a) multiple cameras case study 4d; (b) comparison between reconstructed flexural deflection shapes of the beam (grey line reference shape); (c) percentage error calculated along the beam span; (d) histogram of the mean error. Colored lines reproduce the cases listed in the histogram.

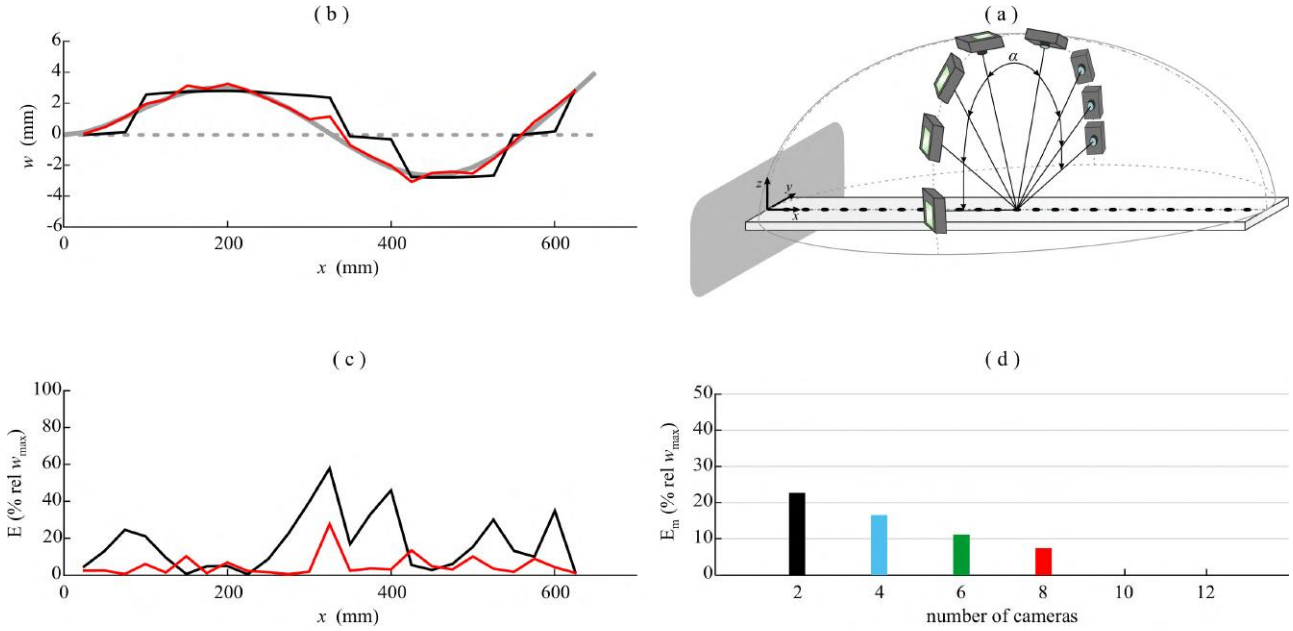

Figure 3.36: Third deflection shape: (a) multiple cameras case study 4d; (b) comparison between reconstructed flexural deflection shapes of the beam (grey line reference shape); (c) percentage error calculated along the beam span; (d) histogram of the mean error. Colored lines reproduce the cases listed in the histogram.

The results presented in Figs. 3.34 - 3.36 show that, as cameras with increasingly larger aperture angle are added, the accuracy of the measurement significantly increases. Indeed, Plot (d) indicates that, when the measurement setup passes from 2 cameras (1 pair) to 8 cameras (4 pairs), the average error of the measurement falls from 20-23% to 6-8%. Moreover, Plot (c) shows that the error over the 25 measurement points drops from peak values of 60% to peak values of 10%.

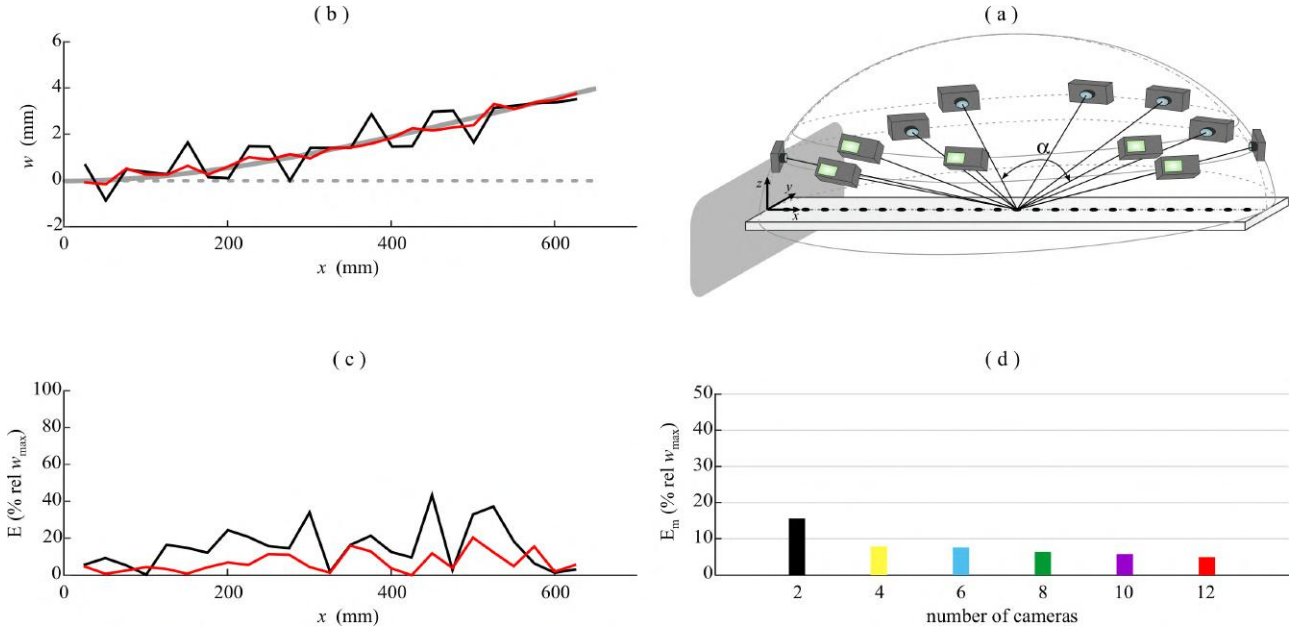

Figure 3.37: First deflection shape: (a) multiple cameras case study 4e; (b) comparison between reconstructed flexural deflection shapes of the beam (grey line reference shape); (c) percentage error calculated along the beam span; (d) histogram of the mean error. Colored lines reproduce the cases listed in the histogram.

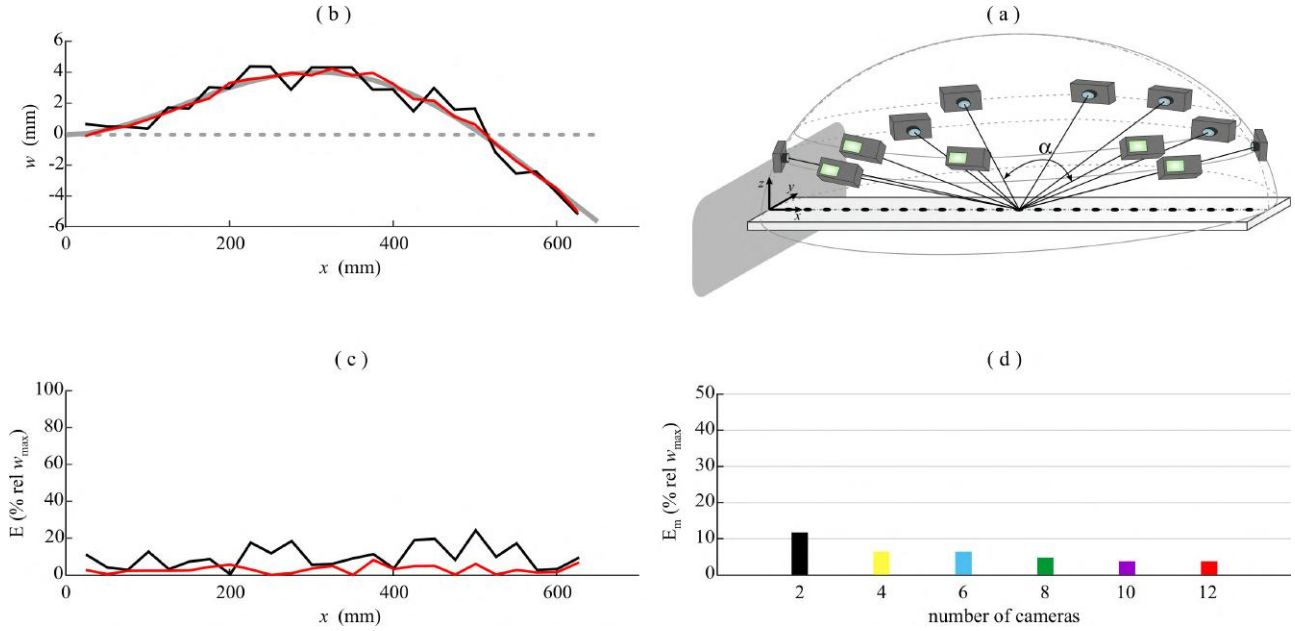

Figure 3.38: Second deflection shape: (a) multiple cameras case study 4e; (b) comparison between reconstructed flexural deflection shapes of the beam (grey line reference shape); (c) percentage error calculated along the beam span; (d) histogram of the mean error. Colored lines reproduce the cases listed in the histogram.

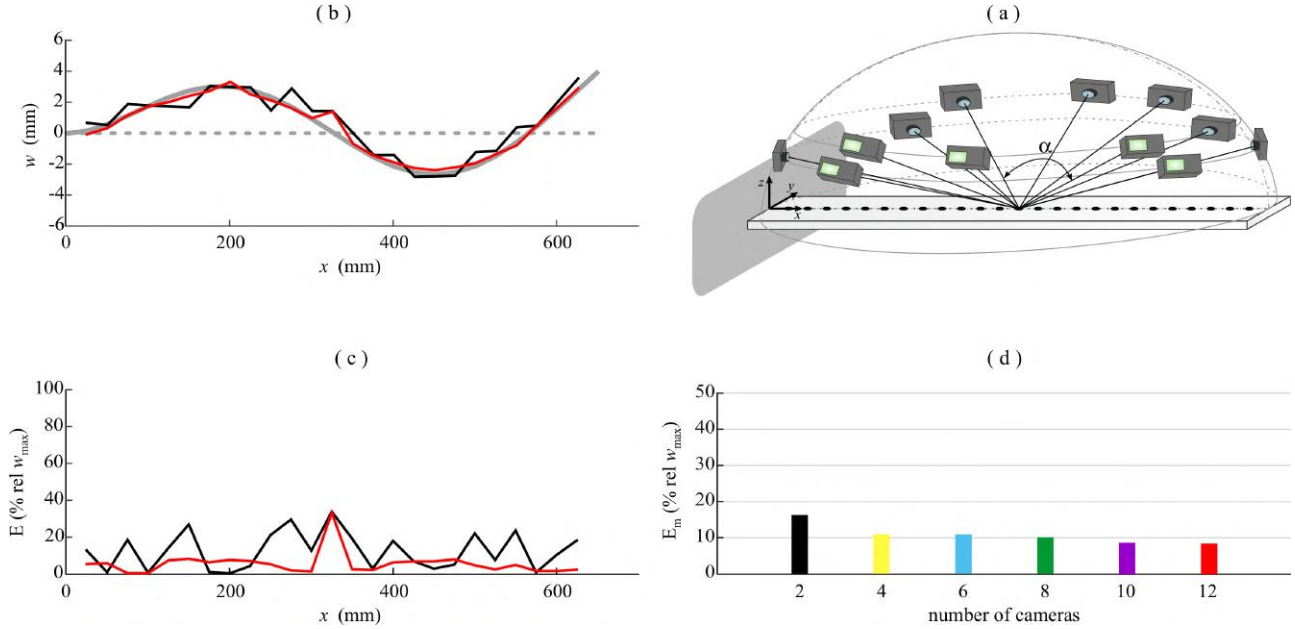

Figure 3.39: Third deflection shape: (a) multiple cameras case study 4e; (b) comparison between reconstructed flexural deflection shapes of the beam (grey line reference shape); (c) percentage error calculated along the beam span; (d) histogram of the mean error. Colored lines reproduce the cases listed in the histogram.

The last Case 4e presented in Figs. 3.37 - 3.39 considers the cameras disposed over a circumference around the beam: the position of each camera is defined in 3.4 - Cases 4e. The results presented in Figs. 3.37 - 3.39 indicate that, as pairs of cameras are added over a circumference, the accuracy of the measurement significantly increases. For instance, considering the first flexural deflection shape, Fig. 3.37 Plot (d) shows that, when the measurement setup passes from 2 cameras (1 pair) to 12 cameras (6

pairs) the average error of the measurement falls from 16% to 5%. Accordingly, Plot (c) shows that the error over the 25 points of measurement drops from peak values of 45% to peak values of 20%. In Fig. 3.38 the second flexural deflection shape is considered. In this case Plot (d) shows that the average error falls from 12% to 3% when the measurement setup passes from 2 cameras to 12 cameras. Moreover, Plot (c) shows that the point error falls from 20% to 5%. Finally, in Fig. 3.39 the third flexural deflection shape is considered. In this case, Plot (d) shows that the average error goes from 16% to 9% while the point error falls from a maximum of 20% to a maximum of 5%, except for one single point at the centre of the beam, when the measurement setup is composed by 6 pairs of cameras.

3.4 Concluding remarks

This chapter has presented a simulation study focussed on the measurement of flexural vibration of distributed structures with multiple cameras. The study has considered a practical model problem composed by a cantilever beam excited by a tonal force at the first three fundamental resonance frequencies of the beam flexural vibration. The study has therefore considered the measurement of the beam deflection shapes at these frequencies, which accurately approximates the first three flexural mode shapes. The study showed that the accuracy of the measurement increases as:

1. the cameras are arranged closer to the vibrating structure;
2. the cameras are separated by large aperture angles;
3. the optical axis of the cameras impinges the structure with small elevation angles;
4. the resolution of the cameras is raised;
5. the number of cameras is increased.

The first and fourth measures reduce the pixel footprint on the object (a.k.a *ground sample distance* in aerial photogrammetry) and thus they increase the camera resolving power. The second and fifth measures are related to the triangulation process, which is cast as a non-linear least squares problem. The conditioning of the system of equations depends on the angle of incidence of conjugate optical rays defining a point in space, which in turn depends on the angular separation of cameras. In particular, the accuracy of the measurements depends on the ratio between disparity and baseline: as the transverse displacement $w(x,t)$ along the beam is due to the flexural vibrations of the beam in the x,z plane, the effect of this ratio is significant when the elevation angle ϕ is varied. As for the number of cameras, increasing the number of equations reduces the variance of the solution. The effect of the third measure is typical of aerial photogrammetry, where nadiral cameras (i.e. pointing downward) suffer from larger errors than oblique cameras. This is because, the bundle adjustment cost function of nadiral cameras is less sensitive to displacements in vertical direction, and actually would become insensitive when

the projection becomes orthographic. For instance, this happens with relatively shallow objects in comparison to their distance from the camera. Measure 1 has also an impact on this aspect. In practice, however, reducing the elevation angle worsen the accuracy of the localization of the markers, which is a relevant problem in the actual measurement process. Overall, the study indicates that the accuracy of the measurement significantly rises when the setup is equipped with an increasingly larger number of cameras, which should be arranged close to the vibrating structure with small elevation angles and large aperture angles between pairs of cameras.

The model problem considered in this chapter was selected for its simplicity and reproducibility into an experimental setup, as it will be seen in Chapter 5. Nevertheless, its vibration field is characterized by a plane of symmetry, so that the effective space where to locate the cameras without them being redundant was halved. Therefore, it is expected that, when more realistic structures characterized by intricate shapes with no plane of symmetry are measured, the effectiveness of multiple cameras will become much more relevant that in the case considered in this study.

Chapter 4

Plate flexural vibration measurements with arrays of cameras

This chapter takes the work presented in Chapter 3 one step forward and considers the measurement with multiple cameras of the time-harmonic flexural vibrations of a plate. Here too, the study is focussed on the measurement of the plate flexural deflection shapes at the first three resonance frequencies, which gives a good estimate of the shape of the first three flexural natural modes of the plate. The chapter is structured in two parts. The first part presents the plate model problem and the theory of flexural vibrations in plates used to simulate the flexural response of the structure. The second part provides a parametric study, similar to the one presented in Section 3.3 of Chapter 3. More specifically, it provides a detailed analysis of the measurement of the plate flexural deflection shapes. The chapter is organized in three sections. Section 4.1 introduces the model problem, which is given by the measurement of the time-harmonic flexural vibration of a thin plate. Then, Section 4.2 presents a comprehensive parametric study, which shows how the distance, the angle of separation, the resolution and the number of cameras influence the accuracy of the measurements. Finally, Section 4.3 summarizes the principal conclusions of the chapter.

4.1 Model problem

Fig. 4.1 shows a sketch of the model problem considered here, which is composed by a plate made of aluminium whose dimensions and physical properties are summarised in Table 4.1. The transverse vibration of the plate is measured at 15×10 points arranged on the surface of the plate. The points are evenly distributed along the two dimensions of the plate with a spacing of 44.5 mm along the x direction and 44.3 mm along the y direction. The simulation study assumes the points have infinitesimal dimension. The positions of these points are measured by multiple cameras such that, as discussed in Chapter 2, triangulation can then be used to reconstruct the transverse displacements of the plate

generated by the flexural vibrations.

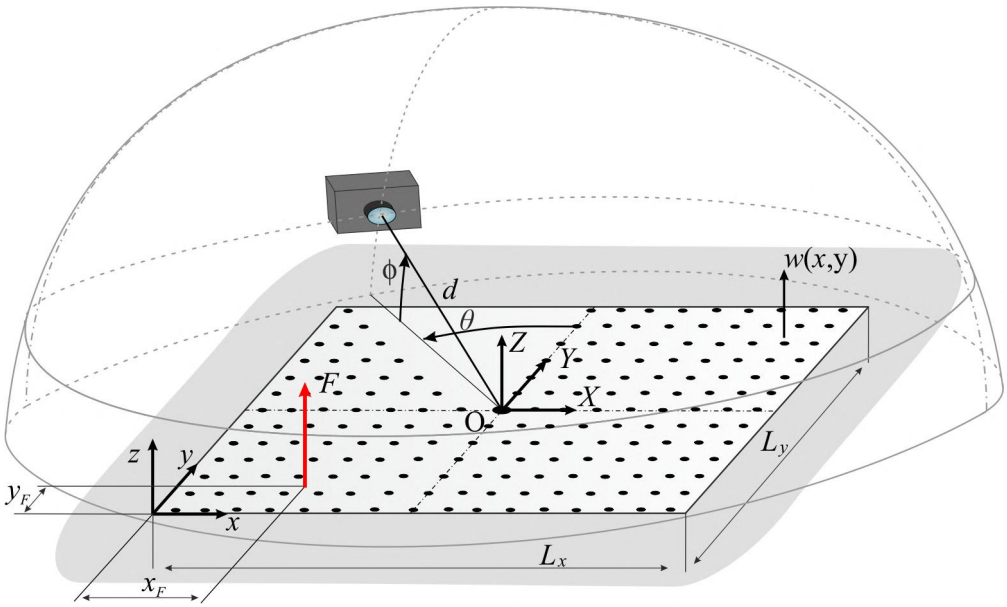

Figure 4.1: Model problem for the measurement of flexural vibration of a plate.

As specified in Fig. 4.1, two Cartesian systems of reference are employed to define the positions of the plate points and the positions of the cameras, which are respectively:

a) the *plate coordinate frame of reference* x, y, z which is located at the bottom left end of the plate;

b) and the so-called *world coordinate frame of reference* X, Y, Z which is located in the middle of the plate.

As done in Chapter 3, for simplicity, the two systems of reference will be called respectively world system of reference and plate system of reference. The former reference system is used for the triangulation whereas the latter is used to define the flexural vibrations of the plate. The transverse displacement $w(x, y, t)$ along the plate is due to the flexural vibrations of the plate in the x, y, z space, which are generated by a transverse time-harmonic force at position (x_F, y_F). The cameras are oriented in such a way as their optical axis points to the origin O of the world system of reference X, Y, Z and thus their image plane [54] is tangent to a hemisphere centred in O. Moreover, the base edge of the rectangular photosensitive sensor is oriented parallel to the base XY plane of the hemisphere. The position of the camera is identified by the position of its focal point C, which, as shown in Fig. 4.1, is defined by spherical coordinates with respect to the world system of reference X, Y, Z, i.e.:

a) the radial distance d;

b) the azimuthal angle θ;

c) the elevation angle ϕ.

The flexural vibration of the plate is governed by the following wave equation [2], [3]:

$$D\left(\frac{\partial^4 w(x,y,t)}{\partial x^4}+\frac{\partial^4 w(x,y,t)}{\partial x^2\partial y^2}+\frac{\partial^4 w(x,y,t)}{\partial y^4}\right)+m\frac{\partial^2 w(x,y,t)}{\partial t^2}=F(x,y,t). \tag{4.1}$$

Here $D=Eh^3/12(1-\nu^2)$ is the bending stiffness and $m=\rho h$ is the mass per unit surface area. Also, $F(x,y,t)$ is the transverse force acting on the plate, which in this case is a time-harmonic point force acting at position x_F, y_F, such that

$$F(x,y,t)=\delta(x-x_F,y-y_F)\mathrm{Re}\Big\{F_0(\omega)e^{j\omega t}\Big\}. \tag{4.2}$$

In this expression, $F_0(\omega)$ is the amplitude of the force, ω is the angular frequency, $j=\sqrt{-1}$ and $\delta(.)$ is the Dirac delta function. As shown in Ref. [2], [3], the flexural response of the plate can be expressed as the linear combination of the natural modes $\phi_n(x,y)$ and the modal coordinates (or generalized coordinates) $q_n(t)$:

$$w(x,y,t)=\mathrm{Re}\Big\{\sum_{n=1}^{\infty}\phi_n(x,y)q_n(t)\Big\}. \tag{4.3}$$

The natural modes of a plate are given by

$$\phi_n(x,y)=2\sin\left(\frac{m_1\pi x}{L_x}\right)\sin\left(\frac{m_2\pi y}{L_y}\right), \tag{4.4}$$

where m_1 and m_2 are the modal indices of the n-th mode, whose values are summarized in Table 4.2. Also, the modal coordinates are given by

$$q_n(t)=\frac{\phi_n(x_F,y_F)}{M[\omega_n^2+j2\xi\omega_n\omega-\omega^2]}F_0(\omega)e^{j\omega t}. \tag{4.5}$$

Here, $M=\rho L_x L_y h$ is the mass of the plate, ξ is the modal damping ratio, which is assumed equal for all modes, and ω_n is the natural frequency, which is given by

$$\omega_n=\sqrt{\frac{D}{m}}\left[\left(\frac{m_1\pi}{L_x}\right)^2+\left(\frac{m_2\pi}{L_y}\right)^2\right], \tag{4.6}$$

where m_1 and m_2 are again the modal indices of the n-th mode.

In general, the modal overlap [2] of flexural vibrations in a plate grows slowly and proportionally to ω [58]. Therefore, when the plate is excited at the resonance frequencies of the low-order natural modes, the response can be expressed in terms of the modal contribution of the resonant mode only. For instance, the flexural response at the first resonance frequency, i.e. for $\omega=\omega_1\sqrt{1-2\xi^2}$, can be satisfactorily expressed as:

Table 4.1: Physical properties of the plate.

Parameter	Value
Length	$L_x = 668$ mm; $L_y = 443$ mm
Thickness	$h = 19.8$ mm
Density	$\rho = 7200$ kg/m^3
Young's modulus	$E = 14 \times 10^{10}$ N/m^2
Poisson ratio	$\nu = 0.31$
Modal damping ratio	$\xi = 0.02$
Position of the force	$x_F = 55$ mm; $y_F = 55$ mm

Table 4.2: Values of the modal indices m_1 and m_2 of the n-th mode.

n	m_1	m_2
1	1	1
2	2	1
3	1	2
4	2	2
5	1	4
6,7,...	...	...

$$w(x, y, t) = \phi_1(x, y)\mathrm{Re}\{q_1(t)\}. \tag{4.7}$$

This expression shows that, for a given instant of time t, the spatial response $w(x, y, t)$ coincides with the natural mode $\phi_1(x, y)$ to within a constant $\mathrm{Re}\{q_1(t)\}$:

$$\mathrm{Re}\{q_1(t)\} = \mathrm{Re}\left\{ \frac{\phi_1(x_F, y_F)}{M[\omega_1^2 + j2\xi\omega_1\omega - \omega^2]} F_0(\omega) e^{j\omega t} \right\}. \tag{4.8}$$

In this chapter, the measurement of the three spatial deflection shapes $w(x, y, t)$ is investigated with respect to the instant t where the time-harmonic function $\mathrm{Re}\{q_1(t)\}$ is maximum, that is for $t = n\pi/\omega$ with $n = 0, 1, 2, \ldots$.

4.2 Parametric studies

The aim of this chapter is to investigate how multiple cameras can increase the accuracy of flexural vibration measurements of plate structures. Therefore, also in this chapter, the formulations presented in Sections 4.1 and 3.2 for the flexural response of a plate and for the optical measurement of displacements by means of triangulation are employed to simulate the measurement of the flexural response of the plate. The analysis considers the measurement of the first three flexural deflection shapes of the plate at the first three fundamental resonance frequencies. The reference deflection shapes are derived from Eq. 4.7 with $F_0(\omega) = 1$ N and $t = \pi/\omega$. Also, the measured deflection shapes are simulated using the formulations presented in Section 3.2 with respect to the displacements at the grid of 15 $\times$ 10 points assuming $F_0(\omega) = 1$ N and $t = \pi/\omega$.

A comprehensive analysis is provided, which shows how the following parameters affect the measurement of the plate flexural response by means of triangulation with a pair or multiple of cameras:

1. the radial distance d of a pair of cameras from the centre of the plate;
2. the aperture angle α between a pair of cameras;
3. the resolution of a pair of cameras;
4. the number of cameras in setups composed by more than 1 pair of cameras.

The setups with multiple camera pairs are arranged with the cameras positioned symmetrically with respect to the vertical planes YZ and XZ that cut the plate in two parts transversely and longitudinally respectively. The geometries, i.e. their positions and numbers, and the type of cameras, i.e. their resolutions, considered in the parametric studies listed above are summarised in Tables 4.3 and 4.4. As done for the beam problem, the accuracy of the reconstruction of the deflection shape is analysed with respect of the average error, which is given by the root mean square error over all the 15 $\times$ 10 measurement points:

$$E_m = \frac{\sqrt{\dfrac{1}{15 \times 10} \sum_{i=1}^{15\times 10} (w_i - w_{r,i})^2}}{w_{max}} 100 \text{ (\% rel. to } w_{max}\text{)}. \tag{4.9}$$

Here w_i is the transverse displacement of the i-th marker reconstructed by the cameras setup whereas $w_{r,i}$ is the reference transverse displacement of the i-th marker given by Eq. 4.7. Also, w_{max} is the maximum reference displacement given with Eq. 4.7. The following sections will illustrate how the four parameters listed above influence the measurement of the first three flexural deflection shapes of the plate shown in Fig. 4.1. The simulation results are reported in a standard framework, which shows:

a) a sketch of the measurement setup with highlighted the varied parameter;

b) a representation of the ideal flexural deflection shape;

c) the measured flexural deflection shape: for clarity, only the best and worst cases are shown;

d) the average error in % with respect to the maximum displacement of the plate (colored lines).

Table 4.3: Positions and resolutions of pairs of cameras ($^*k = 0, 1$).

Cases	Radial distance d [mm]	Aperture angle α [°]	Azimuthal angle θ [°]	Elevation angle ϕ [°]	Resolution [pixel]
1 (Figs. 4.2 - 4.4)	650 750 1000 1500	60	±30	25	320×180
2a (Figs. 4.5 - 4.7)	750	16 60 110 160	± 8 ± 30 ± 55 ± 80	10	320×180
2b (Figs. 4.8 - 4.10)	750	170 140 100 60	±90	5 20 40 60	320×180
2c (Figs. 4.11 - 4.13)	750	16 60 110 160	-90 ± 8 -90 ± 30 -90 ± 55 -90 ± 80	10	320×180
2d (Figs. 4.14 - 4.16)	750	170 140 100 60	k180*	5 20 40 60	320×180
3 (Figs. 4.17 - 4.19)	750	60	±30	25	320×180 640×360 1280×720 1920×1080

Table 4.4: Positions and resolutions of multiple cameras setups ($^*k = 0, 1$).

Cases	Radial distance d [mm]	Azimuthal angle θ [°]	Elevation angle ϕ [°]	Resolution [pixel]
4a (Figs. 4.20 - 4.22)	750	± 7 ±7/±14 ±7/±14/±27 ±7/±14/±27/±30 ±7/±14/±27/±30/±47 ±7/±14/±27/±30/±47/±50	15 15/15 15/15/15 15/15/15/5 15/15/15/5/5 15/15/15/5/5/5	320×180
4a′ (Figs. 4.23 - 4.25)	750	±50 ±50/±47 ±50/±47/±30 ±50/±47/±30/±27 ±50/±47/±30/±27/±14 ±50/±47/±30/±27/±14/±7	15 15/15 15/15/15 15/15/15/5 15/15/15/5/5 15/15/15/5/5/5	320×180
4b (Figs. 4.26 - 4.28)	750	±90 ±90/±90 ±90/±90/±90 ±90/±90/±90/±90	8 8/28 8/28/48 8/28/48/58	320×180
4c (Figs. 4.29 - 4.31)	750	-90 (± 7) -90 (±7/±14) -90 (±7/±14/±27) -90 (±7/±14/±27/±30) -90 (±7/±14/±27/±30/±47) -90 (±7/±14/±27/±30/±47/±50)	15 15/15 15/15/15 15/15/15/5 15/15/15/5/5 15/15/15/5/5/5	320×180
4d (Figs. 4.32 - 4.34)	750	k180* k180*/k180* k180*/k180*/k180* k180*/k180*/k180*/k180*	8 8/28 8/28/48 8/28/48/58	320×180
4e (Figs. 4.35 - 4.37)	750	k180*+7 k180*+(7/27) k180*+(7/27/0) k180*+(7/27/0/90) k180*+(7/27/0/90/47) k180*+(7/27/0/90/47/60)	15 15/15 15/15/15 15/15/15/5 15/15/15/5/5 15/15/15/5/5/5	320×180

4.2.1 Distance d of cameras from the plate

The accuracy of the reconstruction of the plate first three flexural deflection shapes with a pair of cameras arranged with fixed azimuthal θ and elevation ϕ angles and increasingly larger distance d from the centre point of the plate is first considered in this subsection with respect to the geometries and resolution of the cameras summarised in Table 4.3 - Case 1.

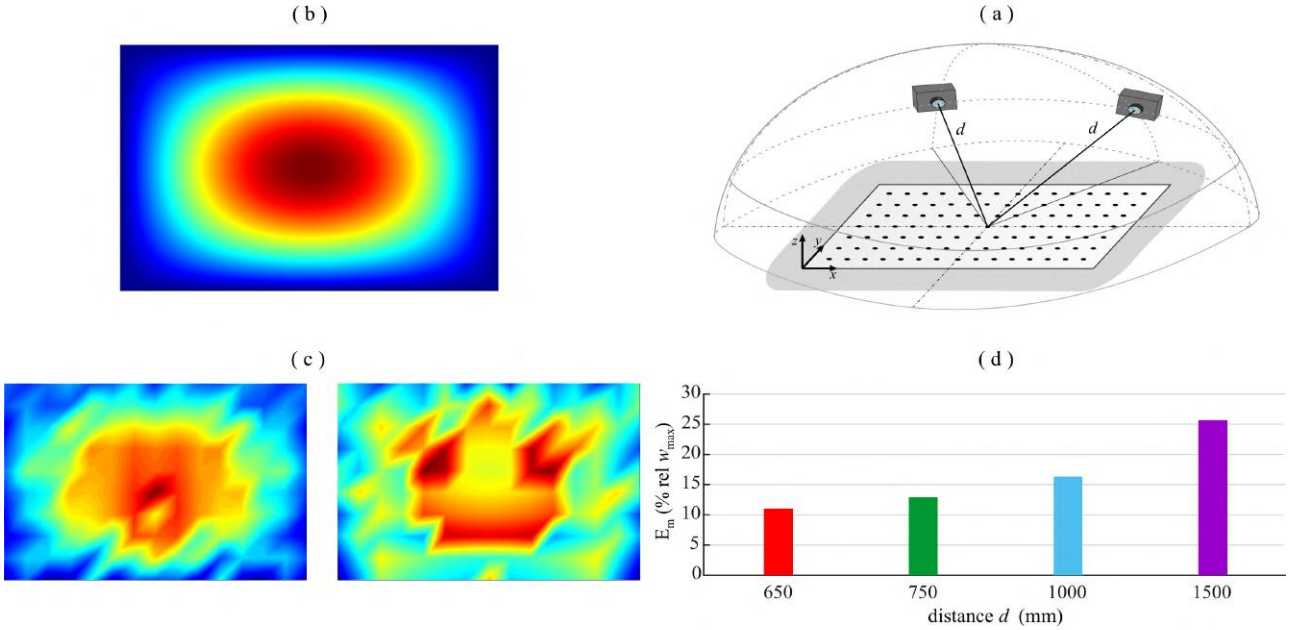

Figure 4.2: First deflection shape: (a) distance case study 1; (b) ideal flexural deflection shape of the plate; (c) comparison between reconstructed flexural deflection shapes of the plate for the smallest (left) and largest (right) distances d; (d) histogram of the mean error.

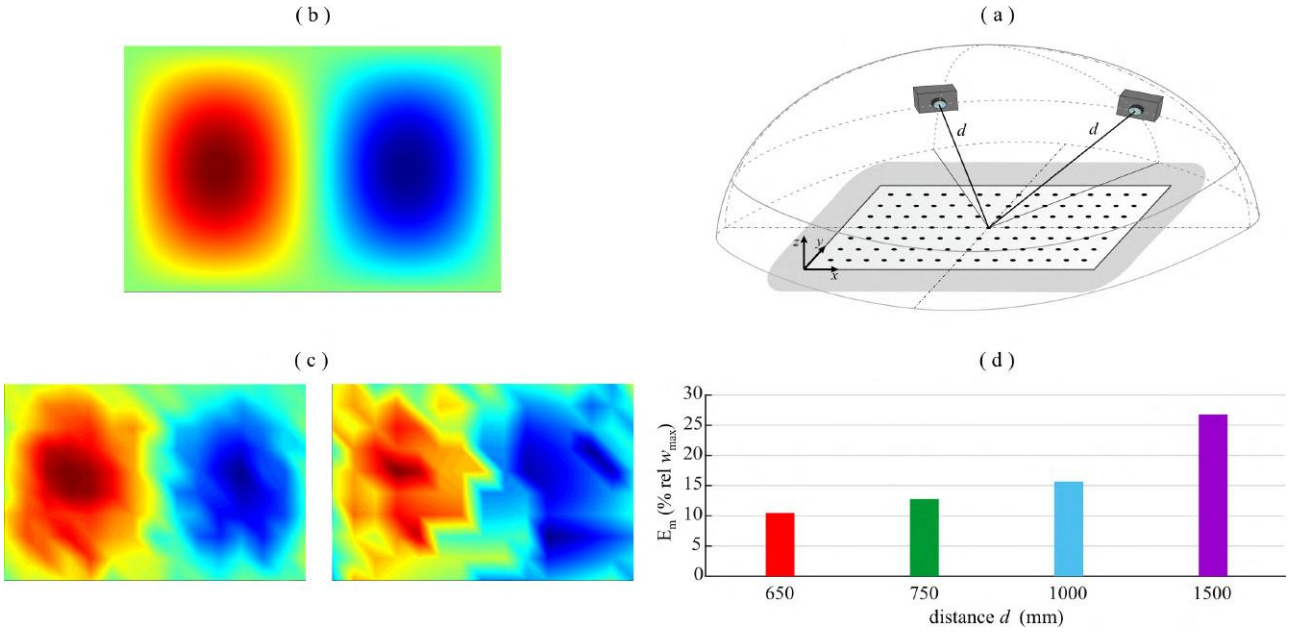

Figure 4.3: Second deflection shape: (a) distance case study 1; (b) ideal flexural deflection shape of the plate; (c) comparison between reconstructed flexural deflection shapes of the plate for the smallest (left) and largest (right) distances d; (d) histogram of the mean error.

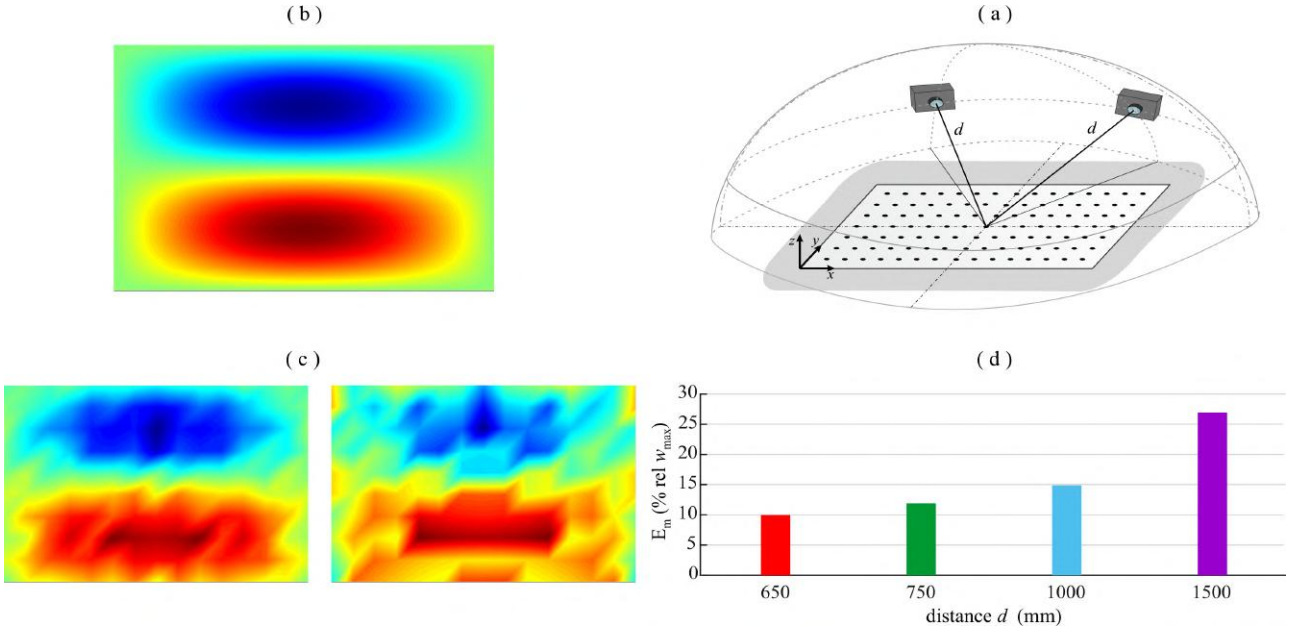

Figure 4.4: Third deflection shape: (a) distance case study 1; (b) ideal flexural deflection shape of the plate; (c) comparison between reconstructed flexural deflection shapes of the plate for the smallest (left) and largest (right) distances d; (d) histogram of the mean error.

As found for the beam, the results presented in Figs. 4.2 - 4.4 suggest that the accuracy of the measurement decreases as the distance of the cameras from the centre of the plate is increased. For example, according to the bar Plot (d) in Fig. 4.2 the average error of reconstruction of the first deflection shape grows from about 12% to about 26% when the distance of the cameras is increased from 650 to 1500 mm. Figs. 4.3 - 4.4 show similar results for the errors calculated when the second and the third flexural deflection shapes are considered respectively. For instance, Fig. 4.3 and Fig. 4.4 Plot (d) show that the average reconstruction error of the second and of the third flexural deflection shapes increases respectively from 11% to 27% and from from 10% to 27% when the distance is increased from 650 mm to 1500 mm.

4.2.2 Aperture angle α between cameras

The accuracy of the reconstruction of the plate first three flexural deflection shapes is now examined assuming the pair of cameras is arranged with fixed distance d from the centre point of the plate and with increasingly larger aperture angle α between the two cameras. As seen in Section 3.3.2, the accuracy of stereo estimations depends on the ratio between disparity and baseline, for a given focal length: thus, similar results could be found for different values of the distance d. Four cases are considered. To start with, the first two configurations are illustrated. In Case 2a, the cameras are arranged over an arc of a circle, which is oriented parallel to the plane of the plate and aligned parallel to the x axis of the plate such that the cameras are all characterised by the same elevation angle $\phi = 10°$ and have increasingly larger aperture angles α, that is, as shown in Table 4.3 - Case 2a, increasingly larger azimuthal angles $\theta = \pm\alpha/2$. Alternatively, in Case 2b, the cameras are arranged

over an arc of a circle, which is oriented orthogonal to the plane of the plate and parallel to the x axis of the plate in such a way as it passes through the center of the plate. Therefore, in this case the elevation ϕ angle of the cameras is varied to generate the increasing aperture angle α as summarised in Table 4.3 - Case 2b.

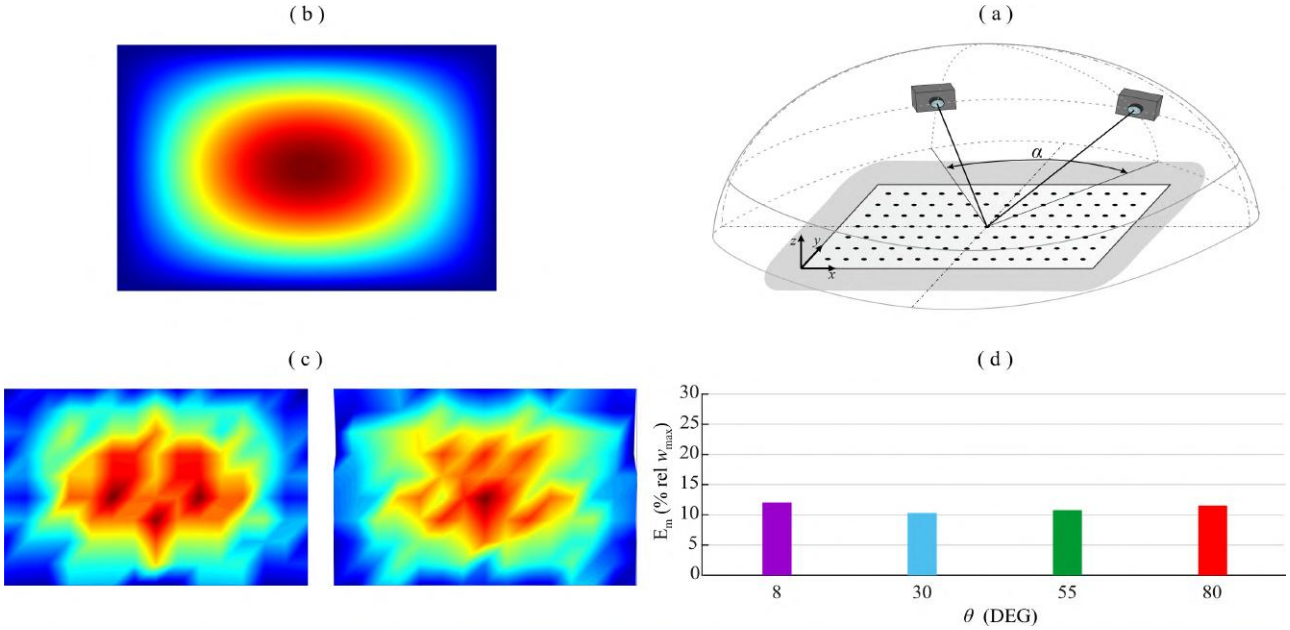

Figure 4.5: First deflection shape: (a) aperture angle case study 2a ($\alpha = 2|\theta|$); (b) ideal flexural deflection shape of the plate; (c) comparison between reconstructed flexural deflection shapes of the plate for the smallest (left) and largest (right) azimuthal angle θ; (d) histogram of the mean error.

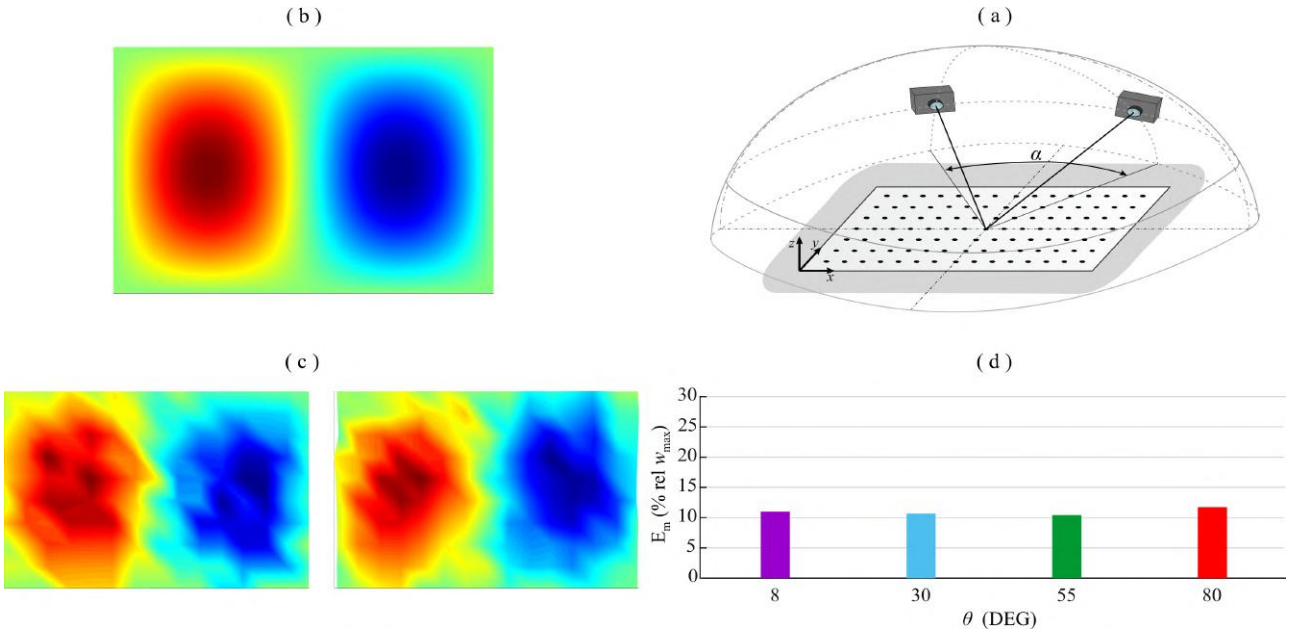

Figure 4.6: Second deflection shape: (a) aperture angle case study 2a ($\alpha = 2|\theta|$); (b) ideal flexural deflection shape of the plate; (c) comparison between reconstructed flexural deflection shapes of the plate for the smallest (left) and largest (right) azimuthal angle θ; (d) histogram of the mean error.

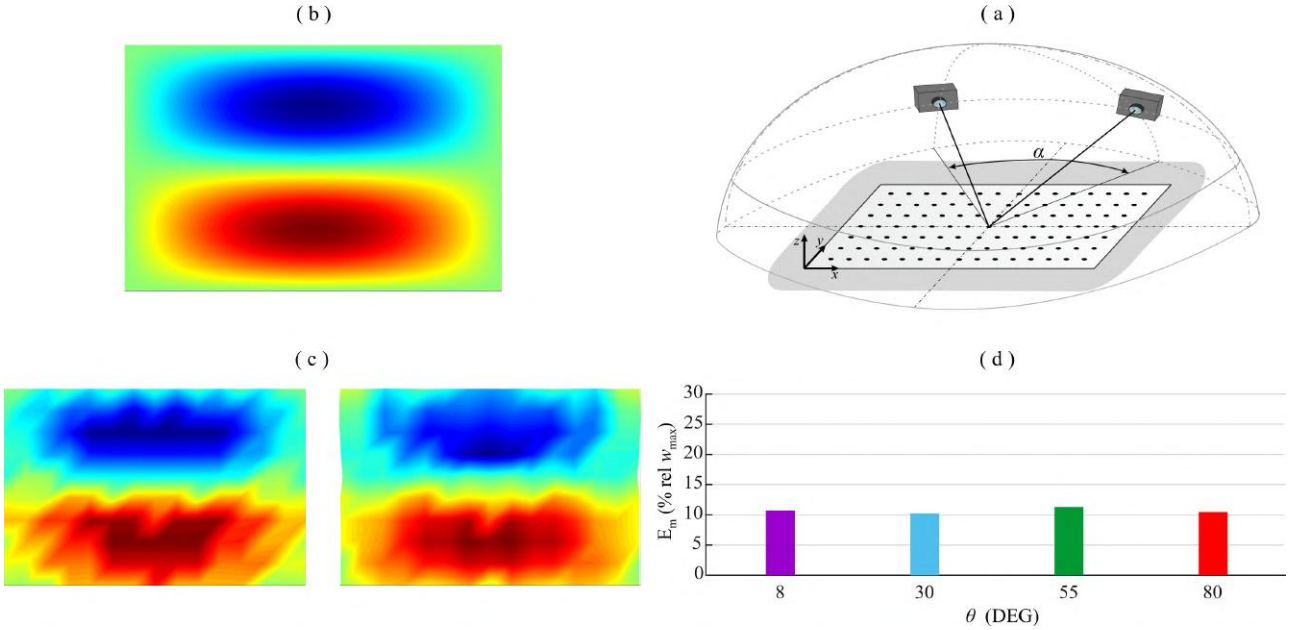

Figure 4.7: Third deflection shape: (a) aperture angle case study 2a ($\alpha = 2|\theta|$); (b) ideal flexural deflection shape of the plate; (c) comparison between reconstructed flexural deflection shapes of the plate for the smallest (left) and largest (right) azimuthal angle θ; (d) histogram of the mean error.

The results presented in Figs. 4.5 - 4.7 indicate that, when the cameras are arranged along the arc of a circle oriented parallel to the plane of the plate such that the cameras have a little elevation angle of 10°, the accuracy of the measurement does not vary significantly as the angle of aperture between the cameras is increased. Indeed, the bar Plot (d) of Figs. 4.5 - 4.7 show that the average error of reconstruction of the three flexural deflection shapes, is comprised between 10% and 13%. These results are in accordance with those presented in Chapter 3 for the beam.

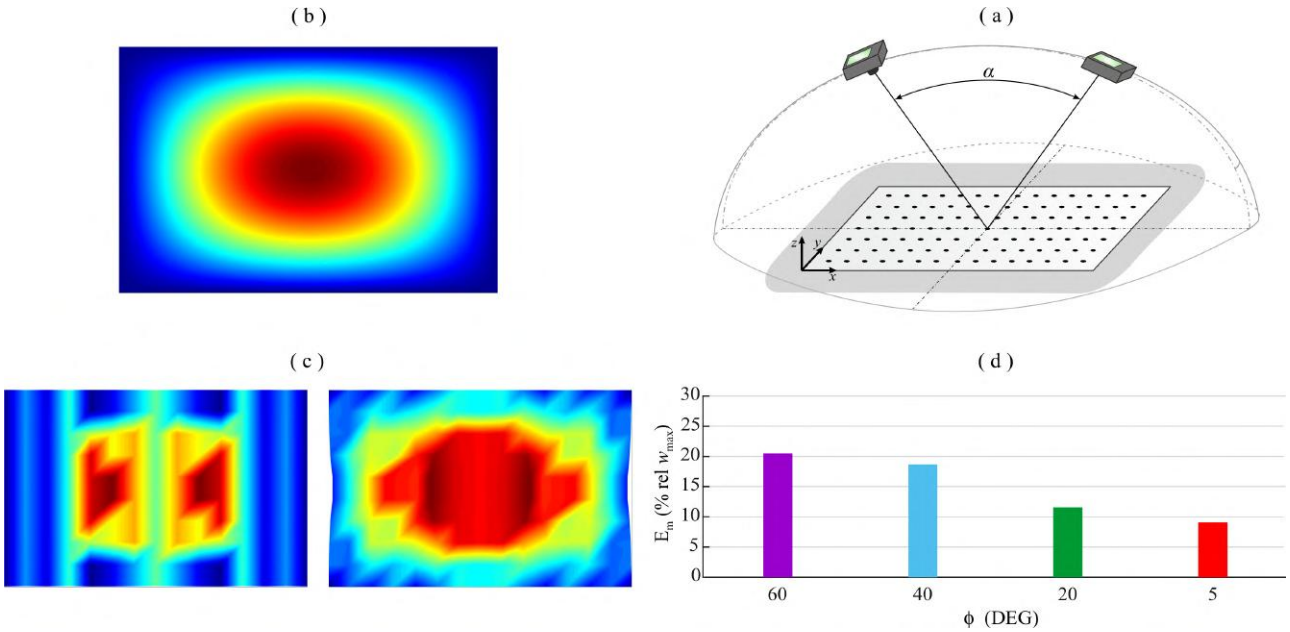

Figure 4.8: First deflection shape: (a) aperture angle case study 2b ($\alpha = 180 - 2\phi$); (b) ideal flexural deflection shape of the plate; (c) comparison between reconstructed flexural deflection shapes of the plate for the largest (left) and smallest (right) elevation angle ϕ; (d) histogram of the mean error.

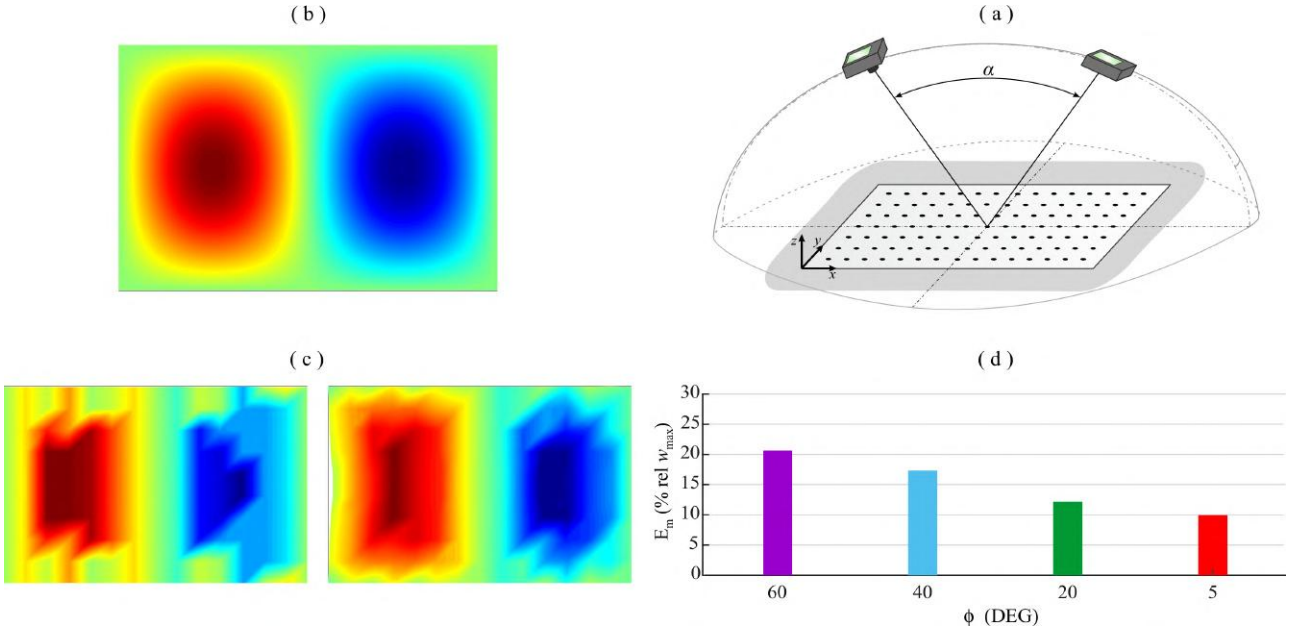

Figure 4.9: Second deflection shape: (a) aperture angle case study 2b ($\alpha = 180 - 2\phi$); (b) ideal flexural deflection shape of the plate; (c) comparison between reconstructed flexural deflection shapes of the plate for the largest (left) and smallest (right) elevation angle ϕ; (d) histogram of the mean error.

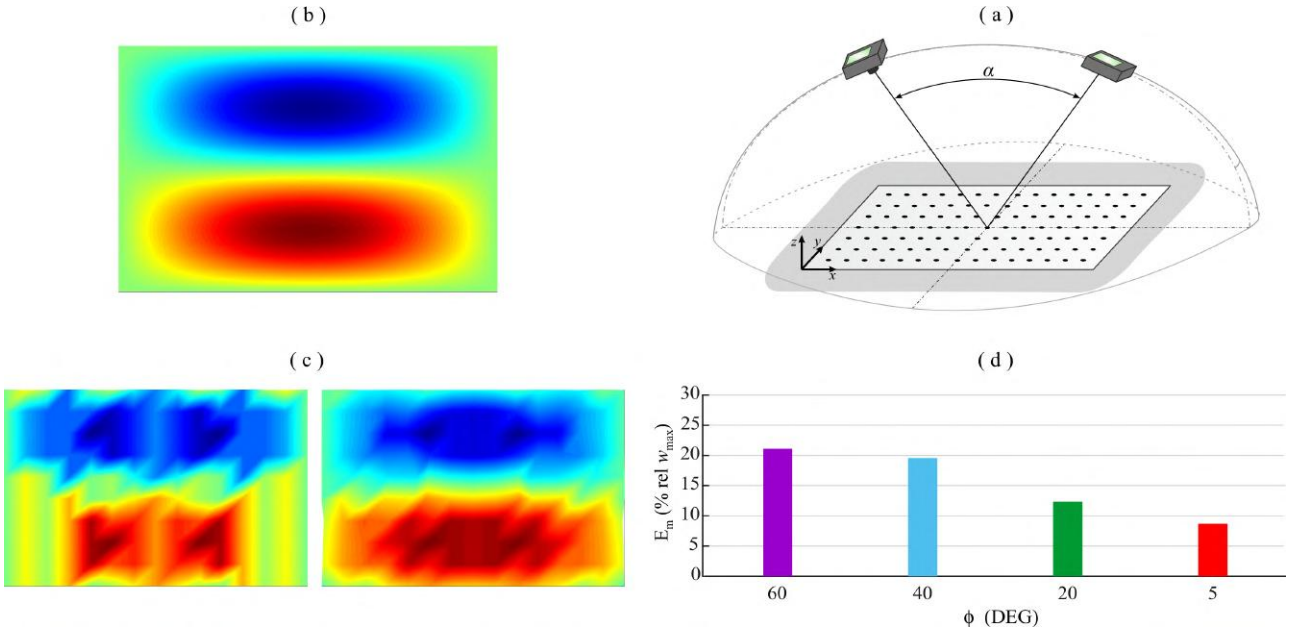

Figure 4.10: Third deflection shape: (a) aperture angle case study 2b ($\alpha = 180 - 2\phi$); (b) ideal flexural deflection shape of the plate; (c) comparison between reconstructed flexural deflection shapes of the plate for the largest (left) and smallest (right) elevation angle ϕ; (d) histogram of the mean error.

In contrast, the results presented in Figs. 4.8 - 4.10 show that, when the cameras are arranged along the arc of circle, which is oriented orthogonal to the plane of the plate and parallel to the x axis of the plate such that it passes through the center of the plate, the accuracy of the measurement does vary significantly as the angle of aperture between the cameras is increased. For instance, the bar Plot (d) of Fig. 4.8, which refers to the first flexural deflection shape, indicates that the average error of reconstruction of the deflection shape passes from 20% to 9% when the angle of aperture is

increased from 60° to 170°. Plot (d) in Fig. 4.9, which refers to the second flexural deflection shape, shows that the average error of reconstruction falls from 21% to 10% while Plot (d) in Fig. 4.10 shows that, when the third flexural deflection shape is considered, the average error of reconstruction of the deflection shape falls from 21% to 9% when the angle of aperture is increased from 60° to 170°. In conclusion, the results presented in Figs. 4.8 - 4.10 indicate that the accuracy of the measurement is strongly influenced by the elevation angle of the cameras. The smaller is this angle the greater is the accuracy of the measurement. In general, to have accurate measurements, the cameras should be arranged over an arc of a circle, which is oriented parallel to the plane of the plate and placed a small distance from the plate itself, so that the cameras are characterized by small elevation angles.

The third and fourth configurations are now discussed. Cases 2c and 2d consider similar arrangements for the two cameras as those seen in Cases 2a and 2b. However, here, the cameras are rotated by $\pi/2$ around the z axis. Therefore, in Case 2c the cameras are arranged over an arc of a circle, which is oriented parallel to the plane of the plate and parallel to the y axis of the plate, such that the cameras are all characterized by the same elevation angle $\phi = 10°$ and have increasingly larger aperture angles α. Thus, as reported in Table 4.3 - Case 2c, increasingly larger azimuthal angles $\theta = \pm\alpha/2$. In Case 2d the cameras are arranged over an arc of a circle, which is oriented orthogonal to the plane of the plate and parallel to the y axis of the plate such that it passes through the center of the plate. As reported in 4.3 - Case 2d, in this case, the elevation angle ϕ varies as the aperture angle is increased.

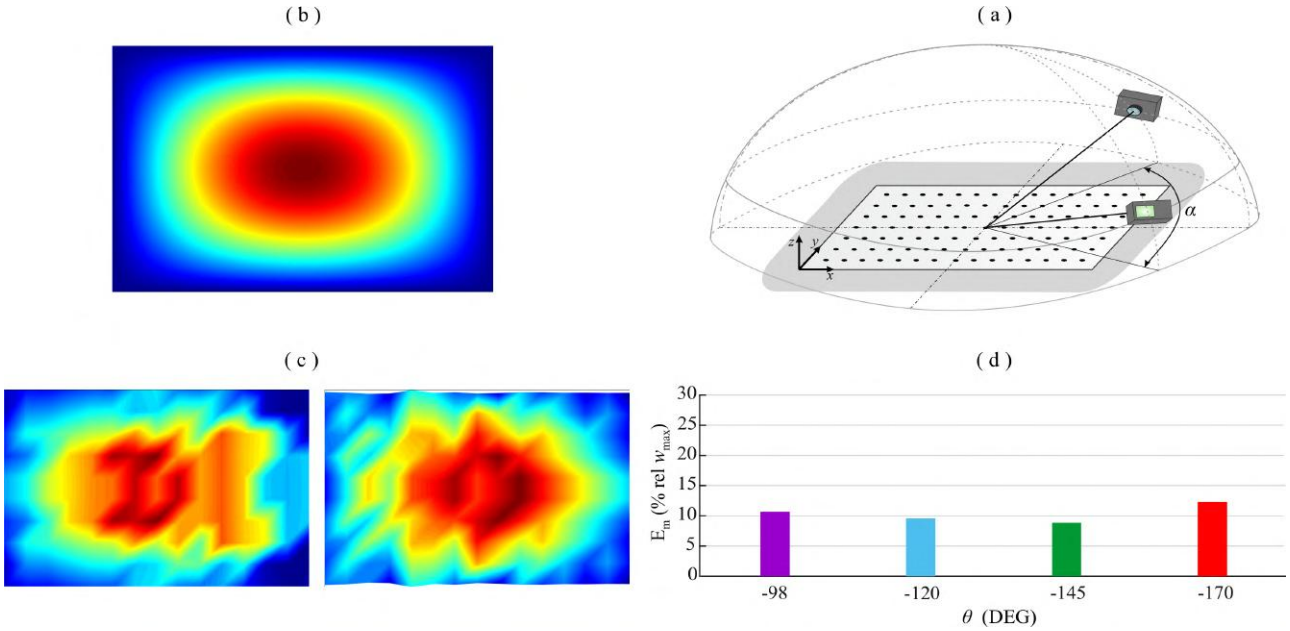

Figure 4.11: First deflection shape: (a) aperture angle case study 2c ($\alpha = 2|\theta|$); (b) ideal flexural deflection shape of the plate; (c) comparison between reconstructed flexural deflection shapes of the plate for the smallest (left) and largest (right) azimuthal angle θ; (d) histogram of the mean error.

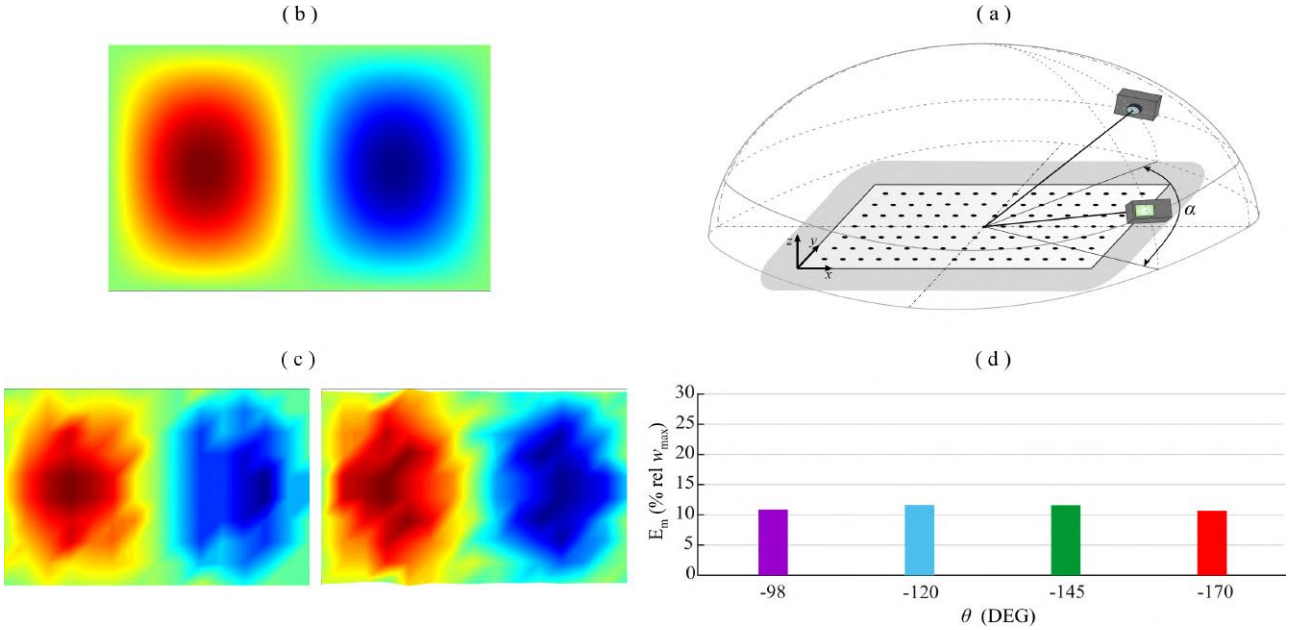

Figure 4.12: Second deflection shape: (a) aperture angle case study 2c ($\alpha = 2|\theta|$); (b) ideal flexural deflection shape of the plate; (c) comparison between reconstructed flexural deflection shapes of the plate for the smallest (left) and largest (right) azimuthal angle θ; (d) histogram of the mean error.

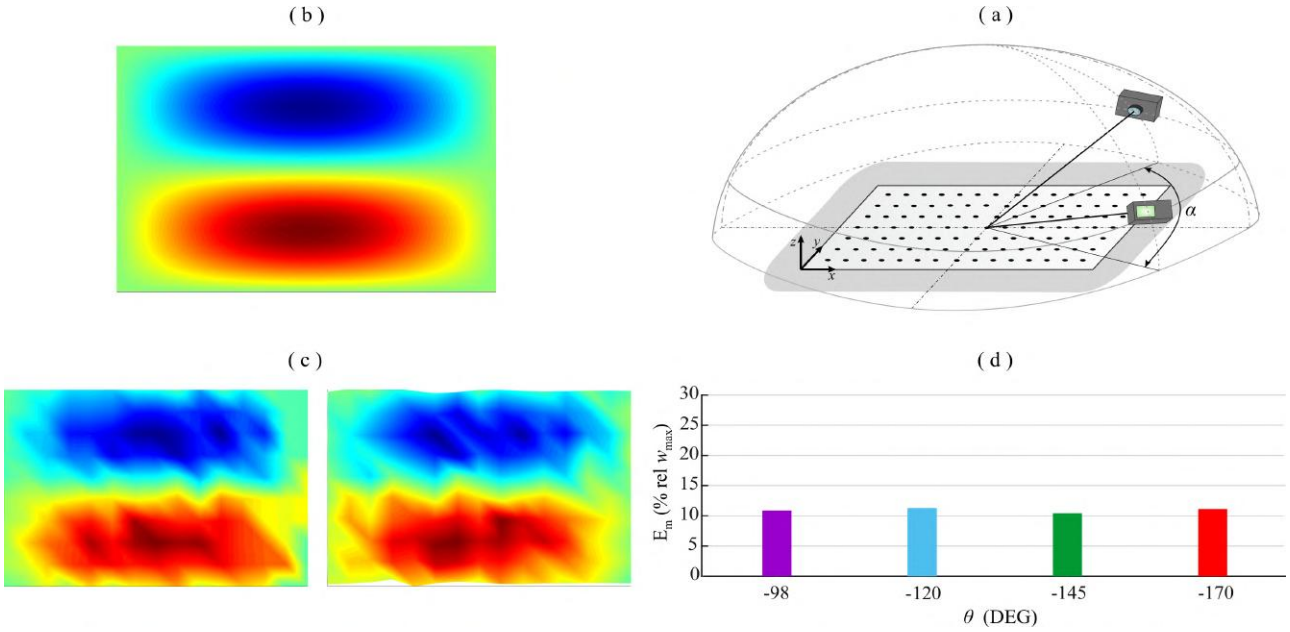

Figure 4.13: Third deflection shape: (a) aperture angle case study 2c ($\alpha = 2|\theta|$); (b) ideal flexural deflection shape of the plate; (c) comparison between reconstructed flexural deflection shapes of the plate for the smallest (left) and largest (right) azimuthal angle θ; (d) histogram of the mean error.

The bar Plot (d) of Figs. 4.11 - 4.13 shows that, when the two cameras are arranged with small elevation angles across the plate with increasingly larger angles α, the average error of reconstruction of the three flexural deflection shapes is always comprised between 8% and 13%.

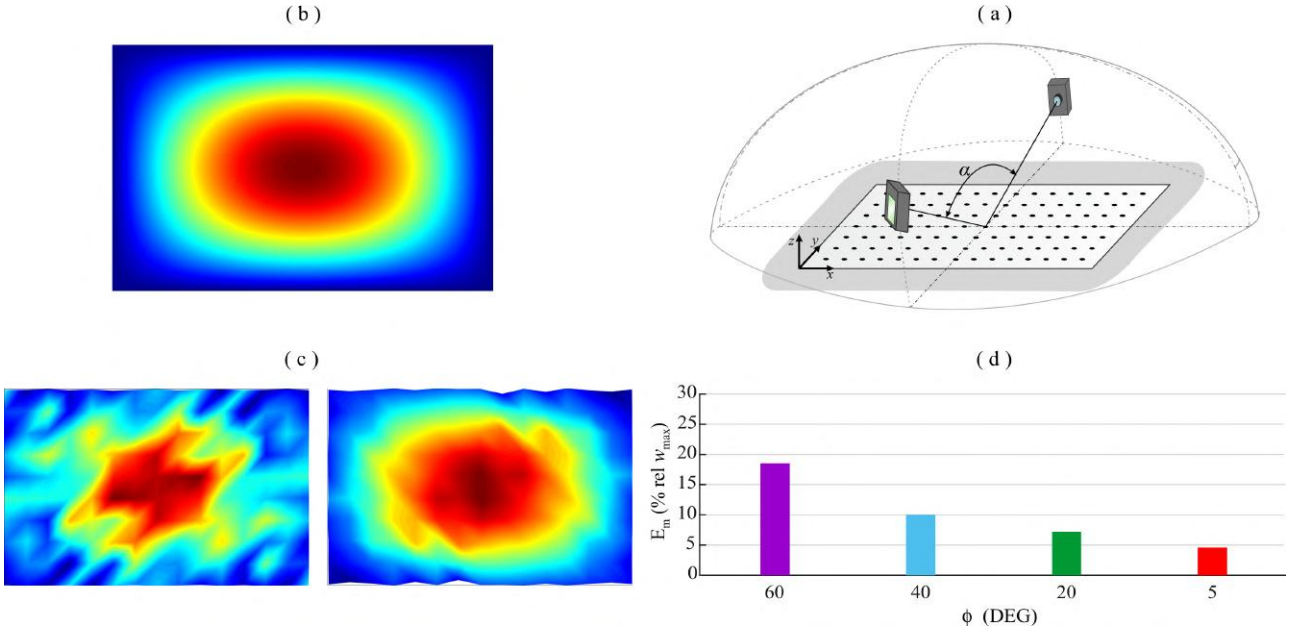

Figure 4.14: First deflection shape: (a) aperture angle case study 2d ($\alpha = 180 - 2\phi$); (b) ideal flexural deflection shape of the plate; (c) comparison between reconstructed flexural deflection shapes of the plate for the largest (left) and smallest (right) elevation angle ϕ; (d) histogram of the mean error.

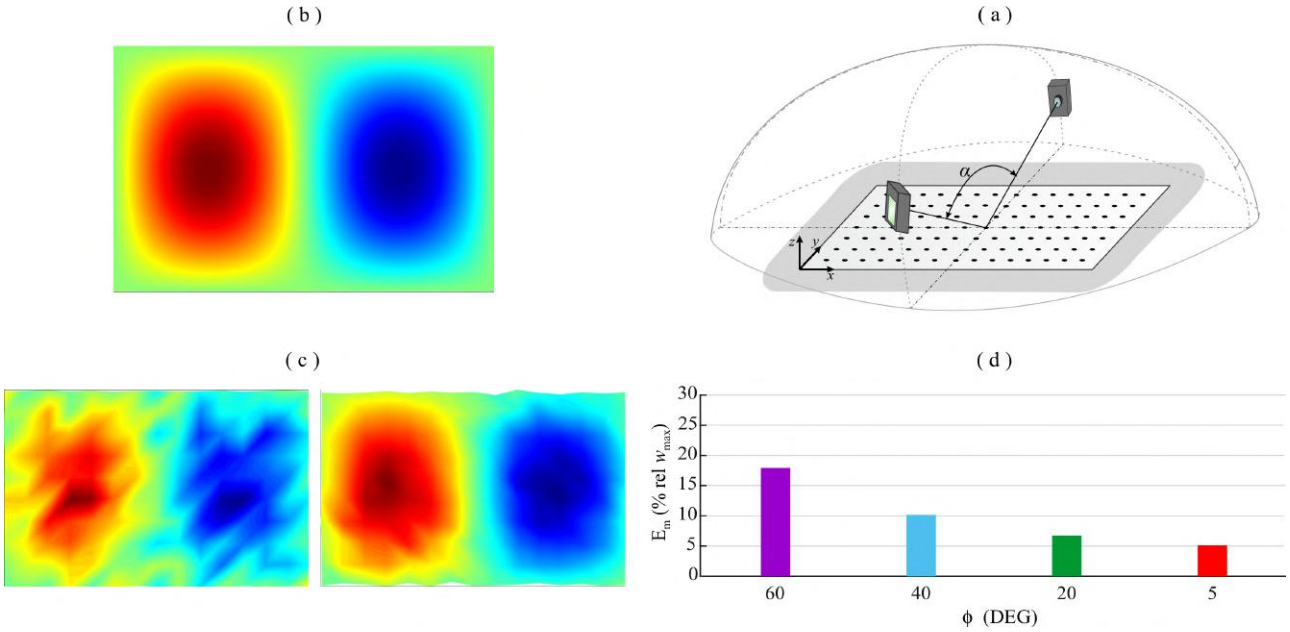

Figure 4.15: Second deflection shape: (a) aperture angle case study 2d ($\alpha = 180 - 2\phi$); (b) ideal flexural deflection shape of the plate; (c) comparison between reconstructed flexural deflection shapes of the plate for the largest (left) and smallest (right) elevation angle ϕ; (d) histogram of the mean error.

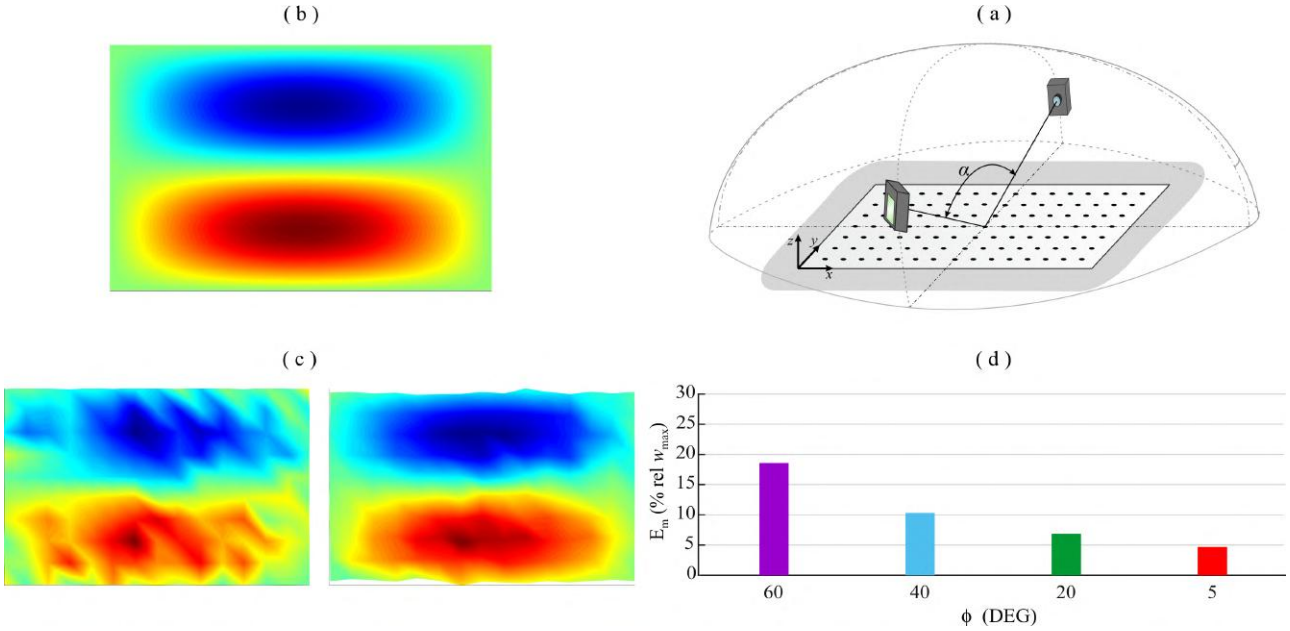

Figure 4.16: Third deflection shape: (a) aperture angle case study 2d ($\alpha = 180 - 2\phi$); (b) ideal flexural deflection shape of the plate; (c) comparison between reconstructed flexural deflection shapes of the plate for the largest (left) and smallest (right) elevation angle ϕ; (d) histogram of the mean error.

Moving to Case 2d with the cameras arranged along an arc oriented orthogonal to the plate, the results presented in Figs. 4.14 - 4.16 indicate that the average error of reconstruction significantly decreases when the angle of aperture is increased from 60° to 170°. More specifically, the bar Plot (d) of Figs. 4.14 - 4.16 shows a clear decrement of the average error of reconstruction from 18-19%, when the angle of aperture is 60°, to 5%, when the angle of aperture is 170°.

4.2.3 Resolution of cameras

The accuracy of the reconstruction of the plate first three flexural deflection shape generated by pairs of cameras with increasingly larger spatial resolution is now investigated. The distance d, the azimuthal θ and elevation ϕ angles and the resolutions of the cameras are listed in Table 4.3 - Case 3.

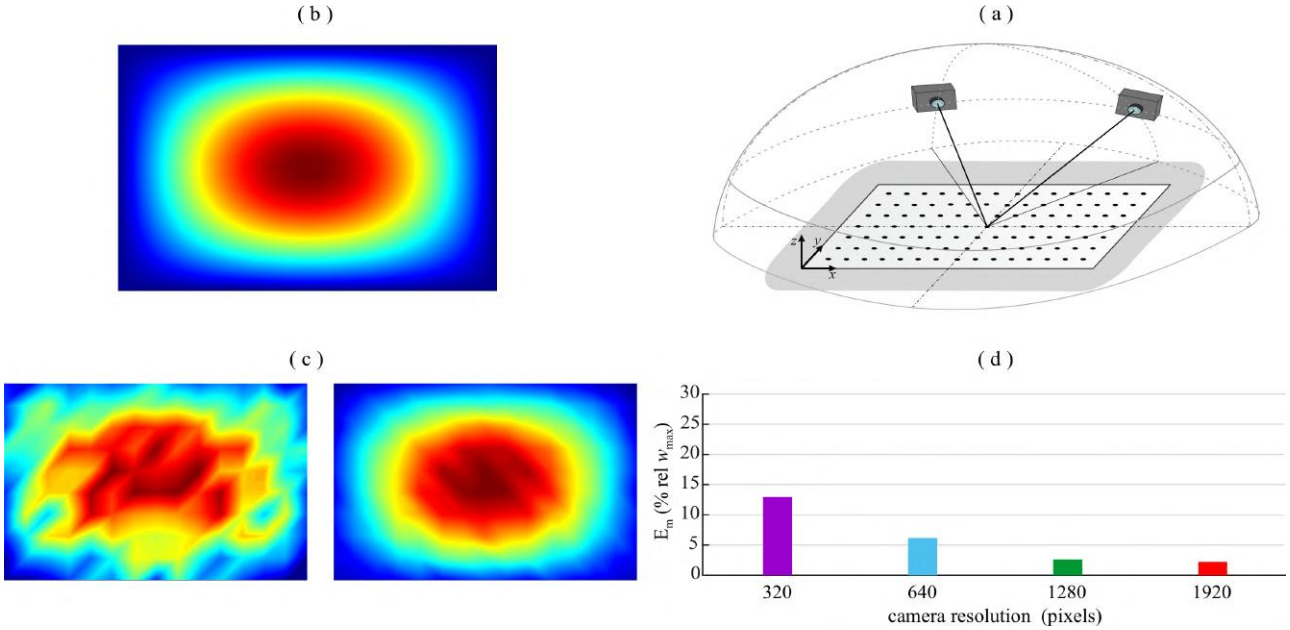

Figure 4.17: First deflection shape: (a) resolution case study 3; (b) ideal flexural deflection shape of the plate; (c) comparison between reconstructed flexural deflection shapes of the plate for the smallest (left) and largest (right) resolution; (d) histogram of the mean error.

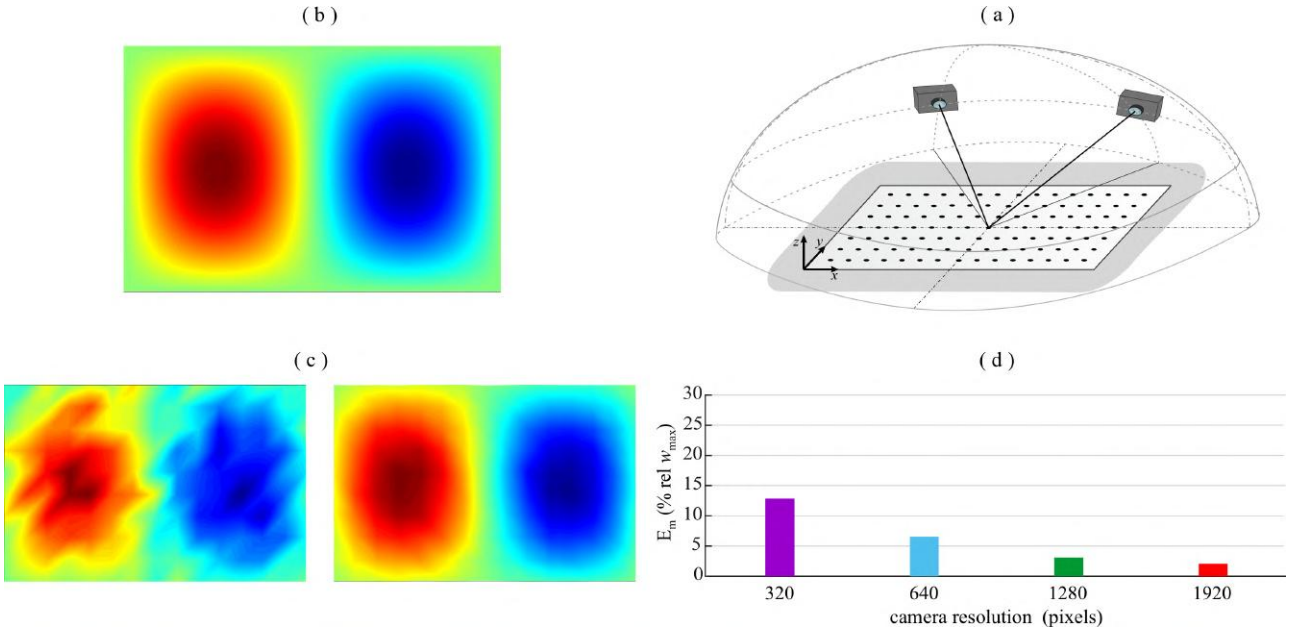

Figure 4.18: Second deflection shape: (a) resolution case study 3; (b) ideal flexural deflection shape of the plate; (c) comparison between reconstructed flexural deflection shapes of the plate for the smallest (left) and largest (right) resolution; (d) histogram of the mean error.

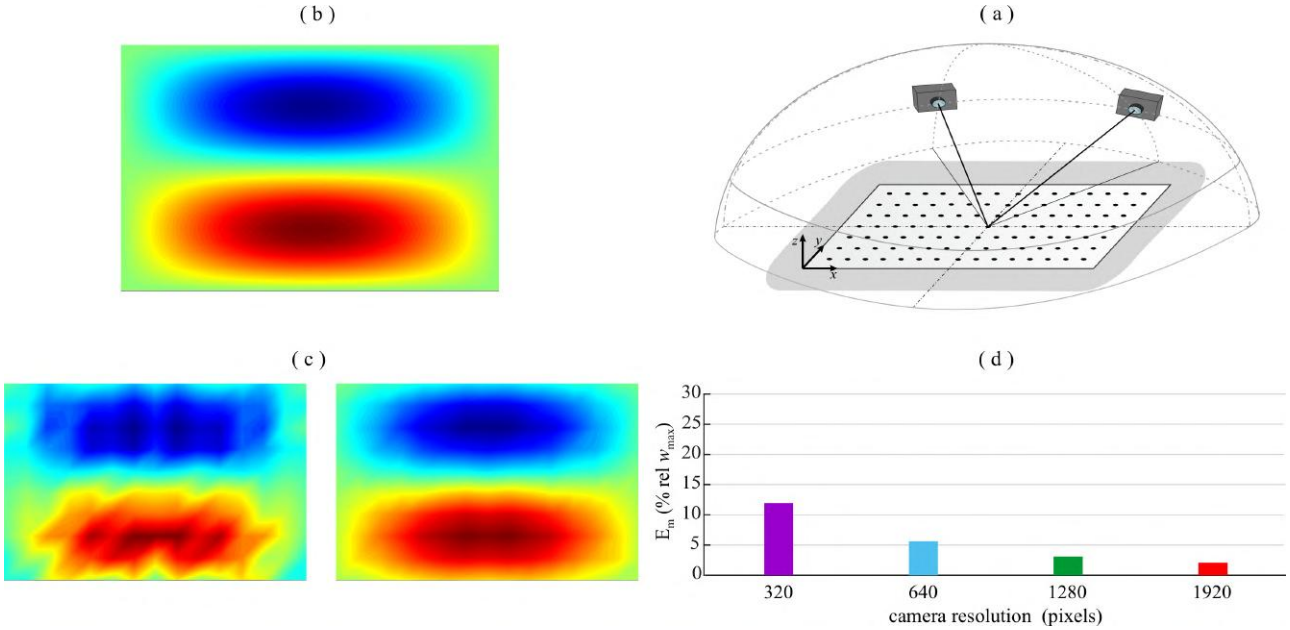

Figure 4.19: Third deflection shape: (a) resolution case study 3; (b) ideal flexural deflection shape of the plate; (c) comparison between reconstructed flexural deflection shapes of the plate for the smallest (left) and largest (right) resolution; (d) histogram of the mean error.

As found from the beam structure, the results presented in Figs. 4.17 - 4.19 unequivocally indicate that the accuracy of the measurement increases as the resolution of the cameras is increased. Similar considerations can be done analyzing the average reconstruction error of the three flexural deflection shapes. In fact, when the number of pixels is raised from 320×180 to 1920×1080, the bar Plot (d) of Figs. 4.17 - 4.19 suggests that the average error of the measurement falls from about 12-13% to 2%.

4.2.4 Arrays composed by more than 2 cameras

To conclude the study on the plate vibrations, the measurement with a multiple cameras setup composed by more than 2 cameras is examined in this subsection. As done in Chapter 3 for the flexural vibrations of the beam, the study considers the sequential addition of pairs of cameras, which are located symmetrically with respect to either the YZ plane or the XZ plane both centered in the middle of the plate. The analysis is organized in two parts. The first part concerns increasingly larger numbers of cameras arranged over an arc of circumference, which, as for the Cases 2a and 2c discussed in Figs. 4.5 - 4.7 and Figs. 4.11 - 4.13, is oriented parallel to the plane of the plate such that the cameras are all characterised by the same elevation angle ϕ and have either increasingly larger or increasing smaller aperture angles α, that is larger or smaller azimuthal angles θ, in the x and y directions with respect to the plate. To avoid redundancy, the exact positions of the cameras are slightly misplaced, both with reference to the azimuthal and the elevation angles. Alternatively, the second part considers increasingly larger numbers of cameras arranged over arc of circumferences, which, as for the Cases 2b and 2d discussed in Figs. 4.8 - 4.10 and Figs. 4.14 - 4.16, are: a) oriented orthogonal to the plane of the plate, b) parallel either to the x or the y axis of the plate and c) pass through the center of the plate.

Here only one configuration is considered where the aperture angle is progressively increased. The exact positions for the various arrangements are summarised in Table 4.4 - Cases 4a, 4b, 4c, 4d. Case 4a is analyzed considering the pairs of cameras are added in reverse order too and is recalled 4a′. Finally, an additional case 4e is also discussed where the cameras are arranged in the whole circumference positioned just above the plate.

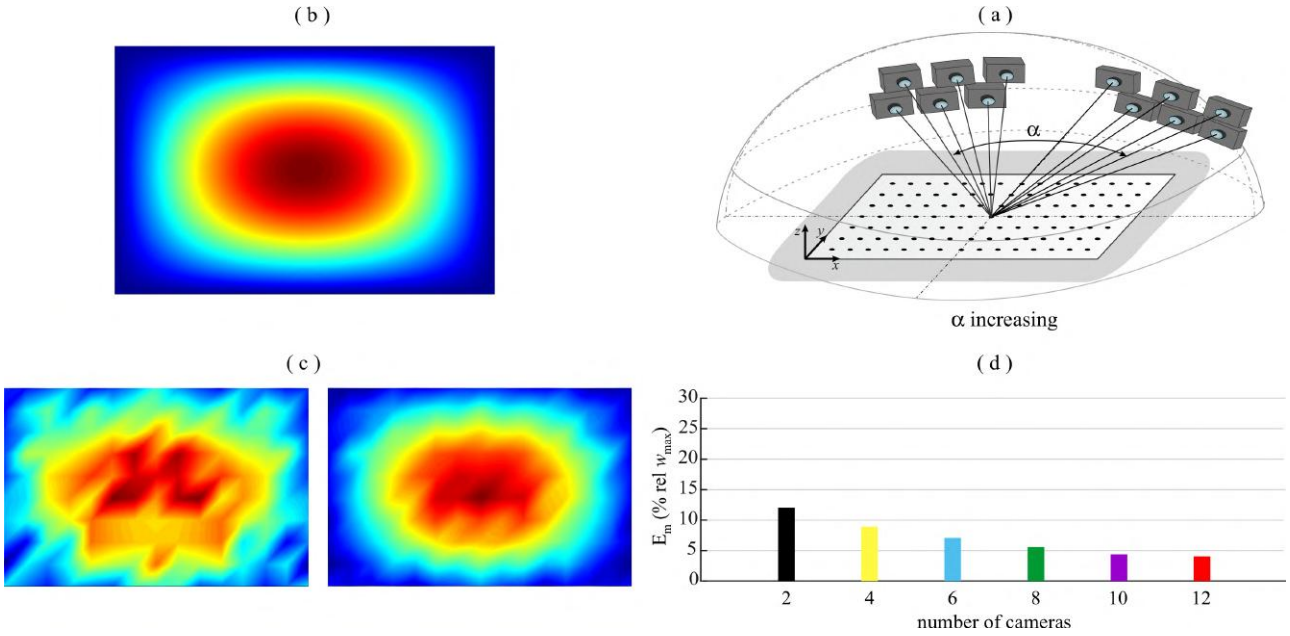

Figure 4.20: First deflection shape: (a) multiple cameras case study 4a; (b) ideal flexural deflection shape of the plate; (c) comparison between reconstructed flexural deflection shapes of the plate for the smallest (left) and largest (right) number of cameras; (d) histogram of the mean error.

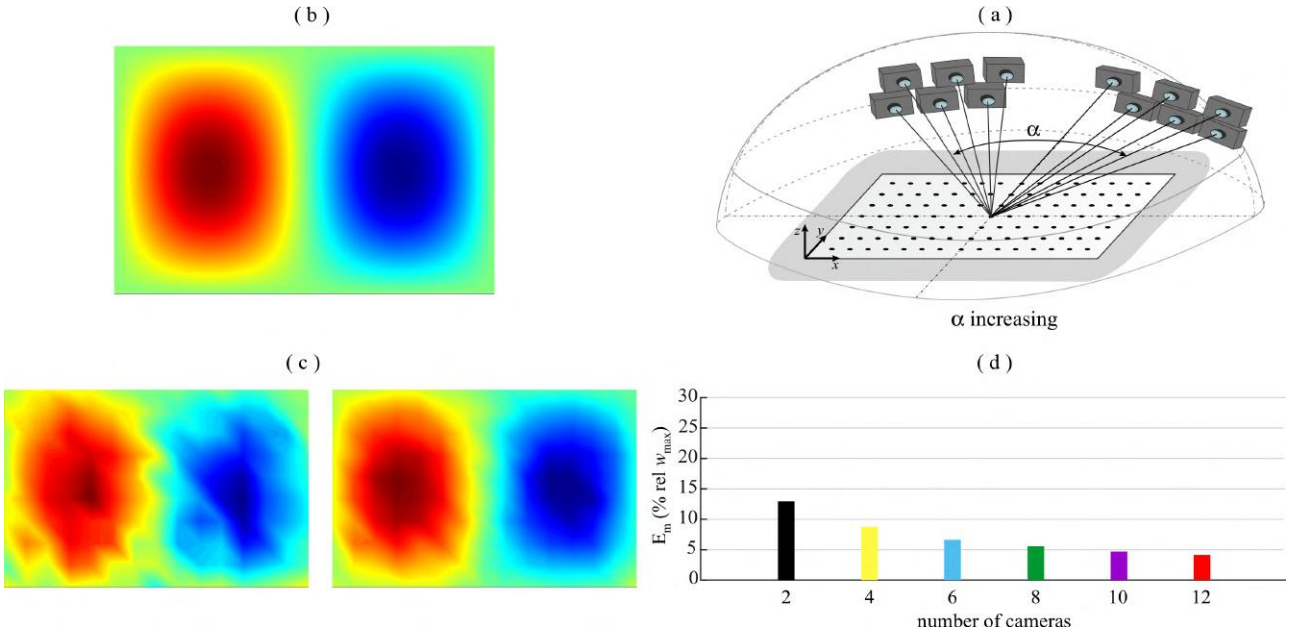

Figure 4.21: Second deflection shape: (a) multiple cameras case study 4a; (b) ideal flexural deflection shape of the plate; (c) comparison between reconstructed flexural deflection shapes of the plate for the smallest (left) and largest (right) number of cameras; (d) histogram of the mean error.

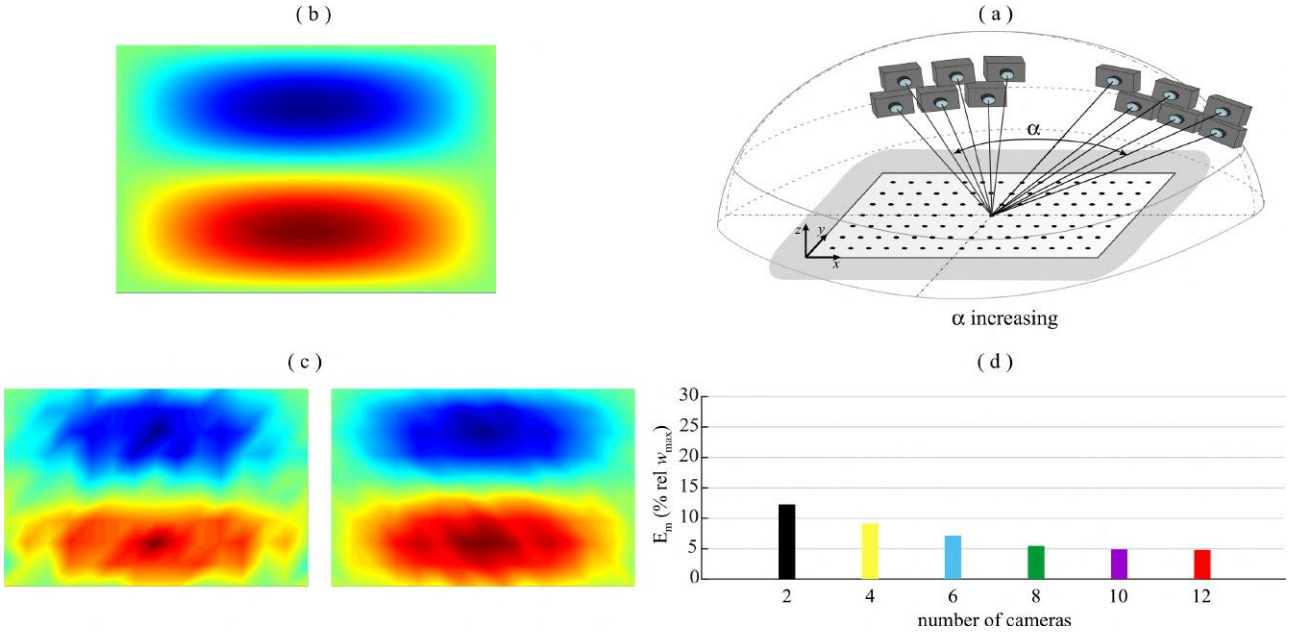

Figure 4.22: Third deflection shape: (a) multiple cameras case study 4a; (b) ideal flexural deflection shape of the plate; (c) comparison between reconstructed flexural deflection shapes of the plate for the smallest (left) and largest (right) number of cameras; (d) histogram of the mean error.

The Case 4a with increasingly larger numbers of cameras arranged over an arc of circumference oriented parallel to the plane of the plate is considered first. The results presented in Figs. 4.20 - 4.22 indicate that, as pairs of cameras with increasingly larger aperture angle are added, the accuracy of the measurement significantly increases. According to Plot (d) of Figs. 4.20 - 4.22, when the measurement setup passes from 2 cameras (1 pair) to 12 cameras (6 pairs) the average error of the measurement falls from 12-13% to 4%.

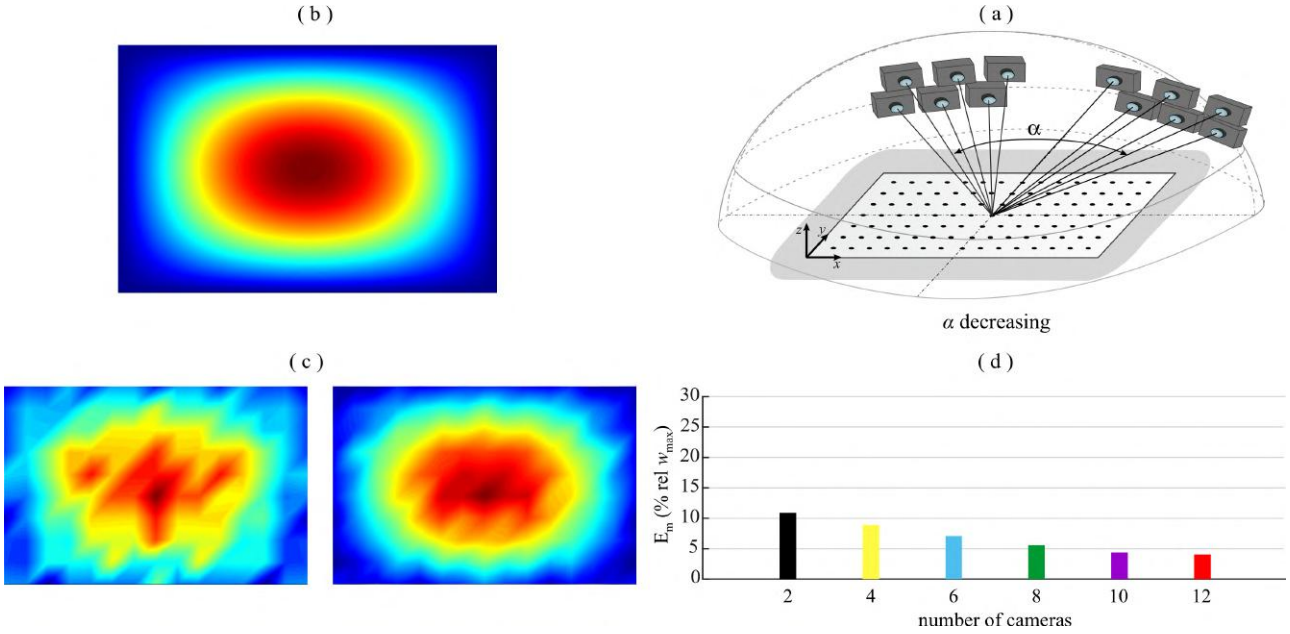

Figure 4.23: First deflection shape: (a) multiple cameras case study 4a′; (b) ideal flexural deflection shape of the plate; (c) comparison between reconstructed flexural deflection shapes of the plate for the smallest (left) and largest (right) number of cameras; (d) histogram of the mean error.

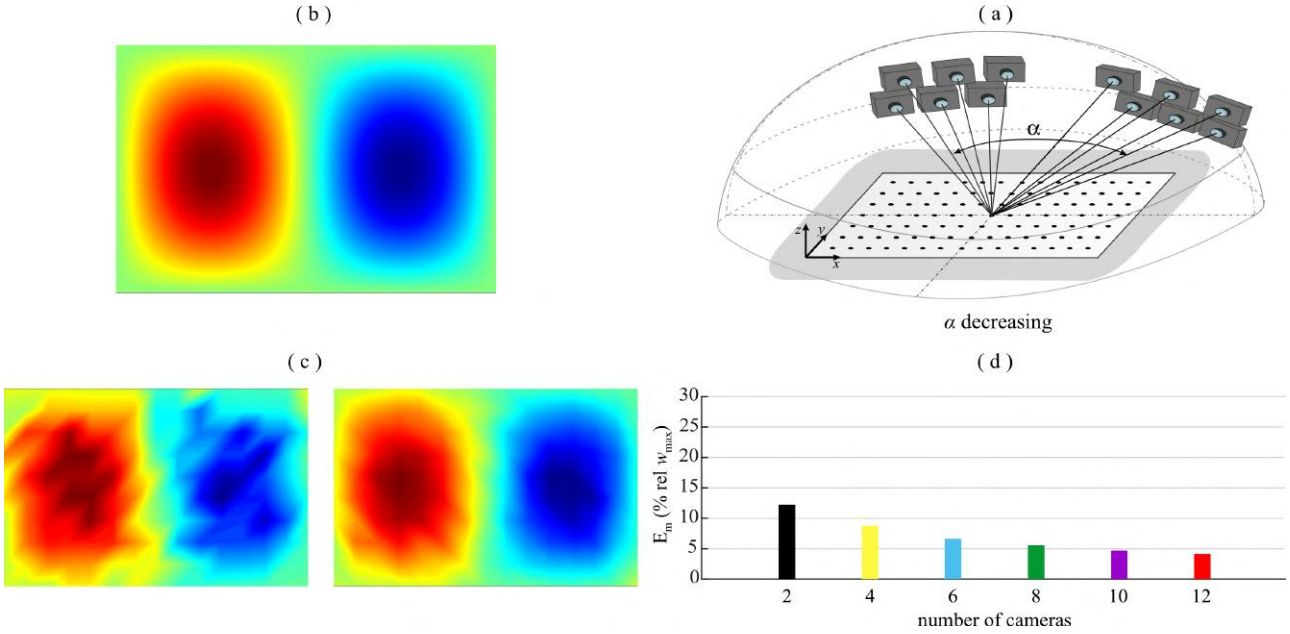

Figure 4.24: Second deflection shape: (a) multiple cameras case study 4a′; (b) ideal flexural deflection shape of the plate; (c) comparison between reconstructed flexural deflection shapes of the plate for the smallest (left) and largest (right) number of cameras; (d) histogram of the mean error.

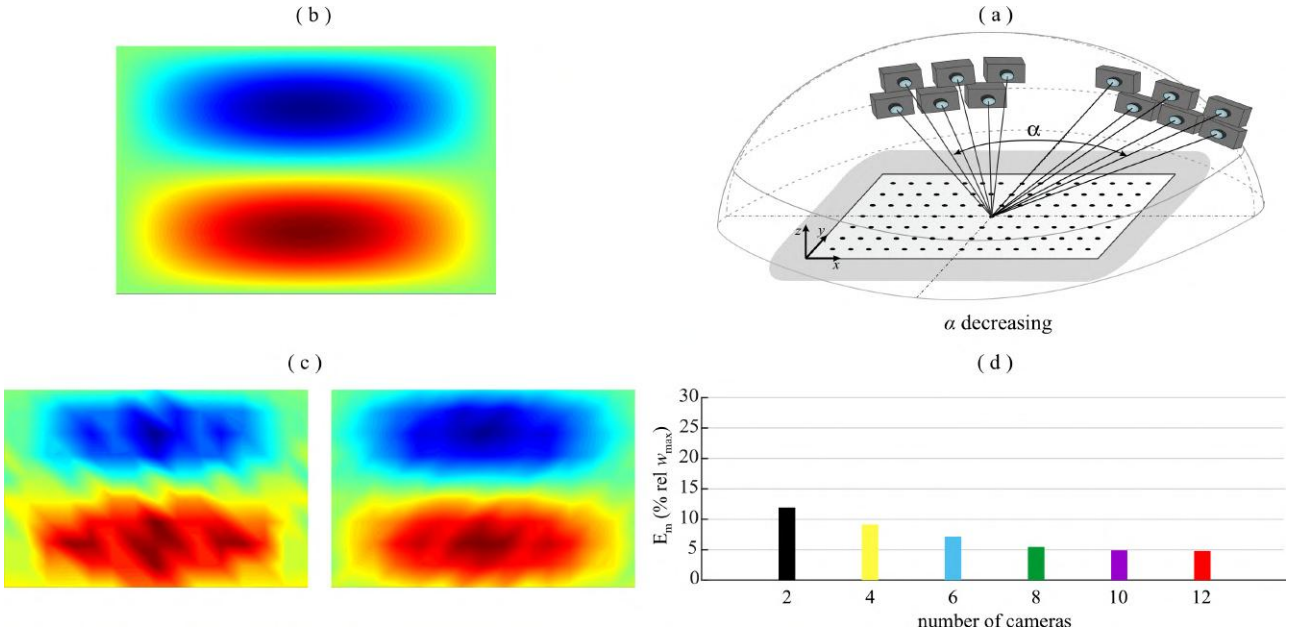

Figure 4.25: Third deflection shape: (a) multiple cameras case study 4a′; (b) ideal flexural deflection shape of the plate; (c) comparison between reconstructed flexural deflection shapes of the plate for the smallest (left) and largest (right) number of cameras; (d) histogram of the mean error.

The results presented for Case 4a′ in Figs. 4.23 - 4.25 show that, if pairs of cameras with increasingly smaller aperture angle are added, the average error still tends to drop but at a smaller rate. As shown in Plot (d) of Figs. 4.23 - 4.25, the average error with the first pair of cameras having a large angle of aperture would be about 11-12% and then would fall again to 4% when a total of 12 cameras is used. As discussed in subsection 4.2.2 (Figs. 4.5 - 4.7, 4.8 - 4.10), the accuracy of the measurement with a pair of cameras increases when the optical axis of the cameras is characterised by a small elevation

angle and a large azimuthal angle. Therefore, when the addition of pairs of cameras starts from a large aperture angle, that is from larger azimuthal angles, the initial averaged and peak errors are smaller than when the addition of pairs of cameras start from a small aperture angle. Nevertheless, the simulation with 12 cameras gives an average error of 4%.

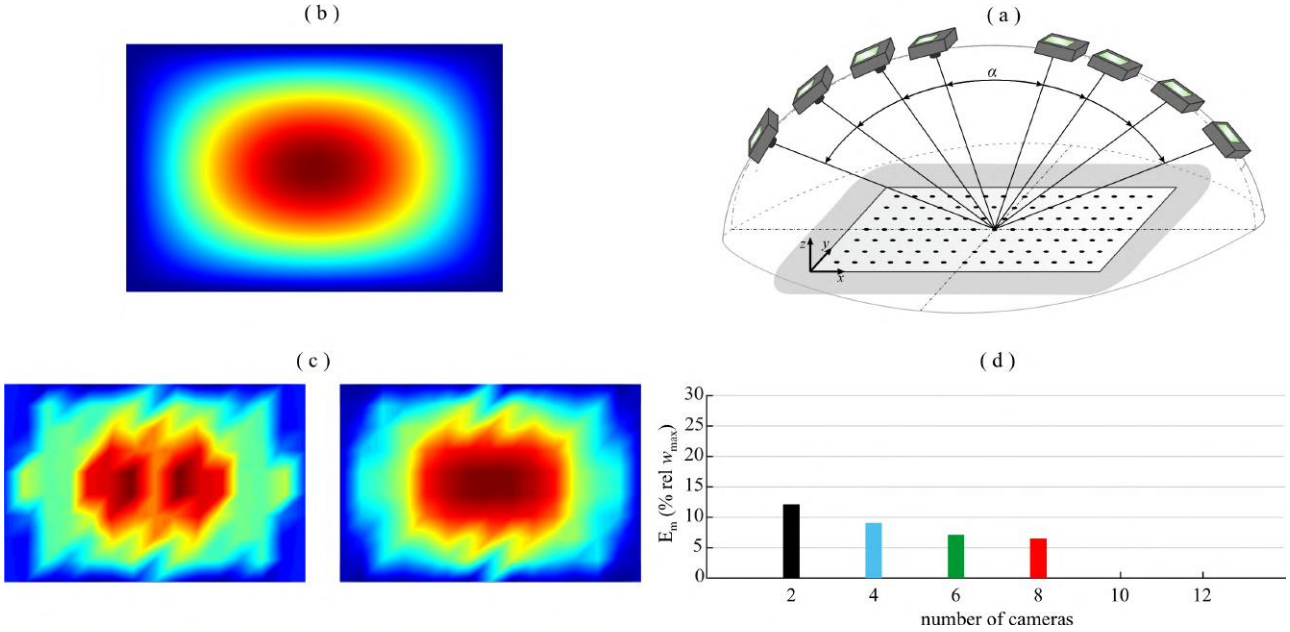

Figure 4.26: First deflection shape: (a) multiple cameras case study 4b; (b) ideal flexural deflection shape of the plate; (c) comparison between reconstructed flexural deflection shapes of the plate for the smallest (left) and largest (right) number of cameras; (d) histogram of the mean error.

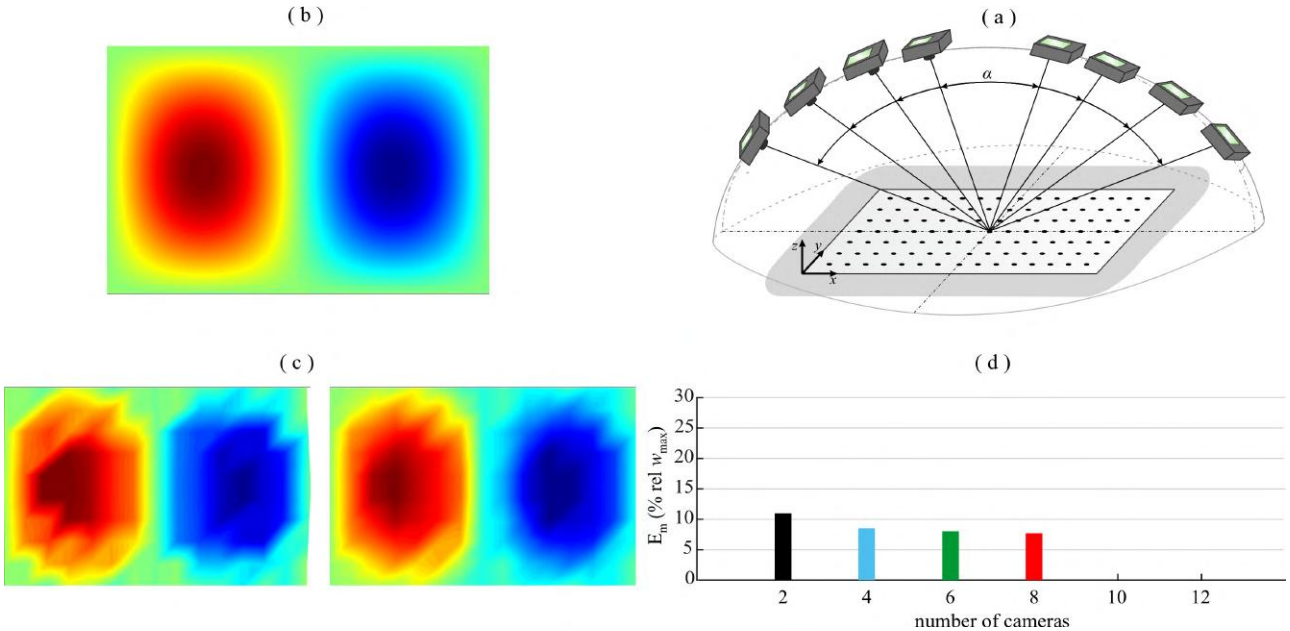

Figure 4.27: Second deflection shape: (a) multiple cameras case study 4b; (b) ideal flexural deflection shape of the plate; (c) comparison between reconstructed flexural deflection shapes of the plate for the smallest (left) and largest (right) number of cameras; (d) histogram of the mean error.

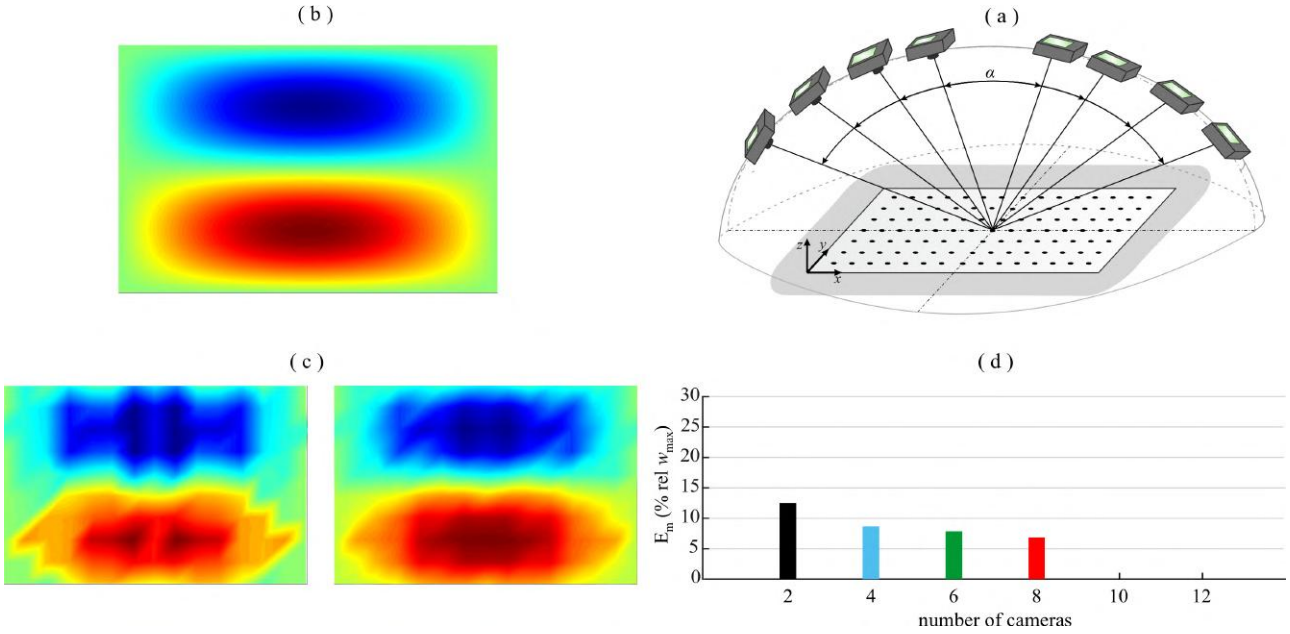

Figure 4.28: Third deflection shape: (a) multiple cameras case study 4b; (b) ideal flexural deflection shape of the plate; (c) comparison between reconstructed flexural deflection shapes of the plate for the smallest (left) and largest (right) number of cameras; (d) histogram of the mean error.

The Case 4b with increasingly larger numbers of cameras arranged over an arc of circumference oriented orthogonal to the plane of the plate, parallel to the x axis of the plate and passing through the center of the plate is now examined. The results presented in Figs. 4.26 - 4.28 show that, as cameras with increasingly larger aperture angle are added, the accuracy of the measurement tends to increase. Similar considerations can be done to analyze the average error of reconstruction of each of the three flexural deflection shapes here considered. For instance, Plot (d) in Figs. 4.26 - 4.28 indicates that, when the measurement setup passes from 2 cameras (1 pair) to 8 cameras (4 pairs), the average error of the measurement falls from 12-13% to 7-8%. Also in this case, if the cameras were added in sequence starting from large aperture angles towards small aperture angles, the error for the first pair would have been smaller. Nevertheless, the final error for the configuration with 8 cameras would have been the same, that is about 7% average error. As shown above and in subsection 4.2.2, to further reduce these errors it would be sufficient to tilt the arc of cameras laterally so that they are characterized by a smaller elevation angle.

Cases 4c, 4d are now investigated, which consider similar arrangements of the cameras as in Cases 4a, 4b but with the cameras rotated by $\pi/2$ with respect to the z axis.

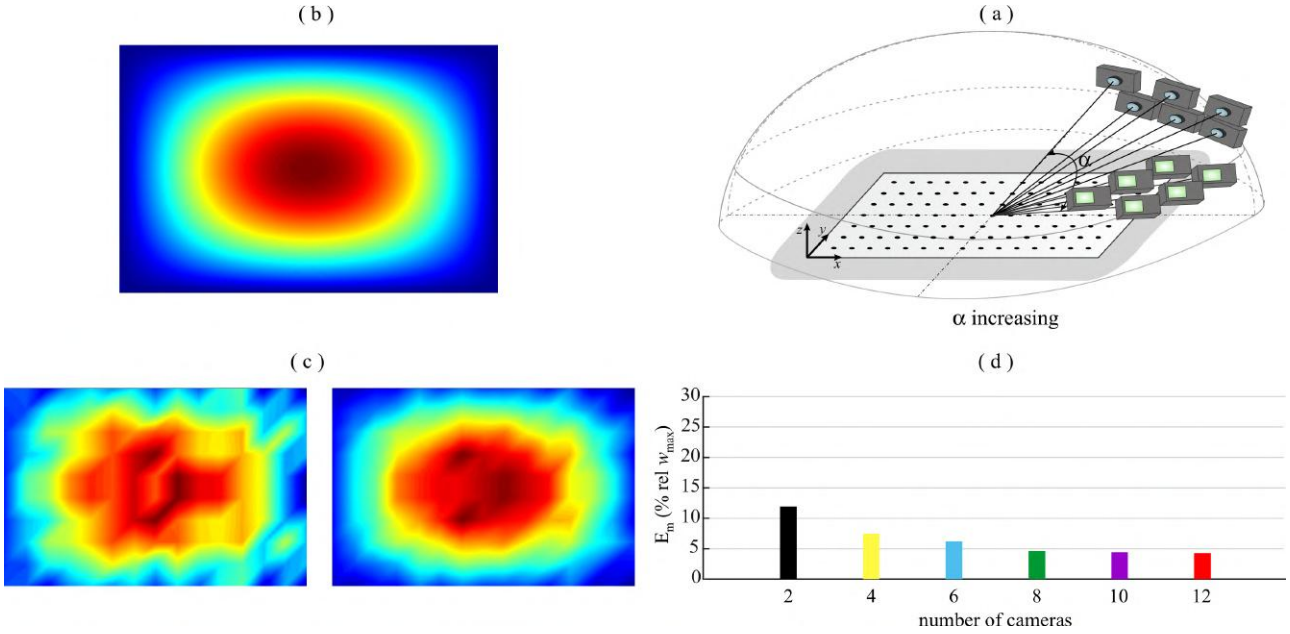

Figure 4.29: First deflection shape: (a) multiple cameras case study 4c; (b) ideal flexural deflection shape of the plate; (c) comparison between reconstructed flexural deflection shapes of the plate for the smallest (left) and largest (right) number of cameras; (d) histogram of the mean error.

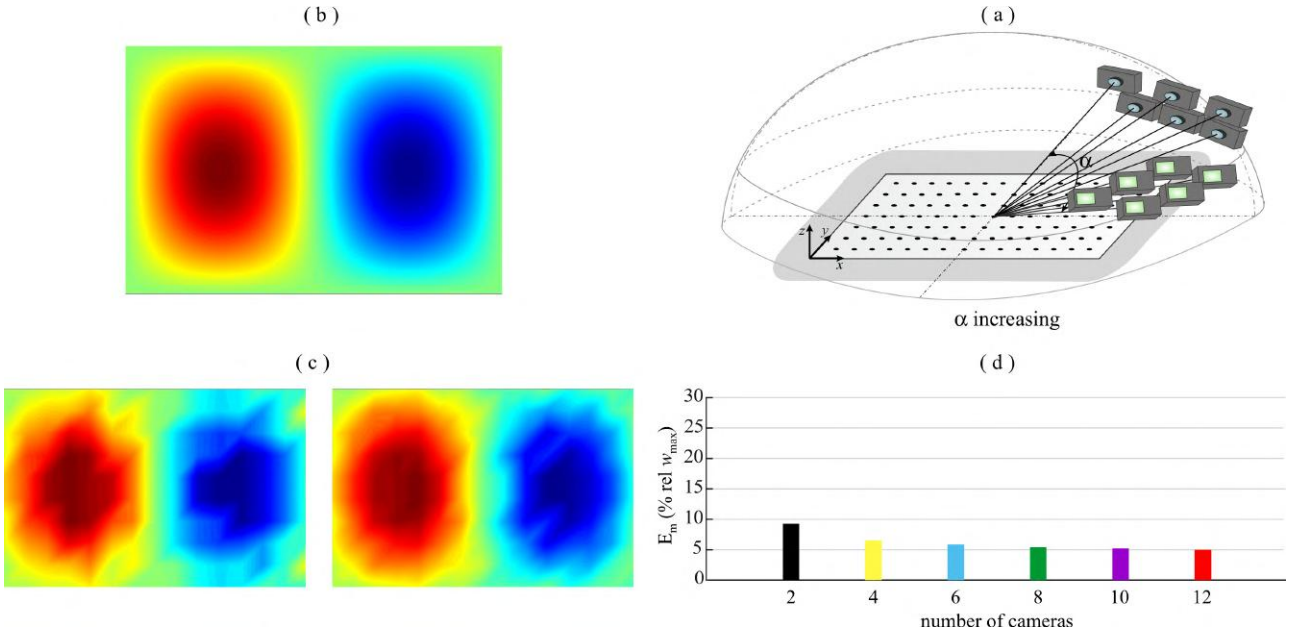

Figure 4.30: Second deflection shape: (a) multiple cameras case study 4c; (b) ideal flexural deflection shape of the plate; (c) comparison between reconstructed flexural deflection shapes of the plate for the smallest (left) and largest (right) number of cameras; (d) histogram of the mean error.

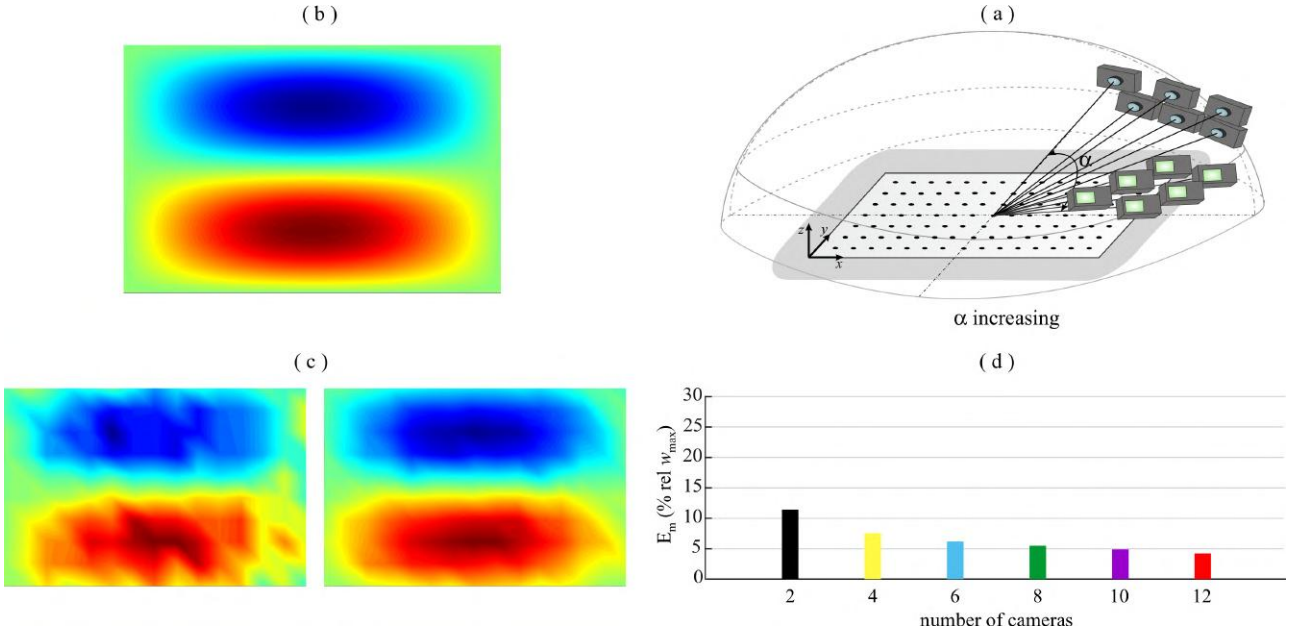

Figure 4.31: Third deflection shape: (a) multiple cameras case study 4c; (b) ideal flexural deflection shape of the plate; (c) comparison between reconstructed flexural deflection shapes of the plate for the smallest (left) and largest (right) number of cameras; (d) histogram of the mean error.

The results presented in Figs. 4.29 - 4.31 for Case 4c indicate that, as pairs of cameras with increasingly larger aperture angle are added, the accuracy of the measurement significantly increases in each of the three cases here considered. For instance, according to Plot (d) in Figs. 4.29 - 4.31, when the measurement setup passes from 2 cameras (1 pair) to 12 cameras (6 pairs) the average error of the measurement falls from about 10-12% to 4%.

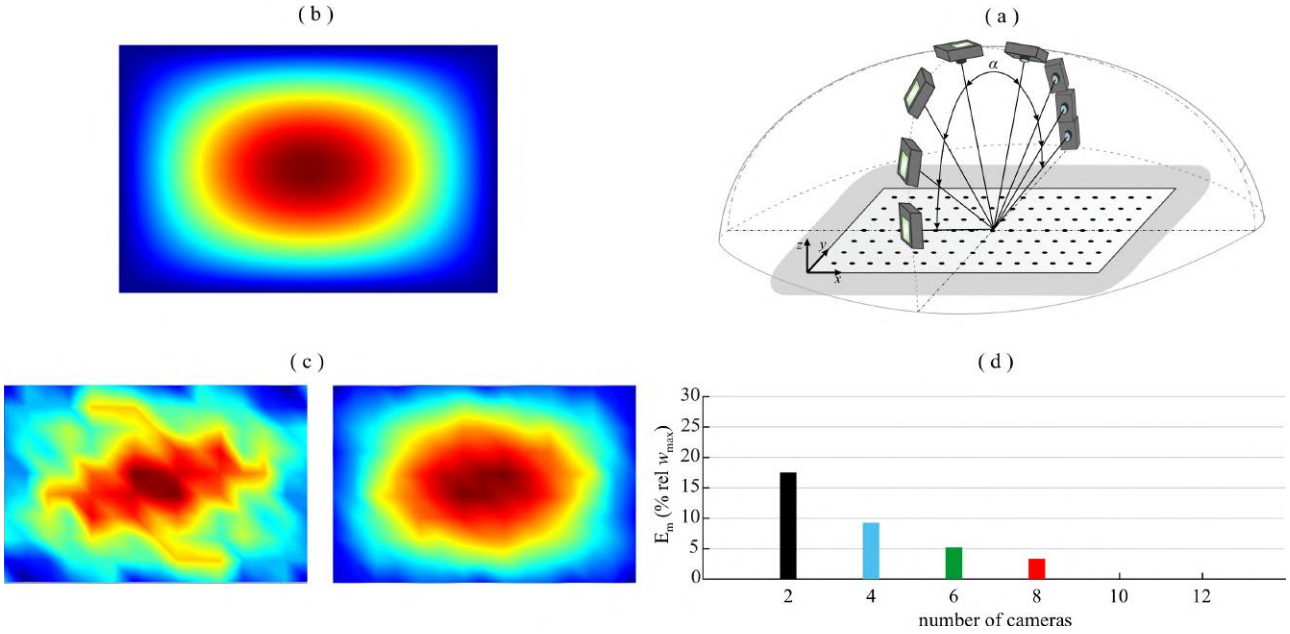

Figure 4.32: First deflection shape: (a) multiple cameras case study 4d; (b) ideal flexural deflection shape of the plate; (c) comparison between reconstructed flexural deflection shapes of the plate for the smallest (left) and largest (right) number of cameras; (d) histogram of the mean error.

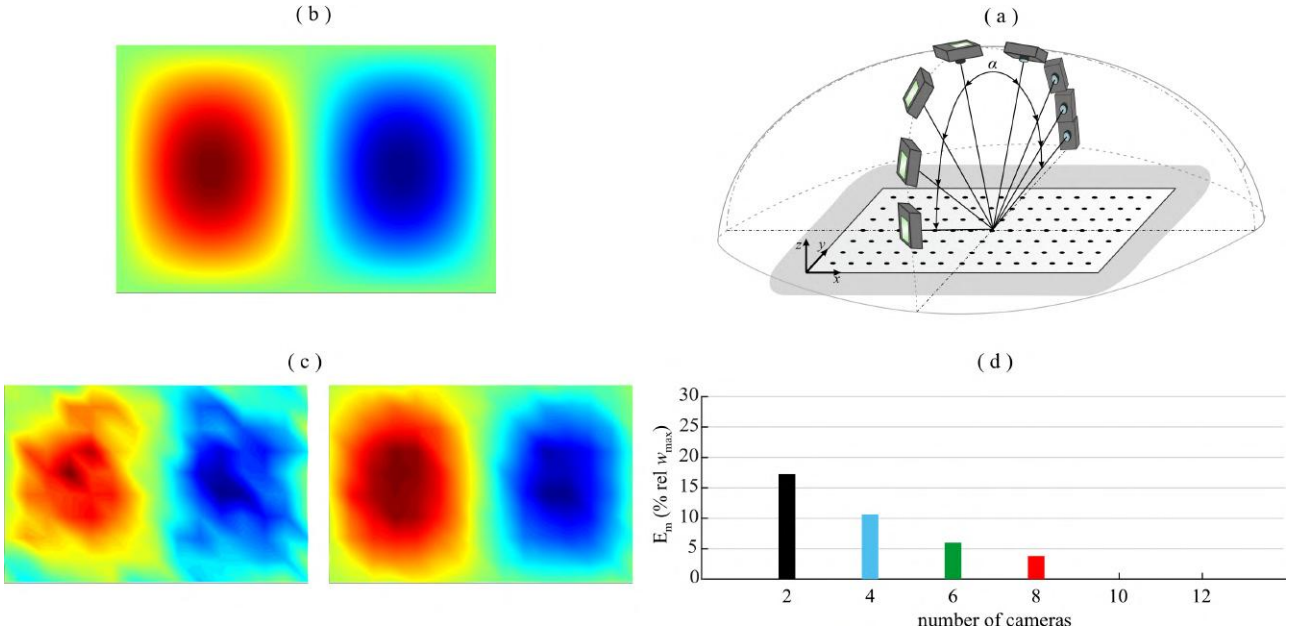

Figure 4.33: Second deflection shape: (a) multiple cameras case study 4d; (b) ideal flexural deflection shape of the plate; (c) comparison between reconstructed flexural deflection shapes of the plate for the smallest (left) and largest (right) number of cameras; (d) histogram of the mean error.

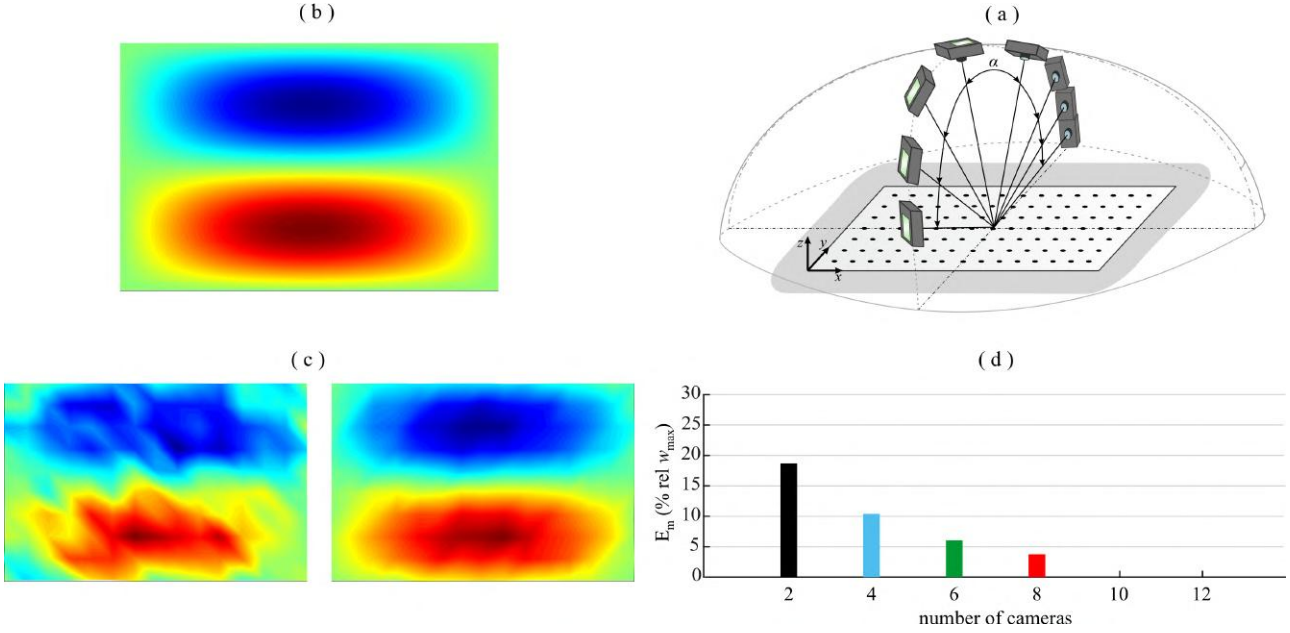

Figure 4.34: Third deflection shape: (a) multiple cameras case study 4d; (b) ideal flexural deflection shape of the plate; (c) comparison between reconstructed flexural deflection shapes of the plate for the smallest (left) and largest (right) number of cameras; (d) histogram of the mean error.

Finally, the results presented in Figs. 4.32 - 4.34 for Case 4d show that, as cameras with increasingly larger aperture angle are added, the accuracy of the measurement significantly increases. Indeed, Plot (d) of Figs. 4.32 - 4.34 indicates that, when the measurement setup passes from 2 cameras (1 pair) to 8 cameras (4 pairs), the average error of the measurement falls form about 17-18% to 3-4%.

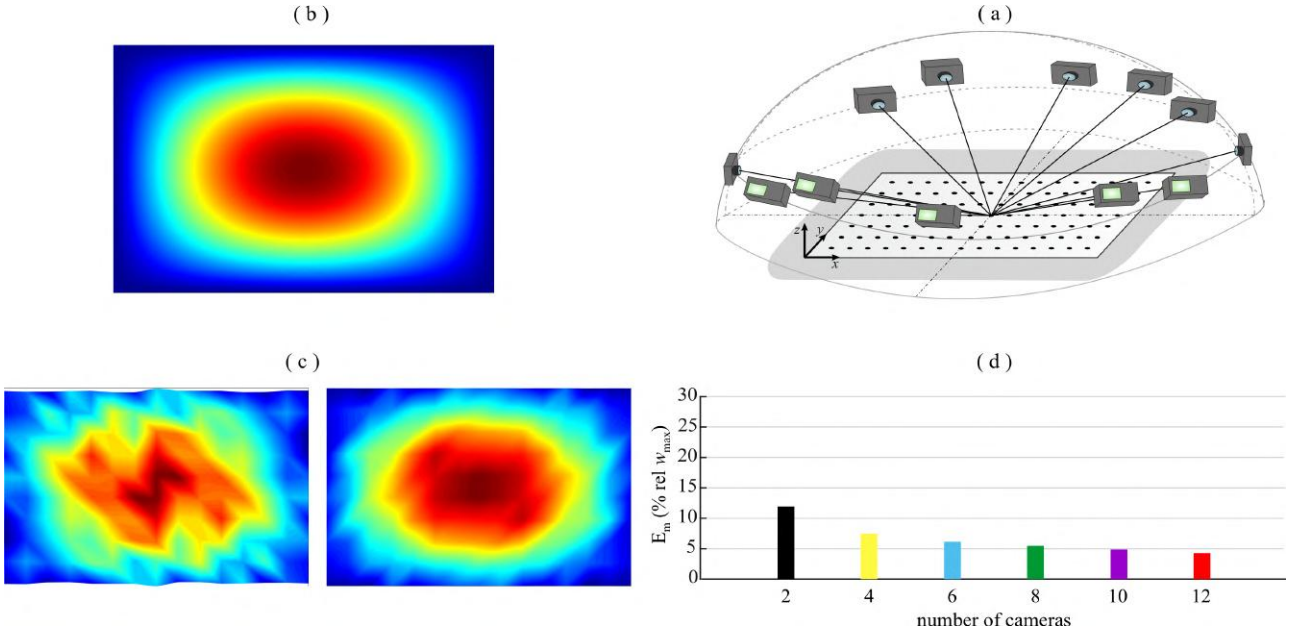

Figure 4.35: First deflection shape: (a) multiple cameras case study 4e; (b) ideal flexural deflection shape of the plate; (c) comparison between reconstructed flexural deflection shapes of the plate for the smallest (left) and largest (right) number of cameras; (d) histogram of the mean error.

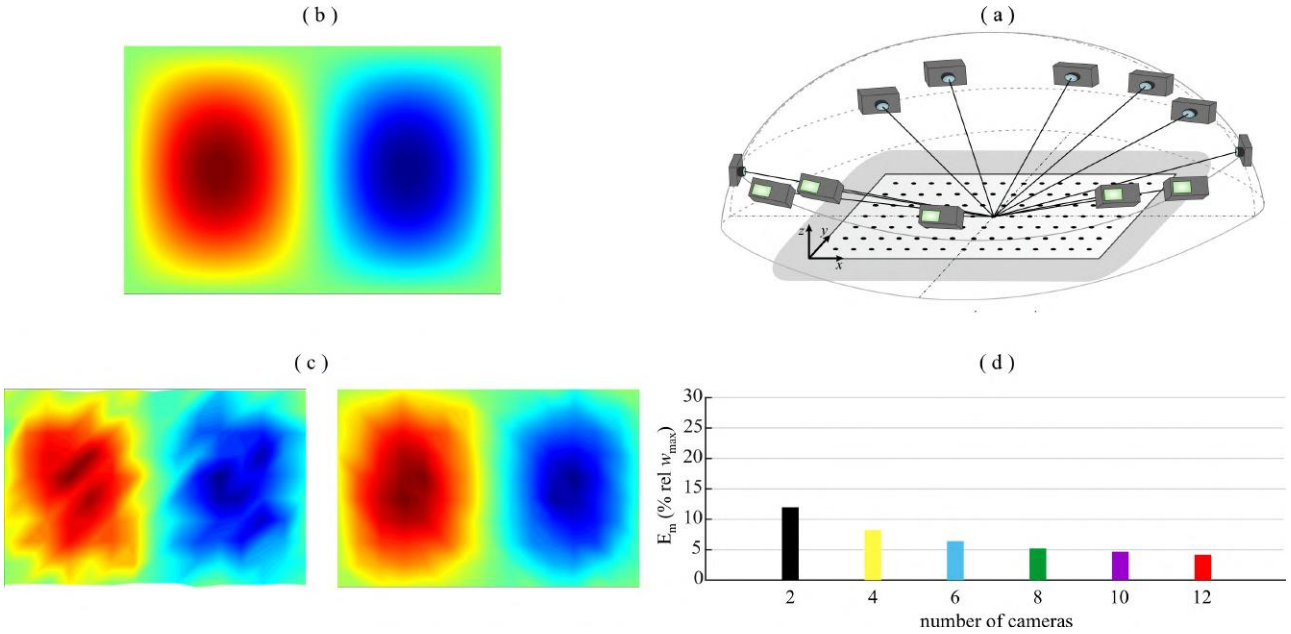

Figure 4.36: Second deflection shape: (a) multiple cameras case study 4e; (b) ideal flexural deflection shape of the plate; (c) comparison between reconstructed flexural deflection shapes of the plate for the smallest (left) and largest (right) number of cameras; (d) histogram of the mean error.

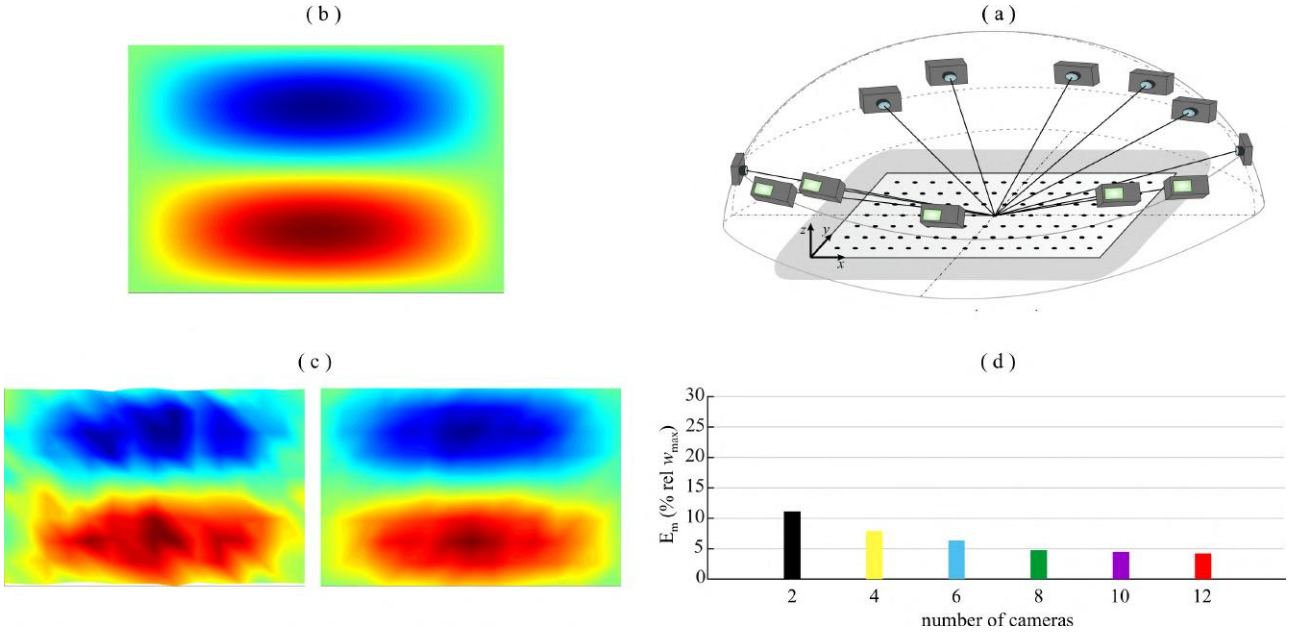

Figure 4.37: Third deflection shape: (a) multiple cameras case study 4e; (b) ideal flexural deflection shape of the plate; (c) comparison between reconstructed flexural deflection shapes of the plate for the smallest (left) and largest (right) number of cameras; (d) histogram of the mean error.

To conclude this analysis, the results for Case 4e are presented in Figs. 4.35 - 4.37, which consider the cameras disposed over a circumference around the plate. The results presented in Figs. 4.35 - 4.37 indicate that, as pairs of cameras are added over the circumference, the accuracy of the measurement significantly increases. For instance, considering the reconstruction of the first flexural deflection shape, Fig. 4.35 Plot (d) shows that, when the measurement setup passes from 2 cameras (1 pair) to 12 cameras (6 pairs), the average error of the measurement falls from 12% to 4%. In Fig. 4.36 the reconstruction of the second flexural deflection shape is considered. Also in this case, Plot (d) shows that the average error falls from 12% to 4% when the measurement setup passes from 2 cameras to 12 cameras. Finally, in Fig. 4.37 the reconstruction of the third flexural deflection shape is considered. In this case, Plot (d) shows that the average error goes from 11% to 4% when the measurement setup is composed by 6 pairs of cameras.

4.3 Concluding remarks

This chapter presented a simulation study focussed on the measurement of flexural vibration of a thin plate with multiple cameras. The study has considered a practical model problem composed by a plate excited by a tonal force at the first three fundamental resonance frequencies of the plate flexural vibration. The study has therefore considered the measurement of the plate deflection shapes at these frequencies, which accurately approximates the first three flexural mode shapes. As found for the measurement of flexural vibrations of a beam, the study showed that the accuracy of the measurement increases as:

1. the cameras are arranged closer to the plate;
2. the cameras are separated by large aperture angles;
3. the optical axis of the cameras impinges the structure with small elevation angles;
4. the resolution of the cameras is raised;
5. the number of cameras is increased.

The presented results are in accordance to those found for the beam in the previous chapter and confirm that increasing the number of cameras improves the quality of the displacement estimation.

Chapter 5

Experimental validation: a vibrating beam

In this chapter, the effectiveness of vibration measurements with multiple cameras is investigated experimentally. The study is divided in two parts. In the first part, the laboratory setup and the algorithms implemented for the experimental validation are described. The second part provides the results of the experiments. This chapter is divided in three sections. In Section 5.1, the laboratory test rig used for the experiment is first described, then the calibration technique and the tracking of the markers algorithm are described in detail. In Section 5.2, the results of the experimental tests employing cameras with increasing resolution or using by an increasing number of cameras are illustrated. Finally, Section 5.3 summarizes the most relevant conclusions of this chapter.

5.1 Experimental setup

The study is based on a rig composed by a cantilever beam, which replicates the model problem discussed in Section 3.1 of Chapter 3 and used to produce the simulation results presented in Section 3.3 of Chapter 3. The principal features of the cantilever beam and cameras setup assembled for this study are first introduced. The procedures used to calibrate the cameras and to track the line of 25 markers printed on the beam are then revised in detail. Also, the numerical implementation of the triangulation method to reconstruct the transverse displacements of the centre points defined by the markers is briefly discussed.

5.1.1 Test rig and cameras setup

In order to ease the comprehension of this chapter, some notions that have been introduced in Chapter 3, and that are used along this chapter, are briefly recalled. To start with, Fig. 5.1 reports the model problem, introduced in Section 3.1 of Chapter 3, which is composed by a cantilever thin beam made of

aluminium.

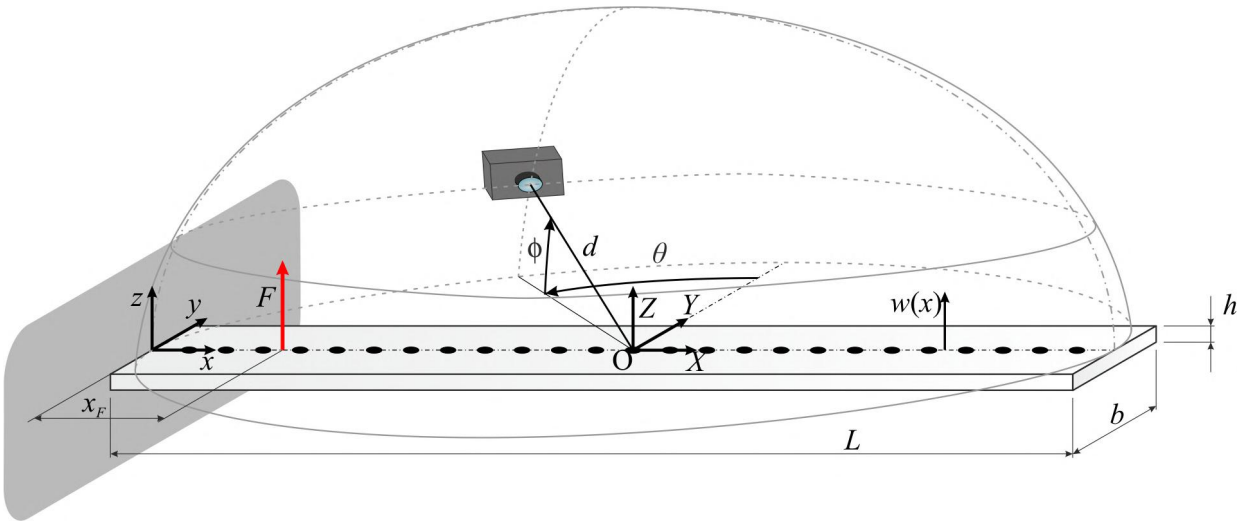

Figure 5.1: Model problem for the measurement of flexural vibration of a cantilever beam.

With respect to Fig. 5.1 two systems of reference were introduced:

a) the *beam system of reference* x, y, z which is located at the clamped end of the beam;

b) and the so-called *world system of reference* X, Y, Z which is located in the middle of the beam.

Finally, it is also recalled that the position of a camera is defined, as shown in Fig. 5.1, by spherical coordinates with respect to the world system of reference X, Y, Z i.e.:

a) the radial distance d;

b) the azimuthal angle θ;

c) the elevation angle ϕ.

Moving now to the experimental setup, Fig. 5.2 (a) and (b) show the test rig built for this study which is composed by a heavy rigid-frame base structure with a cantilever aluminium beam with the dimensions and physical properties given in Table 3.1, here recalled in Table 5.1, and by four cameras. Three lines of 25 markers are printed on the top side of the beam, although only the line printed along the longitudinal axis of the beam has been used in the measurements. The markers have diameter 5 mm and were evenly spaced along the beam with centre distances of 25 mm. The beam is excited in bending by a shaker located at position $x_F = 55$ mm. The shaker was connected to the beam via an impedance head, which was used to measure the point mobility frequency response function at the excitation position. The shaker was driven with a time-harmonic signal at the first fundamental resonance frequency for the flexural response of the beam, which occurred at $f = 4.25$ Hz. To avoid faults in the image post processing phase for the markers tracking, a rather large force excitation was implemented, which produced beam tip displacements of the order of ± 4 mm as in the simulation

results. Both the signal fed to the shaker and the signals measured by the impedance head were recorded and used in the post processing phase to identify the instant of time where the response of the beam, that is the deflection shape, was maximum.

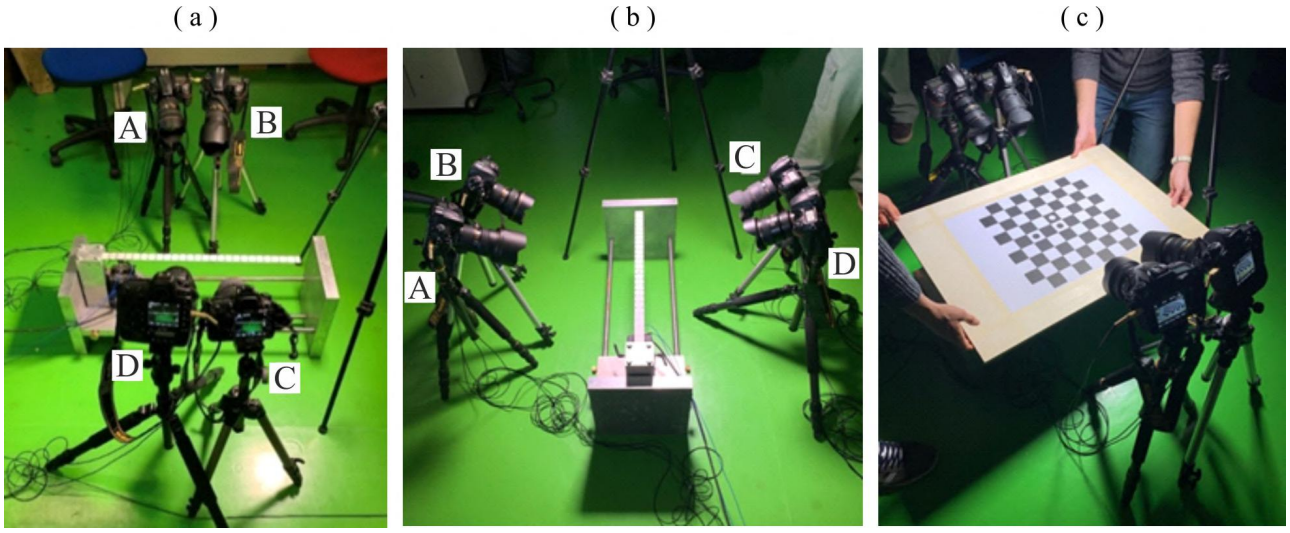

Figure 5.2: Lateral (a) and front (b) view of the experimental setup. Calibration of cameras (c).

As shown in Fig. 5.2 (a) and (b), four off-the-shelf cameras were arranged around the beam. To comply with the simulation study of Section 3.3 of Chapter 3, the cameras were arranged around the beam with the optical axes pointing to the center of the beam in correspondence of the world coordinate frame of reference X, Y, Z. More specifically, they were positioned at the same radial distance $d = 530$ mm from the world center O, with the same elevation angle $\phi = 22°$. Also, for practical reasons linked to the space occupied by the cameras, they were arranged in two pairs, at both lateral sides of the beam. The two couples of cameras were arranged in such a way as to have an aperture angle $\alpha = 20°$, thus with azimuthal angles $\theta = \pm 10°$. Four off the shelf cameras [1] were used, which, as summarized in Table 5.2, had similar, but not identical, characteristics. Nevertheless, they all guaranteed the minimum speed and spatial resolution necessary to carry out the test planned for this study.

5.1.2 Multi camera calibration and tracking of the markers

In this study the Sturm-Maybank-Zhang method [53], [59], was used to calibrate the cameras setup. As shown in Fig. 5.2 (c), a planar checkerboard pattern characterized by a 9×9 array of tiles having dimension 45×45 mm was used. This calibration target was displaced and rotated so that a sequence of shots of the entire checkerboard were taken at arbitrary positions and with arbitrary orientations. A total of 12 images was selected for the calibration post processing, which was implemented with the "Camera Calibration Toolbox for Matlab" [60], [61]. Further details about the "Camera Calibration Toolbox for Matlab" are discussed in Appendix D. The toolbox generated a calibration matrix (see definition in Eq. 3.10) for each snapshot and each camera. Therefore, a total of 12×4 projection matrices

[1] I would like to thank Dr. A. Zanarini for providing his personal photographic equipment.

Table 5.1: Physical properties of the beam.

Parameter	Value
Length	$L = 623$ mm
Width	$b = 30$ mm
Thickness	$h = 3$ mm
Density	$\rho = 2700$ kg/m^3
Young's modulus	$E = 6.9 \times 10^{10}$ n/m^2
Poisson ratio	$\nu = 0.31$
Modal damping ratio	$\xi = 0.02$
Position of the force	$x_F = 55$ mm

Table 5.2: Camera properties.

Camera	Frame rate [fps]	Resolution [pixel]	Distance d [mm]	Aperture angle α [°]	Azimuthal angle θ[°]	Elevation angle ϕ [°]
NIKON D5	60	1920×1080	570	20	10	22
NIKON D850	60	1920×1080	570	20	-10	22
NIKON D810	60	1920×1080	570	20	10	22
NIKON D600	60	1920×1080	570	20	-10	22

were obtained. To refine the interior and exterior parameters of the cameras (defined respectively by the elements of their matrices $\mathbf{K}$ and $[\mathbf{R}|\mathbf{t}]$) with respect to a unique world reference system, the *bundle adjustment method* [54], which is revised in detail in Appendix E, was employed. Similarly to the "re-projection" method discussed in Section 3.2.2, the resulting projection matrix is obtained from a minimisation process of the sum of the square distances between the $j-th$ reprojected point of the $i-th$ camera $\mathbf{m}^r_{i,j}$ and the measured point $\mathbf{m}^j_i$:

$$\chi(\mathbf{M}_j, \mathbf{P}_i) = \min \sum_{i=1}^{N} \sum_{j=1}^{n} ||\mathbf{m}^r_{i,j} - \mathbf{m}^j_i||^2. \tag{5.1}$$

Here, N and n are respectively the number of cameras and corners points of the checkerboard. As a result of this minimization procedure, four refined projection matrices were obtained for the cameras. As discussed in Section 3.2, these four matrices can be used to reconstruct the spatial position of the markers of the beam by means of the triangulation formulation discussed in Subsection 3.2.1. The software is written in Matlab, based on the "Computer Vision Toolkit" [62].

Although the cameras were triggered by a common remote command system, the video recordings showed a non-perfect synchronization. Nonetheless, this problem was suitably solved by synchronizing the cameras with the output signals from the impedance head mounted on the stinger of the shaker, which was acquired from the cameras audio input. More specifically, as anticipated above, the beam

was excited by a harmonic force at the fundamental resonance frequency of flexural vibrations, that is at 4 Hz. The excitation signal was recorded by the cameras via the audio input. During the post processing phase, the audio channel signals recorded by each camera were cross-correlated in order to estimate the time-delays between each camera acquisition. In fact, by aligning the peak of the cross-correlation it was possible to find the time Δt that elapsed between the start of the recording of each camera. This Δt was then converted in a number of frame N_{frame} by using Eq. 5.2:

$$N_{frame} = \Delta t \cdot fps \tag{5.2}$$

where fps represents the frame-rate of the cameras, i.e. 60 frame per second. Thus, once having established a reference camera, it was possible to synchronize the other cameras, with respect to the reference one. Since the estimated delays may not correspond to an integer number of frames, the synchronization accuracy is limited to 1/60 s, which is assumed to be acceptable for this test. The synchronized videos were then considered as a sequence of contiguous synchronized frames. Since the frame rate of the cameras is 60 fps, 15 images were extracted to detect one period of oscillation of the beam. The positions of the markers printed on the beam, were identified from each snapshot with the following three-steps procedure (the process of tracking of the markers is accurately described in Appendix F):

1. definition of the markers template and definition of the search region on the image;
2. removal of perspective distortion by applying an homography transformation [54], which simulates the image that would be captured by a camera with its optical axis perpendicular to the cantilever;
3. identification of the markers position via template matching, i.e. by correlation with a circular template. In fact, having removed perspective distortion, circular markers are indeed circles of known diameter in the images.

The positions of the measurement points were then defined as the centre positions of the markers. At this point the triangulation discussed in Subsection 3.2.1 was implemented to reconstruct the positions of the 25 markers for each frame. The displacements of the 25 points were then reconstructed for one period of the oscillations. The deflection shape of the beam was then straightforwardly reconstructed considering instant t' where the amplitude of the displacements is maximum.

5.2 Experimental results

In this section, the results obtained from the experimental test described previously in Section 5.1 are illustrated. The following two subsections show the measured deflection shapes with respect to two parameters: first, in Subsection 5.2.1, the resolution of the cameras and second, in Subsection 5.2.2,

the number of cameras. The inherent resolution of the four cameras is rather high. Therefore, a set of results with lower resolutions were generated by simply downsampling the recorded images. The results presented in this section are depicted with the same layout of the simulations in Figs. 3.4 - 3.39. Therefore, they encompass:

a) a picture of the measurement setup;

b) the reference deflection shape (grey line) and the measured deflection shapes (colored lines);

c) the point errors in % with respect to the maximum displacement of the beam (colored lines);

d) the average error in % with respect to the maximum displacement of the beam (colored lines).

5.2.1 Resolution

To start with, the reconstruction of the beam flexural deflection shape with different cameras resolutions was investigated. In real measurements, the resolution of the cameras affects both the calibration and the measurement. In fact, the former relies on the detection of the corners of the checkerboard whereas the latter is based on the detection of the markers of the beam. Thus, both depend on the accuracy of the detection of the positions of points, which, as shown in Subsection 3.3.3, is strictly connected to the resolution of the cameras. However, since the aim here is to provide experimental evidence for the simulation results presented in Section 3.3, the calibration has been performed with the highest resolution of the cameras only. This is possible because, according to Eq. 3.10, the camera projection matrix is obtained from the product of the calibration matrix $\mathbf{K}$, which is formed by intrinsic parameters of the camera, and the transformation matrix $\mathbf{G}$, which is formed by extrinsic parameters of the camera. The extrinsic parameters define the positions of the cameras and thus can be obtained by calibrating the setup at the maximum resolution of the cameras. Therefore, the transformation matrix $\mathbf{G}$ obtained from the high-resolution cameras can then be used to define the projection matrix of low-resolution cameras using Eq. 3.10. Instead, the calibration matrix $\mathbf{K}$ will vary depending on the cameras resolution adopted for each measurement. In fact, as seen in Eq. 3.12, this matrix depends on the k_u, k_v factors, which are the inverse of the width and height of the pixel footprint on the camera photosensors. Thus, the matrix $\mathbf{K}$ has to be calculated for every different resolution considered. Nevertheless, the resolution strongly affects the accuracy of the markers detection and thus, the tracking of the markers. Accordingly, the positions of the triangulated points and thus the reconstructed deflection shape for the flexural vibration of the beam at the fundamental resonance frequency, is less accurate as the resolution is set to lower values.

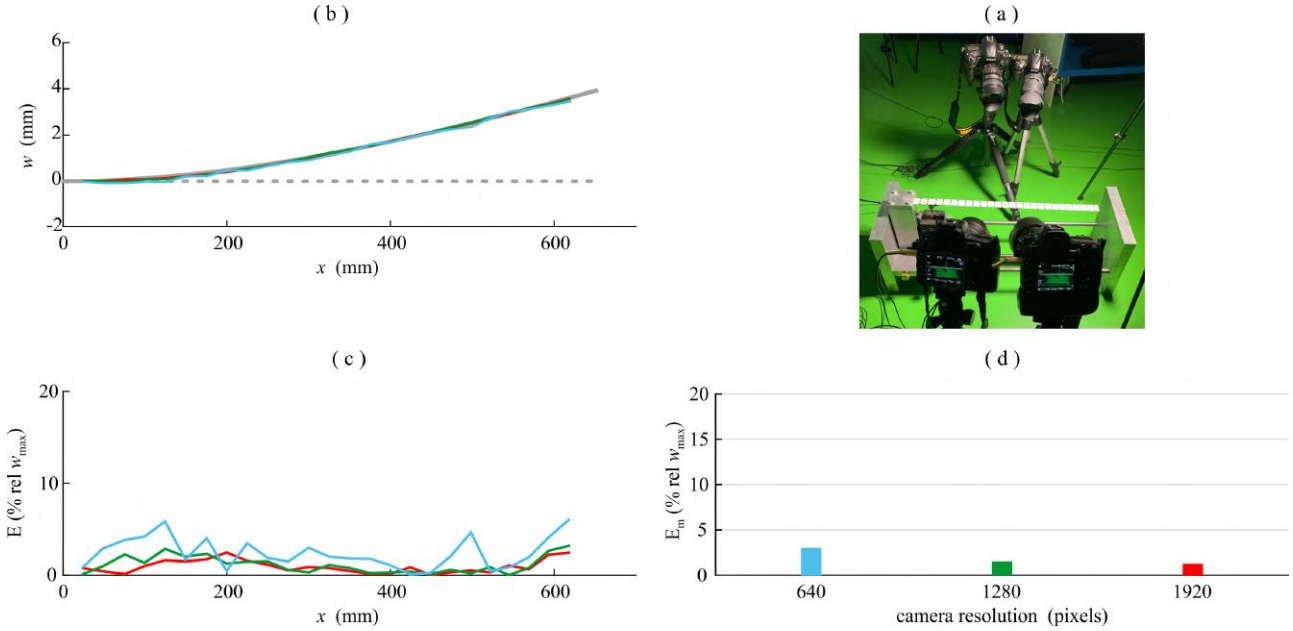

Figure 5.3: (a) resolution of cameras experimental case study; (b) comparison between reconstructed flexural deflection shapes of the beam (grey line reference shape); (c) percentage error calculated along the beam span; (d) histogram of the mean error. Colored lines reproduce the cases listed in the histogram.

Fig. 5.3 shows the deflection shapes measured considering three resolutions of the cameras: 640×360, 1280×720 and 1920×1080. The results confirm that the accuracy of the measurement increases as the resolution of the cameras is increased. For instance, when the number of pixels is raised from 640×360 to 1920×1080, the bar Plot (d) suggests that the average error of the measurement falls from 3% to 1.2%. Moreover, Plot (c) shows that the maximum measurement error for the 25 marker points falls from 6% to 3%. Thus, these results are in accordance with those seen in Subsection 3.3.3 in Chapter 3, where the simulation study on the influence of the resolution on the reconstruction of the deflection shapes of a cantilever beam highlighted an increase of the accuracy of the measurements as the resolution is increased. More specifically, the measurement results presented in Fig. 5.3 closely replicate the simulated ones shown in Fig. 3.19. As indicated in Table 3.3 - Case 3 and Table 5.2, in the experimental setup the cameras were arranged with a smaller elevation angle such that the experimental results presented in Fig. 5.3 are marginally better than the simulation results presented in Fig. 3.19.

5.2.2 Number of cameras

To conclude, the reconstruction of the beam flexural deflection shape with 2, 3 and 4 cameras is discussed. Three cases were considered where the triangulation was performed with the following cameras: first, cameras A-B; second, cameras A-B-C and third, cameras A-B-C-D. The results shown in Fig. 5.4 indicate that, when the triangulation is performed with an increasing number of cameras, the accuracy of the measurement increases. More specifically, when the setup moves from 2 to 4 cameras,

the bar Plot (d) suggests that the average error of the measurement falls from 4% to 1.2%. Moreover, Plot (c) shows that the maximum measurement error for the 25 marker points falls from 12% to 3%.

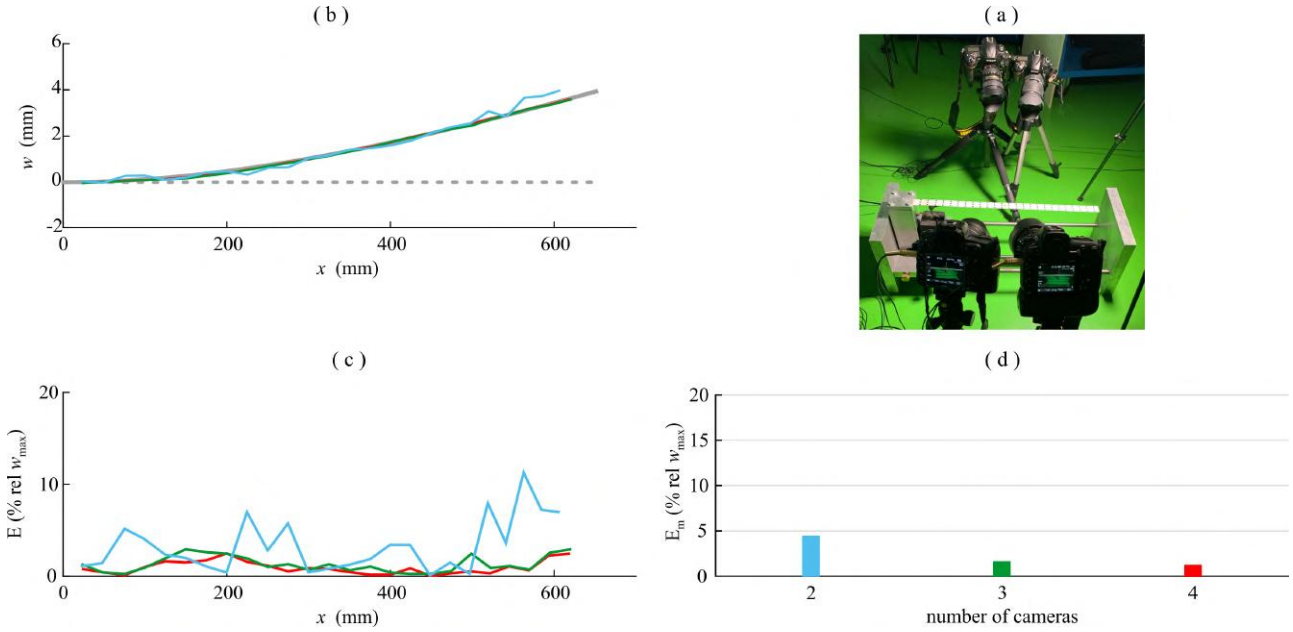

Figure 5.4: (a) multiple cameras experimental case study; (b) comparison between reconstructed flexural deflection shapes of the beam (grey line reference shape); (c) percentage error calculated along the beam span; (d) histogram of the mean error. Colored lines reproduce the cases listed in the histogram.

The experimental results presented in Fig. 5.4 are characterized by a comparatively higher accuracy than the corresponding simulation results presented in Fig. 3.22. This is due to the fact that, to guarantee a proper post processing of the images for the markers tracking, the measurements presented in Fig. 5.4 were carried out with the 1920×1080 pixels resolution whereas the simulations presented in Fig. 3.22 were obtained assuming a camera resolution of 1920×1080 pixels. Nevertheless, the experimental results confirmed the findings sprung up from the simulation study of Subsection 3.3.4 of Chapter 3, which showed how the accuracy of the measurement would significantly increase when more that two cameras are employed.

5.3 Concluding remarks

This chapter has presented an experimental study focussed on the measurement of flexural vibration of distributed structures with multiple cameras. The study has considered the model problem, introduced in Chapter 3, of a cantilever beam excited by a tonal force at the first fundamental resonance frequency of the beam flexural vibration.

Differently to the parametric studies seen in Section 3.3 of Chapter 3, in this chapter, only two variables were considered, that are the resolution of the cameras and the number of cameras. More specifically, the case study of varying resolution took in consideration three increasing values of resolution, i.e 640×360 pixels, 1280×720 pixels and 1920×1080 pixels, while the case with a resolution

of 320×180 pixels, which is contemplated in the parametric study of Subsection 3.3.3 of Chapter 3, was not reported here because the process of tracking the markers did not lead to satisfying results when this low resolution value was considered. On the other hand, the experimental study of the accuracy on reconstruction of the first deflection shape of the cantilever beam with a setup composed by an increasing number of cameras took into consideration a maximum of 4 cameras while the simulation study of Subsection 3.3.4 of Chapter 3 extended the analysis to a maximum of 12 cameras (or 8 depending on the disposition of the cameras, as seen in Subsection 3.3.4). Furthermore, the experimental results presented in Figs. 5.4 are characterized by a comparatively higher accuracy than the corresponding simulation results presented in Subsection 3.3.4 of Chapter 3. Nevertheless, despite these differences between the simulation and the experimental study, the results illustrated in Section 5.2 are in accordance with the findings of the parametric studies seen in Section 3.3 of Chapter 3. In fact, the experimental test showed that the accuracy of the measurement increases as:

1. the resolution of the cameras is raised;
2. the number of cameras is increased.

These considerations are in accordance with those seen in Section 3.4, which summarized the findings of the parametric studies of Section 3.3 of Chapter 3: overall, this study suggests that multiple cameras setups formed by more than two low-resolution and high frame-rate cameras could be effectively employed to measure flexural vibrations of distributed structures.

In conclusion it could be interesting to evaluate possible future extensions of this experimental study:

- it has been noticed that other parameters, such as the distance and the angle of aperture between the cameras, which were considered in the parametric studies of Section 3.3 of Chapter 3, could not be here considered because of practical reasons related to the lack of space in the laboratory. Thus, in the future, it could be interesting to experimentally investigate the influence of the parameters that could not be taken into account in this study;
- in Subection 5.2.2 of this chapter, the experimental study on the influence of the number of the cameras on the accuracy of the measurement took in consideration the combination of cameras A-B, A-B-C and A-B-C-D, defined in Fig. 5.2 (a) and (b). Thus, the study of different combination of cameras, such as A-C, A-D, A-C-D etc., could lead to new results about the relative contribution of each camera;
- considering again the case of a camera setup composed by an increasing number of cameras, the implementation of experimental setups composed by more than 4 cameras could be useful. In this way, the correspondence between the parametric and experimental studies considered in this thesis would be improved;

- as explained in Section 5.1, the cantilever beam considered in the experimental study presented three lines of markers attached on its surface. However, only the central line was considered in compliance with the parametric studies of Section 3.3 of Chapter 3. Thus, it could be interesting to complete the study of the accuracy of the measurement of the vibration of the beam by considering all the three lines of markers. This could bring information not only on the flexural vibration but also on the torsional vibration of the beam.

Chapter 6

Sound radiation estimate from vibration measurements with multiple cameras

This chapter is focused on the estimate of the sound radiation generated by flexural vibrations of thin structures, in particular the sound radiation emitted by flexural vibrations of thin plates. This study takes into account the same plate studied in Chapter 4. The chapter is structured in two parts. In the first part the main principles of sound radiation are revised. The second part provides parametric studies, similar to those presented in Section 3.3 of Chapter 3 and in Section 4.2 of Chapter 4, and is focused on the estimate of the sound radiation obtained from the plate flexural deflection shapes measured with multiple cameras. The chapter is organized in three sections. First, Section 6.1 presents the principles of sound radiation and the approach used to estimate the sound radiation emitted by a structure. According to Ref. [2], the acoustic field generated by a simple vibrating sphere in free space and delimited by a rigid baffle is first introduced. Then, the radiation of a vibrating plane surface, i.e. the plate, is derived with respect to the Rayleigh integral. The second part of the chapter, i.e. Section 6.2, presents a parametric study, which is aimed at understanding the influence that distance, angle of separation, resolution and number of cameras have on the estimate of the sound radiation starting from the reconstructed vibration field. Finally, in Section 6.3, the principal conclusions of this chapter are summarized.

6.1 Estimate of sound radiation

In this section, the main principles of sound radiation are briefly revised. In the first part, the acoustic pressure field generated by two elementary sources, such as a vibrating sphere and a point monopole, is studied. Then, the equations derived for this two simple sound radiators are employed to analyze the acoustic field produced by a more complex distributed structure, such as a plate. Finally, the Rayleigh's integral, which allows to estimate the sound radiation emitted by a distributed structure as

a summation of elementary sources, is introduced.

To start with, a vibrating surface in contact with a fluid is considered: this surface displaces fluid volume at the interface. Therefore, in order to estimate the sound radiated by a complex source, such as a plate, it is useful to firstly investigate the sound field generated by the fluid volume displacement produced by a small element of the vibrating surface. In this way, it is then possible to derive the total sound field generated by a distributed structure as the summation of the contributions of the small element (i.e. the so-called elementary radiators) that compose the structure. However, the principle of superposition can not be applied straightforwardly because the sound field generated by every elementary radiator strongly depends on the geometry of the whole structure of which the elementary surface is part of. Nevertheless, in many practical cases it is possible to apply simple theoretical expressions with reasonable accuracy.

In literature [2], the acoustic pressure in free field (i.e. without reflections) generated by a uniform, radial, harmonic pulsation of a sphere of equilibrium radius a at frequency ω is given by:

$$p(r,t) = \frac{1}{1+jka}\frac{j\omega\rho_0\widetilde{Q}}{4\pi r}e^{j[\omega t-k(r-a)]}. \tag{6.1}$$

Here k is the acoustic wavenumber, r is the radial distance from the centre of the sphere, $\widetilde{Q}$ is the complex amplitude of volume velocity of the source, $j\omega\widetilde{Q}$ is the complex amplitude of volume acceleration corresponding to the quantity dQ/dt, which is the so-called rate of change of volume flow [2]. The sphere is considered to have normal displacement of the surface ξ equal to $\widetilde{\xi}e^{j\omega t}$: thus, $\xi = \widetilde{\xi}e^{j\omega t}$. It is possible to notice that the volume acceleration equals the rate of change of the displacement of fluid volume, which leads to $j\omega\widetilde{Q} = -\omega^2 4\pi a^2\widetilde{\xi}$. Furthermore, the acceleration of the surface is the responsible of sound radiation [2]. Because of the symmetry of the spherical source here considered, the particle velocity vectors are oriented radially. In addition, it is considered the case in which the dimension of the sphere is little with respect to the acoustic wavelength, i.e. $ka \ll 1$. This case is known as *point monopole source*. If these conditions are complied, Eq. 6.1 becomes

$$p(r,t) = j\omega\rho_0\frac{\widetilde{Q}}{4\pi r}e^{j(\omega t-kr)}, \tag{6.2}$$

where $\rho_0\, d\widetilde{Q}/dt$ is the so called *monopole source strength*. The term $e^{-jkr}/4\pi r$ is known as the *free space Green's function*, which establishes the relation between the sound pressure in free field and the harmonic monopole source strength.

The case where a plate, similar to the one seen in the Chapter 4, is the vibrating source is now considered. The plate can be discretized in elementary radiators as illustrated in Fig. 6.1:

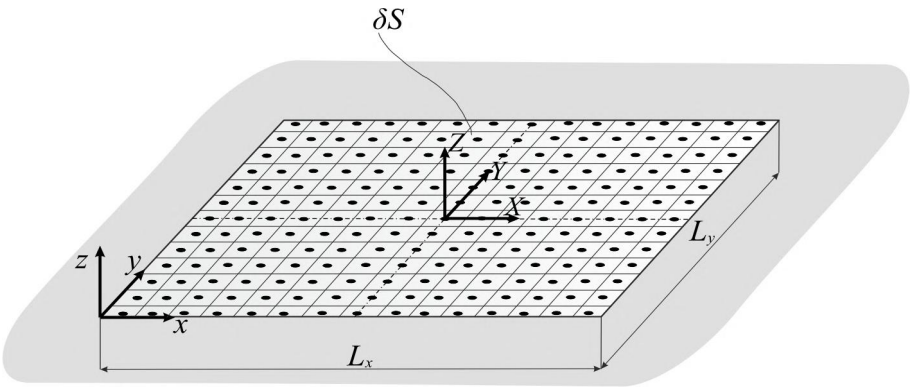

Figure 6.1: Plate divided in elementary radiators.

The considerations previously done upon the elementary sources, can be applied to the elementary radiators which compose the plate here considered. Each of the elementary surfaces in which the plate has been discretized can be seen as a sound radiator shaped as a vibrating piston as illustrated in Fig. 6.2. For acoustic wavelengths greater that the piston characteristic dimension, this vibrating piston can actually be seen as a half sphere delimited by a rigid baffle, whose sound radiation corresponds exactly to that of the sphere (because of symmetry) apart from a factor 2 due to the half surface of radiation.

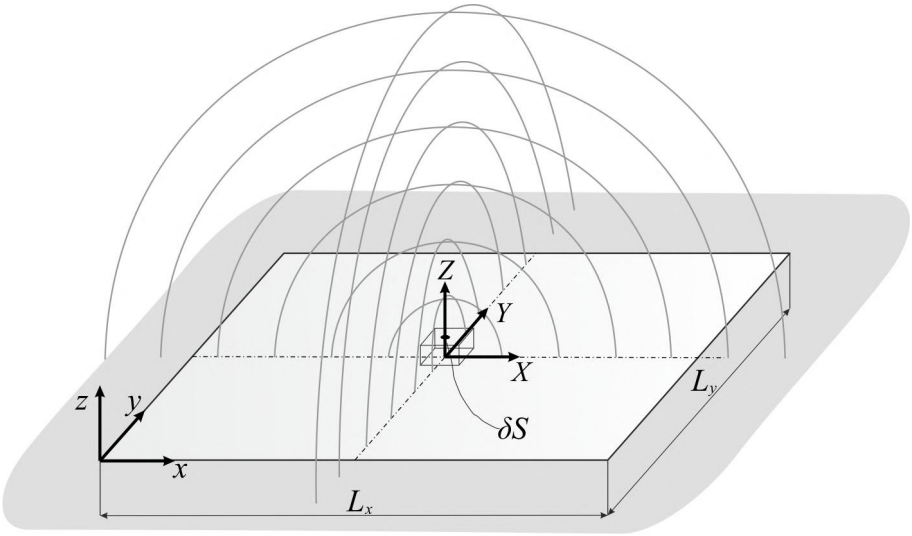

Figure 6.2: Single vibrating element of a plate.

The normal surface velocity of a small piston representing an elemental surface area δS of a plane vibrating surface is defined as $v_n(t)$. Thus, by defining $v_n(t) = \widetilde{v}_n e^{j\omega t}$, it is convenient to calculate the half of the complex amplitude of volume velocity of the source $\widetilde{Q}/2$: $\widetilde{Q}/2 = \widetilde{v}_n \delta S$. Therefore, Eq. 6.2 becomes [2]:

$$p(r,t) = j\omega\rho_0 \frac{2\widetilde{v}_n \delta S}{4\pi r} e^{j(\omega t - kr)}. \tag{6.3}$$

The assumption $\widetilde{Q} = 2\widetilde{v}_n \delta S$ implies that it is possible to consider the field produced by a small volume velocity source independent from the form of distribution of velocity over the source surface. This

consideration is valid when small sources are considered or when the point of observation of the acoustic field is considered to be far from the source region, provided the typical dimension d of the source region satisfies the condition $kd \ll 1$.

The acoustic field radiated by a plane surface can be calculated as the summation (or integral) of the contributions of every single elementary source in which the plate has been discretised. The resulting integral formulation was derived by Lord Rayleigh (1896) [2] as follows:

$$p(\mathbf{r}, t) = \frac{j\omega\rho_0}{2\pi} e^{j\omega t} \int_S \frac{\tilde{v}_n(\mathbf{r}_s) e^{-jkR}}{R} dS. \tag{6.4}$$

Here, $\mathbf{r}$ is the position vector of the observation point, $\mathbf{r}_s$ is the position vector of the elemental surface δS having normal velocity amplitude $\widetilde{v}_n(\mathbf{r}_s)$ and R is the magnitude of the vector $\mathbf{r} - \mathbf{r}_s$: $R = |\mathbf{r} - \mathbf{r}_s|$.

The case shown in Fig. 6.1, where a baffled plate is divided into a grid of R square elements, can now be derived. The transverse vibrations of the elements forming the vibrating surface can be specified in terms of the velocities v_{er} calculated in correspondence of their centre positions, which are identified by the positions of the markers in the structure [2]. If a harmonic motion is considered, the overall vibration of the plate can be characterized by the following column vector of complex amplitudes:

$$\{\tilde{\mathbf{v}}_e\} = \begin{bmatrix} \tilde{v}_{e1} & \tilde{v}_{e2} & \dots & \tilde{v}_{eR} \end{bmatrix}^T. \tag{6.5}$$

The same considerations can be applied to the sound pressure, whose amplitudes of each r-th element can be grouped into a column vector, as

$$\{\tilde{\mathbf{p}}_e\} = \begin{bmatrix} \tilde{p}_{e1} & \tilde{p}_{e2} & \dots & \tilde{p}_{eR} \end{bmatrix}^T. \tag{6.6}$$

The space that surrounds the emitting structure can be in turn discretized in elementary space elements as illustrated in Fig. 6.3. For simplicity only the XZ plane is considered:

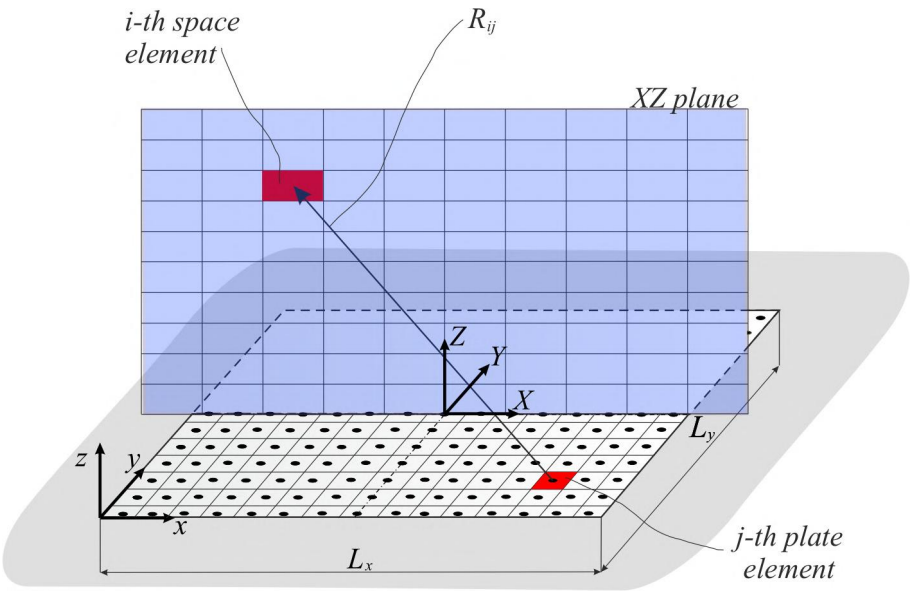

Figure 6.3: Discretization of the space surrounding the plate.

Thus, in the hypothesis that the dimensions of each elementary component of the plate are small with respect to the acoustic wavelength, so that $A_e \ll \lambda$ (where λ is the acoustic wavelength), the pressure on each i-th element of the surrounding space is calculated as the summation of the contribution of pressure generated by the vibration of each j-th element of the plate. Therefore, Eq. 6.4, can be rewritten as [2]:

$$\tilde{p}_{ei}(x_i, z_i) = \sum_{j=1}^{R} \frac{j\omega\rho_0 A_e \, e^{jkR_{ij}}}{2\pi R_{ij}} \tilde{v}_{ej}(x_j, z_j), \tag{6.7}$$

where A_e are the areas of each element of the plate and R_{ij} the distance between the centres of the i-th space element and the j-th plate element.

6.2 Parametric studies

The aim of this section is to investigate if the flexural deflection shapes measured with cameras can be used to estimate the sound radiation. In particular, in this section, the same geometry and characteristics of cameras, as those seen in Section 4.2, are employed, in order to analyze how the estimate of the sound radiation is affected by the reconstruction of the flexural response of a plate which, as seen in Section 4.2, is dependent from the camera setups. Thus, the geometries, i.e. their positions and numbers, and the type of cameras, i.e. their resolutions, considered in this parametric study are the same as those of Tables 4.3 and 4.4 and are here recalled in Tables 6.1 and 6.2.

The flexural response of the plate measured with cameras is used to estimate the sound radiation. More precisely, the analysis of this section considers the estimate of the sound radiation obtained from the measurement of the first three flexural deflection shapes of the plate at the first three fundamental resonance frequencies. The reference acoustic fields were derived from the implementation of Eq. 4.7

and Eq. 6.4 (or Eq. 6.7). In other words, the reference sound radiation, for each deflection shape, is obtained from the sound radiation generated by the flexural deflection shape of the plate, calculated with the mathematical model of Eq. 4.7 with $F_0(\omega) = 1$ N and $t = \pi/\omega$. Also, the sound radiation for each deflection shape, was simulated using again Eq. 6.4 (or Eq. 6.7) with respect to the displacements at the center of the elementary elements detected with the cameras in which the plate has been discretized.

This section presents a thorough parametric study to assess how the following parameters influence the estimate of the sound radiation:

1. the distance d of the cameras from the test structure;
2. the angle of aperture α between the cameras;
3. the resolution of the cameras;
4. the disposition and number of cameras.

For simplicity, the sound radiation will be studied over the XZ plane and over the YZ plane as illustrated in Fig. 6.4:

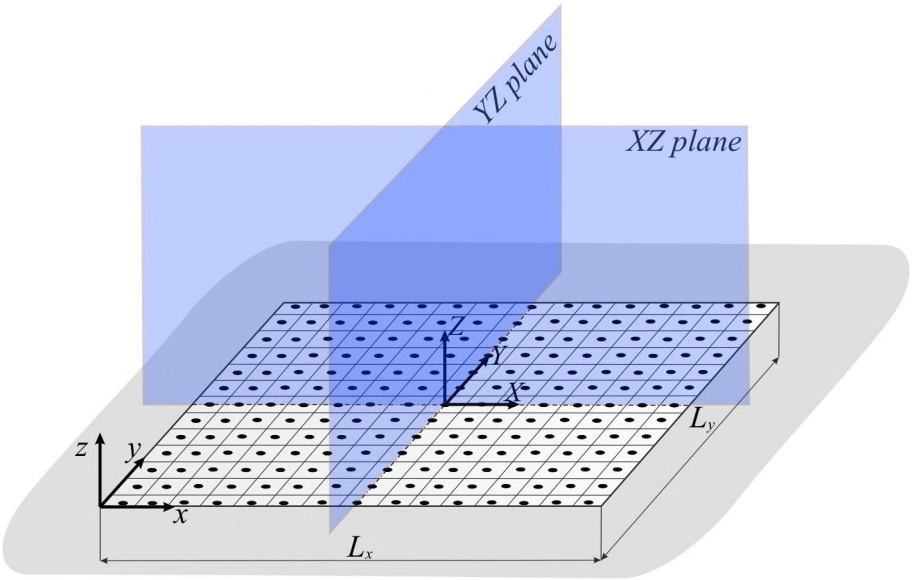

Figure 6.4: Definition of the planes XZ and YZ on which the sound radiation has been calculated.

These planes are discretized in 149 × 99 elements, so that the accuracy of the estimate of the sound radiation is analyzed with respect to the average error given by the root mean square error over all the 149 × 99 measurement points:

$$E_m = \frac{\sqrt{\frac{1}{149 \times 99} \sum_{i=1}^{149 \times 99} (p_i - p_{r,i})^2}}{p_{max}} 100 \text{ (\% rel. to } p_{max}). \tag{6.8}$$

Here, p_i is the acoustic pressure on the i-th space element, i.e. over the i-th element of the XZ plane or the YZ plane, obtained with Eq. 6.4 (or Eq. 6.7) from the vibration of the plate reconstructed by the cameras setup, whereas $p_{r,i}$ is the acoustic pressure on the i-th space element, i.e. over the i-th element of the XZ plane or the YZ plane, again calculated with Eq. 6.4 (or Eq. 6.7) and generated by the vibration of the plate calculated with the mathematical model given by Eq. 4.7. Also, p_{max} is the maximum reference acoustic pressure given by the vibration of the plate calculated again with Eq. 4.7.

The following subsections will illustrate how the four parameters listed above influence the estimate of the sound radiation due to the first three flexural deflection shapes of the plate. The simulation results are reported in a standard framework, which shows:

a) a sketch of the measurement setup with highlighted the varied parameter;

b) comparison between ideal and reconstructed acoustic field on the XZ and YZ planes: for clarity, only the best and worst cases are shown;

c) the average error in % with respect to the maximum acoustic pressure value. The histogram of the average error is composed by two bars for each value assumed by the varied parameter: the bar on the left refers to the average error calculated over the XZ plane while the bar on the right refers to the average error calculated over the YZ plane.

It is important to notice that the acoustic field radiated by the plate strongly depends on the shape of the flexural deflection. In particular, as seen in Section 4.2, the first deflection shape is characterized by a bell-shape while the second and the third deflection shapes are characterized by bipole bell-shapes oriented along the x and along the y directions respectively. These modes generate respectively a monopole-like or a bipole-like sound radiation fields. More specifically, the second flexural deflection shape is characterized by a bi-polar behavior along the x direction which generates an acoustic field composed by two poles of opposite sign over the XZ plane whereas the YZ plane, which is positioned over the modal line, is characterized by an approximately zero acoustic pressure. On the other hand, the third flexural deflection shape is characterized by a bi-polar sound radiation along the y direction, which generates an acoustic field composed by two poles of opposite sign over the YZ plane whereas the XZ plane, which, in this case, is the plane positioned over the modal line, is characterized by an approximately zero acoustic pressure. As it will be seen in the next subsections, these distributions of acoustic radiation affect the distribution of the average error. For instance, the average error of the estimated acoustic radiation obtained from the first deflection shape, presents comparable values in both the XZ and YZ planes, due to the monopole nature of the distribution of the sound pressure associated to this particular deflection shape. However, the acoustic pressure fields obtained when the second and the third deflection shapes are considered, present significantly different average errors over the XZ and the YZ planes due to the nature of their sound radiation distribution, which are characterized by

dipole geometries along a specific direction. More precisely, when the acoustic radiation obtained from the second flexural deflection shape is considered, the average error over the XZ plane are comparable to the ones obtained for the acoustic radiation obtained from the first flexural deflection shape. In contrast, the relative error over the YZ plane assumes very high values. In fact, in Eq. 6.8, the difference $(p_i - p_{r,i}) \neq 0$ while $p_{max} \approx 0$ over the YZ plane. Similarly, the acoustic radiation obtained from the third flexural deflection shape is characterized by average errors over the YZ plane comparable to the ones obtained for the acoustic radiation of the first flexural deflection shape. Alternatively, the values of the relative error over the XZ plane assume very high values. Here, in Eq. 6.8, the difference $(p_i - p_{r,i}) \neq 0$ while $p_{max} \approx 0$ over the XZ plane.

For these reasons, in the next sections, the average errors are discussed for the planes in which the values can be compared, that is: over both the XZ and the YZ planes when the acoustic field is obtained from the first flexural deflection shape, over the XZ plane only when the acoustic field is obtained from the second flexural deflection shape and over the YZ plane only when the acoustic field is obtained from the third flexural deflection shape.

Table 6.1: Positions and resolutions of pairs of cameras ($^*k = 0, 1$).

Cases	Radial distance d [mm]	Aperture angle α [°]	Azimuthal angle θ [°]	Elevation angle ϕ [°]	Resolution [pixel]
1 (Figs. 6.5 - 6.7)	650 750 1000 1500	60	±30	25	320×180
2a (Figs. 6.8 - 6.10)	750	16 60 110 160	± 8 ± 30 ± 55 ± 80	10	320×180
2b (Figs. 6.11 - 6.13)	750	170 140 100 60	±90	5 20 40 60	320×180
2c (Figs. 6.14 - 6.16)	750	16 60 110 160	-90 ± 8 -90 ± 30 -90 ± 55 -90 ± 80	10	320×180
2d (Figs. 6.17 - 6.19)	750	170 140 100 60	k180*	5 20 40 60	320×180
3 (Figs. 6.20 - 6.22)	750	60	±30	25	320×180 640×360 1280×720 1920×1080

Table 6.2: Positions and resolutions of multiple cameras setups ($^*k = 0, 1$).

Cases	Radial distance d [mm]	Azimuthal angle θ [°]	Elevation angle ϕ [°]	Resolution [pixel]
4a (Figs. 6.23 - 6.25)	750	± 7 ±7/±14 ±7/±14/±27 ±7/±14/±27/±30 ±7/±14/±27/±30/±47 ±7/±14/±27/±30/±47/±50	15 15/15 15/15/15 15/15/15/5 15/15/15/5/5 15/15/15/5/5/5	320×180
4a′ (Figs. 6.26 - 6.28)	750	±50 ±50/±47 ±50/±47/±30 ±50/±47/±30/±27 ±50/±47/±30/±27/±14 ±50/±47/±30/±27/±14/±7	15 15/15 15/15/15 15/15/15/5 15/15/15/5/5 15/15/15/5/5/5	320×180
4b (Figs. 6.29 - 6.31)	750	±90 ±90/±90 ±90/±90/±90 ±90/±90/±90/±90	8 8/28 8/28/48 8/28/48/58	320×180
4c (Figs. 6.32 - 6.34)	750	-90 (± 7) -90 (±7/±14) -90 (±7/±14/±27) -90 (±7/±14/±27/±30) -90 (±7/±14/±27/±30/±47) -90 (±7/±14/±27/±30/±47/±50)	15 15/15 15/15/15 15/15/15/5 15/15/15/5/5 15/15/15/5/5/5	320×180
4d (Figs. 6.35 - 6.37)	750	k180* k180*/k180* k180*/k180*/k180* k180*/k180*/k180*/k180*	8 8/28 8/28/48 8/28/48/58	320×180
4e (Figs. 6.38 - 6.40)	750	k180*+7 k180*+(7/27) k180*+(7/27/0) k180*+(7/27/0/90) k180*+(7/27/0/90/47) k180*+(7/27/0/90/47/60)	15 15/15 15/15/15 15/15/15/5 15/15/15/5/5 15/15/15/5/5/5	320×180

6.2.1 Distance d of cameras from the plate

In this subsection, the accuracy of the estimate of the acoustic radiation obtained from the reconstruction of a plate first three flexural deflection shapes with a pair of cameras positioned at increasingly larger distance d from the middle point of the plate is considered. The azimuthal θ and elevation ϕ angles are fixed. The geometries and resolution of the cameras are summarized in Table 6.1 - Case 1.

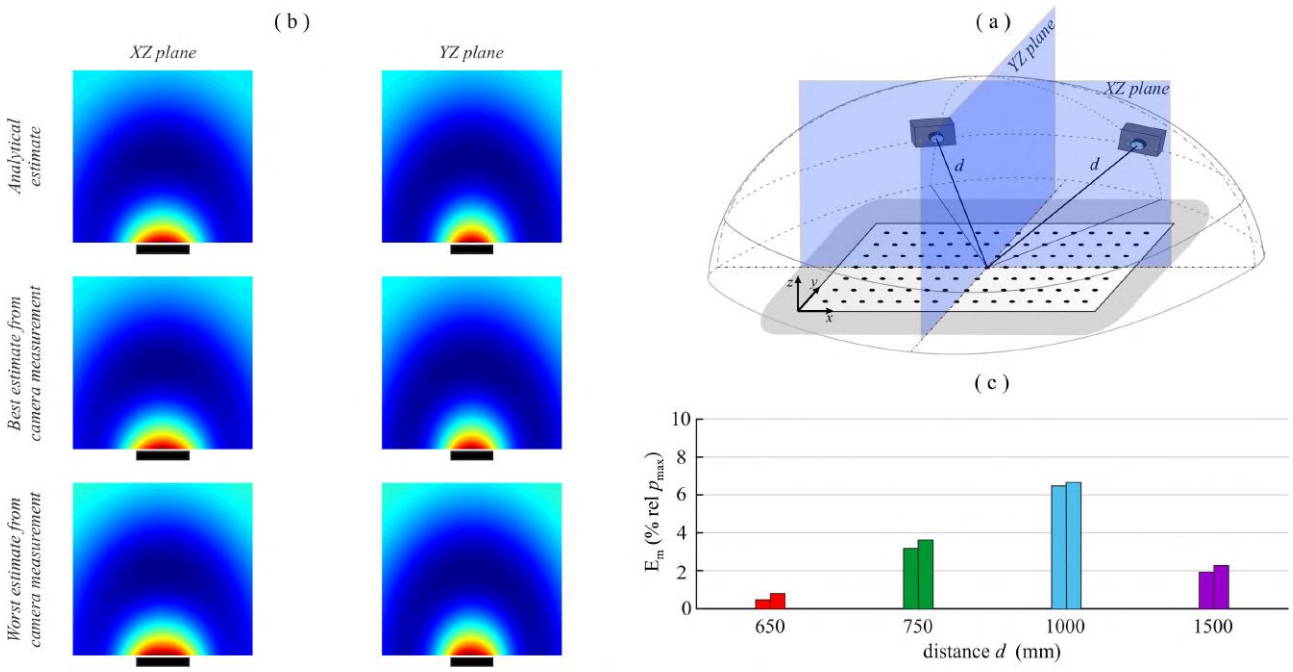

Figure 6.5: First deflection shape: (a) distance case study 1; (b) comparison between ideal (i.e. from analytical model), best and worst case (i.e. from best and worst reconstructed flexural vibration with cameras setup) acoustic fields; (c) histogram of the mean error.

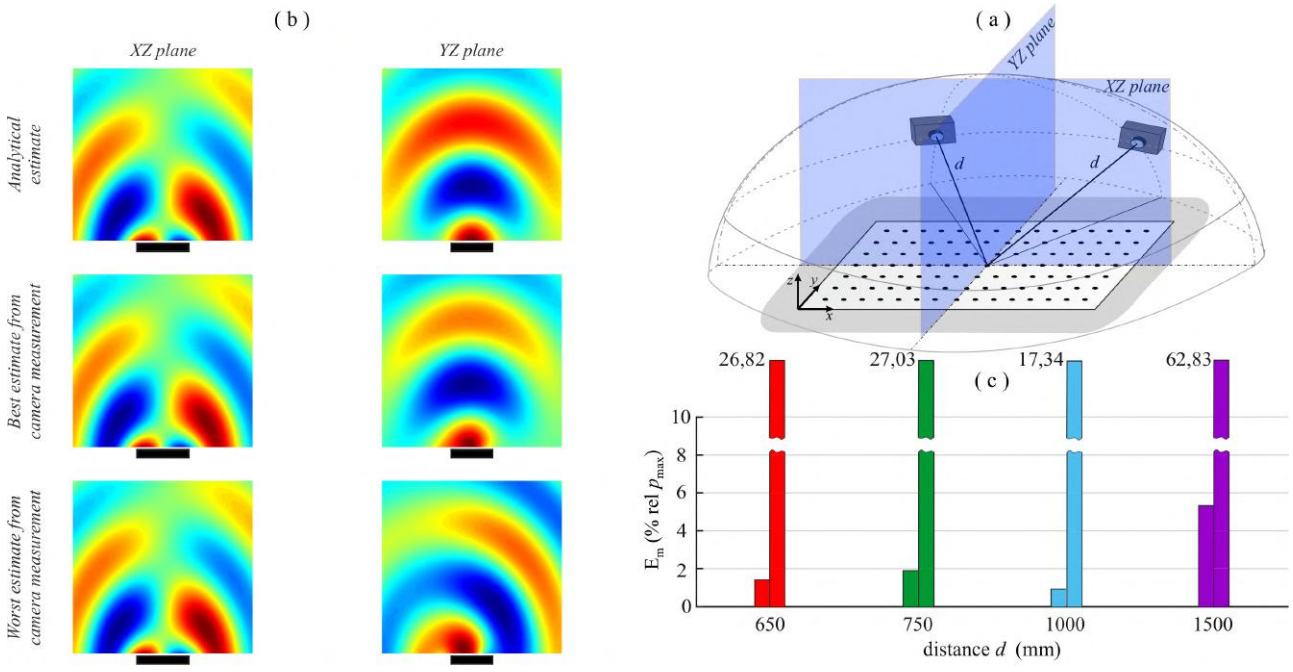

Figure 6.6: Second deflection shape: (a) distance case study 1; (b) comparison between ideal (i.e. from analytical model), best and worst case (i.e. from best and worst reconstructed flexural vibration with cameras setup) acoustic fields; (c) histogram of the mean error.

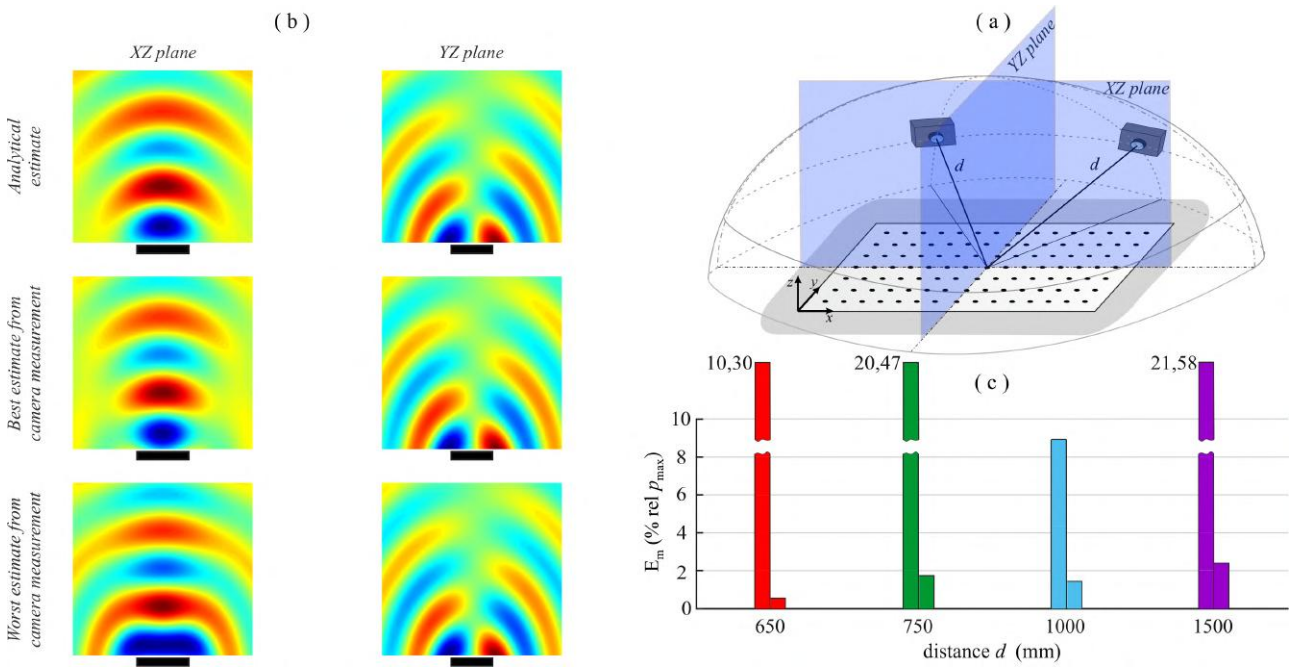

Figure 6.7: Third deflection shape: (a) distance case study 1; (b) comparison between ideal (i.e. from analytical model), best and worst case (i.e. from best and worst reconstructed flexural vibration with cameras setup) acoustic fields; (c) histogram of the mean error.

The results presented in Figs. 6.5 - 6.7 denote that the accuracy of the estimate of the acoustic radiation obtained from reconstruction of the first three flexural deflection shapes of the plate does not follow a specific trend when the distance of the cameras from the centre of the plate is increased. This result is in contrast with the findings of Figs. 4.2 - 4.4 for the accuracy of reconstruction of the plate flexural deflection shapes. For instance, according to the bar Plot (c) in Fig. 6.5, which gives the estimate of the acoustic field obtained from the reconstruction of the first flexural deflection shape, the average error grows, for both the XZ and YZ plane, from less than 1% to about 7% when the distance of the cameras is increased from 650 to 1000 mm then falls to about 2% for a 1500 mm distance. The bar Plot (c) of Fig. 6.6, which gives the estimate of the acoustic field obtained from the reconstruction of the second flexural deflection shape, shows that the average error over the XZ plane is always less than 2% when the distance of the cameras is increased from 650 to 1000 mm and raises to over 5% for a 1500 mm distance. Similarly the bar Plot (c) of 6.7 shows that, when the acoustic field obtained from the reconstruction of the third flexural deflection shape is considered, the average error over the YZ plane is always less than 2% when the distance of the cameras is increased from 650 to 1000 mm whereas grows over 2% for a 1500 mm distance. A discussion on these results and on a similar behavior found with respect to the variation of other parameters, is postponed to Section 6.3.

6.2.2 Aperture angle α between cameras

The accuracy of the estimate of the acoustic radiation obtained from the reconstructed first three flexural deflection shapes of a plate when a pair of cameras is arranged with fixed azimuthal distance d

from the middle point of the plate and increasingly larger aperture angle α between the two cameras is here examined. The same four cases of Section 4.2.2 are considered. To start with, the first two configurations are considered. In Case 2a, the cameras are arranged over an arc of a circle, which is oriented parallel to the plane of the plate and aligned parallel to the x axis of the plate. In this case, the varied parameter is the azimuthal angle θ and thus, as reported in Table 6.1 - Case 2a, the angle of aperture between the cameras α, as $\theta = \pm\alpha/2$. In Case 2b, the cameras are arranged over an arc of a circle, which is oriented orthogonal to the plane of the plate, which is parallel to the x axis of the plate and passes through the center of the plate. Therefore, in this case the elevation ϕ angle of the cameras is varied to generate the increasing aperture angle α as summarized in Table 6.1 - Case 2b.

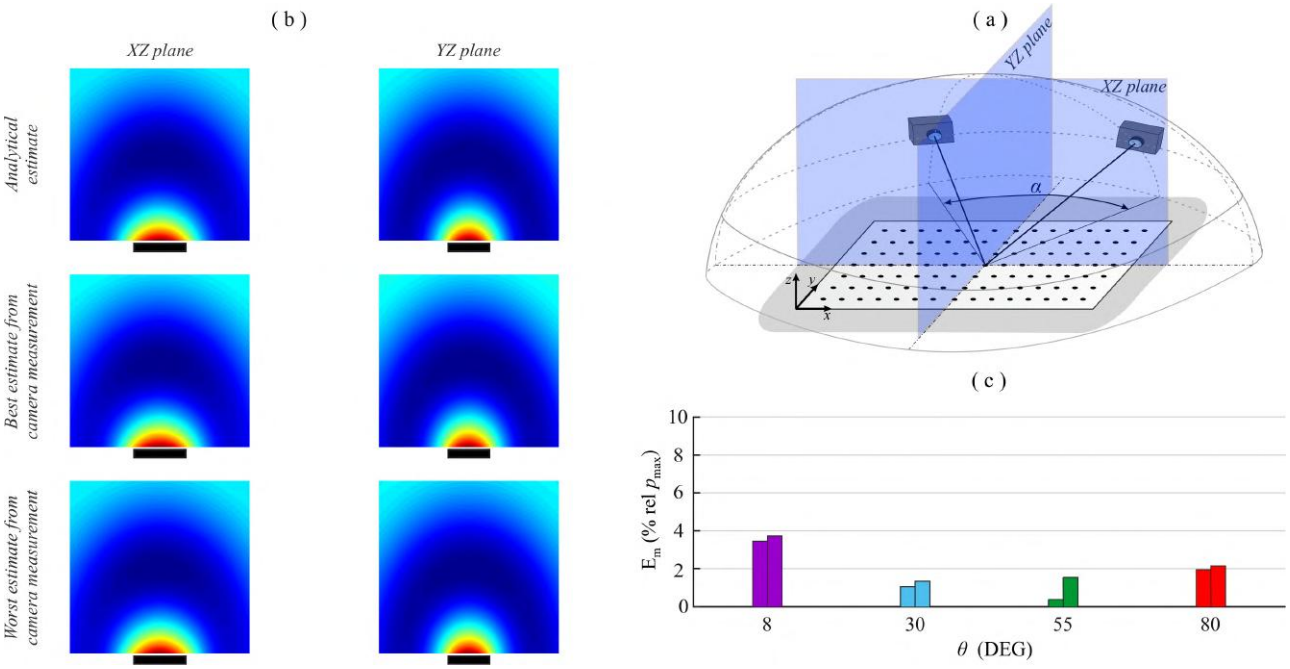

Figure 6.8: First deflection shape: (a) aperture angle case study 2a ($\alpha = 2|\theta|$); (b) comparison between ideal (i.e. from analytical model), best and worst case (i.e. from best and worst reconstructed flexural vibration with cameras setup) acoustic fields; (c) histogram of the mean error.

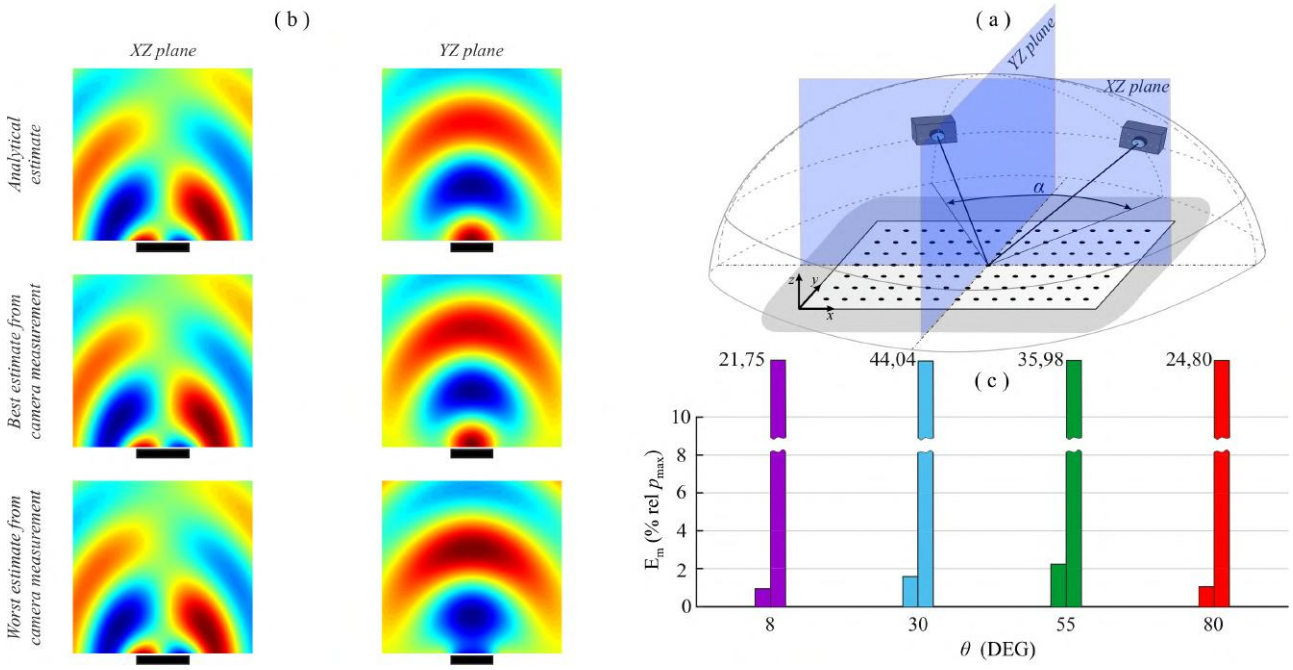

Figure 6.9: Second deflection shape: (a) aperture angle case study 2a ($\alpha = 2|\theta|$); (b) comparison between ideal (i.e. from analytical model), best and worst case (i.e. from best and worst reconstructed flexural vibration with cameras setup) acoustic fields; (c) histogram of the mean error.

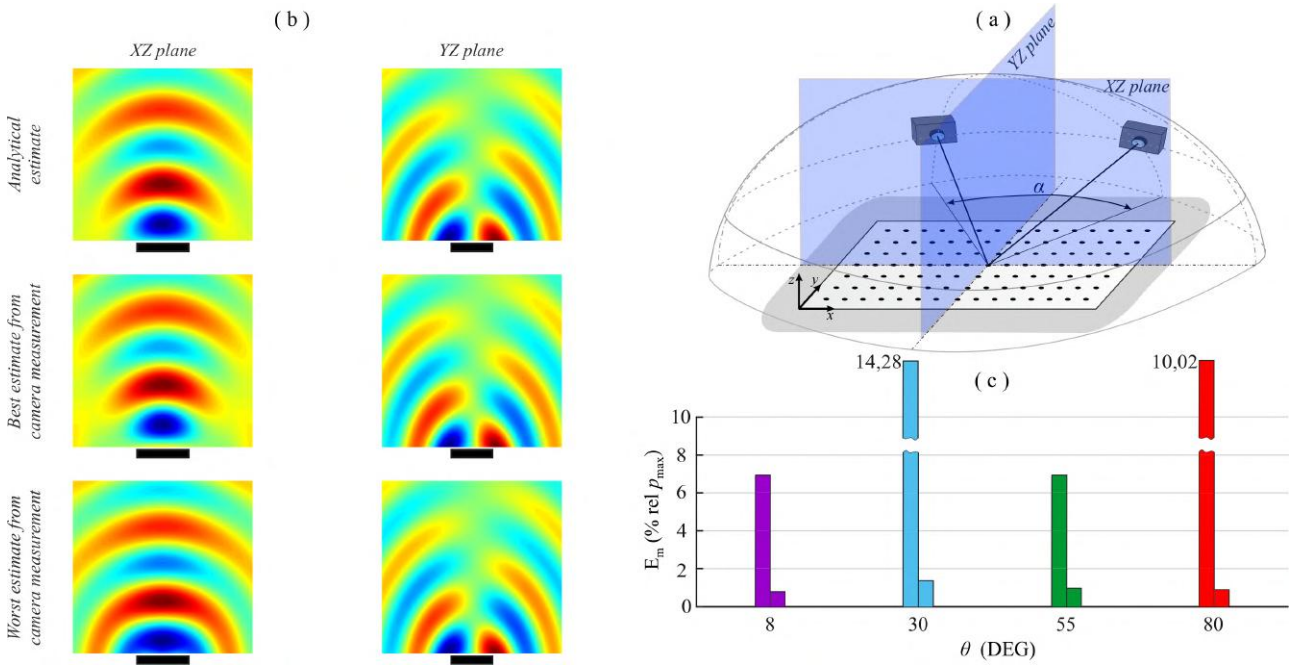

Figure 6.10: Third deflection shape: (a) aperture angle case study 2a ($\alpha = 2|\theta|$); (b) comparison between ideal (i.e. from analytical model), best and worst case (i.e. from best and worst reconstructed flexural vibration with cameras setup) acoustic fields; (c) histogram of the mean error.

The results presented in Figs. 6.8 - 6.10 indicate that, when the cameras are arranged along the arc of a circle oriented parallel to the plane of the plate such that the cameras have a little elevation angle of 10°, the accuracy of the sound radiation estimate does not vary significantly as the angle of aperture between the cameras is increased. Indeed, the bar Plot (c) of Fig. 6.8 indicates that the average error is between 0.5% and 4% for both the XZ and the YZ planes. Similarly, Figs. 6.9 and 6.10 show that

the average error over the XZ plane and over the YZ plane of the acoustic field obtained from the reconstruction of the second and the third flexural deflection shape of the plate is between 0.5% and 3% respectively.

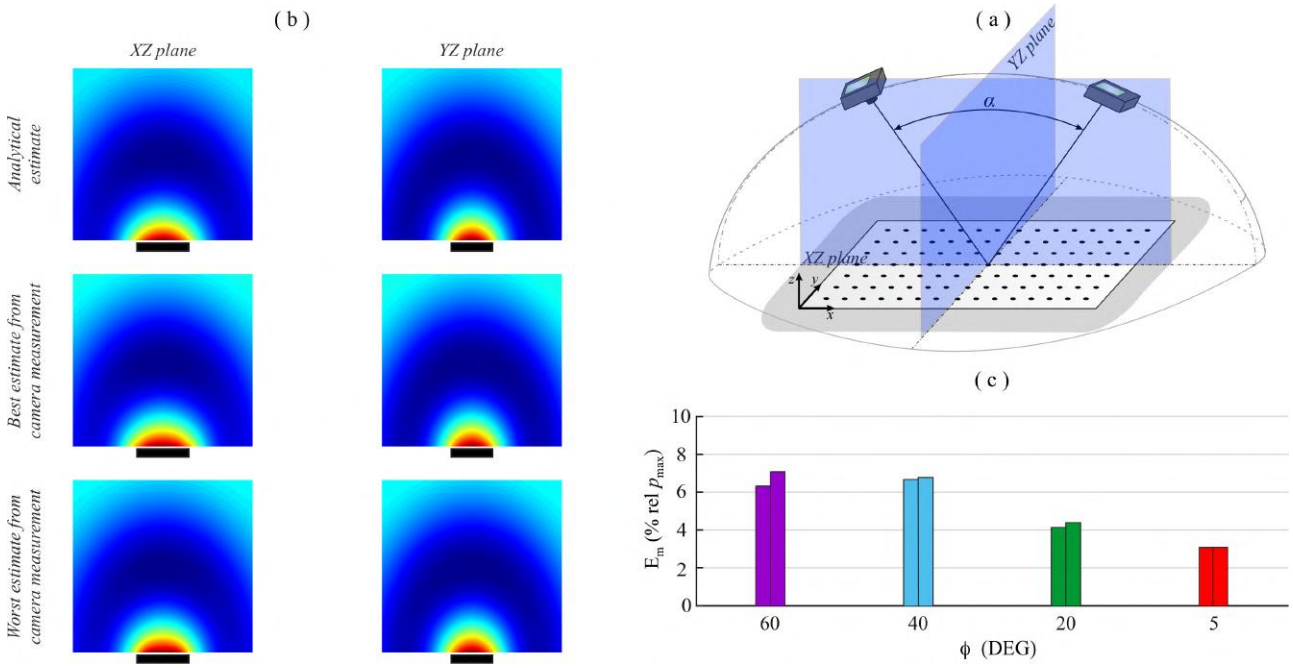

Figure 6.11: First deflection shape: (a) aperture angle case study 2b ($\alpha = 180 - 2\phi$); (b) comparison between ideal (i.e. from analytical model), best and worst case (i.e. from best and worst reconstructed flexural vibration with cameras setup) acoustic fields; (c) histogram of the mean error.

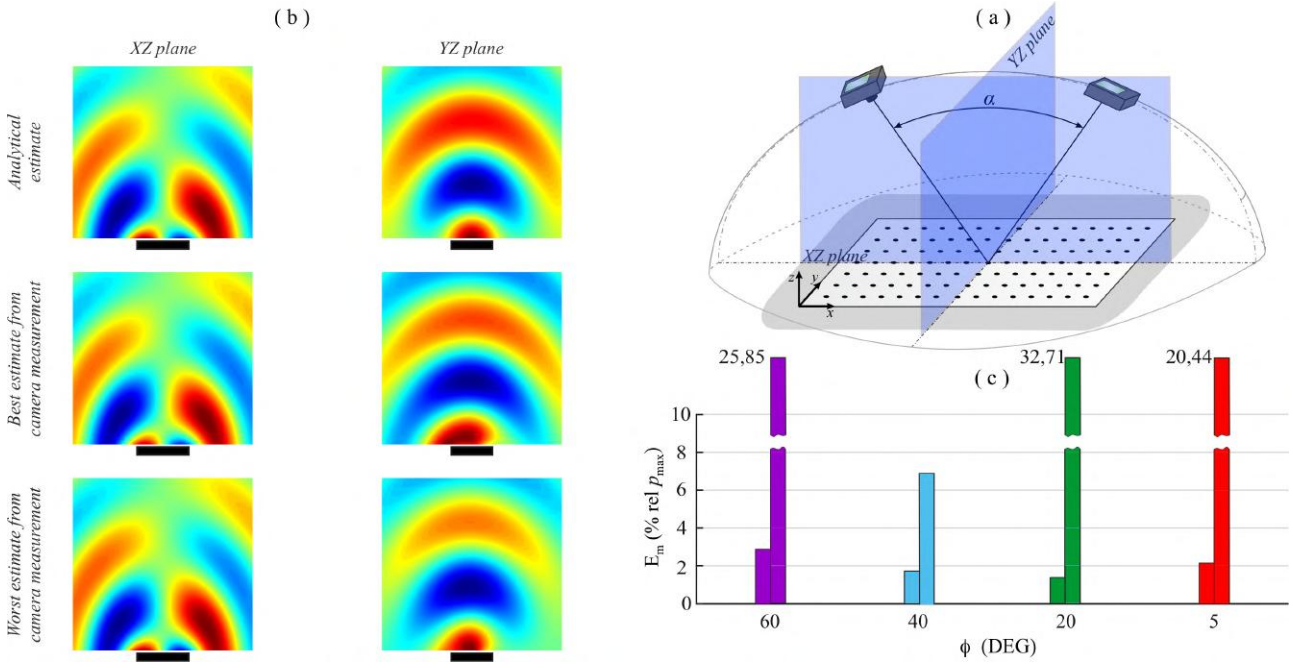

Figure 6.12: Second deflection shape: (a) aperture angle case study 2b ($\alpha = 180 - 2\phi$); (b) comparison between ideal (i.e. from analytical model), best and worst case (i.e. from best and worst reconstructed flexural vibration with cameras setup) acoustic fields; (c) histogram of the mean error.

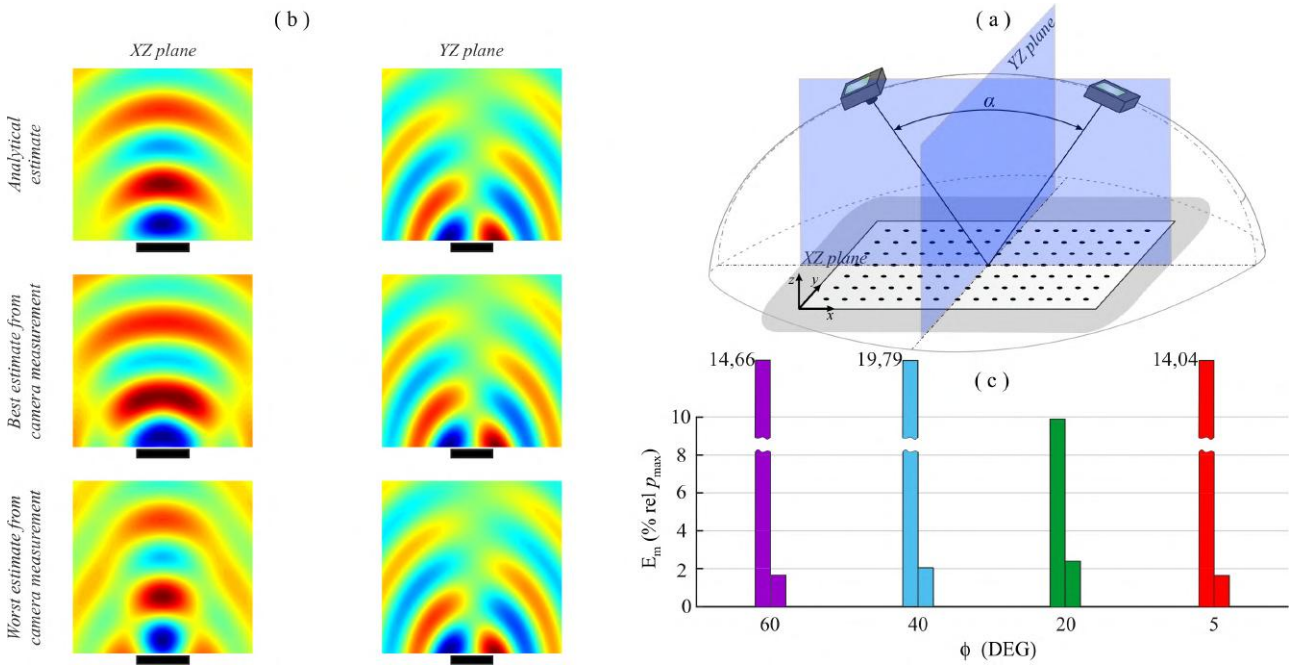

Figure 6.13: Third deflection shape: (a) aperture angle case study 2b ($\alpha = 180 - 2\phi$); (b) comparison between ideal (i.e. from analytical model), best and worst case (i.e. from best and worst reconstructed flexural vibration with cameras setup) acoustic fields; (c) histogram of the mean error.

Alternatively, the results presented in Fig. 6.11 show that, when the acoustic pressure is estimated from the reconstruction of the first flexural deflection shape and the cameras are arranged along the arc of a circle which: a) is oriented orthogonal to the plane of the plate, b) is parallel to the x axis of the plate and c) passes through the center of the plate, the accuracy of the estimate does vary significantly as the angle of aperture between the cameras is increased. Indeed, the bar Plot (c) indicates that the average error passes from about 7% to 3.5% when the angle of aperture is increased from 60° to 170°. However, Figs. 6.12 - 6.13 show that, when the estimate of the acoustic radiation from the reconstruction of the second and of the third flexural deflection shape is considered, the average error does not vary significantly: Plot (c) in both the figures shows that the average error is always between 1% and 3%. In conclusion, the results presented in Fig. 6.11 indicate that the accuracy of the estimate of the sound radiation obtained from the reconstruction of the first flexural deflection shape of the plate is strongly influenced by the elevation angle of the cameras whereas this parameter does not significantly affect the estimate of the sound radiation obtained from the second and from the third flexural deflection shapes.

The third and fourth configurations, i.e. Cases 2c and 2d, are now discussed. In these cases, the cameras are arranged with the same geometry of Cases 2a and 2b but, in contrast to these cases, the cameras are rotated by $\pi/2$ around the z axis. Therefore, Case 2c is characterized by cameras arranged with the same elevation angle $\phi = 10°$ and increasingly larger aperture angles α over an arc of a circle oriented parallel to the plane of the plate and to the y axis, as reported in Table 6.1 - Case 2c. In Case 2d the cameras are arranged over an arc of a circle, which: a) is parallel to the y axis of the plate, b) is

orthogonal to the plane of the plate and c) passes through the center of the plate. Therefore, in this case, as reported in 6.1 - Case 2d, the elevation angle ϕ varies as the aperture angle is increased.

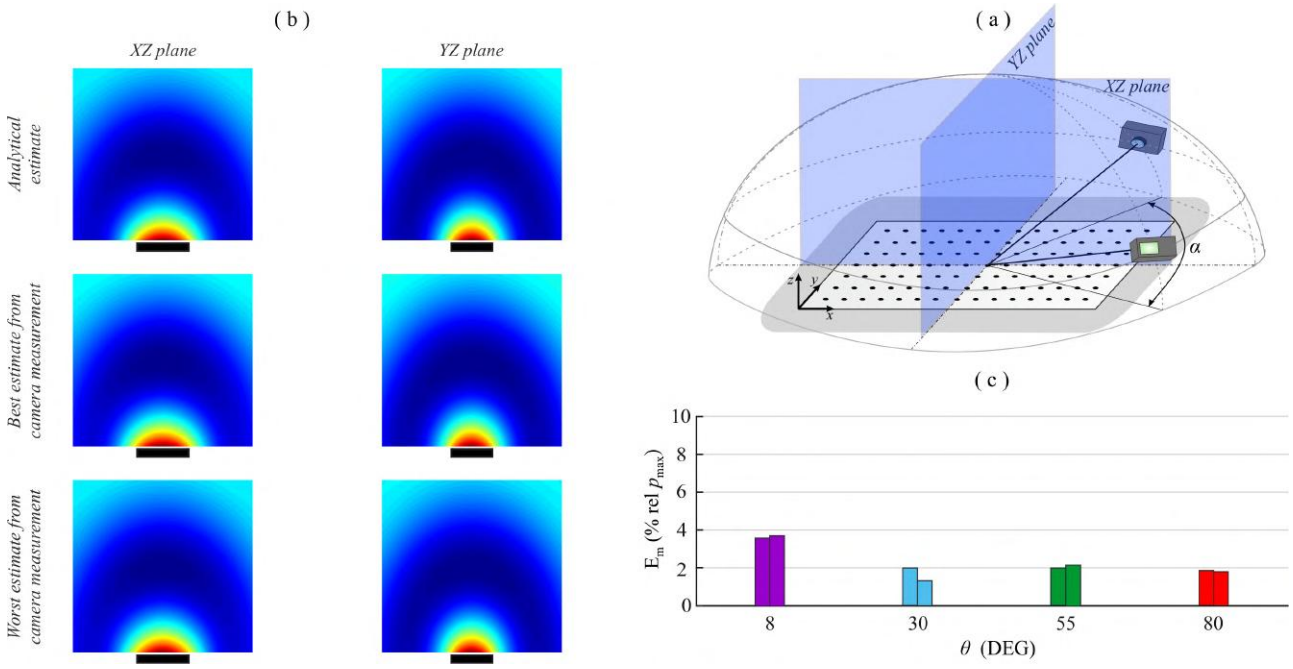

Figure 6.14: First deflection shape: (a) aperture angle case study 2c ($\alpha = 2|\theta|$); (b) comparison between ideal (i.e. from analytical model), best and worst case (i.e. from best and worst reconstructed flexural vibration with cameras setup) acoustic fields; (c) histogram of the mean error.

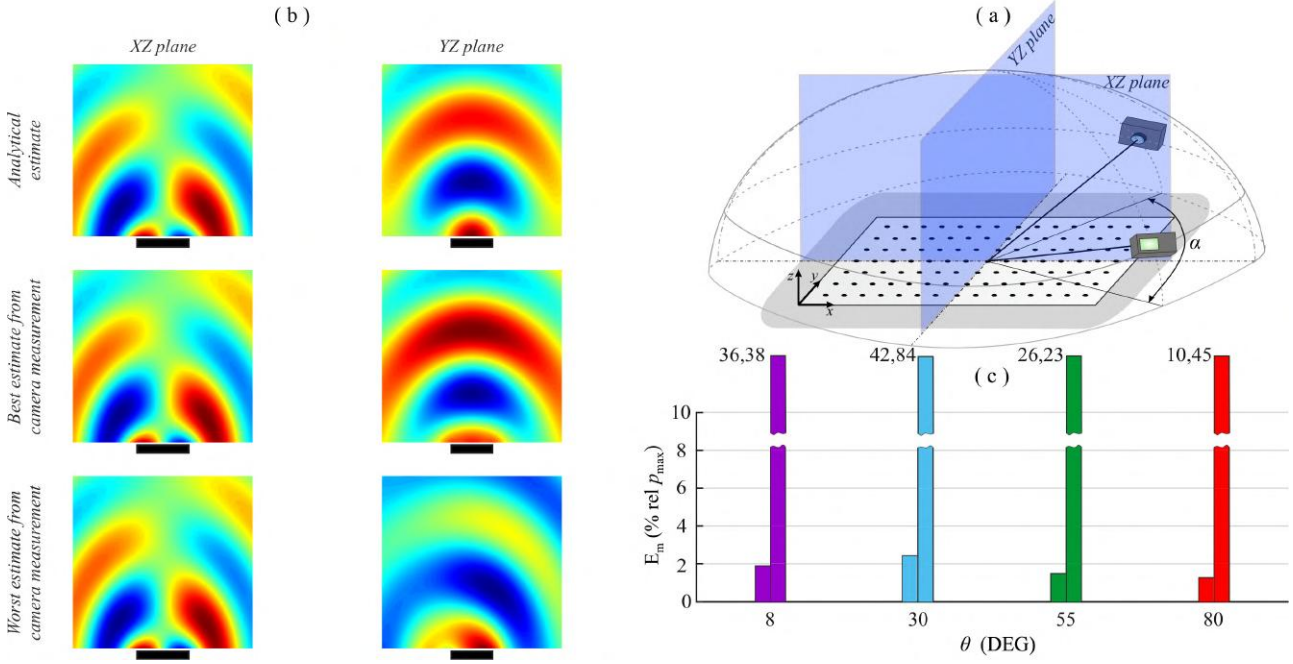

Figure 6.15: Second deflection shape: (a) aperture angle case study 2c ($\alpha = 2|\theta|$); (b) comparison between ideal (i.e. from analytical model), best and worst case (i.e. from best and worst reconstructed flexural vibration with cameras setup) acoustic fields; (c) histogram of the mean error.

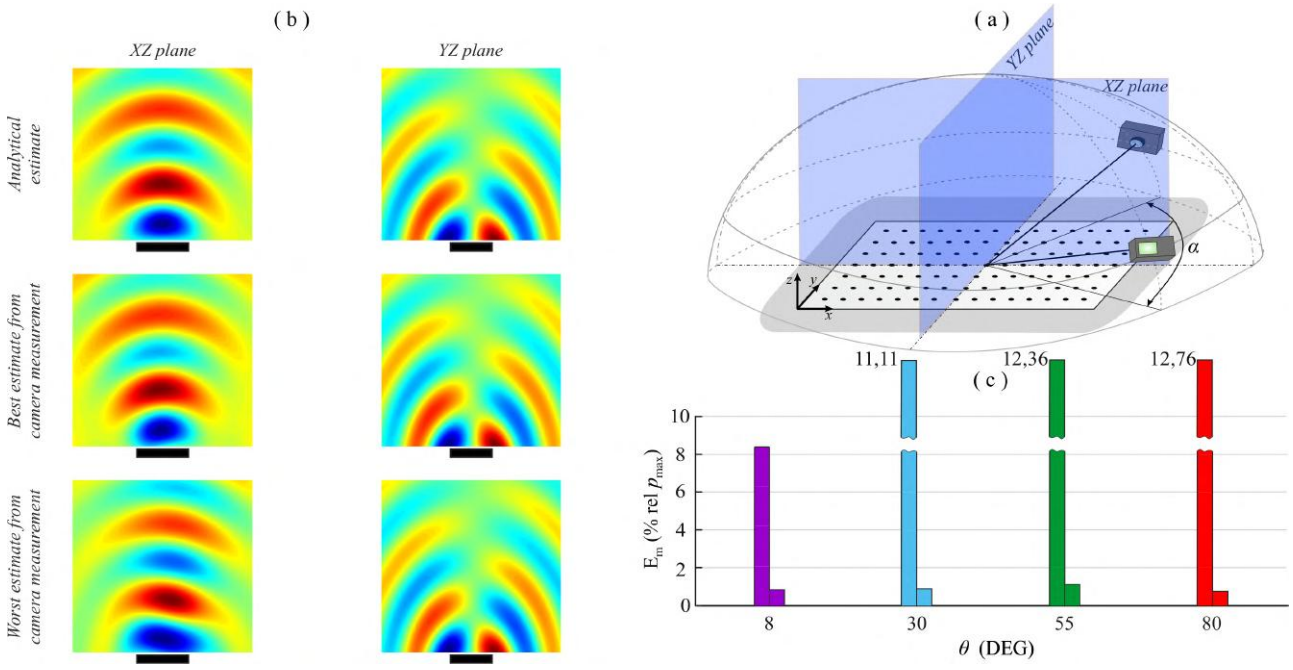

Figure 6.16: Third deflection shape: (a) aperture angle case study 2c ($\alpha = 2|\theta|$); (b) comparison between ideal (i.e. from analytical model), best and worst case (i.e. from best and worst reconstructed flexural vibration with cameras setup) acoustic fields; (c) histogram of the mean error.

The bar plot (c) of Figs. 6.14 - 6.16 indicates that the average error of the estimate of the sound radiation obtained from the reconstruction of each of the first three flexural deflection shapes of the plate is always between 1% and 4%: these results are thus similar to the ones seen in Figs. 6.8 - 6.10.

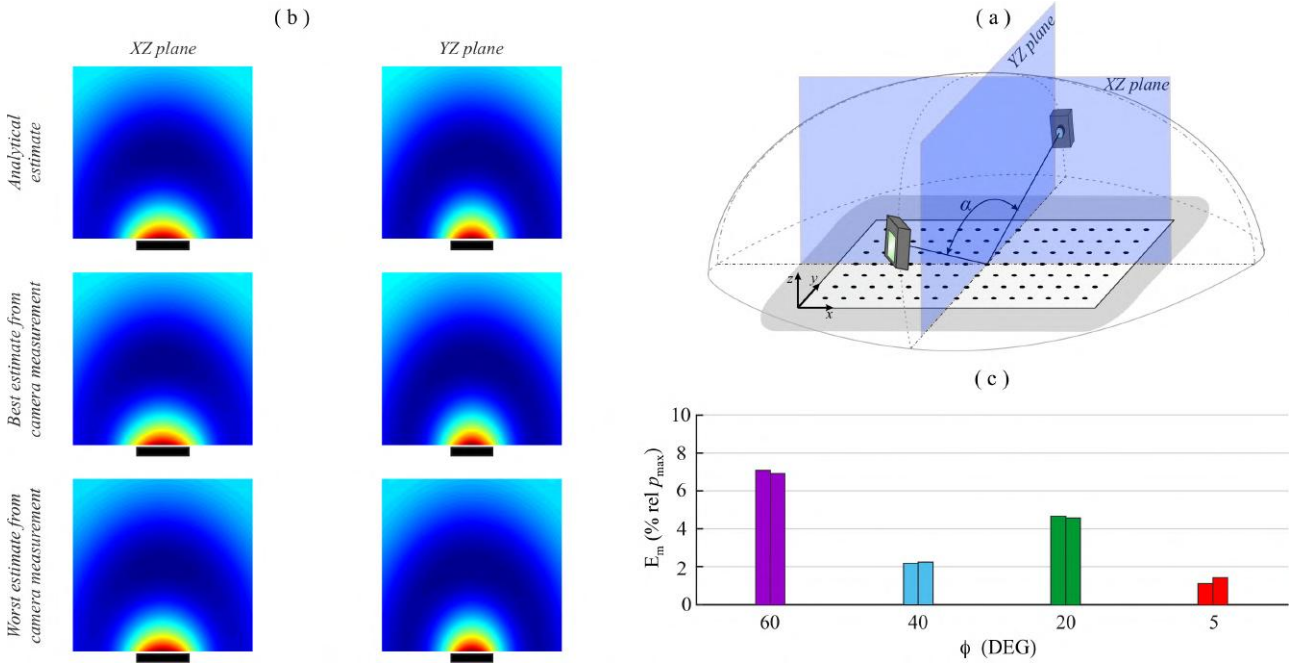

Figure 6.17: First deflection shape: (a) aperture angle case study 2d ($\alpha = 180 - 2\phi$); (b) comparison between ideal (i.e. from analytical model), best and worst case (i.e. from best and worst reconstructed flexural vibration with cameras setup) acoustic fields; (c) histogram of the mean error.

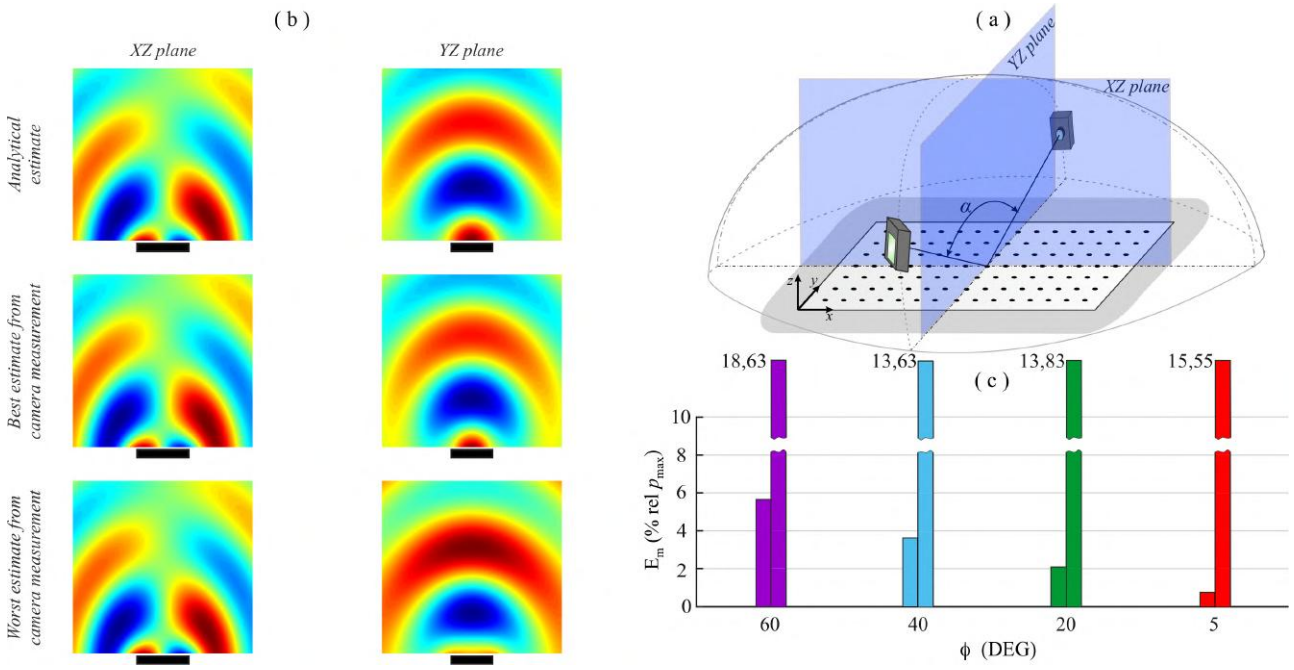

Figure 6.18: Second deflection shape: (a) aperture angle case study 2d ($\alpha = 180 - 2\phi$); (b) comparison between ideal (i.e. from analytical model), best and worst case (i.e. from best and worst reconstructed flexural vibration with cameras setup) acoustic fields; (c) histogram of the mean error.

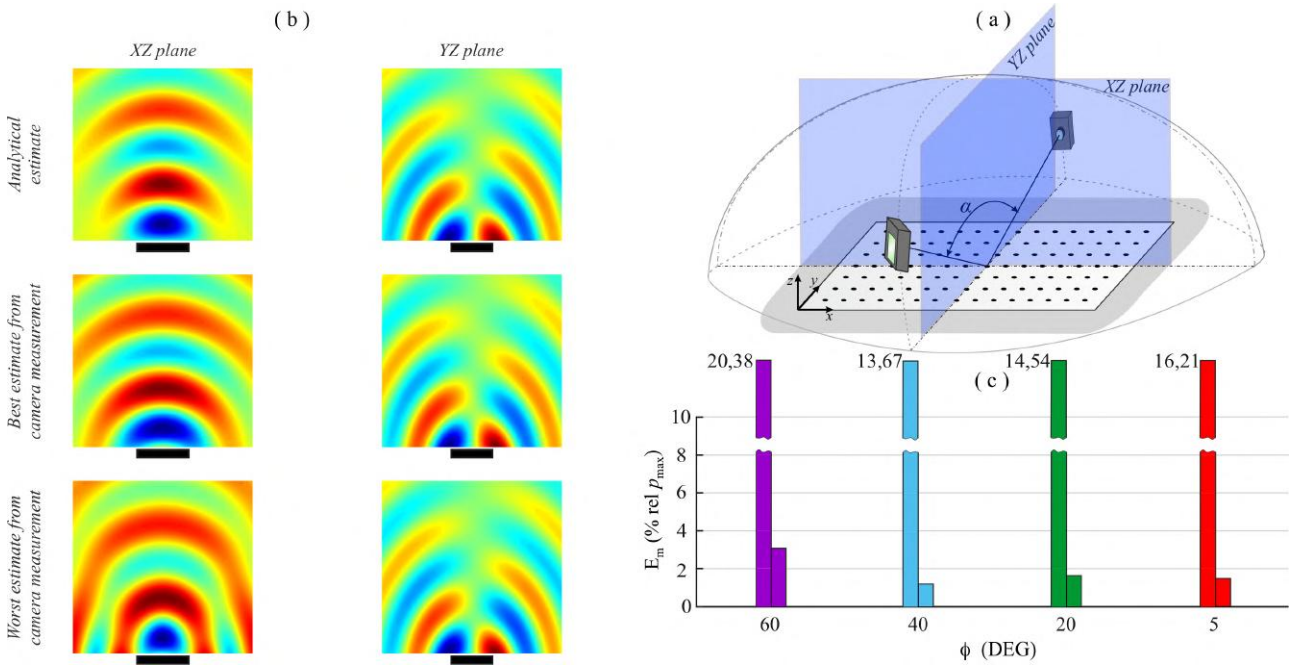

Figure 6.19: Third deflection shape: (a) aperture angle case study 2d ($\alpha = 180 - 2\phi$); (b) comparison between ideal (i.e. from analytical model), best and worst case (i.e. from best and worst reconstructed flexural vibration with cameras setup) acoustic fields; (c) histogram of the mean error.

Case 2d with the cameras arranged along an arc oriented orthogonal to the plate is now considered. The results presented in Fig. 6.17, Plot (c) indicates that the average error passes from 7% to 1% when the angle of aperture is increased from 60° to 170°. Nevertheless, in this case, similarly to the results of Section 6.2.1, the error does not follow a regular trend. Analogous considerations can be done on Plot (c) of Fig. 6.19 where the estimate of the acoustic radiation obtained from the reconstruction

of the third flexural deflection shape of the plate is considered. Here the error falls from 3% to 1.5%. However, Plot (c) in Fig. 6.18, which regards the estimate of the acoustic radiation obtained from the reconstruction of the second flexural deflection shape of the plate, shows a monotonous decrease of the average error from about 6% to about 1%.

6.2.3 Resolution of cameras

This section investigates the accuracy of the estimate of the acoustic radiation emitted by the reconstructed first three flexural deflection shapes of a plate with a pair of cameras characterized by increasingly larger spatial resolution. The distance d, the azimuthal θ and elevation ϕ angles and the resolutions of the cameras are listed in Table 6.1 - Case 3.

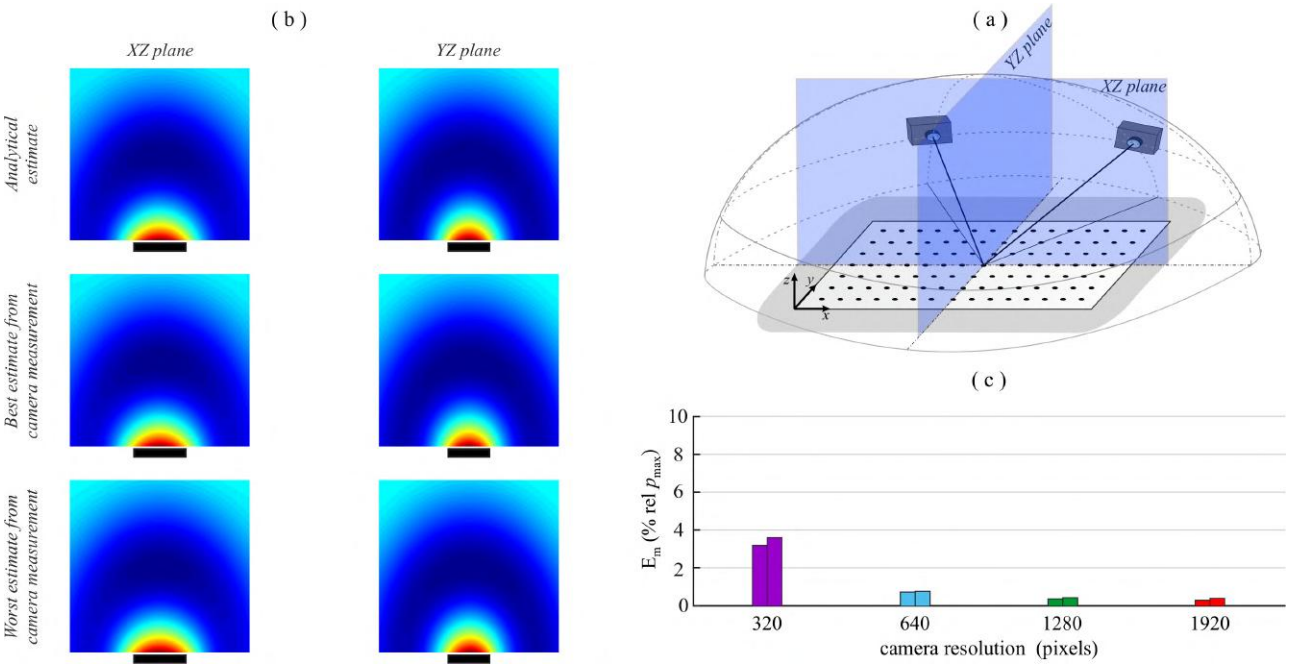

Figure 6.20: First deflection shape: (a) resolution case study 3; (b) comparison between ideal (i.e. from analytical model), best and worst case (i.e. from best and worst reconstructed flexural vibration with cameras setup) acoustic fields; (c) histogram of the mean error.

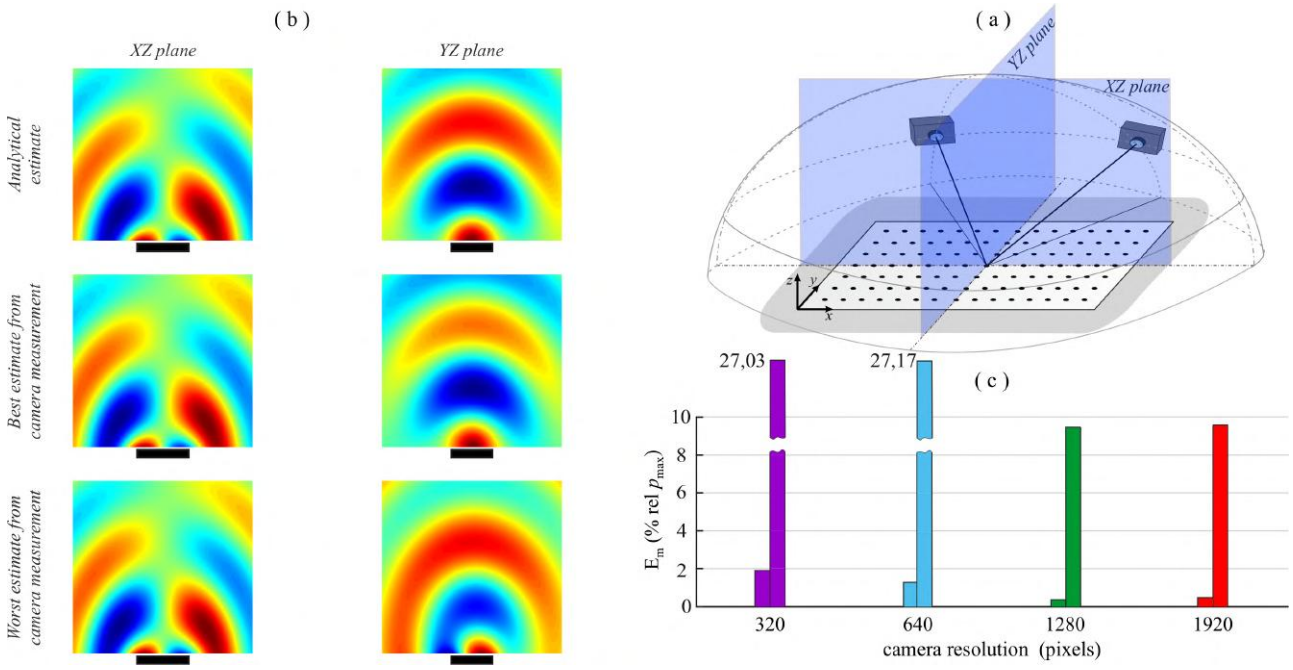

Figure 6.21: Second deflection shape: (a) resolution case study 3; (b) comparison between ideal (i.e. from analytical model), best and worst case (i.e. from best and worst reconstructed flexural vibration with cameras setup) acoustic fields; (c) histogram of the mean error.

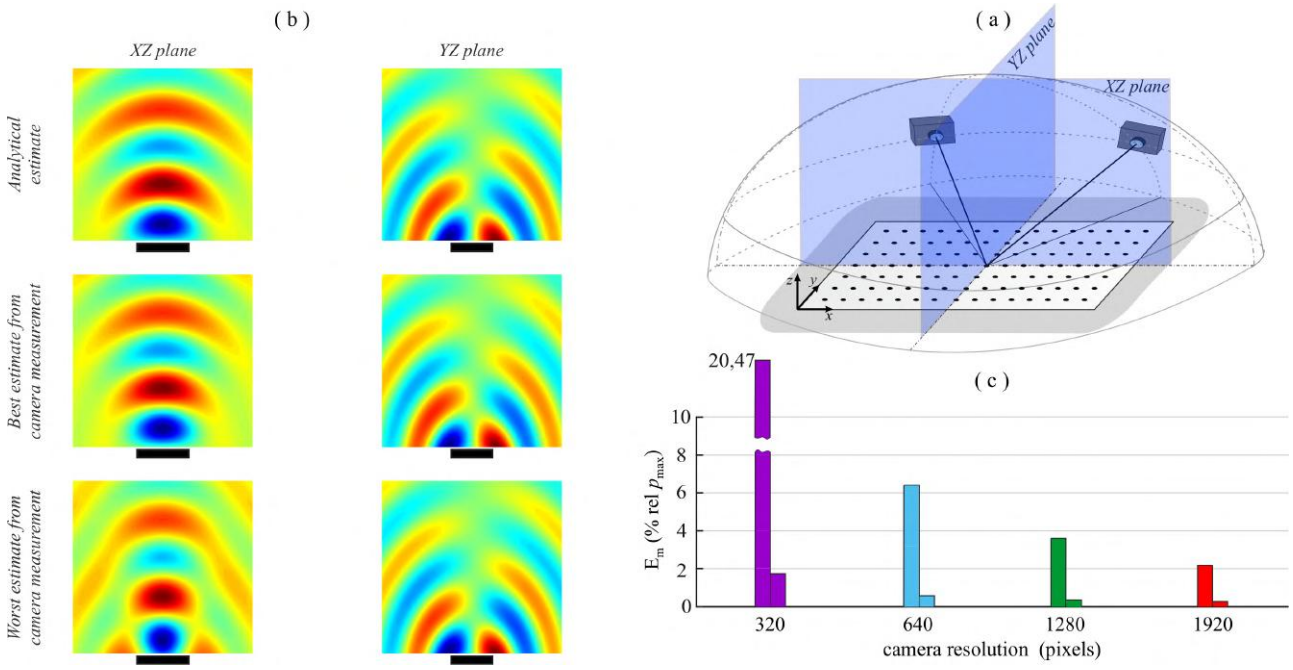

Figure 6.22: Third deflection shape: (a) resolution case study 3; (b) comparison between ideal (i.e. from analytical model), best and worst case (i.e. from best and worst reconstructed flexural vibration with cameras setup) acoustic fields; (c) histogram of the mean error.

The results presented in Figs. 6.20 - 6.22 indicate that the accuracy of the measurement increases as the resolution of the cameras is increased. For instance, when the number of pixels is raised from 320×180 to 1920×1080, the bar Plot (c) of Fig. 6.20 suggests that the average error of the estimate falls from about 3.5% to less than 1%. Similarly, the bar Plot (c) of Figs. 6.21 - 6.22 shows that the average error goes from 2% to less than 1% for the estimate of the sound radiation derived from the

reconstruction of both the second and the third flexural deflection shapes of the plate.

6.2.4 Arrays composed by more than 2 cameras

To conclude, the accuracy of the estimate of the acoustic radiation obtained from vibration measurements of the flexural response of a plate with multiple camera setups composed by more than 2 cameras is examined in this subsection. In parallel to Section 4.2.4, in this section, the estimate of the pressure field generated by the reconstructed first three flexural deflection shapes of a plate obtained by a setup arranged with a sequential addition of pairs of cameras, which are located symmetrically with respect to either the YZ plane or the XZ plane both centered in the middle of the plate, is considered. The analysis is organized in two parts. The first part concerns the estimate of the sound radiation obtained from the flexural deflection shapes reconstructed with increasingly larger numbers of cameras arranged over an arc of circumference, which, as for the Cases 2a and 2c discussed in Figs. 6.8 - 6.10 and Figs. 6.14 - 6.16, are oriented parallel to the plane of the plate such that the cameras are all characterized by the same elevation angle ϕ and have either increasingly larger or increasing smaller azimuthal angles θ, in the x and y directions with respect to the plate. Instead, the second part considers a setup composed by increasingly larger numbers of cameras arranged over arc of circumferences, which, as for the Cases 2b and 2d discussed in Figs. 6.11 - 6.13 and Figs. 6.17 - 6.19, are oriented in such a way as they are: a) orthogonal to the plane of the plate, b) parallel either to the x or the y axis of the plate and c) pass through the center of the plate. Here only one configuration is considered where the aperture angle is progressively increased. The exact positions of the cameras are the same as those seen in Section 4.2.4 and are recalled in Table 6.2 - Cases 4a, 4b, 4c, 4d. Case 4a is also analyzed, where the pairs of cameras are added in reverse order too, and is denoted as 4a$'$. Finally, an additional case 4e is discussed where the cameras are arranged in the circumference positioned just above the plate.

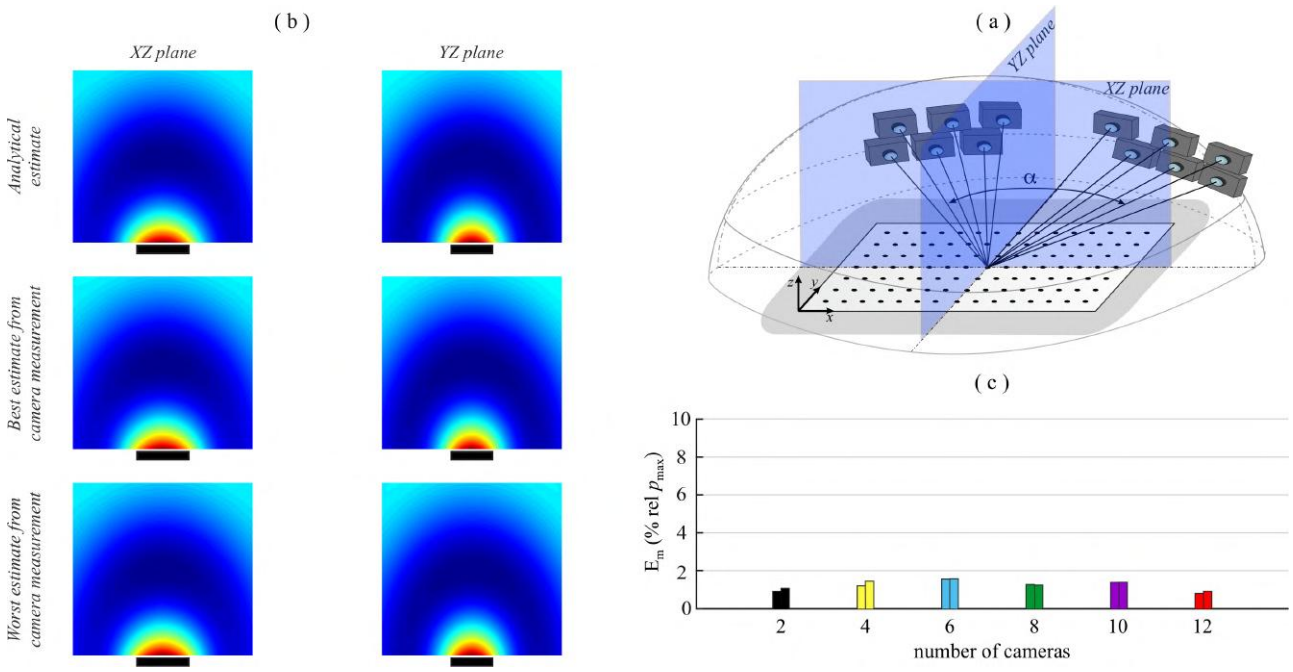

Figure 6.23: First deflection shape: (a) multiple cameras case study 4a; (b) comparison between ideal (i.e. from analytical model), best and worst case (i.e. from best and worst reconstructed flexural vibration with cameras setup) acoustic fields; (c) histogram of the mean error.

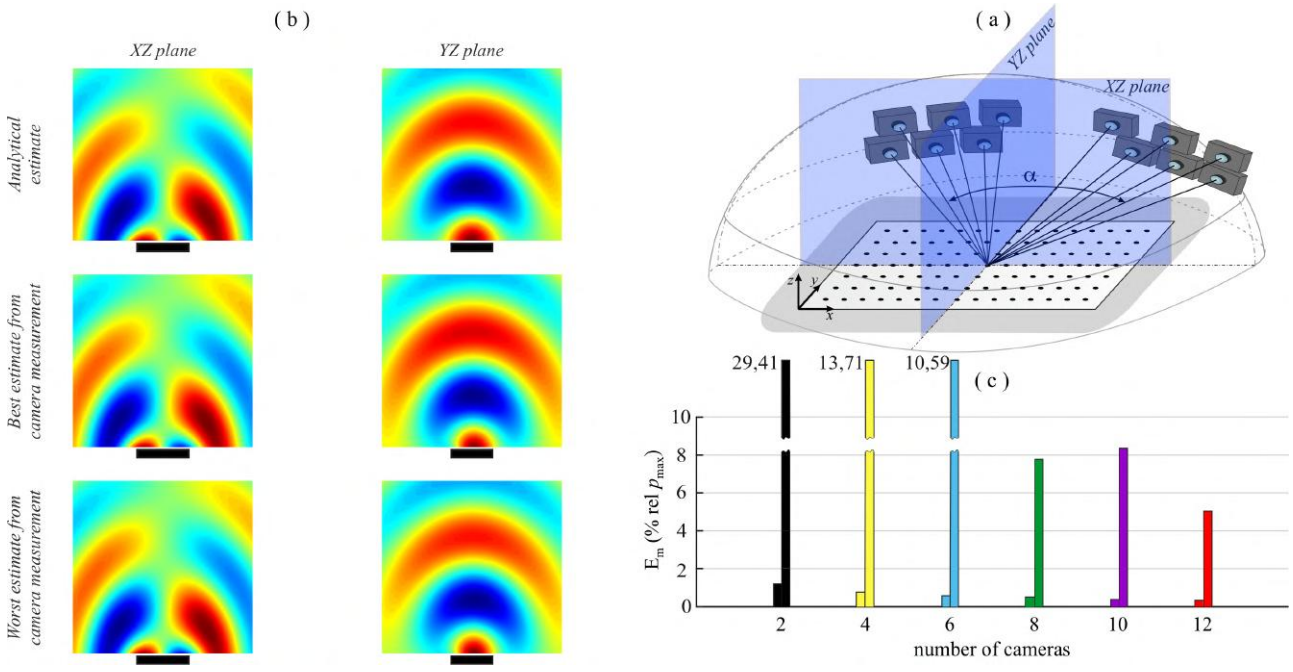

Figure 6.24: Second deflection shape: (a) multiple cameras case study 4a; (b) comparison between ideal (i.e. from analytical model), best and worst case (i.e. from best and worst reconstructed flexural vibration with cameras setup) acoustic fields; (c) histogram of the mean error.

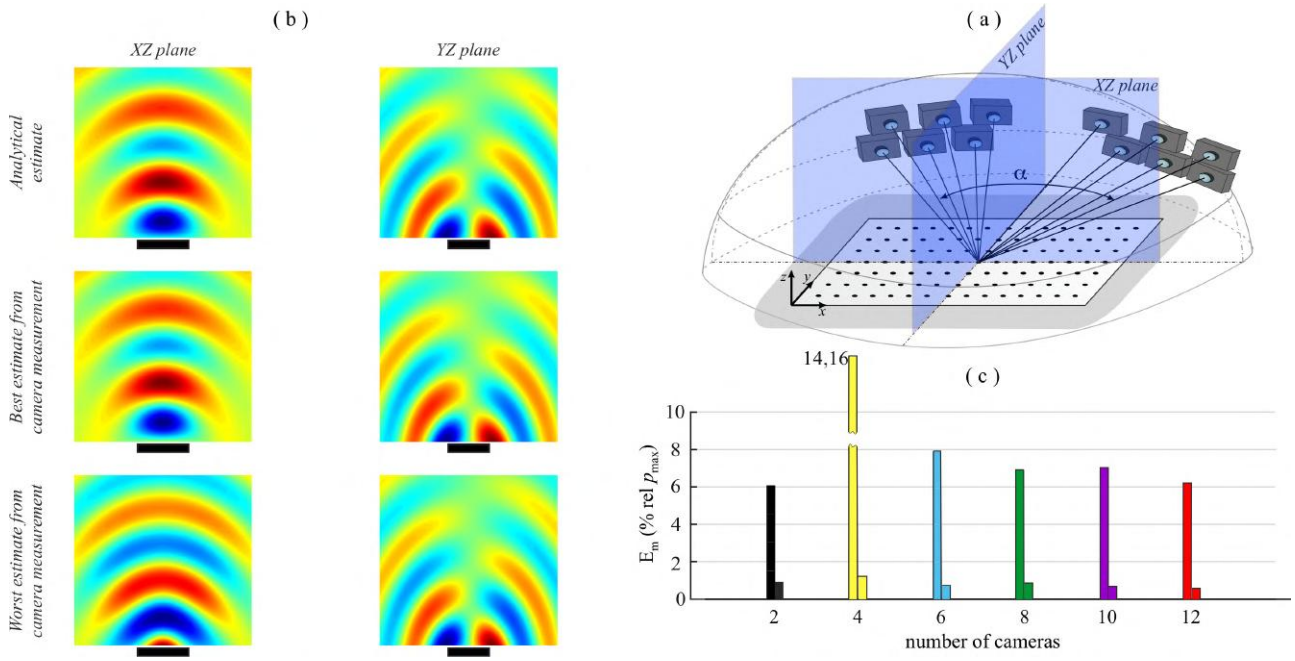

Figure 6.25: Third deflection shape: (a) multiple cameras case study 4a; (b) comparison between ideal (i.e. from analytical model), best and worst case (i.e. from best and worst reconstructed flexural vibration with cameras setup) acoustic fields; (c) histogram of the mean error.

To start with, the estimate of the sound radiation obtained from the reconstructed first three flexural deflection shapes with a setup arranged with increasingly larger numbers of cameras displaced over an arc of circumference oriented parallel to the plane of the plate is considered (Case 4a). The results presented in Figs. 6.23 - 6.25 indicate that, as pairs of cameras with increasingly larger aperture angle are added, the accuracy of the estimate of the sound radiation does not increase as seen in the equivalent case for the measurement of the flexural vibrations of the plate shown in Figs. 4.20 - 4.22. For instance, according to Plot (c), when the measurement setup passes from 2 cameras (1 pair) to 12 cameras (6 pairs) the average error of the estimate of the sound radiation is constantly lower than 2% for all the three cases of the estimate of the sound radiation from the reconstruction of the first three flexural deflection shapes of the plate.

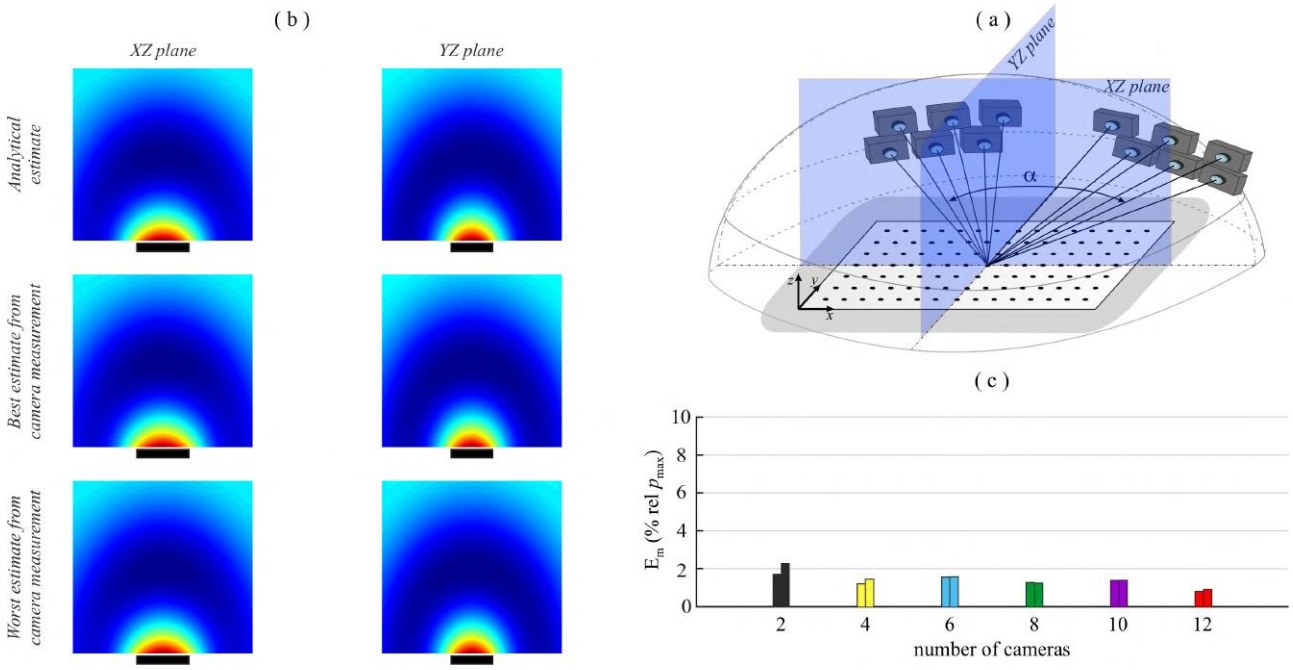

Figure 6.26: First deflection shape: (a) multiple cameras case study 4a′; (b) comparison between ideal (i.e. from analytical model), best and worst case (i.e. from best and worst reconstructed flexural vibration with cameras setup) acoustic fields; (c) histogram of the mean error.

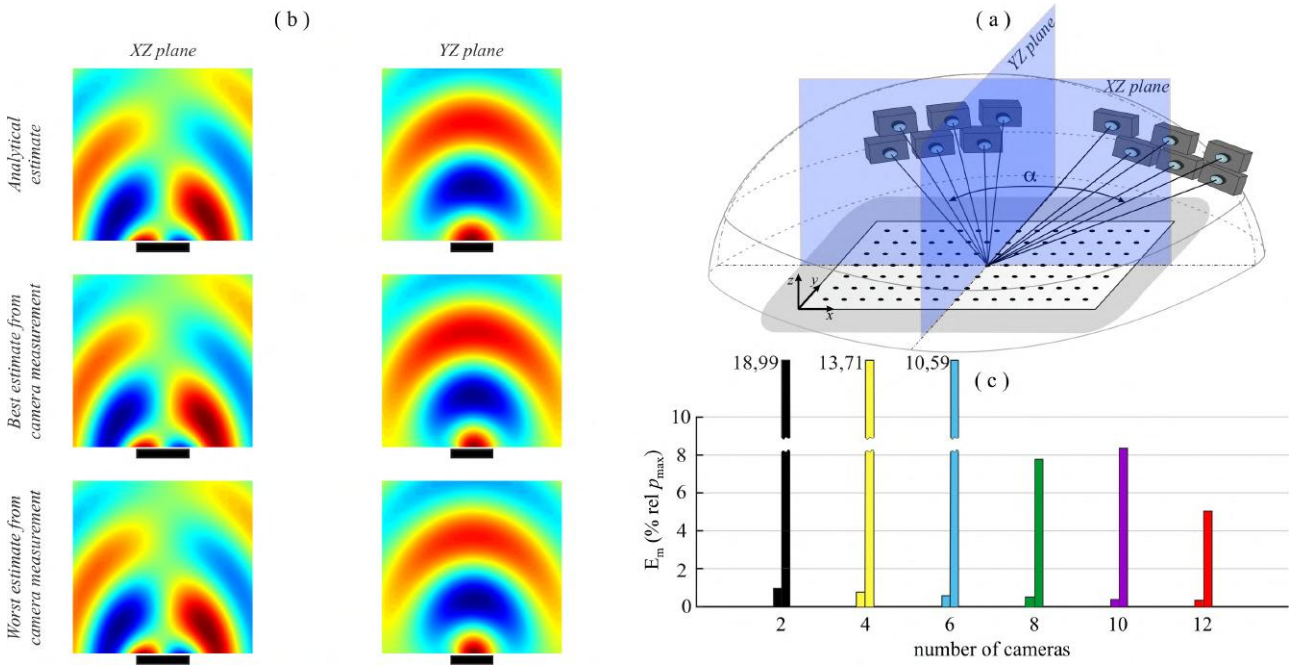

Figure 6.27: Second deflection shape: (a) multiple cameras case study 4a′; (b) comparison between ideal (i.e. from analytical model), best and worst case (i.e. from best and worst reconstructed flexural vibration with cameras setup) acoustic fields; (c) histogram of the mean error.

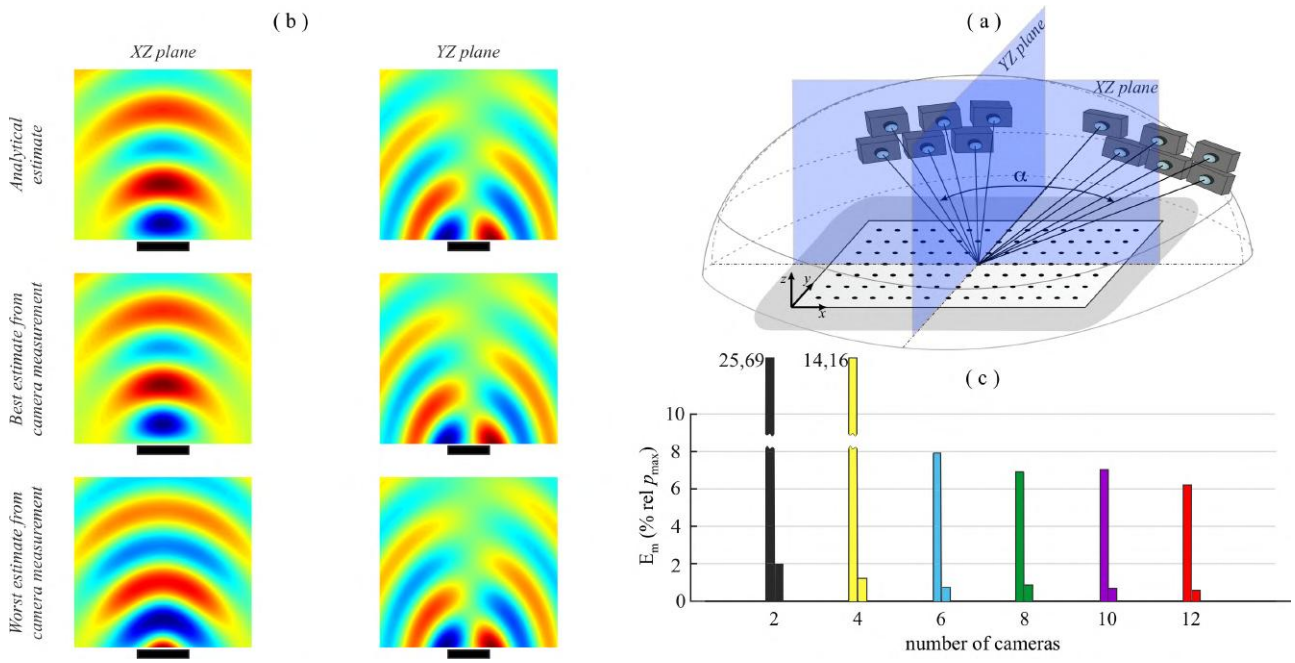

Figure 6.28: Third deflection shape: (a) multiple cameras case study 4a′; (b) comparison between ideal (i.e. from analytical model), best and worst case (i.e. from best and worst reconstructed flexural vibration with cameras setup) acoustic fields; (c) histogram of the mean error.

Similarly, the results presented Figs. 6.26 - 6.28 show that, if pairs of cameras with increasingly smaller aperture angle were added (Case 4a′), the average error still does not vary significantly. Indeed, as shown in Plot (c) of Figs. 6.26 - 6.28, the average error of the estimate is again almost constant with values between 1% and 2.5% even when more cameras are added.

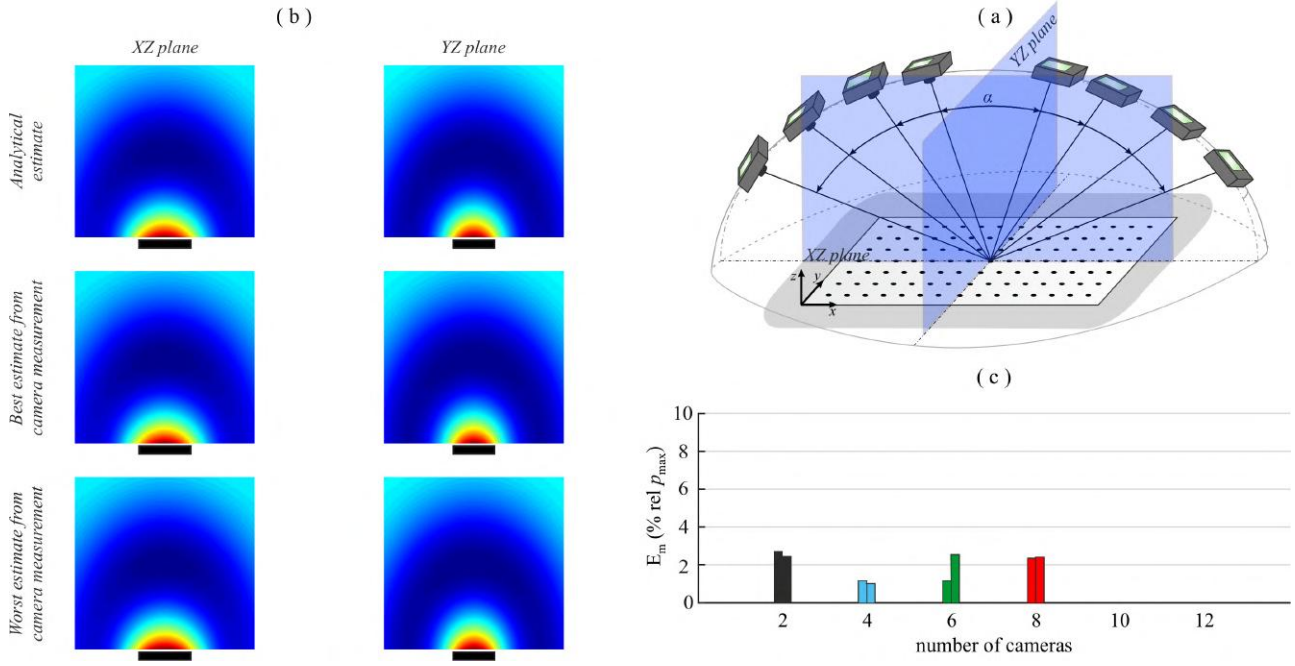

Figure 6.29: First deflection shape: (a) multiple cameras case study 4b; (b) comparison between ideal (i.e. from analytical model), best and worst case (i.e. from best and worst reconstructed flexural vibration with cameras setup) acoustic fields; (c) histogram of the mean error.

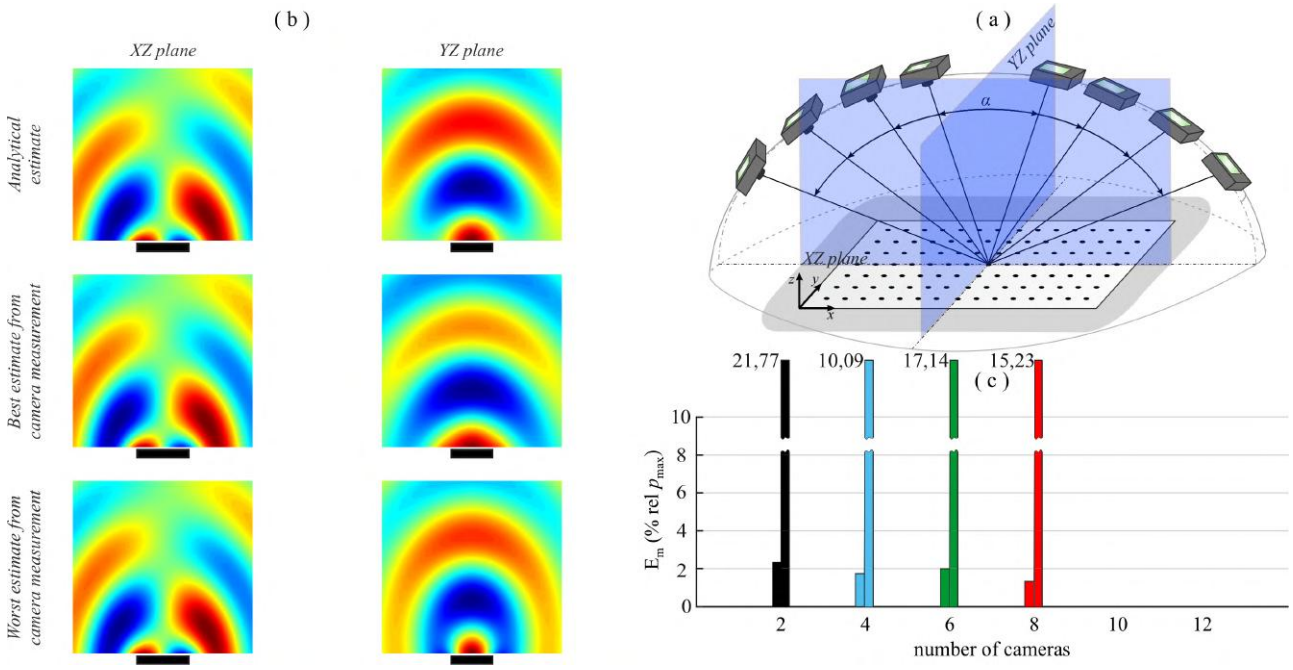

Figure 6.30: Second deflection shape: (a) multiple cameras case study 4b; (b) comparison between ideal (i.e. from analytical model), best and worst case (i.e. from best and worst reconstructed flexural vibration with cameras setup) acoustic fields; (c) histogram of the mean error.

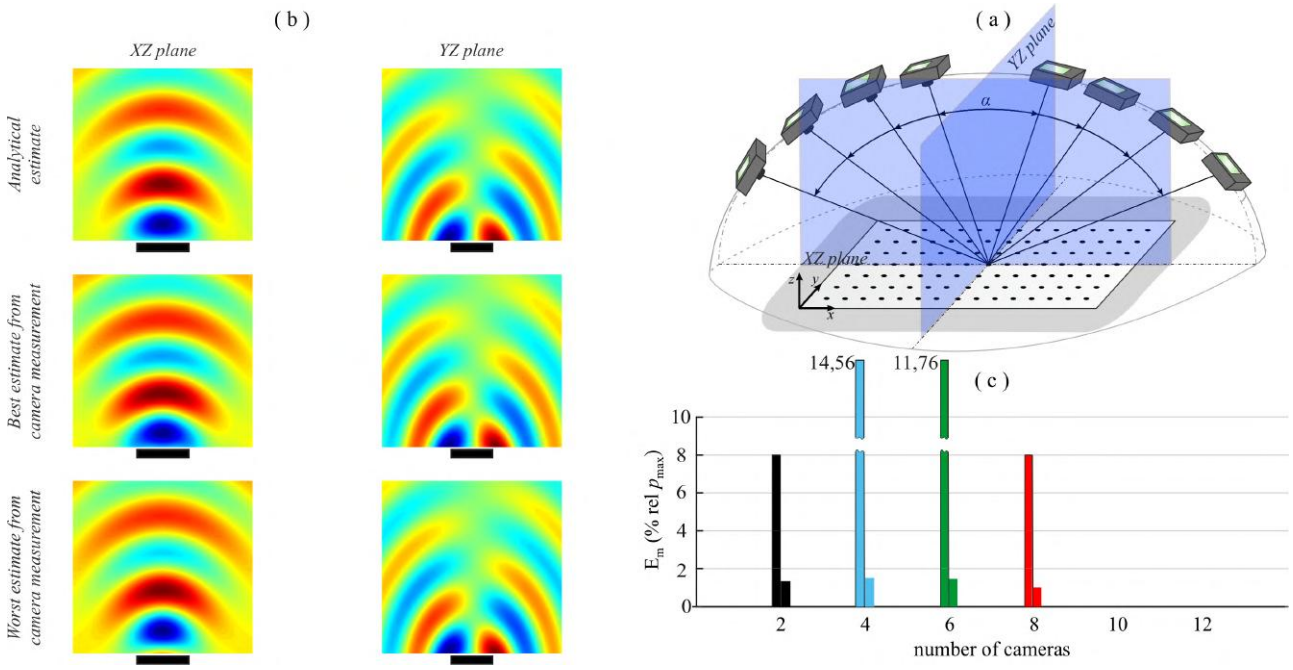

Figure 6.31: Third deflection shape: (a) multiple cameras case study 4b; (b) comparison between ideal (i.e. from analytical model), best and worst case (i.e. from best and worst reconstructed flexural vibration with cameras setup) acoustic fields; (c) histogram of the mean error.

The estimate of the sound radiation obtained from the reconstruction of the first three flexural deflection shapes of the plate with a setup composed by increasingly larger numbers of cameras arranged over an arc of circumference oriented in such a way they are: a) orthogonal to the plane of the plate, b) parallel to the x axis of the plate and c) passing through the center of the plate is now examined (Case 4b). The results presented in Figs. 6.29 - 6.31 show again that, as cameras with increasingly

larger aperture angle are added, the accuracy of the estimate of the sound radiation does not vary significantly. Similar considerations can be done to analyze the average error of the estimate of the sound radiation obtained from the reconstruction of each of the three flexural deflection shapes here considered. Indeed, Plot (c) of Figs. 6.29 - 6.31 indicates that, when the measurement setup passes from 2 cameras (1 pair) to 8 cameras (4 pairs), the average error of the estimate is between 1% and 3%.

Cases 4c, 4d are now investigated, which consider similar arrangements of the cameras as in Cases 4a, 4b but with the cameras rotated by $\pi/2$ with respect to the z axis.

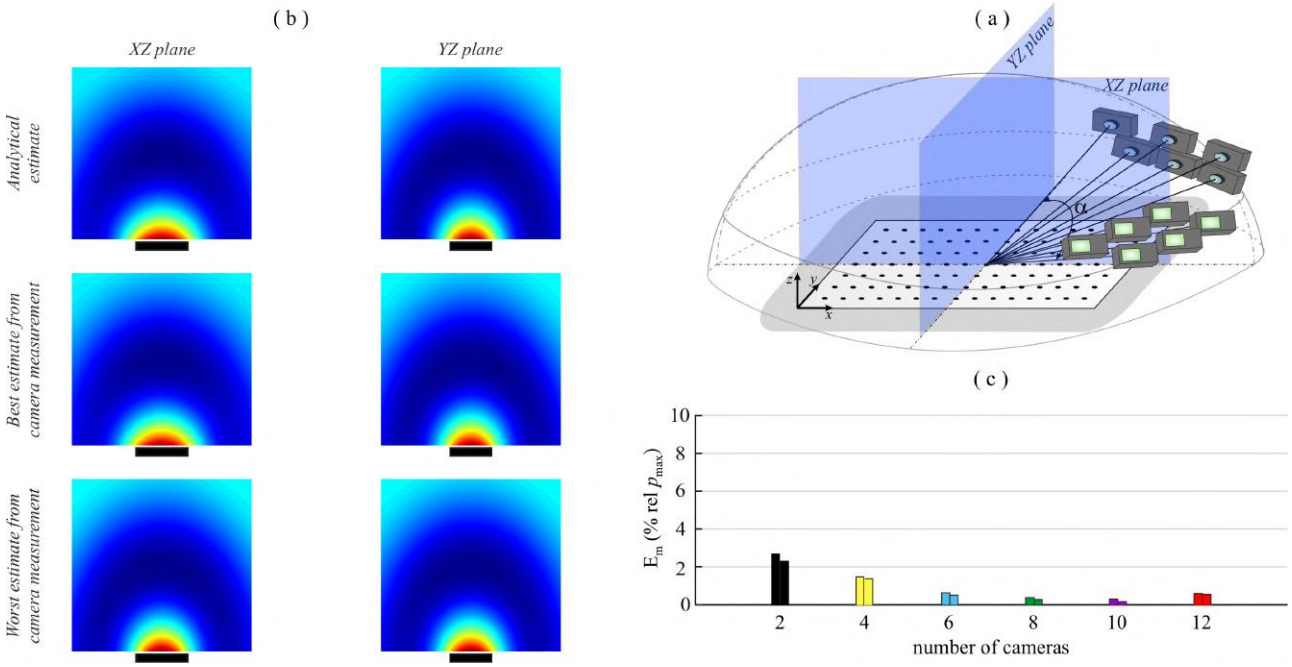

Figure 6.32: First deflection shape: (a) multiple cameras case study 4c; (b) comparison between ideal (i.e. from analytical model), best and worst case (i.e. from best and worst reconstructed flexural vibration with cameras setup) acoustic fields; (c) histogram of the mean error.

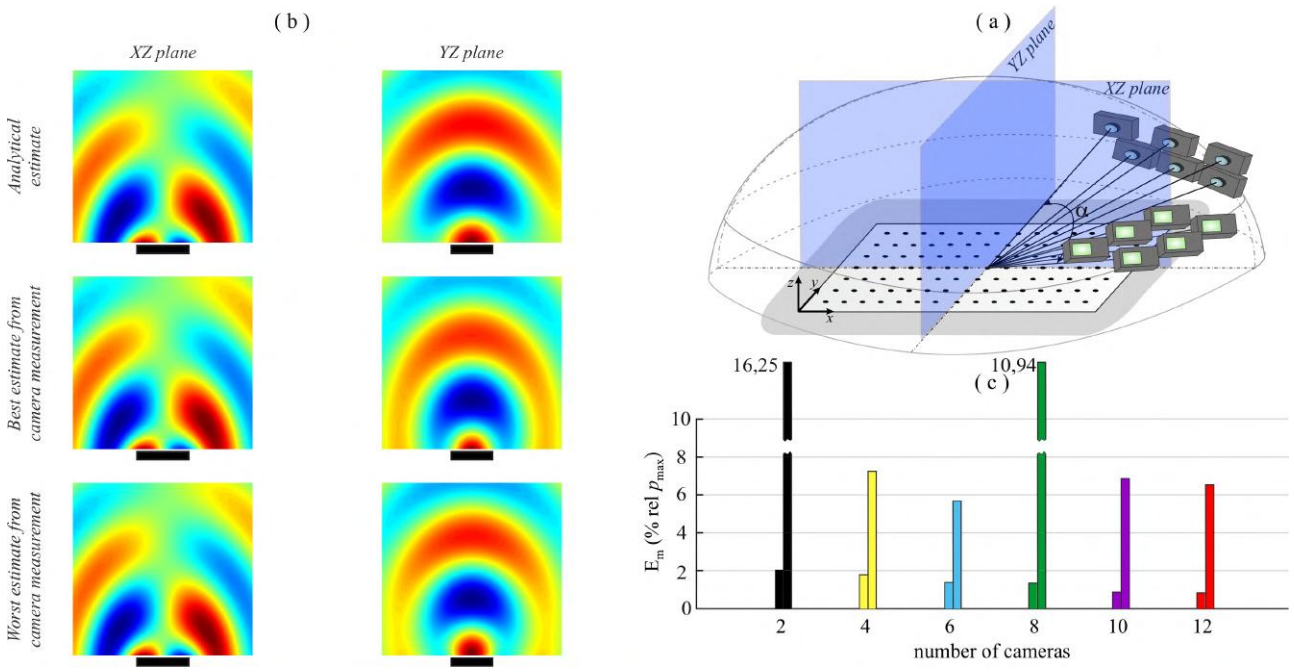

Figure 6.33: Second deflection shape: (a) multiple cameras case study 4c; (b) comparison between ideal (i.e. from analytical model), best and worst case (i.e. from best and worst reconstructed flexural vibration with cameras setup) acoustic fields; (c) histogram of the mean error.

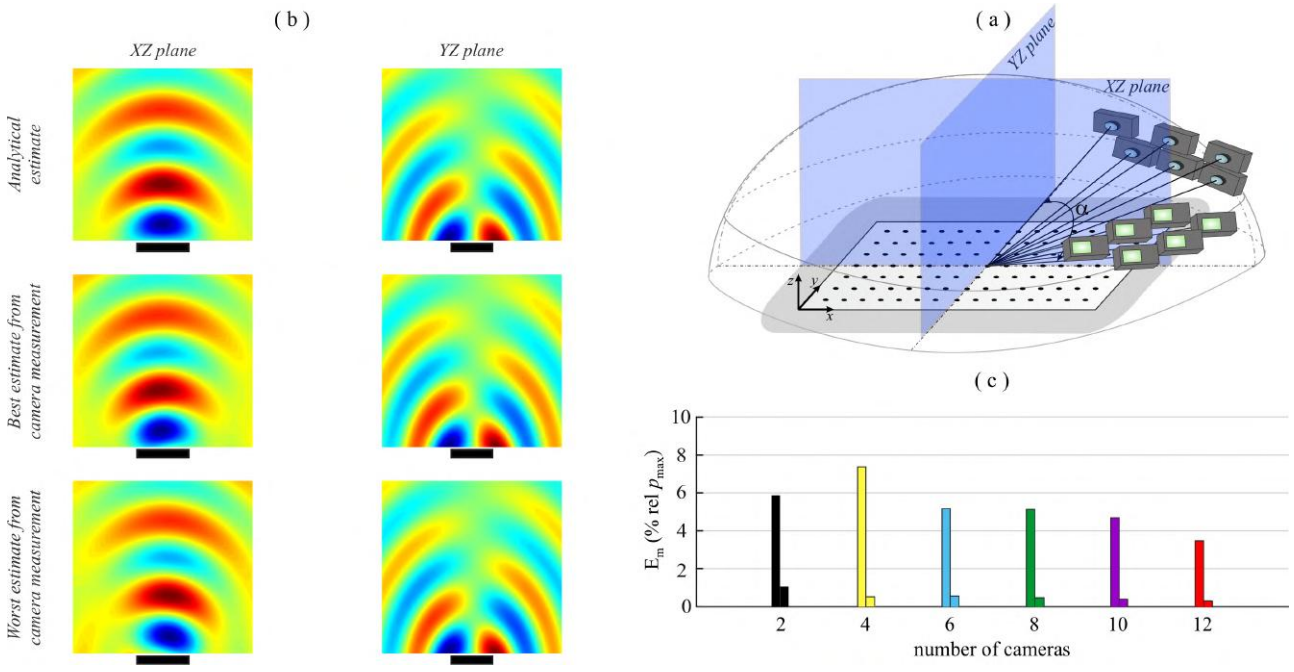

Figure 6.34: Third deflection shape: (a) multiple cameras case study 4c; (b) comparison between ideal (i.e. from analytical model), best and worst case (i.e. from best and worst reconstructed flexural vibration with cameras setup) acoustic fields; (c) histogram of the mean error.

The results presented in Figs. 6.32 - 6.34 indicate that, as pairs of cameras with increasingly larger aperture angles are added, the accuracy of the estimate increases. For instance, according to Plot (c) of Figs. 6.32 - 6.33, when the measurement setup passes from 2 cameras (1 pair) to 12 cameras (6 pairs) the average error of the estimate passes from about 2% to 0.5%. The results of Fig. 6.34 Plot (c), which refers to the acoustic radiation obtained from the reconstruction of the third flexural deflection

shape, show that the error of the estimate of the acoustic radiation still tends to decrease but with smaller values. In particular, when the measurement setup passes from 1 pair of cameras to 6 pairs of cameras the average error falls from 1% to less than 0.5%.

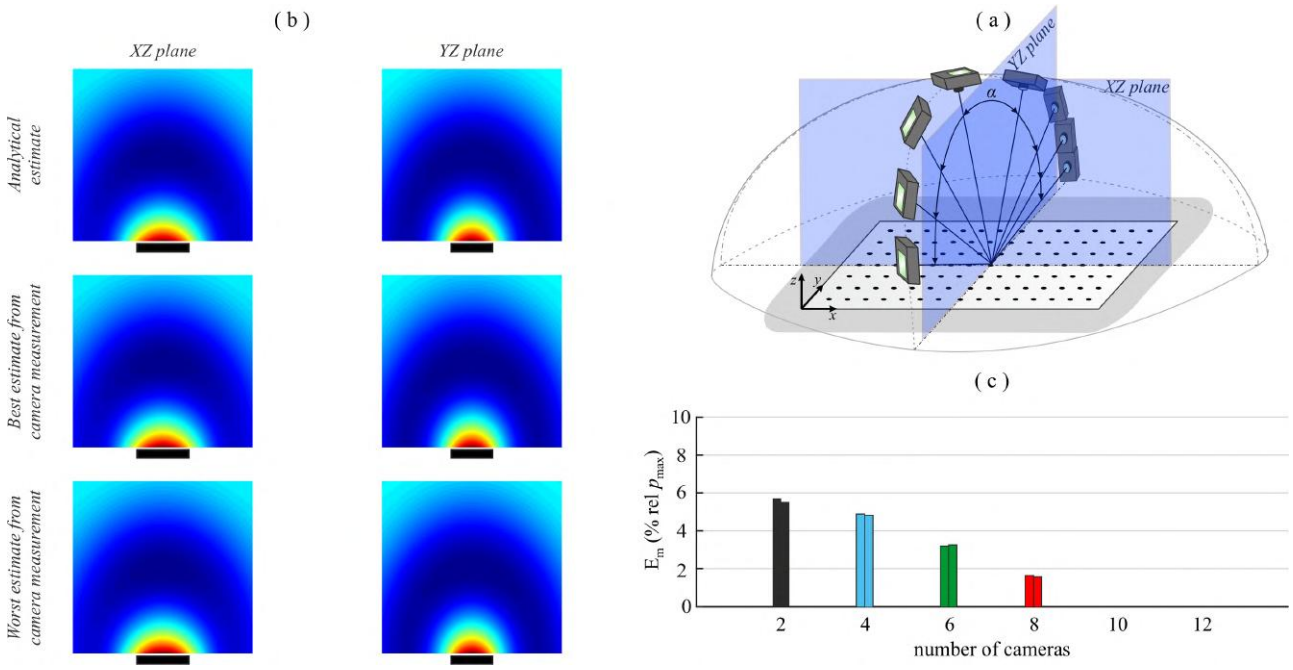

Figure 6.35: First deflection shape: (a) multiple cameras case study 4d; (b) comparison between ideal (i.e. from analytical model), best and worst case (i.e. from best and worst reconstructed flexural vibration with cameras setup) acoustic fields; (c) histogram of the mean error.

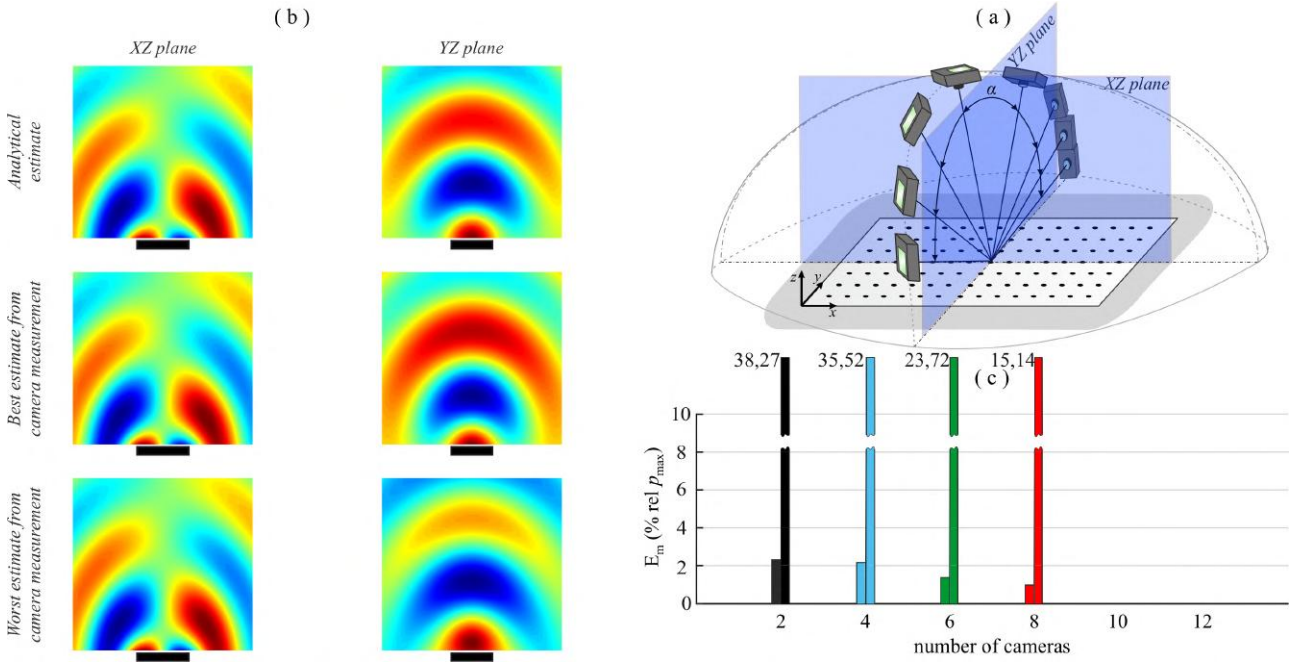

Figure 6.36: Second deflection shape: (a) multiple cameras case study 4d; (b) comparison between ideal (i.e. from analytical model), best and worst case (i.e. from best and worst reconstructed flexural vibration with cameras setup) acoustic fields; (c) histogram of the mean error.

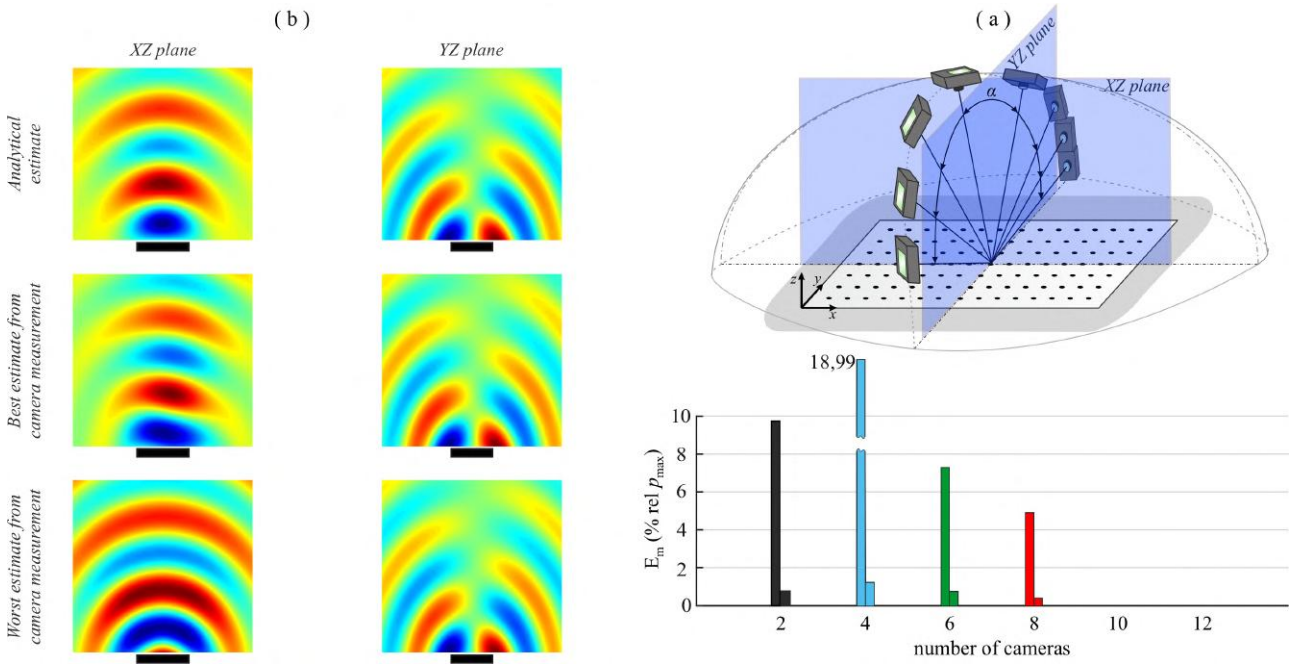

Figure 6.37: Third deflection shape: (a) multiple cameras case study 4d; (b) comparison between ideal (i.e. from analytical model), best and worst case (i.e. from best and worst reconstructed flexural vibration with cameras setup) acoustic fields; (c) histogram of the mean error.

In parallel, the results presented in Figs. 6.35 - 6.36 show that, as cameras with increasingly larger aperture angle are added, the accuracy of the estimate significantly increases. Indeed, Plot (c) of Fig. 6.35 indicates that, when the measurement setup passes from 2 cameras (1 pair) to 8 cameras (4 pairs), the average error of the estimate falls form 6% to 2% while Plot (c) of Fig. 6.36 shows a decrement of the average error from about 2% to less than 1%. However, when the estimate of the acoustic radiation is based on the reconstruction of the third flexural deflection shape, that is the case analyzed in Fig. 6.37, the average error presents again a random distribution with respect to the increase of the number of the cameras. Nevertheless, this error never exceed 1.5%.

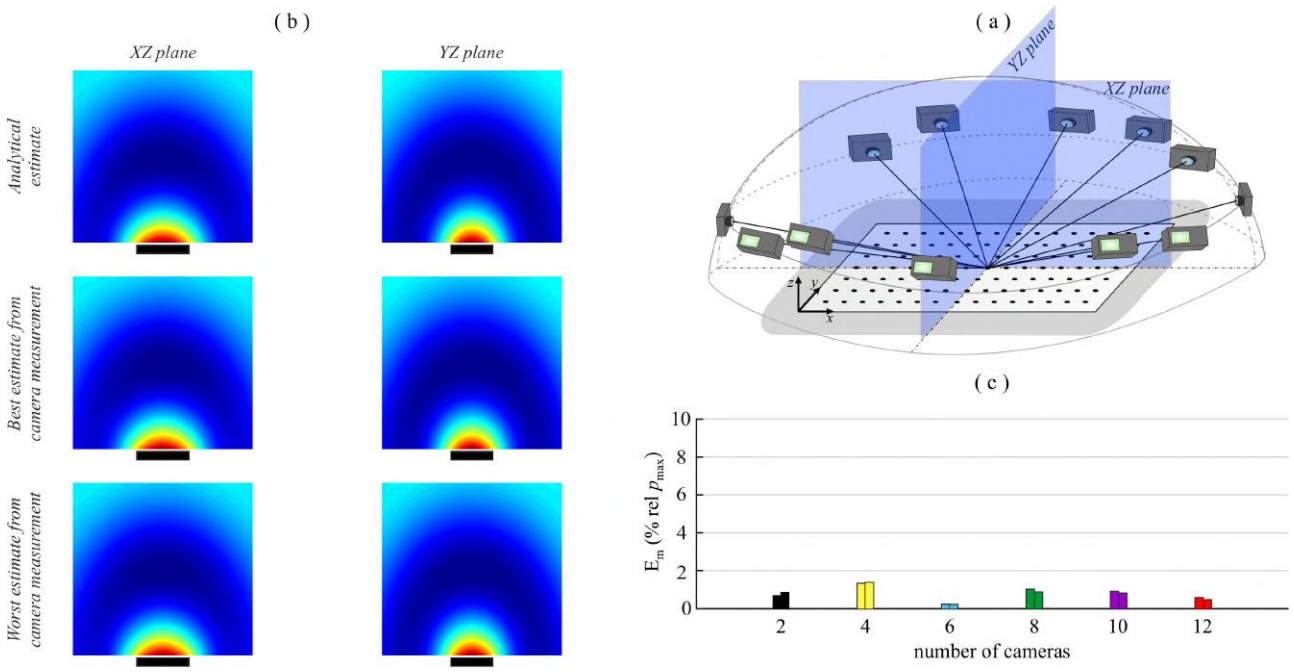

Figure 6.38: First deflection shape: (a) multiple cameras case study 4e; (b) comparison between ideal (i.e. from analytical model), best and worst case (i.e. from best and worst reconstructed flexural vibration with cameras setup) acoustic fields; (c) histogram of the mean error.

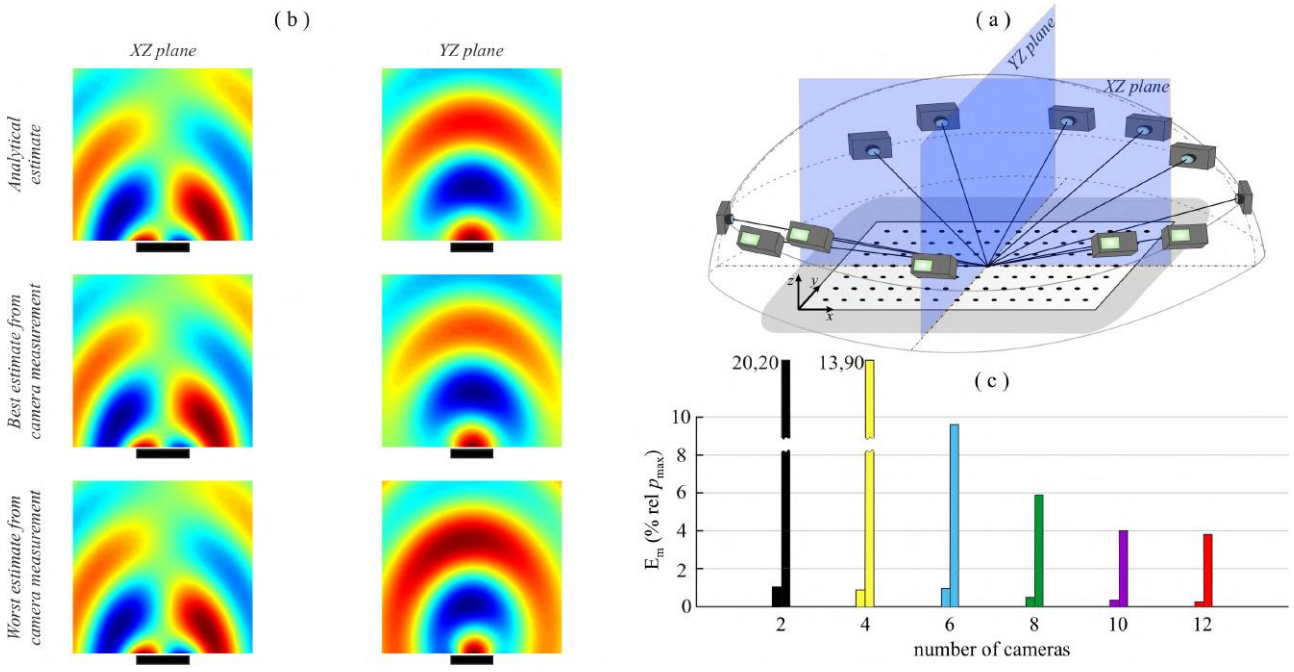

Figure 6.39: Second deflection shape: (a) multiple cameras case study 4e; (b) comparison between ideal (i.e. from analytical model), best and worst case (i.e. from best and worst reconstructed flexural vibration with cameras setup) acoustic fields; (c) histogram of the mean error.

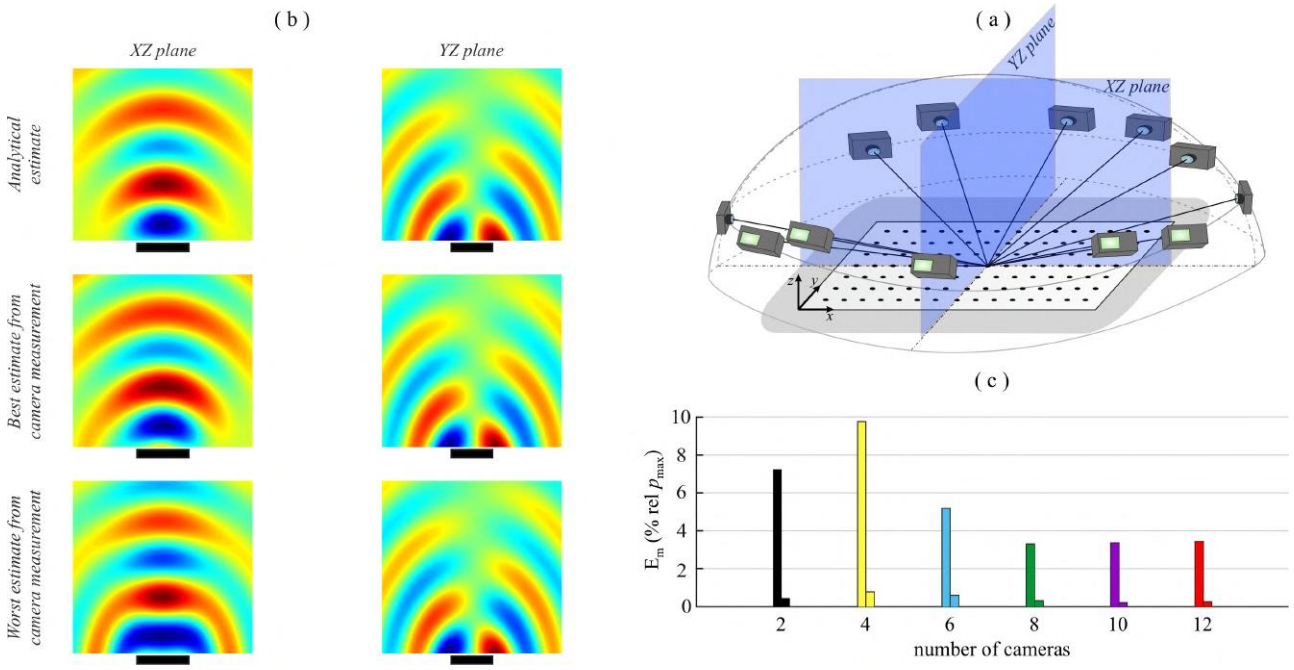

Figure 6.40: Third deflection shape: (a) multiple cameras case study 4e; (b) comparison between ideal (i.e. from analytical model), best and worst case (i.e. from best and worst reconstructed flexural vibration with cameras setup) acoustic fields; (c) histogram of the mean error.

The last case 4e presented in Figs. 6.38 - 6.40 considers the estimate of the sound radiation obtained from the reconstruction of the first three flexural deflection shapes of the plate considering a setup with cameras over a circumference around the plate. The position of each camera is defined in 6.2 - Cases 4e. The results presented in Figs. 6.38 - 6.40 indicate that, as pairs of cameras are added over the circumference, the accuracy of the estimate does not vary significantly. For instance, according to Plot (c) of Figs. 6.38 - 6.40, when the measurement setup passes from 2 cameras (1 pair) to 12 cameras (6 pairs) the average error of the estimate of the acoustic radiation is always less than 2% and does not have a consistent variation with respect to the increase of the number of the cameras.

6.3 Concluding remarks

This chapter has presented a simulation focussed on the estimate of the sound radiation based on the measurement of flexural vibration of distributed structures with multiple cameras. The study has considered the model problem introduced in Chapter 4 composed by a plate excited by a tonal force at the first three fundamental resonance frequencies of the plate flexural vibration. Thus, in this chapter, the measurements of the plate deflection shapes at these frequencies, which accurately approximates the first three flexural mode shapes, have been considered and then, from each of the measured deflection shapes, the acoustic field radiated by the plate has been estimated. The study showed how the accuracy of the estimate of the sound radiation varies with respect to:

1. the distance of the cameras from the test structure;
2. the angle of aperture between the cameras;
3. the elevation angle of the cameras;
4. the resolution of the cameras;
5. the disposition and number of cameras.

Differently to what found for the measurement of the cantilever beam and of the plate flexural modes, in Chapters 3 and 4 respectively, the accuracy of the reconstructed sound field radiation does not show a regular trend with respect to the parameters listed above. As seen in Section 4.2 of Chapter 4, the reconstruction of the flexural deflection shape of a structure, in this case a plate, is dependent from the varied parameter considered: thus, the reconstructed position of each marker on the structure presents errors in defect or in excess with respect of the effective position of the marker. As seen in section 6.1, each elementary radiator, in which the structure is discretized, can be seen as a vibrating piston, therefore each marker can be seen itself as the centre of the surface of a vibrating piston (see Fig. 6.2). Consequently, an error in defect of reconstruction of the position of the marker corresponds to a piston generating an acoustic pressure which is underestimated. On the contrary, an error in excess of reconstruction of the position of the marker corresponds to a piston generating an acoustic pressure which is overestimated. The total average error of the estimate of the acoustic radiation of Eq. 6.8 is the result of a sum of underestimated and overestimated values due to the approximated contributions of acoustic pressure deriving from the reconstructed positions of the elementary vibrating pistons in which the structure has been discretized. Overall, these errors compensate in the computation of Rayleigh's integral. This phenomenon leads to two main considerations on the average errors for the estimate of the sound radiation considered in Subsections 6.2.1 - 6.2.4: first, the average error of the estimate of the sound radiation appears to have small values, i.e. always $< 10\%$ (except over the YZ plane, when the estimate of the sound radiation is obtained from the reconstruction of the second

flexural deflection shape, and over the XZ plane, when the estimate of the sound radiation is obtained from the reconstruction of the third flexural deflection shape); second, there is no correspondence between the average error of reconstruction of the flexural deflection shape seen in seen in Sections 4.2.1 - 4.2.4 of Chapter 4 and the average error of the estimate of the acoustic radiation seen in this chapter. In particular, the average error of the estimate of the sound radiation presents mostly a non-consistent variation for each varied parameter.

Chapter 7

Conclusions

This thesis presented a comprehensive study upon the effectiveness of the implementation of setups composed by multiple (i.e. more than two) cameras for the measurement of the flexural vibration and the estimate of the sound radiation emitted by distributed structures.

The thesis is divided into six main chapters, plus this last concluding one. Chapter 1 of the thesis introduced the most common techniques employed in vibration and sound radiation measurements. In Chapter 2, the theoretical aspects on the working principles of cameras were revised, with particular attention on the pinhole model and the triangulation technique. Chapter 3 was divided into two main parts. In the first part of the chapter the principles of the flexural vibrations of a cantilever beam were revised. In the second part, the influence on the accuracy of vibration measurements of five parameters, such as the distance of the cameras from the measured structure, the aperture between the cameras, the elevation angle of the cameras, the resolution of the cameras and the number of cameras, was investigated by means of a parametric study. In Chapter 4, the results obtained in Chapter 3, for the case of a cantilever beam, were extended to the case of a planar structure, i.e. a plate. This chapter was divided into two parts: a first part, where the theoretical principles for the flexural vibrations of a plate were introduced, and a second part, in which, similarly to Chapter 3, the influence on the accuracy of reconstruction of the flexural vibrations of a plate of the five parameters listed above was investigated. In Chapter 5, the findings of the parametric studies conducted in Chapter 3 and Chapter 4 on the accuracy of the measurements of flexural vibrations of distributed structures were experimentally verified. More specifically, in this chapter, the same distributed structure of Chapter 3, i.e. a cantilever beam, was considered. This chapter was divided into two parts. In the first part, the experimental setup and procedures were presented. In the second part, the influence on the accuracy of the measurement of the first flexural deflection shape of the cantilever beam with increasing resolution cameras and an increasing number of cameras were experimentally examined. Finally, in Chapter 6 the estimate of the sound radiation emitted by distributed structures was considered. In particular, in this chapter, the same distributed structure of Chapter 4, i.e. a plate, was considered. This chapter was

divided into two sections. In the first section the theoretical principles of sound radiation were revised. Thus, in the second section, a parametrical study was performed. The main goal of this parametric study was to estimate the sound radiation emitted by the reconstructed first three flexural deflection shapes of the plate given by the parametric studies of Chapter 4. Thus, in other words, the influence on the estimate of the sound radiation of the five parameters listed above, which affect the reconstruction of the flexural deflection shapes and by consequence the generated acoustic field, was examined.

The work of this thesis led to the following conclusions:

- Chapter 3 showed that the accuracy of the measurement of a beam flexural deflection shapes increases as:

    1. the cameras are arranged closer to the beam. This is due to the fact that a reduction of the distance between the cameras and the structure implies a reduction of the pixel footprint on the object, which means an increased resolving power of the cameras;
    2. the cameras in the measurement setup are separated by large aperture angles. This conclusion is related to the geometrical principles on which the triangulation technique relies on (as seen in Chapter 2). In fact, the accuracy of the detection of the position of a point in space depends on the angle of incidence with which the optical ray of a camera impinges on the scene: this, in turn, is dependent from the angle of separation between the cameras;
    3. the cameras in the measurement setup are disposed with small elevation angles. In fact, cameras which are disposed perpendicular (i.e. with large elevation angles) with respect to a vibrating object, are insensitive to vertical displacements. However, on the other hand, too small elevation angles worsen the accuracy of the localization of the markers, which is a relevant problem in the actual measurement process;
    4. the cameras have of a high spatial resolution. Similarly to the considerations done about the influence of the distance on the accuracy of a measurement, an increase of the resolution determines a decrement of the pixel footprint on the object which, by consequence, leads to a larger resolving power of the cameras;
    5. the number of cameras is increased. This conclusion is due to the fact that an increasing number of cameras implies an increasing number of equation in the resolution of the triangulation process which is a non-linear least squares problem. Thus, increasing the number of equations reduces the variance of the solution and therefore increases the accuracy of the triangulation process.

- Similarly, Chapter 4 showed that the accuracy of the measurement of the flexural deflection shapes of a plate, increases as:

    1. the cameras are arranged as close as possible to the plate;

2. the cameras are separated by large azimuthal angles;
3. the optical axis of the cameras impinges the structure with small elevation angles;
4. the cameras present high resolutions;
5. the number of cameras is increased.

Here again, these concluding remarks were derived from a parametric study only. Nevertheless, these results are in accordance with the ones of Chapter 3.

- In Chapter 5, the findings of Chapter 3 and Chapter 4 on the accuracy of the measurement of the flexural vibrations of distributed structures were experimentally validated. In particular, it was verified that the accuracy of the measurement increases as:

  1. the resolution of the cameras is raised;
  2. the number of cameras is increased.

  As previously mentioned, the experimental study was conducted on a cantilever beam. However, the findings of this study are in accordance with those of Chapter 3, which, in turn are in accordance with the results of Chapter 4. Thus, it is reasonable to conclude that the experimental work validated the simulation results of both Chapter 3, in which a cantilever beam is considered, and Chapter 4, where a plate is considered.

- Chapter 6 showed that the considerations on the accuracy of reconstruction of the flexural deflection shapes of a plate seen in Chapter 4, are not directly applicable for the estimate of the sound radiation emitted by a plate. More specifically, the five parameters here considered (i.e. the distance of the cameras from the structure, the aperture between the cameras, the elevation angle of the cameras, the resolution and the number of cameras), which influence the accuracy of reconstruction of the deflection shapes and, thus, the sound radiation emitted by the structure, affect the accuracy of the estimate of the sound radiation in a non-consistent way. This is due to the fact that the sound radiation depends on the combination of the individual contribution of vibrating elements, so that estimation errors can compensate or be amplified depending on the particular spatial position of the considered point.

In conclusion, this study has demonstrated the effectiveness of the implementation of a multiple low-resolution cameras setup for increasing the accuracy of the measurements of flexural vibrations of distributed structures. These measurements can also be used to estimate the sound radiation with acceptable accuracy. This work has shown that the use of multiple, relatively cheap, low-resolution cameras can be beneficial to perform vibration measurements in practical applications.

7.1 Future work

As seen in the previous section, this work mainly aimed to demonstrate how five parameters of camera setups affect the accuracy of reconstruction of the deflection shape of two simple structures, such as a cantilever beam and a plate, and how they influence the estimate of the sound radiation generated by a plate. Particular attention was given to the effect derived by the addition of multiple cameras to the setup. Thus, some possible extensions of this work are:

- Performing experimental measures to validate the findings of the parametric study of Section 3.3 for more than one flexural deflection shape;
- Performing experimental measures on the cantilever beam involving more than one line of markers aligned only on the longitudinal axis. As a consequence, it could be possible to investigate not only flexural deflection shapes but also torsional ones;
- Performing experimental measures to validate the findings of the parametric study of Section 4.2 about the influence of the five considered parameter on the accuracy of reconstruction of the flexural deflection shape of a plate. Simulation results were validated by actual experiments measuring the flexural deflection shape of a cantilever beam;
- Performing experimental measures to validate the findings of the parametric study of Section 6.2 about the influence of the five considered parameters on the estimate of the sound radiation;
- Verifying the effectiveness of multiple cameras when structures characterized by intricate shapes with no plane of symmetry are measured.

References

[1] R. Del Sal, L. Dal Bo, E. Turco, A. Fusiello, A. Zanarini, R. Rinaldo, P. Gardonio, *Vibration measurements with multiple cameras*, Mech. Syst. Signal Pr. 157 (2021) 107742.

[2] F. Fahy, P. Gardonio, *Sound and Structural Vibration. Radiation, Transmission and Response*, second ed. Academic Press, London, 2007.

[3] L. Meirovitch, *Principles and Techniques of Vibration*, Prentice Hall, Upper Saddle River, 1997.

[4] J. Baqersad, P. Poozesh, C. Niezrecki, P. Avitabile, *Photogrammetry and optical methods in structural dynamics - a review*, Mech. Syst. Signal Pr. 86 (2017) 17-34. https://doi.org/10.1016/j.ymssp.2016.02.011.

[5] G. Cloud, *Optical Methods of Engineering Analysis, Cambridge University Press*, 1998.

[6] T. Schmidt, J. Tyson, K. Galanulis, *Full-field dynamic displacement and strain measurement using advanced 3d image correlation photogrammetry: part 1*, Exp. Tech. 27 (2003) 47-50,. http://dx.doi.org/10.1111/j.1747-1567.2003.tb00115.x.

[7] D.L.B.R. Jurjo, C. Magluta, N. Roitman, P.B. Gonçalves, *Experimental methodology for the dynamic analysis of slender structures based on digital image processing techniques*, Mech. Syst. Signal Process. 24 (2010) 1369-1382. http://dx.doi.org/10.1016/j.ymssp.2009.12.006.

[8] A. Zanarini, *On the role of spatial resolution in advanced vibration measurements for operational modal analysis and model updating*, Proceedings of the ISMA2014 Conference, 2014.

[9] C. Warren, C. Niezrecki, P. Avitabile, P. Pingle, *Comparison of FRF measurements and mode shapes determined using optically image based, laser, and accelerometer measurements*, Mech. Syst. Signal Process, 25 (2011) 2191-2202. http://dx.doi.org/10.1016/j.ymssp.2011.01.018.

[10] G. Rosi, R. Paccapeli, J. Pouget, F. dell'Isola, *Control of sound radiation and transmission by distributed passive piezoelectric networks*, 16th International Congress on Sound and Vibration 2009, ICSV 2009. 3.

[11] R. Burtch, *History of photogrammetry, Notes of the Center for Photogrammetric Training*, (2004).

[12] A. Gruen, *Fundamentals of videogrammetry a review*, Hum. Mov. Sci.16 (1997) 155-187. https://doi.org/10.1016/S0167-9457(96)00048-6.

[13] W. H. Peters; W. F. Ranson, *Digital imaging techniques in experimental stress analysis*, OPTICE.

[14] M. Sutton, W. Wolters, W. Peters, W. Ranson, S. McNeill, *Determination of displacements using an improved digital correlation method*, Image and Vision Computing Vol. 4 (1983) pp. 143-150.

[15] T. Chu, W. Ranson, M. Sutton, *Applications of digital-image-correlation techniques to experimental mechanics*, Exp. Mech. 25 (1985) 232-244.

[16] P. Luo, Y. Chao, M. Sutton, W. Peters III, *Accurate measurement of three-dimensional deformations in deformable and rigid bodies using computer vision*, Exp.Mech.33 (1993) 123-132. https://doi.org/10.1007/BF02322488.

[17] L. Yu, B. Pan, *Single-camera high-speed stereo-digital image correlation for full-field vibration measurement*, Mech. Syst. Signal Pr., 94 (2017) 374-383. https://doi.org/10.1016/j.ymssp.2017.03.008.

[18] S. Barone, P. Neri, A. Paoli, A.V. Razionale, *Low-frame-rate single camera system for 3D full-field high-frequency vibration measurements*, Mech. Syst. Signal Pr., vol. 123, pp. 143?152, 2019. https://doi.org/10.1016/j.ymssp.2019.01.016.

[19] S. Bhowmicka, S. Nagarajaiaha, *Identification of full-field dynamic modes using continuous displacement response estimated from vibrating edge video*, J. Sound Vib., Vol. 489 (2020), 115657. https://doi.org/10.1016/j.jsv.2020.115657.

[20] D. Gorjup, J. Slavic, A. Babnik, M. Boltezar, *Still-camera multiview Spectral Optical Flow Imaging for 3D operating-deflection-shape identification*, Mech. Syst. Signal Pr., Vol. 152 (2021), 107456. https://doi.org/10.1016/j.ymssp.2020.107456.

[21] M.A. Sutton, J.J. Orteu, H. Schreier, *Image Correlation for Shape, Motion and Deformation Measurements: Basic Concepts, Theory and Applications,*, Springer Science & Business Media, 2009.

[22] T. Liu, A.W. Burner, T.W. Jones, D.A. Barrows, *Photogrammetric techniques for aerospace applications*, Prog. Aerosp. Sci. 54 (2012) 1-58.

[23] X. Su, Q. Zhang, *Dynamic 3-D shape measurement method: a review*, Opt. Lasers Eng. 48 (2010) 191-204
http://dx.doi.org/10.1016/j.optlaseng.2009.03.012.

[24] R. Jiang, D.V. Jáuregui, K.R. White, *Close-range photogrammetry applications in bridge measurement: literature review*, Measurement 41 (2008) 823-834.

[25] C.C. Chang, Y.F. Ji, *Flexible videogrammetric technique for three-dimensional structural vibration measurement*, J. Eng. Mech. 133 (2007) 656-664.
http://dx.doi.org/10.1061/(ASCE)0733-9399(2007)133:6(656).

[26] J. Carr, J. Baqersad, C. Niezrecki, P. Avitabile, *Full-field dynamic strain on wind turbine blade using digital image correlation techniques and limited sets of measured data from photogrammetric targets*, Exp. Tech. http://dx.doi.org/10.1111/ext.12129.

[27] K.S. Son, H.S. Jeon, J.H. Park, J.W. Park, *Vibration displacement measurement technology for cylindrical structures using camera images*, Nucl. Eng. Technol.
http://dx.doi.org/10.1016/j.net.2015.01.011.

[28] R.C. Gonzalez, E. Richard, Woods, *Digital Image Processing*, Prentice Hall Press, ISBN 0-201-18075-8, 2002.

[29] G. Busca, A. Cigada, M. Vanali, E. Zappa, *Vision-based Vibration Monitoring of a Large Steel Structure*, Experimental Vibration Analysis for Civil Engineering Structures (EVACES), Experimental Vibration Analysis for Civil Engineering Structures, Varenna, Italy, 2011, 561-568.

[30] S. Patsias, W. Staszewskiy, *Damage detection using optical measurements and wavelets*, Struct. Health Monit. 1 (2002) 5-22.

[31] U.P. Poudel, G. Fu, J. Ye, *Structural damage detection using digital video imaging technique and wavelet transformation*, J. Sound Vib. 286 (2005) 869-895.
http://dx.doi.org/10.1016/j.jsv.2004.10.043.

[32] M.G. Gilbert, S.S. Welch, *STS-74/MIR photogrammetric appendage structural dynamics experiment*, Proceedings of the 1996 37th AIAA/ASME/ASCE/AHS/ASC Structures, Structural Dynamics, and Materials Conference. Part 4 (of 4), April 15, 1996-April 17, 1996, AIAA, Salt Lake City, UT, USA, 1996, 1594-1604.

[33] M.G. Gilbert, S.S. Welch, R.S. Pappa, M.E. Demeo, *STS-74/Mir photogrammetric appendage structural dynamics experiment preliminary data analysis*, Proceedings of the 1997 38th AIAA/ASME/ASCE/AHS/ASC Structures, Structural Dynamics, and Materials Conference. Part 4 (of 4), April 7, 1997-April 10, 1997, AIAA, Kissimmee, FL, USA, 1997, 566-576.

[34] L. Yu, B. Pan, *Single-camera stereo-digital image correlation with a four-mirror adapter: optimized design and validation*, Opt. Laser. Eng. 87 (2016) 120-128.
https://doi.org/10.1016/j.optlaseng.2016.03.014.

[35] J. R. Blandino, R. S. Pappa, J. T. Black, *Modal identification of membrane structures with videogrammetry and laser vibrometry*, 44th AIAA/ASME/ASCE/AHS/ASC Structures, Structural 25 Dynamics and Materials Conference, 07-10 April 2003, Norfolk Virginia, 1745 (2003).
https://doi.org/10.2514/6.2003-1745.

[36] H. Lee, H. Rhee, *3-D measurement of structural vibration using digital close-range photogrammetry*, Sensor Actuat. A-Phys. 196 (2013) 63-69.
https://doi.org/10.1016/j.sna.2013.03.010.

[37] P. Frank Pai, D.Feng, Y. Duan, *High-fidelity camera-based method for noncontact vibration testing of structures*, 54th AIAA/ASME/ASCE/AHS/ASC Structures, Structural Dynamics and Materials Conference, 8-11 April 2013, Boston Massachusetts.
http://doi.org/10.2514/6.2013-1898.

[38] J. Baqersad, C. Niezrecki, P. Avitabile, *Full-field dynamic strain prediction on a wind turbine using displacements of optical targets measured by stereophotogrammetry*, Mech. Syst. Signal Pr. 62-63 (2015) 284?295.
https://doi.org/10.1016/j.ymssp.2015.03.021.

[39] P. Poozesh, J. Baqersad, C. Niezrecki, P. Avitabile, Eric Harvey, Rahul Yarala, *Large-area photogrammetry based testing of wind turbine blades*, Mech. Syst. Signal Pr. 86B (2017) 98-115.
https://doi.org/10.1016/j.ymssp.2016.07.021.

[40] J. Orteu, *3-D computer vision in experimental mechanics*, Opt. Laser Eng. 47 (2009) 282-291, 2009.
https://doi.org/10.1016/j.optlaseng.2007.11.009.

[41] M. N. Helfrick, C. Niezrecki, P. Avitabile, T. Schmidt, *3D digital image correlation methods for full-field vibration measurement*, Mech. Syst. Signal Pr. 25 (2011) 917-927.
https://doi.org/10.1016/j.ymssp.2010.08.013.

[42] W. Wang, J. E. Mottershead, A. Ihle, T. Siebert, H. R. Schubach, *Finite element model updating from full-field vibration measurement using digital image correlation*, J. Sound Vib. 330 (2011) 1599-1620.
https://doi.org/10.1016/j.jsv.2010.10.036.

[43] J. Baqersad, J. Carr, T. Lundstrom, C. Niezrecki, P. Avitabile, M. Slattery, *Dynamic characteristics of a wind turbine blade using 3D digital image correlation*, Proc. SPIE 8348, Health Monitoring of

Structural and Biological Systems 2012, 834821 (20 April 2012).
https://doi.org/10.1117/12.915377.

[44] J. Carr, J. Baqersad, C. Niezrecki, P. Avitabile, M. Slattery, *Dynamic Stress-Strain on Turbine Blades Using Digital Image Correlation Techniques Part 2: Dynamic Measurements*. In: Mayes R. et al. (eds) Topics in Experimental Dynamics Substructuring and Wind Turbine Dynamics, Volume 2. Conference Proceedings of the Society for Experimental Mechanics Series (2012). Springer, New York, NY.
https://doi.org/10.1007/978-1-4614-2422-2_21.

[45] F. Chen, X. Chen, X. Xie, X. Feng, L. Yang, *Full-field 3D measurement using multi-camera digital image correlation system*, Opt. Laser. Eng. 51 (2013) 1044-1052.
https://doi.org/10.1016/j.optlaseng.2013.03.001.

[46] D. Gorjup, J. Slavic, M. Boltezar, *Frequency domain triangulation for full-field 3D operating-deflection-shape identification*, Mech. Syst. Signal Pr. 133 (2019) 106287.
https://doi.org/10.1016/j.ymssp.2019.106287.

[47] A. Zanarini, *Broad frequency band full field measurements for advanced applications: Point-wise comparisons between optical technologies*, Mech. Syst. Signal Pr. 98 (2018) 968-999.
https://doi.org/10.1016/j.ymssp.2017.05.035.

[48] A. Zanarini, *Competing optical instruments for the estimation of Full Field FRFs*, Measurement 140 (2019) 100-119.
https://doi.org/10.1016/j.measurement.2018.12.017.

[49] A. Zanarini, *Full field optical measurements in experimental modal analysis and model updating*, J. Sound Vib. 442 (2019) 817-842.
https://doi.org/10.1016/j.jsv.2018.09.048.

[50] J. Javh, J. Slavic, M. Boltezar, *The subpixel resolution of optical-flow-based modal analysis*, Mech. Syst. Signal Pr. 88 (2017) 89-99.
https://doi.org/10.1016/j.ymssp.2016.11.009.

[51] J. Javh, J. Slavic, M. Boltezar, *High frequency modal identification on noisy high-speed camera data*, Mech. Syst. Signal Pr. 98 (2018) 344-351.
https://doi.org/10.1016/j.ymssp.2017.05.008.

[52] J. Javh, J. Slavic, M. Boltezar, *Measuring full-field displacement spectral components using photographs taken with a DSLR camera via an analogue Fourier integral*, Mech. Syst. Signal Pr. 100 (2018) 17-27.
https://doi.org/10.1016/j.ymssp.2017.07.024.

[53] E. Shechtman, Y. Caspi, M. Irani, *Space-Time Super-Resolution*, IEEE Trans. Pattern Anal. Mach. Intell. 27 (2005) 531-545.
https://doi.org/10.1109/TPAMI.2005.85.

[54] R. Hartley, A. Zisserman, *Multiple View Geometry in Computer Vision*, Cambridge University Press, Cambridge, 2004.

[55] E. H. Adelson, J. Y. A. Wang, *Single lens stereo with a plenoptic camera*, IEEE Transactions on Pattern Analysis and Machine Intelligence Vol. 14 (1992) pp. 99-106.

[56] T. Beberniss, T. Eason, S. Spottswood, *High-speed 3D digital image correlation measurements of long-duration random vibration; recent advancements and noted limitations*, Proceedings of International Conference on Noise and Vibration Engineering (ISMA), Katholieke Universiteit Leuven, Belgium, 2012.

[57] P. Gardonio, M.J. Brennan, *Mobility and Impedance Methods in Structural Dynamics*, in F. Fahy, J. Walker (Eds), Advanced Applications in Acoustics, Noise and Vibration, Spon Press London, 2004, pp. 387-447.

[58] P. Gardonio, E. Turco, *Tuning of vibration absorbers and Helmholtz resonators based on modal density/overlap parameters of distributed mechanical and acoustic systems*, J. Sound Vib. 451 (2019) 32-70.
https://doi.org/10.1016/j.jsv.2019.03.015.

[59] P.F. Sturm, S.J. Maybank, *On Plane-Based Camera Calibration: A General Algorithm, Singularities, Applications*, Proceedings of the 1999 IEEE Computer Society Conference on Computer Vision and Pattern Recognition, Fort Collins, CO, USA, 1999, vol. 1, pp. 432-437.
https://doi.org/10.1109/CVPR.1999.786974.

[60] J.-Y. Bouget, Camera Calibration Toolbox for Matlab, http://www.vision.caltech.edu/bouguetj/calib_doc/, 2015

[61] Z. Zhang, *Flexible Camera Calibration by Viewing a Plane from Unknown Orientations*, in Proceedings of the Seventh IEEE International Conference on Computer Vision, Kerkyra, Greece, 1999.
https://doi.org/10.1109/ICCV.1999.791289.

[62] A. Fusiello, Computer Vision Toolbox for Matlab, Camera Calibration Toolbox for Matlab, http://www.dpia.uniud.it/fusiello/demo/toolkit, 2019

Appendix A

Optics of thin lenses

In this appendix the fundamental principles of lenses are revised. Usually, the optics of a camera is composed by a combination of lenses. However, for simplicity, in this appendix a simplified optical model, composed by a single thin lens, is considered. The model is illustrated in Fig. A.1.

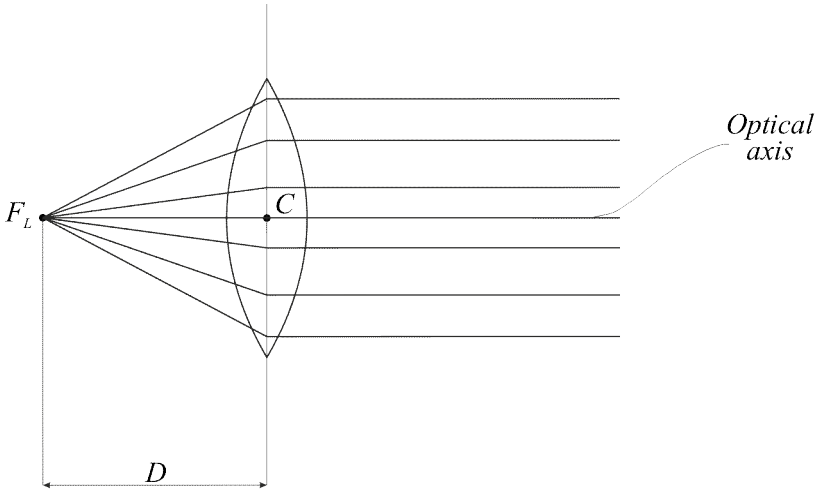

Figure A.1: Working principle of a thin lens.

The principal properties of thin lenses can be summarized as follows:

1. light rays that are parallel to the optical axis are refracted by the lens. The refraction forces the light rays to pass through the *focus of the lens*, $\mathbf{F}_L$;

2. light rays that pass through the *center of the lens* $\mathbf{C}$ are unaltered.

Furthermore, the distance between $\mathbf{F}_L$ and $\mathbf{C}$ is the so-called *focal length of the lens*, D.

A generic point $\mathbf{M}$ of a scene is now considered: the image of this point, i.e. $\mathbf{M}'$, which is the so-called *conjugate point*, can be individuated from the intersection between the light ray parallel to the optical axis, which is refracted by the lens and passes through $\mathbf{F}_L$, and the unaltered light ray which passes through $\mathbf{C}$ as illustrated in Fig. A.2.

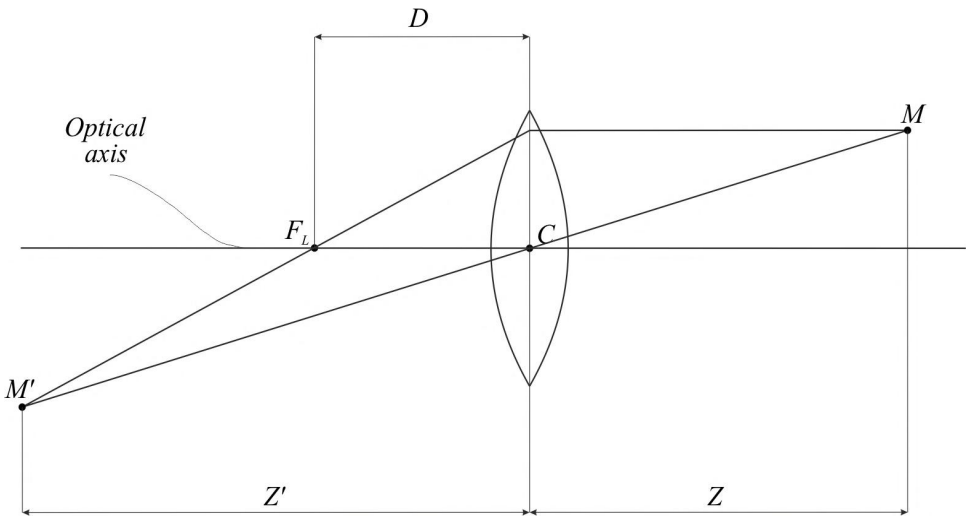

Figure A.2: Construction of the image of a point.

Therefore, by using the theorems of similar triangles, it is possible to write Eq. A.1, which is the so-called *equation of thin lenses*:

$$\frac{1}{Z} + \frac{1}{Z'} = \frac{1}{D}, \tag{A.1}$$

where Z is the distance of the image of the point from the lens, Z' is the distance at which the image of the point is projected on focus and D is the focal length of the lens. If Eq. A.1 is not verified, the image of the point appears out of focus, creating the so-called *circle of confusion*. As long as the circle of confusion does not overcome the dimensions of the photosensitive element, the image is on focus: thus, there is a range of depth in which the points are on focus and this is the so-called *field of depth*. The field of depth is inversely proportional to the diameter of the lens.

Note how the thin lens model is consistent with the pinhole model, with **C** in Fig. A.2 taking the role of the centre of projection. All the rays deviated by the lens toward the image of a point on focus contribute to the amount of light captured by the sensor. It is important also to notice that the focal length of the lens is a different quantity from the focal length of the pinhole camera: that is why a different notation has been used in this appendix even if the two quantities are denoted with the same name in the respectively specific literature.

Appendix B

Optical field

In this appendix, the simplified and most commonly used pinhole model is introduced. A single camera, represented by its center of projection **C** which is distant f (i.e the focal length) from the film or sensor AB, and a point **P** are considered in a CXZ system of reference centered in the center of projection **C** of the camera (Fig. B.1 (a) and (b)).

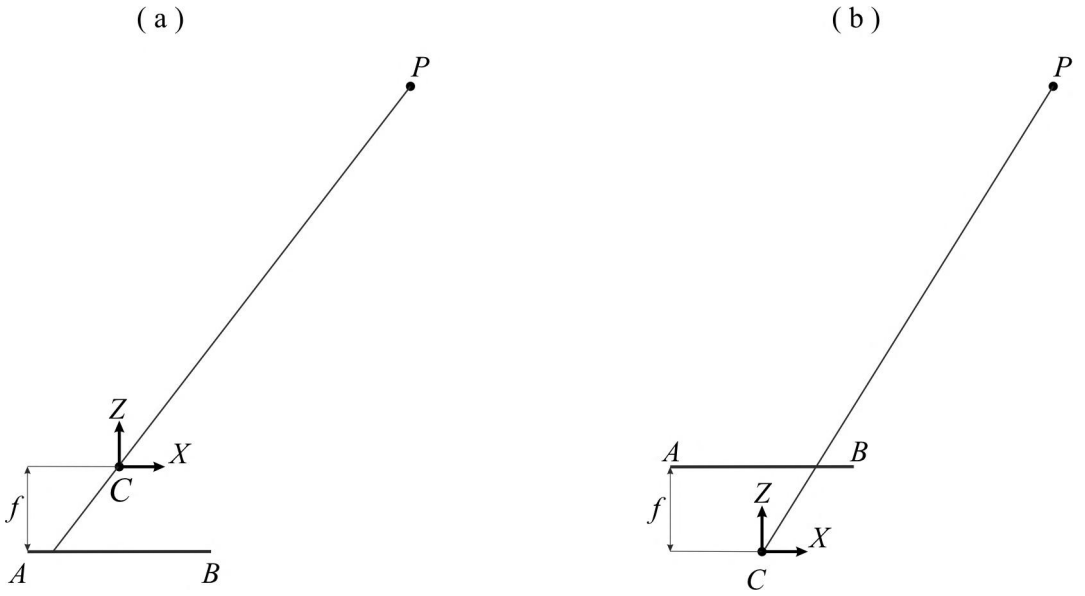

Figure B.1: Pinhole model of a camera: (a) typical pinhole model; (b) simplified pinhole model.

The film (or, in a digital camera, the sensor), represents the image plane of the camera. The typical pinhole model, derived from the physics of the camera, is illustrated in Fig. B.1 (a) (see also the treatment in Chapter 2): here, the image plane is located behind the center of projection. However, in computer vision, the simplified pinhole camera model shown in Fig. B.1 (b), in which the image plane is placed in front of the center of projection, is usually adopted. This model implies that the focal length f is measured along the positive Z semi-axis, which, in turn, implies that f assumes positives values. As a consequence, Eq. 2.8 of Chapter 2 for the pinhole model, here reported in Eq. B.1, can be written without any negative sign

$$\frac{f}{Z} = \frac{u}{X} = \frac{v}{Y}. \tag{B.1}$$

A direct effect of this change of signs, is that the objects of a scene projected on the image plane will no more appear turned upside-down nor left-right.

It is now considered the case in which two cameras are parallel and aligned, i.e. the so called *normal case*.

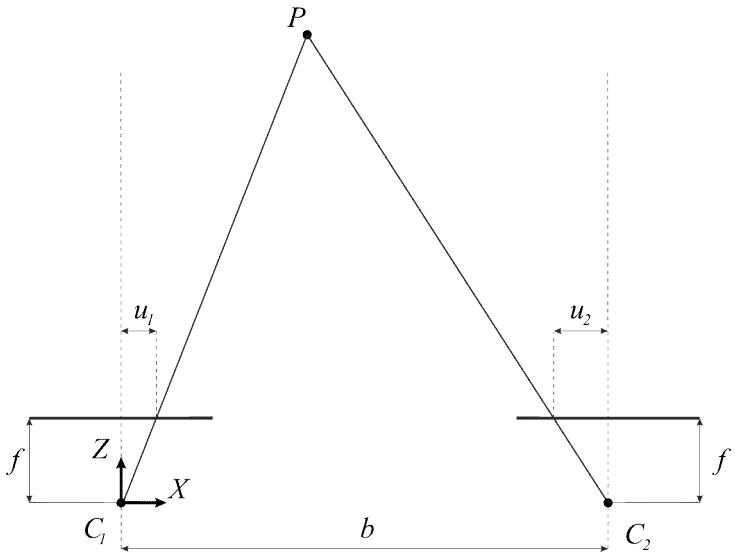

Figure B.2: Triangulation: some definitions.

Thus, with reference to the simple case illustrated in Fig. B.2, it is possible to introduce the so-called *baseline* b, which is the distance between the centers of projection of the cameras, and the so-called *binocular disparity*, given by $u_1 + u_2$.

Appendix C

Homogeneous coordinates

In this appendix, the concept of homogeneous coordinates is analyzed in some detail. To start with, the idea of *perspective projection* is recalled. As shown in Fig. C.1, a camera represented by its center of projection **C** and its image plane R, is considered. The perspective projection allows to convert a point **M** of the 3D space on the image plane of the camera by intersecting the line that passes through **M** and through the center of projection **C** with the image plane (see Fig. C.1).

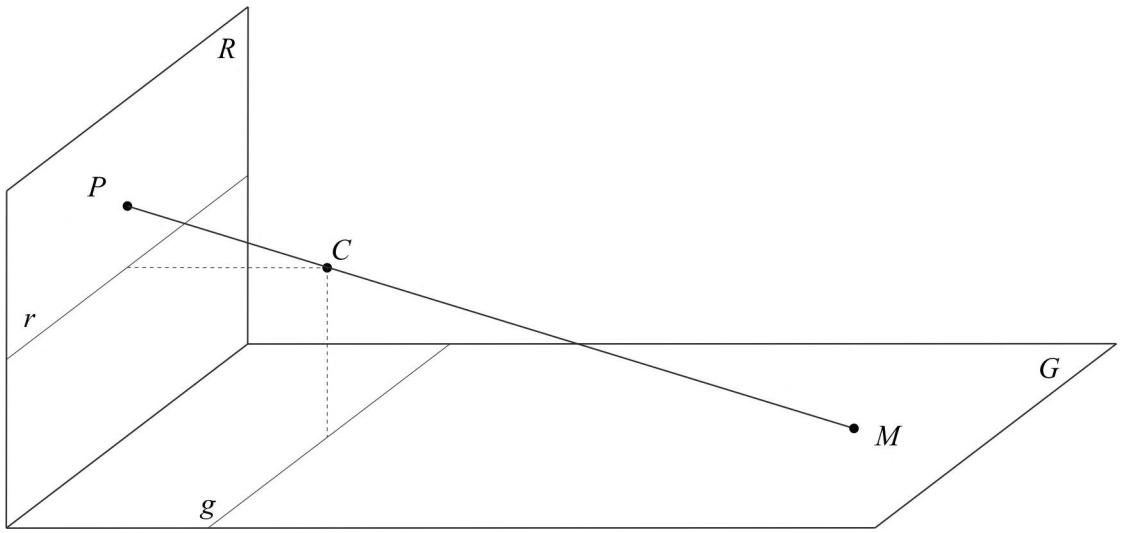

Figure C.1: Perspective projection of a ground plane G orthogonal to the image plane R. Lines g and r are particular cases.

If the projection of a plane G orthogonal to the image plane R is considered, it is possible to notice that line g, the intersection between G and the plane which is parallel to R and includes **C**, cannot be projected on R. Similar consideration can be done for the line r that belongs to R. To avoid this problem, the so-called *line at infinite* is added to the usual Euclidean plane $\mathbb{R}^2$. This is an ideal line which allows to make the following two considerations: a) the projection of line g on the image plane can now be defined and corresponds to the *line at infinite* of R; b) line r, which had no correspondence on plane G, can now be defined and corresponds to the *projection of the line at infinite* of plane G.

The *projective plane* $\mathbb{P}^2$, defined as the plane $\mathbb{R}^2$ with the addition of the line at infinite l_∞, can

now be introduced. In this plane all the lines have one point in common: when two parallel lines are considered, their common point is the so-called *point at infinite*. The introduction of the points at infinite allows to introduce the *homogeneous coordinates*. The position of a generic point identified by a pair of cartesian coordinates (x, y), can be expressed in homogeneous coordinates (u, v, w) with respect to Eq. C.1:

$$x = \frac{u}{w}, \qquad y = \frac{v}{w}. \tag{C.1}$$

Proportional terns of homogeneous coordinates (u, v, w) represent the same point: when $w \neq 0$, the tern represent a *proper* point (finite), whereas when $w = 0$ the tern represents an *improper* point (at infinite).

Appendix D

Calibration Toolbox for Matlab

In this appendix, the calibration procedure with the *Calibration Toolbox for Matlab* [60] is described by means of four main steps. The procedure is based on Zhang's work [61]. One of the cameras of the experimental setup illustrated in Fig. 5.2 is considered for reference. Several pictures of a checkerboard with known physical dimensions are taken in different positions and orientations. The checkerboard is shown in Fig. 5.2 (c) and here reported in Fig. D.1.

Figure D.1: Calibration procedure.

1. The calibration guide of the toolbox, here reported in Fig. D.2, is run.

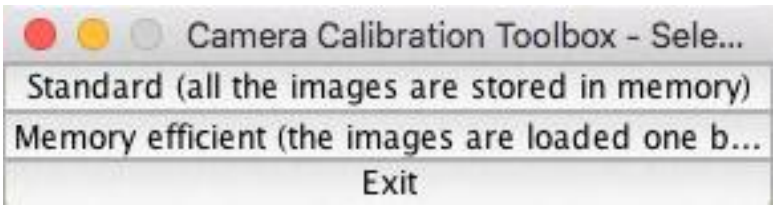

Figure D.2: Menu.

As seen in Subsection 5.1.2, a number of images taken by the camera are considered. Even if three images are theoretically sufficient, in our experiment we consider 12 images of the checkerboard, freely translated and rotated in space [61]. Thus, as all the 12 images considered for the camera are stored in memory, the *Standard (all images are stored in memory)* option is selected.

2. A second window is now opened as in Fig. D.3:

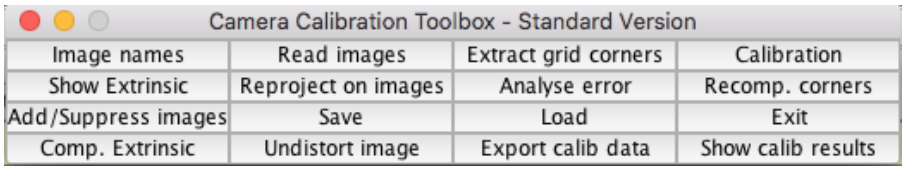

Figure D.3: Options window.

Thus, *Image names* is selected: in the Matlab window, it is asked to specify the name and the format of the images. Then, by clicking on *Read images*, the images are uploaded.

3. The option *Extract grid corners* is now selected. This operation consists in the selection of four corners for each image to delimit the part of the image in which the software will look for the squares of the checkerboard: in this case, as the 9×9 squares checkerboard is not fully visible by all the cameras for the 12 common images selected, in this work the four corners that are chosen will identify a 5×7 square checkerboard. The order of selection of the corners is important: the first selected corner is considered to be the origin of the reference system attached to the checkerboard. The selection of the three following points determines the orientation of the reference system: thus, it is crucial that the origin and the orientation of the reference systems attached to each image of the checkerboard are consistent between every image. This procedure is illustrated in Fig. D.4 (only one image is considered).

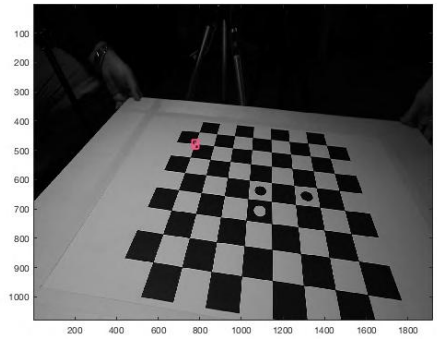

(a) *Selection of the first corner: this point becomes the origin of the reference system attached to the checkerboard.*

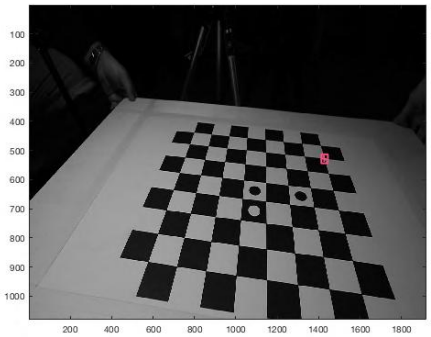

(b) *Selection of the second corner: the orientation selected is clockwise.*

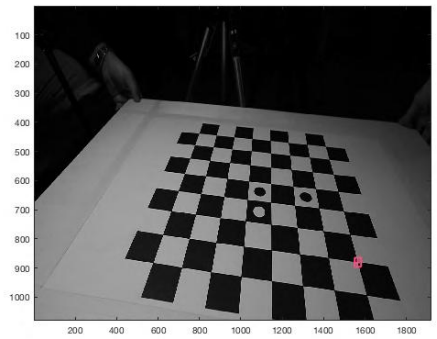

(c) *Selection of the third corner.*

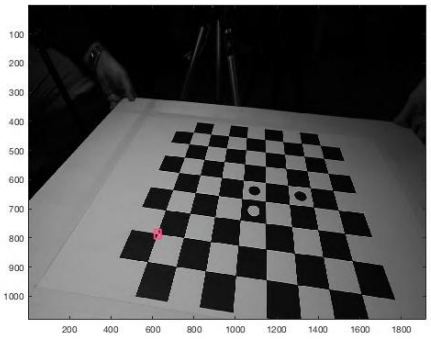

(d) *Selection of the fourth and last corner.*

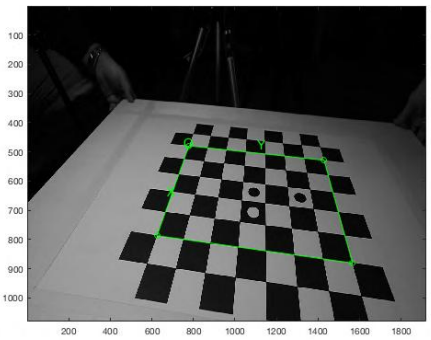

(e) *The selection of the four corners leads to the identification of 5x7 squares checkerboard.*

Figure D.4: Selection of the corners of the grid.

Thus, the program automatically counts the number of squares in both dimensions and shows the predicted grid corners in absence of distortion as shown in Fig. D.5:

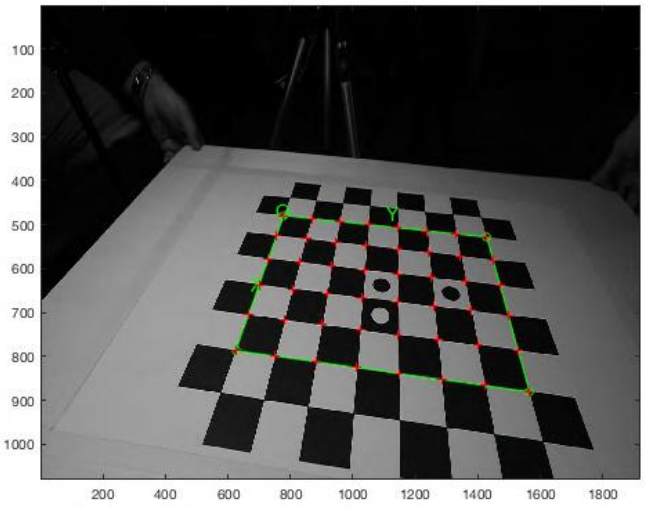

Figure D.5: Recognition of the squares in the selected grid.

If the extracted corners (in red) are close to those of the physical checkerboard, it is possible to skip to the next step. Otherwise, if the image presents a strong distortion, the software allows to guess an initial value for the distortion coefficient (usually called as k_c) and recalculates the position of the corners: this operation can be done several times until the results are satisfactory (i.e. the red crosses are as close as possible to those of the physical checkerboard). This procedure is applied to all the 12 images.

4. The *Calibration* button on the menu of Fig. D.3, is selected: the software computes the calibration on the basis of the corners extracted in each image. The calibration is done in two steps: first, an initialization step, then a non-linear optimization step. The initialization step computes a closed-form solution for the calibration parameters not including any lens distortion. The non-linear optimization step minimizes the total re-projection error over all the calibration parameters. The optimization is done by iterative gradient descent with an explicit computation of the Jacobian matrix. It is possible to refine the results by clicking on *Recomp. corners* in the menu of Fig. D.3: in this way the re-projected grid is used as initial guess locations for the corner. Then, the *Calibration* option has to be computed again. As a result, this calibration procedure gives a matrix of intrinsic parameters $\mathbf{K}$ and a matrix of extrinsic parameters $\mathbf{P}_i$ for each image (i.e. in this case $i = 1, 2, \ldots 12$). Thus, each matrix of extrinsic parameters represents the rototranslation transformation that relates the coordinates of a generic point in the camera reference system with its coordinates in the 3D reference system attached to the checkerboard, which is supposed to lie on the X_i, Y_i plane with $Z_i = 0$. Therefore, for the $i - th$ image (with $i = 1, 2, \ldots 12$), the perspective projection matrix $\mathbf{P}_i$ is given by Eq. D.1:

$$\mathbf{P}_i = \mathbf{K} \left[\mathbf{R}_i \mid \mathbf{t}_i \right], \tag{D.1}$$

where $\mathbf{K}$ is the matrix of the intrinsic parameters and $\left[\mathbf{R}_i \mid \mathbf{t}_i\right]$ is the matrix of the extrinsic parameters. In particular $\mathbf{R}_i$ is the matrix that represents the rotation of coordinates between the reference system of the camera and the reference system of the $i-th$ grid (i.e. the grid of the $i-th$ image) and $\mathbf{t}_i$ is the vector that represents the translation.

The twelve resulting matrices of perspective projection represent all the same camera with different orientations depending on the orientation of the checkerboard in each image. Thus, it is possible to pick one of these matrices as representative of the considered camera: in this work $\mathbf{P}_1$, i.e. the matrix of perspective projection relative to the first image of the checkerboard is taken. By repeating the procedure for all the four cameras A, B, C, D, four MPPs referred to the first checkerboard, i.e. $\mathbf{P}_{1,A}$, $\mathbf{P}_{1,B}$, $\mathbf{P}_{1,C}$, and $\mathbf{P}_{1,D}$, are obtained. The MPP estimates for the four cameras can be refined using the bundle adjustment method explained in Appendix E: the coordinates of the corners of the checkerboard in the first image can be obtained from $\mathbf{P}_{1,j}$ (with $j = A, B, C, D$), so that these matrices can be refined through the minimization of the re-projection error. At the end of the calibration process, the 3D location of a point in space, referred to the reference system of the checkerboard in the first image, can be obtained by triangulation.

Appendix E

Bundle Adjustment

In this appendix, the *bundle adjustment* method, which is a procedure applied in photogrammetry when several cameras are used to detect a scene, is described. This method is based on the minimization of the global error of reprojection of all the 3D points that are visible in the images.

N cameras detecting n points are considered. The $j-th$ camera is defined by its perspective projection matrix $\mathbf{P}^j$. The $i-th$ point $\mathbf{M}_i$ in a 3D space $OXYZ$ and its projection $\mathbf{m}_i^j$ on the image plane of the $j-th$ camera, are defined in accordance with Fig. 2.6, here reported in Fig. E.1 for simplicity.

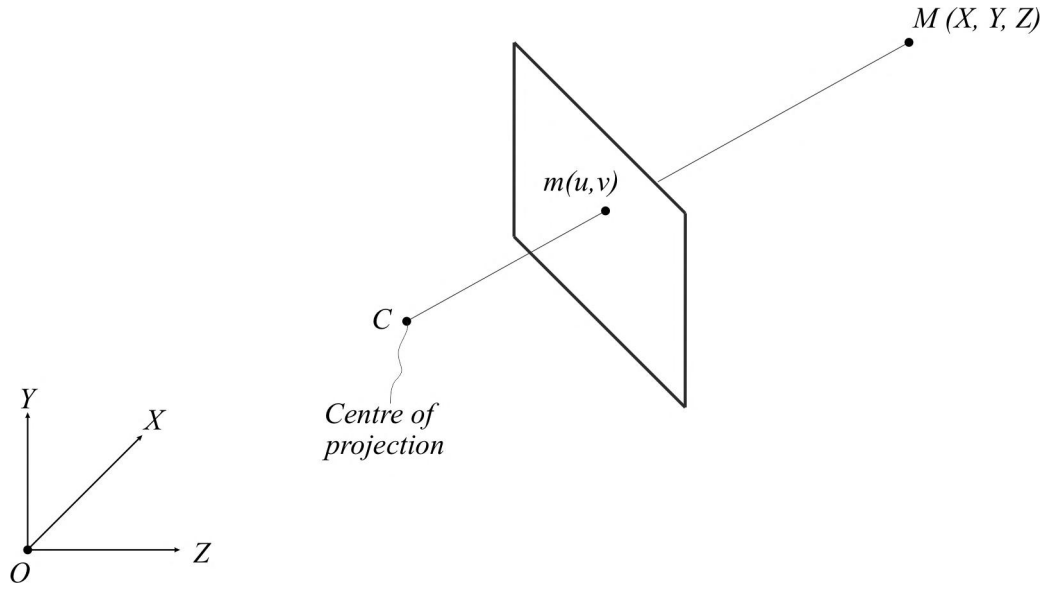

Figure E.1: Projection of a point $\mathbf{M}_i$ on the image plane.

The main goal of bundle adjustment is to recalculate the extrinsic parameters of the N cameras as well as the n positions of the 3D points in order to minimize the square distances between the $i-th$ point reprojected through the $j-th$ camera, i.e. $\mathbf{P}^j\mathbf{M}_i$, and the measured point $\mathbf{m}_i^j$. This minimization relies on the following Eq. E.1:

$$\min_{\mathbf{R}^j,\mathbf{T}^j,\mathbf{M}_i} \sum_{j=1}^{N}\sum_{i=1}^{n} d(\mathbf{K}^j[\mathbf{R}^j \mid \mathbf{T}^j]\mathbf{M}_i, \mathbf{m}_i^j)^2. \tag{E.1}$$

In this equation, $\mathbf{K}^j$ is the matrix of the intrinsic parameters of the $j-th$ camera, $[\mathbf{R}^j \mid \mathbf{T}^j]$ is the matrix of the extrinsic parameters of the $j-th$ camera and d is the distance on the euclidean plane. Furthermore, the intrinsic parameters can also be considered as varied parameters in Eq. E.1: as a consequence, the bundle adjustment method allows also to refine the values of the intrinsic parameters. This is useful especially when the values of these parameters come from unreliable estimates (i.e. autocalibration [54]). The minimization of Eq. E.1 is a least squares solution of a system of non linear equations.

Appendix F

Marker tracking

In this appendix, the algorithm for the tracking of the markers is revised in detail. To start with, the position of the reference system attached to the beam and the enumeration of the markers are recalled with respect to a schematic representation of Fig. 5.2 (b), here reported for simplicity in Fig. F.1.

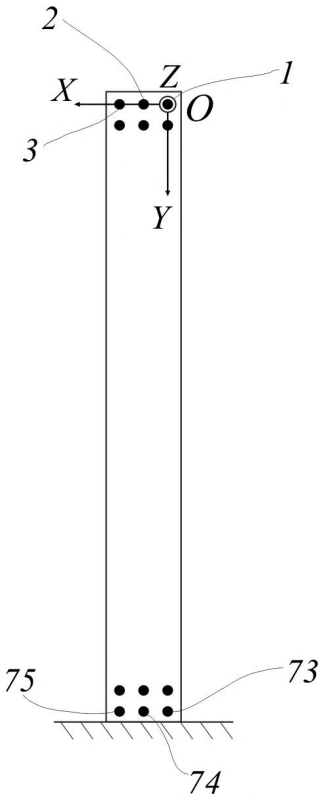

Figure F.1: Numeration of the markers.

The algorithm for tracking the markers is implemented after the synchronization of the recordings of the measurement of the vibration of the beam and the subdivision of these recordings in single frames, as discussed in Subsection 5.1.2. Each frame represents a screenshot of the beam in a certain position: a single frame of the recorded video is reported in Fig. F.2. In this appendix, similarly to Appendix D, only Camera A of Fig. 5.2 is considered.

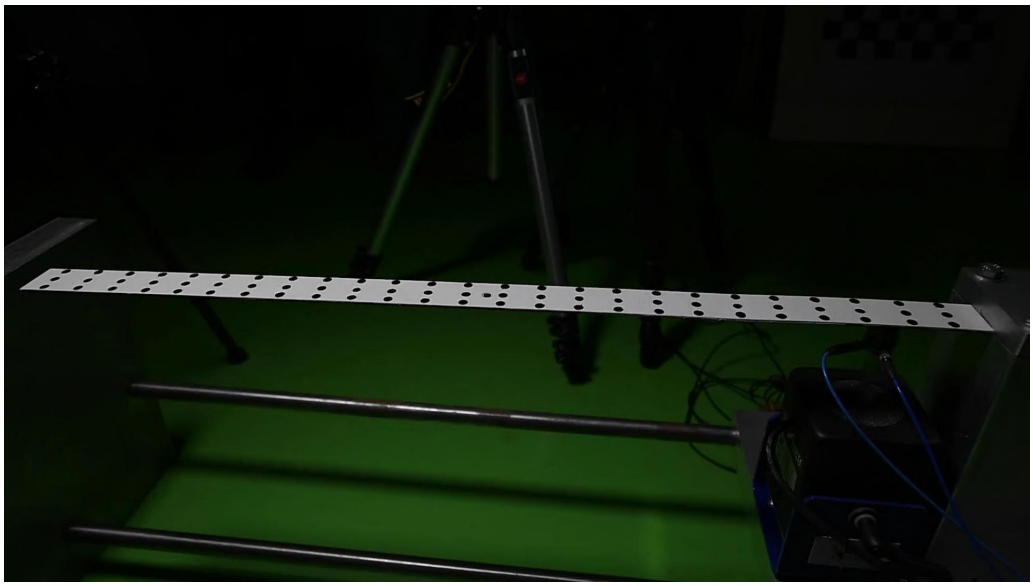

Figure F.2: Frame 1 of camera A.

The position and the orientation of the camera distort the shape of the markers that will no longer appear circular. Thus, it is necessary to apply a homography [54] in order to undistort the image. The homography is defined by selecting four points on the image: the order of selection of these points has to be compliant with the one used during the calibration (as seen in Appendix D) and with the reference system attached to the beam of Fig. F.1. Furthermore, the image is represented in black and white to emphasize the contrast between the beam, the markers and the surrounding space. The procedure of selection of the points is represented in Fig. F.3:

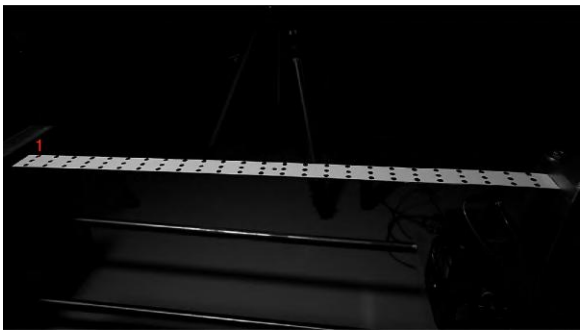

(a) *Selection of the first corner: this point becomes the origin of the reference system attached to the checkerboard.*

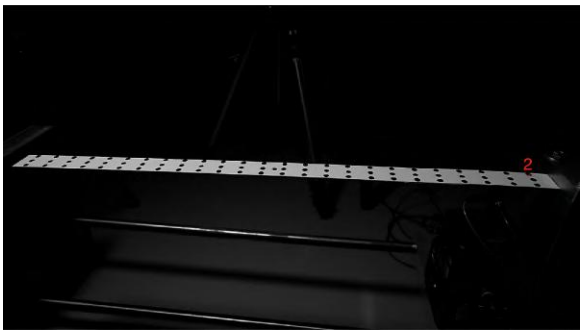

(b) *Selection of the second corner: the orientation selected is clockwise.*

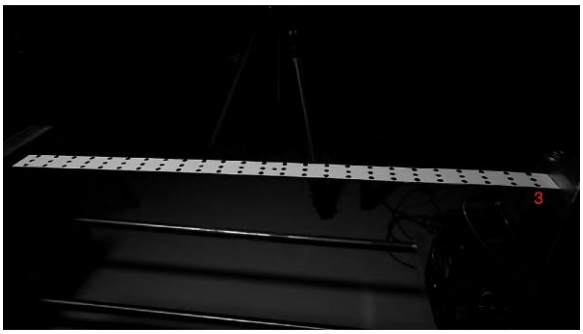

(c) *Selection of the third corner.*

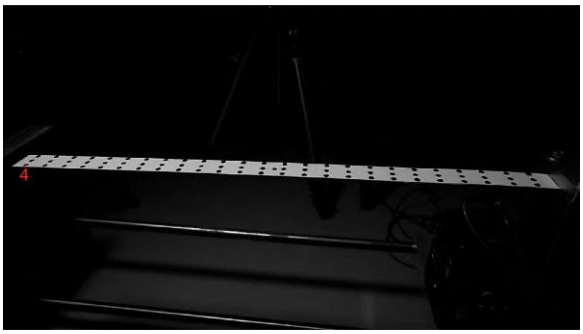

(d) *Selection of the fourth and last corner.*

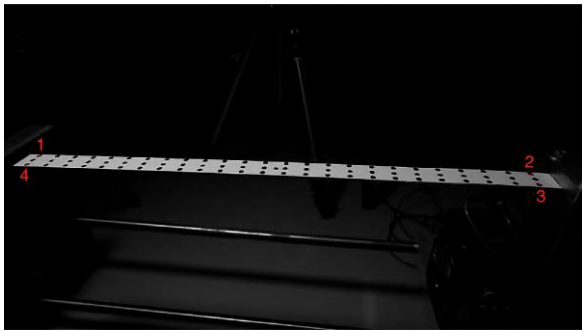

(e) *The selection of the four corners.*

Figure F.3: Selection of the corners for the homography.

The homography leads to a representation of the beam on the plane OXY as illustrated in Fig. F.4. This image of the undistorted beam is cropped in order eliminate unnecessary elements that do not belong to the beam and that can thus interfere with the detection of the markers.

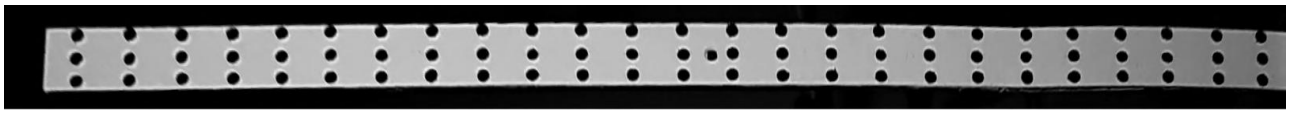

Figure F.4: Beam after homography and black and white transformation.

The position of the markers is identified by means of a matching algorithm which searches for the maximum correspondence between a template and the undistorted image of the beam. Here, the

markers have a circular shape of 5 mm diameter, therefore the template is set accordingly. In order to ease the matching, an ideal grid of 76 points, which is represented by the purple crosses in Fig. F.5 and in Fig. F.6 (a), is implemented on the image: each point of this ideal grid will be considered as the starting searching point for the nearest marker. As seen in Subsection 5.1.1 and in Fig. F.1, three lines of 25 markers are attached on the beam, for a total of 75 markers. However, the ideal grid is composed of 76 markers, as seen in Fig. F.5. In fact, the beam considered in the experimental study has a hole, which is the only point not aligned to any row of markers. Thus, to ease the matching, the hole is tracked as a marker and excluded in post processing.

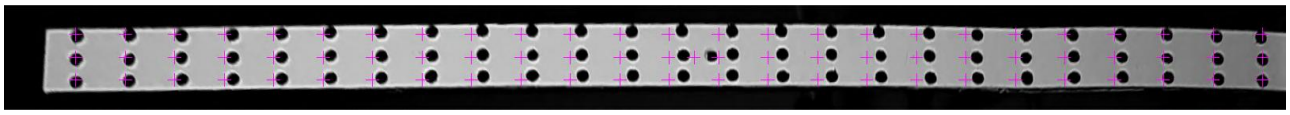

Figure F.5: Comparison between marker grid and ideal grid (purple crosses).

Now, the points that best correspond to the template are detected: the matching relies on the so called Hungarian method which is a combinatorial optimisation algorithm that solves the assignment problem in polynomial time. The result of the matching is reported in Fig. F.6:

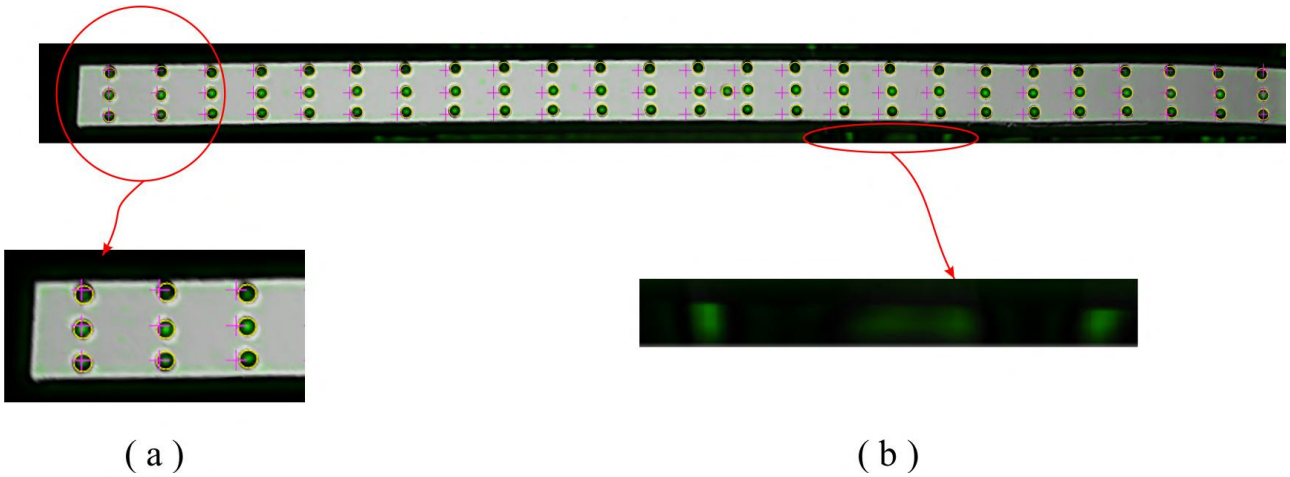

Figure F.6: Beam with detected markers: (a) detail of the purple crosses of the ideal beam; (b) detail of external parts of the beam recognized as valid points by the matching algorithm.

The green colored elements of Fig. F.6 represent the parts of the image in which the correspondence between the image and the template is maximum accordingly to the matching algorithm. As previously seen, the template matching algorithm searches for points in the whole image. Thus, it is possible that unwanted regions of the image, in this case outside the beam, could be recognized as valid points: an example is given in Fig. F.6 (b). This issue becomes more problematic as the resolution of the cameras is decreased. Thus, the two steps of cropping the image and implementing the ideal grid, seen in Fig. F.4 and F.5, are crucial: these two processes limit the field of research so that unnecessary points can be excluded.

Finally, the last step of the tracking process can be executed. This last step consists in the

application of the inverse of the homography seen in Fig. F.3, so that the detected points can be represented in the image space of the camera. The result is shown in Fig. F.7 in which the green crosses represent the points identified by the algorithm of tracking of the markers: it is possible to notice that, in this case, the markers where all successfully recognized.

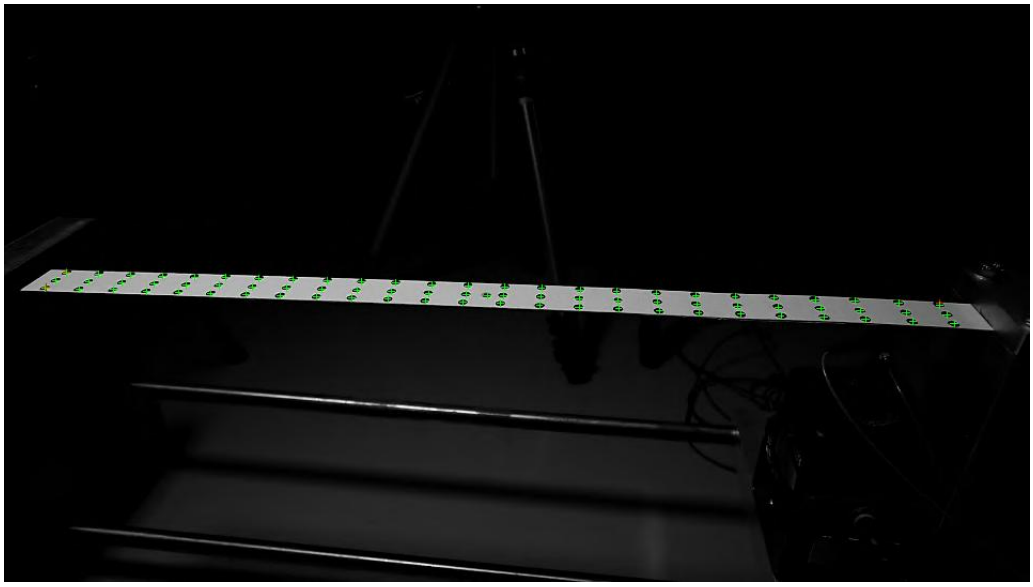

Figure F.7: Beam with detected markers represented in the image space of camera A.

This process is repeated for every frame considered and for every camera. The position of the markers identified with this procedure will be used in the triangulation process to reconstruct the displacement of the beam.